GDAŃSK UNIVERSITY
OF TECHNOLOGY
FACULTY OF CHEMISTRY

The author of the PhD dissertation: Dominik Knozowski
Scientific discipline: Chemical Sciences

DOCTORAL DISSERTATION

Title of PhD dissertation: Composite Materials Based on Silicon Oxycarbide as Anodes for Lithium-Ion Batteries

Title of PhD dissertation (in Polish): Materiały Kompozytowe Oparte o Tlenowęgliki Krzemu jako Anody do Ogniw Litowo-Jonowych

Supervisor *signature*	Second supervisor *signature*
Dr hab. inż Monika Wilamowska-Zawłocka, prof. PG	<Title, degree, first name and surname>
Auxiliary supervisor *signature*	Cosupervisor *signature*
<Title, degree, first name and surname>	<Title, degree, first name and surname>

Gdańsk, year 2022

STATEMENT

The author of the PhD dissertation: <first name, surname>

I, the undersigned, agree that my PhD dissertation entitled:
Composite Materials Based on Silicon Oxycarbide as Anodes for Lithium-Ion Batteriesmay be used for scientific or didactic purposes.[1]

Gdańsk,..................................... ....

signature of the PhD student

Aware of criminal liability for violations of the Act of 4th February 1994 on Copyright and Related Rights (Journal of Laws 2006, No. 90, item 631) and disciplinary actions set out in the Law on Higher Education (Journal of Laws 2012, item 572 with later amendments),[2] as well as civil liability, I declare, that the submitted PhD dissertation is my own work.

I declare, that the submitted PhD dissertation is my own work performed under and in cooperation with the supervision of Monika Wilamowska-Zawłcka.

This submitted PhD dissertation has never before been the basis of an official procedure associated with the awarding of a PhD degree.

All the information contained in the above thesis which is derived from written and electronic sources is documented in a list of relevant literature in accordance with art. 34 of the Copyright and Related Rights Act.

I confirm that this PhD dissertation is identical to the attached electronic version.

Gdańsk,..................................... ....

signature of the PhD student

I, the undersigned, agree to include an electronic version of the above PhD dissertation in the open, institutional, digital repository of Gdańsk University of Technology, Pomeranian Digital Library, and for it to be submitted to the processes of verification and protection against misappropriation of authorship.

Gdańsk,..................................... ....

signature of the PhD student

---

[1] Decree of Rector of Gdansk University of Technology No. 34/2009 of 9th November 2009, TUG archive instruction addendum No. 8.

[2] Act of 27th July 2005, Law on Higher Education: Chapter 7, Criminal responsibility of PhD students, Article 226.

GDAŃSK UNIVERSITY
OF TECHNOLOGY
FACULTY OF CHEMISTRY

DESCRIPTION OF DOCTORAL DISSERTATION

The Author of the PhD dissertation: Dominik Knozowski

Title of PhD dissertation: Composite Materials Based on Silicon Oxycarbide as Anodes for Lithium-Ion Batteries

Title of PhD dissertation in Polish: Materiały Kompozytowe Oparte o Tlenowęgliki Krzemu jako Anody do Ogniw Litowo-Jonowych

Language of PhD dissertation: English

Supervision: Dr hab. inż Monika Wilamowska-Zawłocka, prof. PG

Date of doctoral defense:

Keywords of PhD dissertation in Polish: Materiały kompozytowe; Tlenowęgliki krzemu; Ceramika pochodzenia polimerowego; Magazynowanie energii; Baterie litowo-jonowe

Keywords of PhD dissertation in English: Composite materials, Silicon Oxycarbides; Polymer Derived Ceramics; Energy storage; Lithium-ion batteries

Summary of PhD dissertation in Polish: W niniejszej pracy opisano właściwości kompozytów podwójnych SiOC/grafit i SiOC/cyna, a także kompozytów potrójnych SiOC/grafit/cyna powstałych na bazie różnych prekursorów preceramicznych. Pierwszym etapem prac była synteza materiałów różnymi metodami, m.in. zol-żel oraz hydrosilisowania. Aby zapobiec procesowi sedymentacji i aglomeracji grafitu podczas żelowania, bez konieczności dodawania surfaktantów lub zagęszczaczy, opracowano metodę przyspieszonego żelowania i jednoczesnej homogenizacji z wykorzystaniem ultradźwięków wysokiej mocy. Metoda ta umożliwiła jednorodne rozprowadzane cząstek grafitu w blendzie polimerowej, a ponadto wytworzone ciepło skróciło proces żelowania z kilku dni do kilku godzin. W kolejnym etapie wykonano badania strukturalne i elektrochemiczne uzyskanych kompozytów. Dokładnie zbadano różnymi technikami fazę węglową, ceramiczną oraz cynową pod kątem ilości, struktury, morfologii, dystrybucji, a także pod kątem reakcji jakie mogły zajść podczas procesów syntezy badanych kompozytów. W przypadku badań elektrochemicznych skupiono się przede wszystkim na zależności pomiędzy ilością dodatku do ceramiki, rodzajem prekursora preceramicznego i wynikającą z tego mikrostrukturą otrzymanych kompozytów, a ich właściwościami elektrochemicznymi.

Summary of PhD dissertation in English: In this work, the properties of binary SiOC/graphite and SiOC/tin, as well as ternary SiOC/graphite/tin obtained from various preceramic precursors are described. During the first step, the materials were synthesized using various techniques such as sol-gel and hydrosilylation. To prevent sedimentation and agglomeration of graphite particles during the gelation stage without using surfactants and thickeners, a new gelation technique with utilizing simulations homogenisation and high-power ultrasounds was developed. This method enables a uniform distribution of graphite particles in a polymer blend. In addition, heat generated during this process shortens the gelation time from a few days to a few hours. In the second step, structural and electrochemical characterisation of the obtained materials was conducted. The carbon, ceramic and tin phases were carefully studied in terms of the quantity, structure, morphology, distribution, and in terms of possible reactions that could occur during the synthesis of the materials. In the case of electrochemical measurements, primary focus was on relationships between the content of the additives, the preceramic precursor type, and the resulting microstructure of the composites which influences their final electrochemical properties.

GDAŃSK UNIVERSITY
OF TECHNOLOGY
FACULTY OF CHEMISTRY

Fundusze Europejskie
Inteligentny Rozwój

Rzeczpospolita Polska

FNP Fundacja na rzecz Nauki Polskiej

Unia Europejska
Europejski Fundusz Rozwoju Regionalnego

Part of the work was financially supported by Foundation for Polish Science under REINTEGRATION program, project Nº POIR.04.04.00-00-4582/17-00.

Contents

List of selected abbreviations

BDDA	-	1,4-butanediol diacrylate
BET method	-	a method developed by Brunauer, Emmett, and Teller for specific surface area measurements
BSE (SEM)	-	backscattering mode in scanning electron microscopy
CMC	-	carboxymethyl cellulose
CNTs	-	carbon nanotubes
CV	-	cyclic voltammetry
CVD	-	chemical vapour deposition
DDCA	-	dry chemical control additives
DVB	-	divinylbenzene
EDL	-	electrochemical double layer
EDX	-	energy dispersive X-ray spectrometer
EELS (PEELS)	-	electron energy loss spectroscopy (parallel electron energy loss spectroscopy)
EIS	-	electrochemical impedance spectroscopy
EtOH	-	ethanol
FCE	-	first-cycle Coulombic efficiency
FT-IR	-	Fourier-transformed infrared spectroscopy
GDC	-	the galvanostatic charge-discharge technique
HAADF	-	high-angle annular dark-field imaging
LIBs	-	lithium-ion batteries
Li_xSn	-	tin alloys with the different lithium-tin ratio
LTO	-	lithium titanate oxide
MAS NMR	-	magic angle spinning solid-state nuclear magnetic resonance

MN GF-2 - glass fibre filter, thickness 0.65 mm

NMP - N-methyl 2-pyrrolidone

OTES - octyltriethoxysilane

PDCs - polymer derived ceramics

PhTES - phenyltriethoxysilane

PMHS - polymethylhydroxiloxane

PVDF - polyvinylidene fluoride

SE (SEM) - secondary electrons mode in scanning electron microscopy

SECM - scanning electrochemical microscopy

SEI - solid-electrolyte interphase

SEM - scanning electron microscopy

SFG - spherical graphite provided by Imerys Graphite & Carbon Company

SiCNs - silicon carbon nitrades

SiOCs - silicon oxycarbides

SiO_x - sub-silicon oxides

SOC - state of charge

SPR-684 - inorganic polymer resin provided by Starfire Systems company

SSA - specific surface area, $m^2\ g^{-1}$

STEM - scanning transmission electron microscopy

TEM - transmission electron microscopy

TGA-DSC - thermal gravimetric analysis conjugated with differential scanning calorimetry

VTES - vinyltriethoxysilane

XPS - X-ray photoelectron spectroscopy

XRD - X-ray diffractography

Streszczenie rozprawy doktorskiej

Tlenowęgliki krzemu (*ang. silicon oxycarbides*, SiOCs,) stanowią grupę materiałów ceramicznych o bardzo zróżnicowanych właściwościach fizyko- i elektrochemicznych w zależności od struktury i składu chemicznego. SiOCs są interesującymi materiałami anodowym do zastosowań w bateriach litowo-jonowych ze względu na swoją wysoką aktywność elektrochemiczną wobec jonów litu i nawet dwukrotnie większą pojemność elektryczną niż powszechnie stosowany grafit. Jednakże, główną wadą materiałów opartych na SiOC jako anod baterii Li-jonowych jest duża nieodwracalna pojemność pierwszego cyklu wprowadzania jonów litu. Zminimalizować ten problem oraz polepszyć ogólne parametry elektrochemiczne można poprzez odpowiedni dobór prekursorów preceramicznych, a także tworzenie kompozytów z innymi materiałami. W projektowaniu nowych materiałów trzeba mieć na uwadze, że właściwości końcowe otrzymanych kompozytów mogą diametralnie różnić się w zależności od proporcji poszczególnych komponentów oraz zastosowanego prekursora, a wynik takiego połączenia może być odmienny niż wskazywałyby na to właściwości poszczególnych składników.

W niniejszej pracy opisano właściwości kompozytów podwójnych SiOC/grafit i SiOC/cyna, a także kompozytów potrójnych SiOC/grafit/cyna powstałych na bazie różnych prekursorów preceramicznych. Pierwszym etapem prac była synteza materiałów różnymi metodami, m.in. zol-żel oraz hydrosilisowania. Aby zapobiec procesowi sedymentacji i aglomeracji grafitu podczas żelowania, bez konieczności dodawania surfaktantów lub zagęszczaczy, opracowano metodę przyspieszonego żelowania i jednoczesnej homogenizacji z wykorzystaniem ultradźwięków wysokiej mocy. Metoda ta umożliwiła jednorodne rozprowadzane cząstek grafitu w blendzie polimerowej, a ponadto wytworzone ciepło skróciło proces żelowania z kilku dni do kilku godzin.

W kolejnym etapie wykonano badania strukturalne i elektrochemiczne uzyskanych kompozytów. Dokładnie zbadano różnymi technikami fazę węglową, ceramiczną oraz cynową pod kątem ilości, struktury, morfologii, dystrybucji, a także pod kątem reakcji jakie mogły zajść podczas procesów syntezy badanych kompozytów. W przypadku badań elektrochemicznych skupiono się przede wszystkim na zależności pomiędzy ilością dodatku do ceramiki, rodzajem prekursora preceramicznego i wynikającą z tego mikrostrukturą otrzymanych kompozytów, a ich właściwościami elektrochemicznymi. Wykazano, że dodatek

grafitu do ceramiki bogatej w węgiel powodował polepszenie właściwości podczas ładowania wysokimi prądami, z kolei pojemność elektryczna nie ulegała poprawie. Z kolei wprowadzenie grafitu do ceramiki ubogiej w węgiel powodowało wzrost pojemności, w szczególności podczas ładowania niskimi gęstościami prądu. Ponadto, największą poprawę powyższych właściwości zaobserwowano, gdy dodatek grafitu do ceramiki bogatej w węgiel był wysoki, a do ubogiej – niski. Niespodziewanym efektem był też fakt, że dodatek grafitu minimalizował nieodwracalną pojemność pierwszego cyklu tylko w przypadku ceramiki o niskiej zawartości węgla. Z kolei w przypadku kompozytów potrójnych, dodatek grafitu umożliwił wprowadzenie nanocząstek cyny w ilości większej, niż opisywanej wcześniej w literaturze, bez utraty stabilności finalnego materiału w wydłużonych cyklach ładowania i rozładowania.

Abstract

Silicon oxycarbides (SiOCs) are a class of materials with a wide range of physicochemical and electrochemical properties, depending on their structure and elemental composition. SiOCs are very appealing anodic materials for application in lithium-ion batteries due to their high electrochemical activity towards lithium ions and up to twice as high electrochemical capacity as the commonly used graphite. However, the main drawback of SiOC-based materials for anodes in lithium-ion batteries is high irreversible capacity of the first lithiation cycle. An appropriate selection of the preceramic precursor as well as creation of composites with other materials can reduce the problem of high irreversible capacity and, at the same time, it can improve general electrochemical properties of the final material. In the design of new composites, one has to bear in mind that the final properties of the obtained materials strongly depend on their components and the preceramic precursor used, and that the final material can somewhat vary from what can be expected, considering the properties of the starting components.

In this work, the properties of binary SiOC/graphite and SiOC/tin, as well as ternary SiOC/graphite/tin obtained from various preceramic precursors are described. During the first step, the materials were synthesized using various techniques such as sol-gel and hydrosilylation. To prevent sedimentation and agglomeration of graphite particles during the gelation stage without using surfactants and thickeners, a new gelation technique with utilizing simulations homogenisation and high-power ultrasounds was developed. This method enables ~~a~~ uniform distribution of graphite particles in a polymer blend. In addition, heat generated during this process shortens the gelation time from a few days to a few hours.

In the second step, structural and electrochemical characterisation of the obtained materials was conducted. The carbon, ceramic and tin phases were carefully studied in terms of the quantity, structure, morphology, distribution, and in terms of possible reactions that could occur during the synthesis of the materials. In the case of electrochemical measurements, primary focus was on relationships between the content of the additives, the preceramic precursor type, and the resulting microstructure of the composites–which influences their final electrochemical properties. It was shown that the addition of graphite to a carbon-rich ceramic improved the rate capability of the material. However, the electrochemical capacity was not enhanced. On the other hand, introduction of graphite into a

carbon-poor ceramic increased its electrochemical capacity, in particular when low current densities were applied. The most significant improvement of the electrochemical performance was observed when graphite was added in large quantities to carbon-rich ceramics, and in small quantities to the carbon-poor ceramic. Furthermore, unexpectedly, addition of graphite reduced the irreversible capacity of the first lithiation cycle only in carbon-poor ceramic composites. In the case of ternary composites, the addition of graphite allows for the introduction of tin nanoparticles in a higher amount than previously reported in the literature without the loss of the cycling stability.

Theoretical part

Introduction

Lithium-ion batteries (LIBs) are considered one of the most important inventions of the 20th century. It is a basic device that currently penetrated practically all areas of our life, starting from portable electronics such as laptops, smartphones, LCDs, and ending on afresh emerging electric bikes, cars, and other electric vehicles.[1] To give the perspective in numbers, in 2020 global battery market was valued at 108.4 billion USD ,[2] with ~40% being shared by LIBs,[3] and it is only expected to grow at a 14.1% rate every year between 2020-2027. Such a big growth is inseparably connected to ever-growing customers' demands. However, in recent years, there is observed a crisis in improving battery performance, dropping from 7-8%[4] annual gains in the past decade to only 1-2% in recent years.[5] The blame for this state is put onto the anodic materials, as the cathodes were a usually bigger concern and therefore nowadays there are plenty of cathodic materials to choose from.[4] As for anodes, in practice, there are only three groups of materials currently available: graphite, $Li_4Ti_5O_{12}$ (LTO), and graphite with the addition of silicon or sub-silicon oxides (SiO_x, $0 \leq x \leq 2$).[6,7] Right now the highest capacity is achieved by graphite/SiO_x and graphite/Si anodes thanks to the high capacity of SiO_x (above 1965 mAh g^{-1}) and Si (~3600 mAh g^{-1}) in contrast to 372 mAh g^{-1} offered by the graphite. Unfortunately, the content of SiO_x and Si in such anodes does not exceed 5% due to performance problems.[6,8]

The solution to the limitations of electrochemical performance of today's anodic materials is composite anodes. Composites combine the desired properties of various materials in one, new material. Usually, composite materials are produced in a way that one component exhibits extraordinary features, like high capacity or good electrochemical stability, while the second one mitigates the drawbacks of the first material. The key issue is the proper selection of components for composites and their homogeneous mixing. The materials should be combined synergistic, i.e. the properties of the final material should be better than both components used separately. With that regard, silicon oxycarbides (SiOCs) are a very promising component of anodic composite materials, as they exhibit desired electrochemical properties (high capacity, good stability, decent conductivity) and their physicochemical properties and structure can be easily tailored to match other components of the composite materials.[9]

The main focus of this work are the synthesis, electrochemical and physicochemical characterisation of the selected anodic composite materials. The study was conducted on three different systems: SiOCs/graphite, SiOCs/tin nanoparticles and SiOCs /graphite/tin nanoparticles. The SiOCs/graphite composites were studied the most extensively, as the commercially used graphite was the component to minimize the main drawback of SiOCs, high initial irreversible capacity. Tin nanoparticles were incorporated into silicon oxycarbide and SiOCs/graphite matrices due to the high theoretical capacity of tin. The work is divided into 10 chapters. Chapter 1 provides a general introduction to lithium-ion batteries, i.e. working principle, basic equations, construction of lithium-ion batteries, and typical material base. The chapters 2-4 present a literature survey concerning structural studies, physical properties, synthesis, and electrochemical features (lithiation process, solid-electrolyte interface formation, etc.) of SiOCs, graphite, and tin. Chapter “Materials” lists the materials and techniques used in the studies, along with the list of equipment. Chapters 5 and 6 present the syntheses procedures and a detailed description of conducted measurements. Chapters 7-9 present the results of the conducted research on SiOCs/graphite, SiOCs/tin nanoparticles and SiOCs/graphite/tin nanoparticles, respectively. The last chapters summarize the research and suggest further direction for the development of the presented composites.

Chapter 1. Lithium-ion batteries

1.1. General Information

Lithium-ion batteries (LIBs) are energy storage devices, which took their name from lithium ions – key components of electrochemical reactions.[10] Lithium ions are considered the most appealing ions due to the small size, high charge-to-size ratio, and the lowest electrochemical potential of $Li \leftrightarrow Li^+$ transition. Therefore, lithium-based batteries are one of the most developed battery technologies in the world.[11–13]

LIBs belong to the family of secondary (rechargeable) batteries. It means that after a natural (spontaneous) process of discharging of the electrochemical cell unit, it can be reversible charged (i.e. it can return to the previous chemical state) by applying external current. Thus, secondary batteries can be used effectively hundreds of times, in contrast to primary batteries, which after discharge cannot be reused effectively.[14]

LIBs are the most advanced energy storage devices currently available. The typical evaluation of energy storage devices is based on specific power and specific energy (power/energy divided by the mass of the device), which is presented in the Ragone plot (**Figure 1.1**). LIBs have both the highest specific energy (90 – 250 Wh kg^{-1}) and specific power (up to 10 000 W kg^{-1}) among all currently available batteries. Additionally, LIBs possess a series of other positive features, which are superior compared to other battery systems:

- long life cycle - 1000-2000 cycles in comparison to few hundred for other batteries (lead-acid, NiCd, NiMH),
- fast charging time - 1-4 h in comparison to over 8 h for lead-acid batteries,
- high cell voltage - over 3 V compared to 2 V or below for other battery systems,
- low toxicity,
- high Columbic efficiency - over 99% in contrast to 90% for other battery systems,
- low self-discharge,
- maintenance-free - does not require obligatory full discharging or full charging after a certain working period, it can be used after manufacturing until the end of the life.[15,16]

The biggest drawback of LIBs compared to other battery systems is the high cost and limited temperature window. Moreover, there are safety concerns, related to overcharge, overdischarge, overheating, temperature shocks, thermal runaway, etc.[17] These concerns force the application of intelligent battery protection circuits or cooling systems.[17,18]

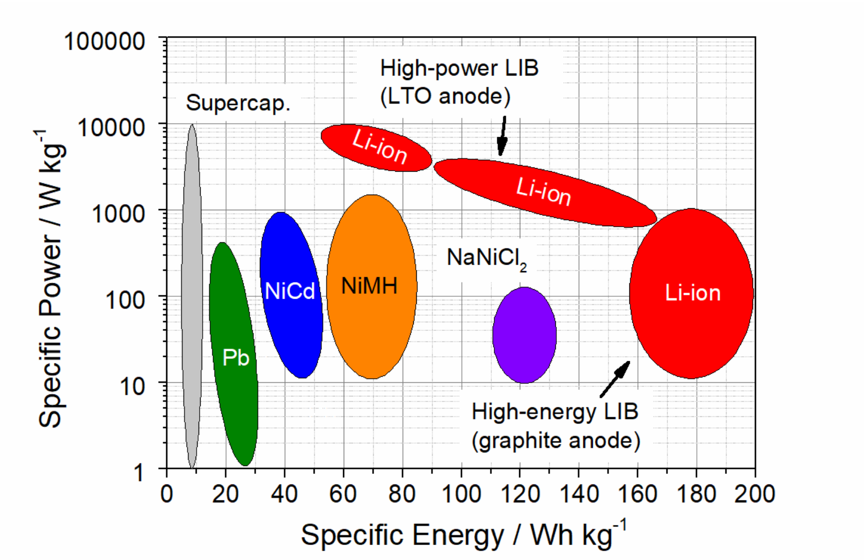

Figure 1.1. Ragone plot of energy storage devices

1.2. Electrochemical Principle

The working principle of LIBs is based on the processes occurring in four main cell components: anode, cathode, electrolyte, and external electrical connection. The anode and cathode are the two main components of the battery, on which reversible reactions with lithium ions occur. During these reactions, lithium ions are reversibly bonded or released from active material, and, in parallel, electrons are also bonded or released. These processes can be described as follows: [14]

$$Cathode: Li_xG^{pos.} \quad \underset{discharge}{\overset{charge}{\rightleftarrows}} \quad G^{pos.} + xLi^+ + xe^- \tag*{1)}$$

$$Anode: G^{neg.} + yLi^+ + ye^- \quad \underset{discharge}{\overset{charge}{\rightleftarrows}} \quad Li_yG^{neg.} \tag*{2)}$$

$$Cumulative: Li_xG^{pos.} + G^{neg.} + xLi^+ + xe^- \quad \underset{dischar.}{\overset{char.}{\rightleftarrows}} \quad G^{pos.} + xLi^+ + xe^- + Li_xG^{neg.} \tag*{3)}$$

$$Cumulative\ (simplified):\ Li_x G^{pos.} + G^{neg.} \underset{dischar.}{\overset{char.}{\rightleftarrows}} G^{pos.} + +Li_x G^{neg.} \qquad 4)$$

Where:

$G^{pos.}$ – cathode material

$G^{neg.}$ – anode material

In principle, in both anode and cathode lithium insertion and deinsertion processes occur, however, the reactions on the anode and cathode occur at vastly different potentials. The midpoint voltage (vs. Li/Li^+) for the cathode is between 3.45 – 4.6 V, while for anodes is between 0.2 – 1.5 V. This implies that connecting cathode in a form of $G^{pos.}$ to $Li_xG^{neg.}$ the anode in an electrochemical cell causes a spontaneous natural flow of electrons and ions from the anode to the cathode, so the process known as a discharge of a battery cell. The role of electrolyte and external electrical connections is to separate these two flows: electrons migrate through the electrical conductor, while ions flow through the electrolyte. This is achieved due to the physical properties of these media: the electrical conductor has a high electric conductivity but poor ionic conductivity, and electrolyte - *vice versa.*[14]

Graphical presentation of these processes are shown in **Figure 1.2**.

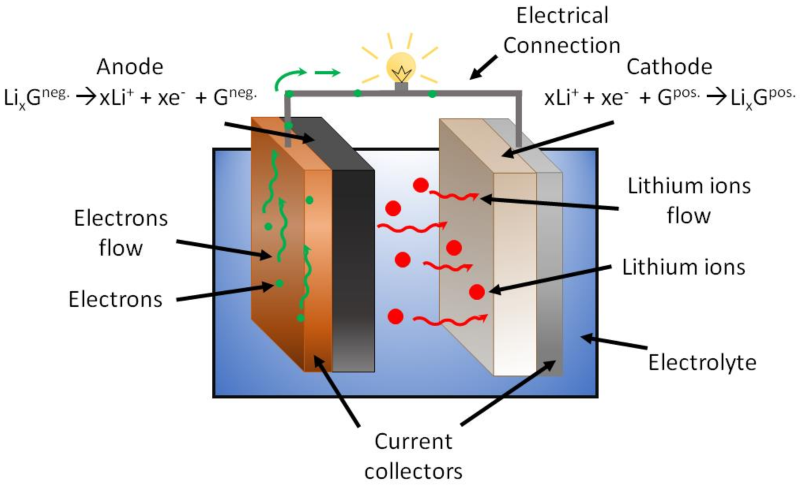

Figure 1.2. *Schematic process of spontaneous discharge of Li-ion batteries.*

From the thermodynamic point of view, the discharge of LIBs is related to the change of the Gibbs free energy (ΔG(x)), according to equation 5:

$$\Delta G(x) = -nFE_0(x) \qquad 5)$$

where: $E_0(x)$ – electromotive force (reaction advancement rate) (V), n – number of exchanged electrons, F – Faraday constant (~96 485 C).[14,19]

Electromotive force is equal to the difference between the standard electrode potential of the cathode and anode (open circuit potential). When the conditions are other than standard, an electromotive force describes the Nernst equation:

$$E = E_0 \pm \frac{RT}{nF} ln \frac{\sum_{i=1}^{n} Ox_i^{a_i}}{\sum_{i=1}^{n} Red_i^{b_i}} \qquad 6)$$

where: R – gas constant (8.314 J K^{-1} mol^{-1}), T – temperature (K), Ox – the activity of oxidized form, Red - the activity of reduced form, a, b - stoichiometric factors.[14,19]

From the practical point of view, the most important parameters of a battery are energy and power provided by the battery. Power is described as:

$$Power = IE \qquad 7)$$

where: I – current (A), E – electromotive force (V)

Energy is expressed by the equation:

$$Energy = \int E(C)dC \qquad 8)$$

where: E – electromotive force (V), C – electrochemical capacity (mAh g^{-1}).

Electrochemical capacity is defined as:

$$C = \frac{nF}{3.6\,MW} \qquad 9)$$

where: C - electrochemical capacity (mAh g^{-1}), n – number of exchanged electrons (in reaction 5)), F - Faraday constant (C), MW – molecular weight of the reactant.[20]

Generally, the capacity could be understood as the number of electrons that are consumed during electrochemical reactions within a certain potential window. Looking back at the equation (8), the highest energy is achieved when: *i)* the electrochemical reactions occur at the highest possible potential for the cathode and the lowest for the anode, *ii)* there is a massive exchange of the electrons during these reactions, i.e. the material has a high electrochemical capacity. Therefore, one of the goals of battery research is to produce materials with high capacity and low reaction potential with lithium ions for anodes, and high reaction potential for cathodes.

Power, on the other hand, is more related to the electromotive force than to capacity. However, the capacity, and thus energy, decreases when a high current is applied. Thus, the second most studied parameter during battery research is the change of capacity with the current increase, commonly known as the rate capability evaluation.

1.3. Battery Components

The typical LIB consists of the following components: anode, cathode, and electrolyte, which are the main electrochemical cell components, and additional parts, such as current collectors, separators, cans, or gaskets.[14]

As the anode materials, there are three commercially used materials: lithium titanate oxide (LTO), graphite, and silicon-based (Si and SiO_x) materials. Graphite is a staple anodic material used in most applications, while silicon and graphite/silicon anodes are a new high–energy option, and LTO is considered a safer alternative, used in i.e. power grids or medical devices.[6,14,16,21] Properties of graphite concerning its utilisation in LIBs are discussed in Chapter 3.

As the cathode materials, there are numerous materials available on the market. The oldest cathode material is $LiCoO_2$ (LCO). The problem with LCO is the high cobalt content, which is considered a harmful and expensive material. Thus, alternatives have been developed over the years, such as $LiMn_2O_4$, (LMO), $LiFePO_4$ (LFP), which does not contain cobalt, and materials with vastly reduced cobalt content, like $LiNiCoAlO_2$ (NCA) and the family of NMC materials ($LiNi_{1/3}Mn_{1/3}Co_{1/3}O_2$, $LiNi_{0.5}Mn_{0.3}Co_{0.2}O_2$, $LiNi_{0.6}Mn_{0.2}Co_{0.2}O_2$) with lower cobalt and higher nickel content. NMC materials have similar potential and capacity to LCO, and they exhibit better stability during thermal abuse. NCA materials have higher capacity, but for a cost of lower potential. LMO on the other hand has a lower capacity, but higher potential.

Predictions for the year 2025 show, that most of the market will be taken by NMC materials.[6,14,16,21]

Electrolytes used in batteries are organic solvents with lithium salts. The most popular solvents are carbonates due to their stability, safety, and compatibility with other components of LIBs. Among different carbonates, the important ones for battery applications are ethylene carbonate (EC), propylene carbonate (PC), dimethyl carbonate (DMC), ethyl methyl carbonate (EMC), diethyl carbonate (DEC), fluoroethylene carbonate (FEC). In the battery system, typical electrolyte composition consists of 2 – 5 solvents, with approx. 2% additives such as FEC or VC (vinyl carbonate). Lithium salts include various fluorine-containing salts. The main advantage of these salts is high ionic conductivity in organic media. The most popular salt is $LiPF_6$. However, due to high reactivity with water, which leads to the evolution of HF, other systems are under development. Among available salts, the important ones to mention are $LiBF_6$, $LiB(C_2O_4)_2$, $LiN(CF_3SO_2)_2$, $LiN(FSO_2)_2$. [14,16,21–23]

To achieve a high volumetric capacity and to avoid dead volume, the distance between the anode and cathode has to be very small. The steady distance and electrical separation are provided by separators. Separators are usually made of two or three layers of polyethylene and polypropylene, with a total thickness of 10 – 25 μm. Some companies offer also ceramic separators such as Al_2O_3 or AlOOH.[14]

The remaining elements of LIBs are the battery case and supporting items like current collectors. Anodic current collectors are usually made of thin copper foil, while the cathodic current collectors are made of aluminium.[14]

1.4. Battery Types

LIBs are currently produced in four different cell types: cylindrical, prismatic, pouch, and coin (**Figure 1.3**).[6,24] Cylindrical batteries are by far the most popular. They are commonly used in power tools, medical instruments, laptops, e-bikes. The main advantage of that construction is higher volumetric capacity compared to other types, moreover, they are cheaper to produce and have lower capacity fade than prismatic counterparts.[6,25,26] However, they are hard to scale up due to problems with battery management systems and thus only small cylindrical cells can be found on the market. [17] Products of that type are described using

5 digits. In that description, the first two digits designate the diameter of the cell (in mm), while the remaining three are the height (in tenths of mm). There are multiple variations of cylindrical cells, like 20700, 21700, or 22700. By far the most popular is the 18650 cell. Such cell has a volumetric energy density of 600 – 650 W L^{-1} and 248 Ah kg^{-1} (the 3 Ah cell) of gravimetric capacity.[27]

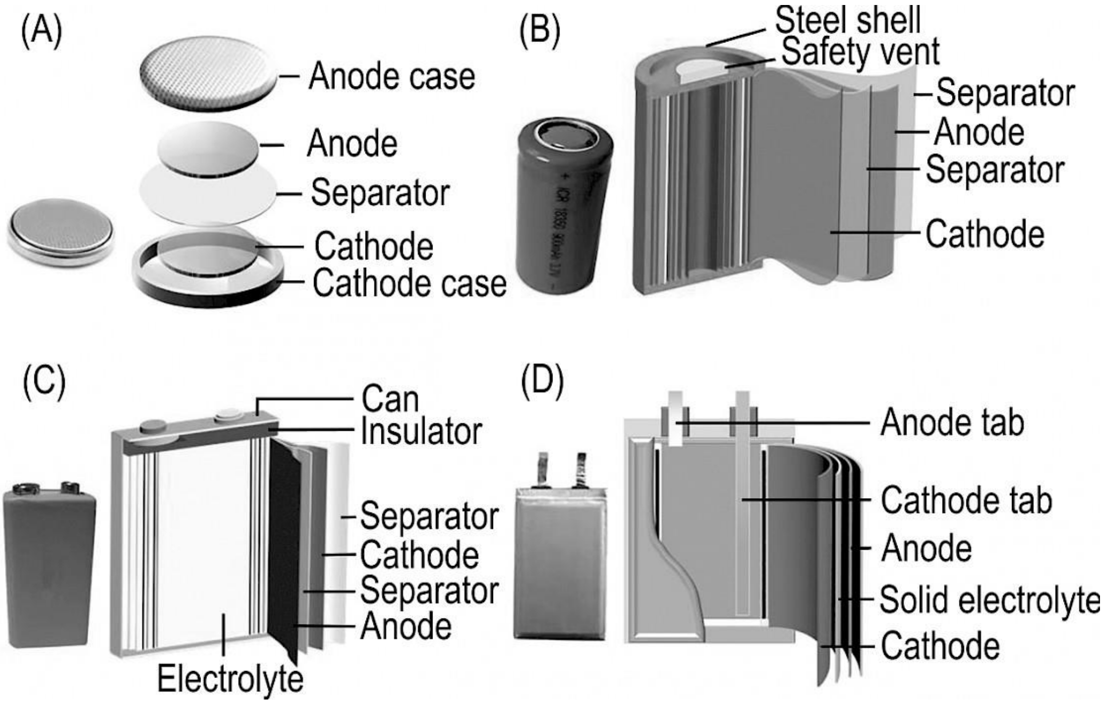

Figure 1.3. *Types of battery configurations. a) coin, b) cylindrical, c) prismatic and d) pouch.*[24]

The second type of battery is the coin cell. This type of cell is used in small portable devices, and laboratory tests. The lack of safety vents does not allow for charging more than 16 h due to swelling problems. On the other hand, this is a cheap and compact design of a battery.[27]

The third type of battery cell is a prismatic cell. That type of battery is usually met in smart electronic devices, such as smartphones, tablets, and thin laptops. The main advantage over cylindrical cells is facile size adaptability (generally thinner size), relative ease to create a battery pack, and low volume of dead mass.[6,26,27] The capacity of the prismatic cell ranges from 800 mAh to 4000 mAh. The biggest problem with this type of cell is small swelling, which starts after ~500 cycles.[27]

The last type of battery cell that can be found on the market is a pouch cell. This type of cell can be found in drones, laboratory testing cells, as well as in bigger energy storage systems. In contrast to other designs, the pouch cells employ flexible, aluminised laminate film as the case instead of typical metallic cans. That change enables the most efficient use of space (90 – 95% of packing efficiency). The capacity depends on the applications, i.e. for energy storage systems 40 Ah cells are used. The main drawback is electrode swelling (around a 10% increase in volume), which can occur after 500 cycles.[14,27]

Chapter 2. Polymer-Derived Ceramics

Polymer derived ceramics (PDCs) are a family of materials, whose common feature is that they can be obtained from a preceramic polymer by pyrolysis in inert of the reactive atmosphere. The family of PDCs inlcude many ceramic materials, like silicon oxycarbides (SiOCs), silicon carbonitrides (SiCN), silicon oxynitrides (SiON) or silicon boron nitrides (SiBN). The type of ceramic depends on the starting Si-polymer (**Figure 2.1**) and on its later modifications. The main advantage of PDCs is their versatility in processing and shaping, exceptional stability towards oxidation and corrosion, and good thermal properties up to temperatures around 1000°C.[9,28]

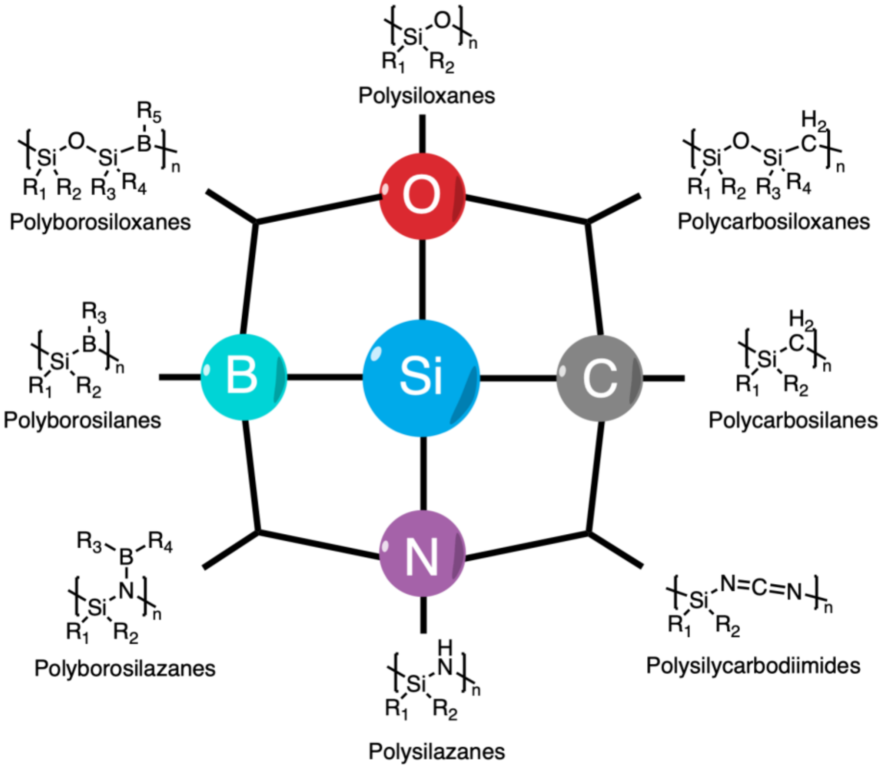

Figure 2.1. *Family of main classes of Si-polymers as precursors for PDCs synthesis.* [29]

2.1. Silicon oxycarbides

Silicon oxycarbides (SiOCs) are ceramic materials which belong to the family of PDCs. Due to their characteristic black colour, they are commonly known as black glass.[28] The general formula of SiOCs can be expressed as SiO_xC_y, + C_{free}, where C_{free} corresponds to the free carbon phase created during the pyrolysis process. A typical feature of these materials is the presence of Si-C and Si-O bonds and lack of C-O connections.[30–32]

2.1.1. Structure of silicon oxycarbides

SiOCs are classified as amorphous materials, where silicon atoms are coordinated tetrahedrally by carbon and oxygen. These bonds create the following tetrahedral units: SiO_2, SiO_3C, SiO_2C_2, $SiOC_3$ and SiO_4. In the literature,[9] the types of tetreaedra-where silicon is in the centre while oxygen and carbon are on the corners are commonly known as mixed bonds silicon tetrahedra. Carbon present in SiOCs exhibits two types of hybridisation: sp^3 carbon connected to silicon atoms, and sp^2 carbon free carbon phase.[9] The amount of carbon depends on the organic functional groups present in the preceramic polymer. Aromatic groups (like phenyl) provide higher amount of carbon in the final ceramic than alkyl groups. The structure of the ceramic also depends on the silicon-to-oxygen ratio. If the ceramic is obtained through pyrolysis in argon atmosphere, the silicon-to-oxygen ratio is the same as in the case of the preceramic polymer.[30]

The structure of SiOCs is described by models developed by Saha and Raj,[33] and Wigdeon et al.[34]. The model proposed by Saha and Raj assumes the existence of silicon-rich nanodomains and a graphene cage-like network. According to this model, silicon tetrahedra create randomly distributed spots separated from each other by a few layers of graphene. Schematically, this model is shown in **Figure 2.2 a)**. The average size of the silicon nanodomains is between 1 and 3 nm, while the thickness of the graphite walls is from 0.8 to 1.5 nm.

The second model was developed by Wigdeon et al.[34], based on the results of high-resolution ^{29}Si NMR spin-lattice relaxation studies. In this model, SiOCs consist of a 3D chain of SiO_xC_{4-x} tetrahedral units with voids filled with free carbon nanodomains. The main backbone is created with oxygen-rich SiO_xC_{4-x} tetrahedra ($x \geq 2$), while carbon-rich tetrahedral ($x < 2$) are placed between the carbon nanodomains and oxygen-rich tetrahedra **Figure 2.2 b)**. In carbon-rich SiOCs, the carbon-rich silicon tetrahedra may also form a continuous network **Figure 2.2 c)**, and when the carbon content is high enough, graphene nanodomains may also be connected.[34,35]

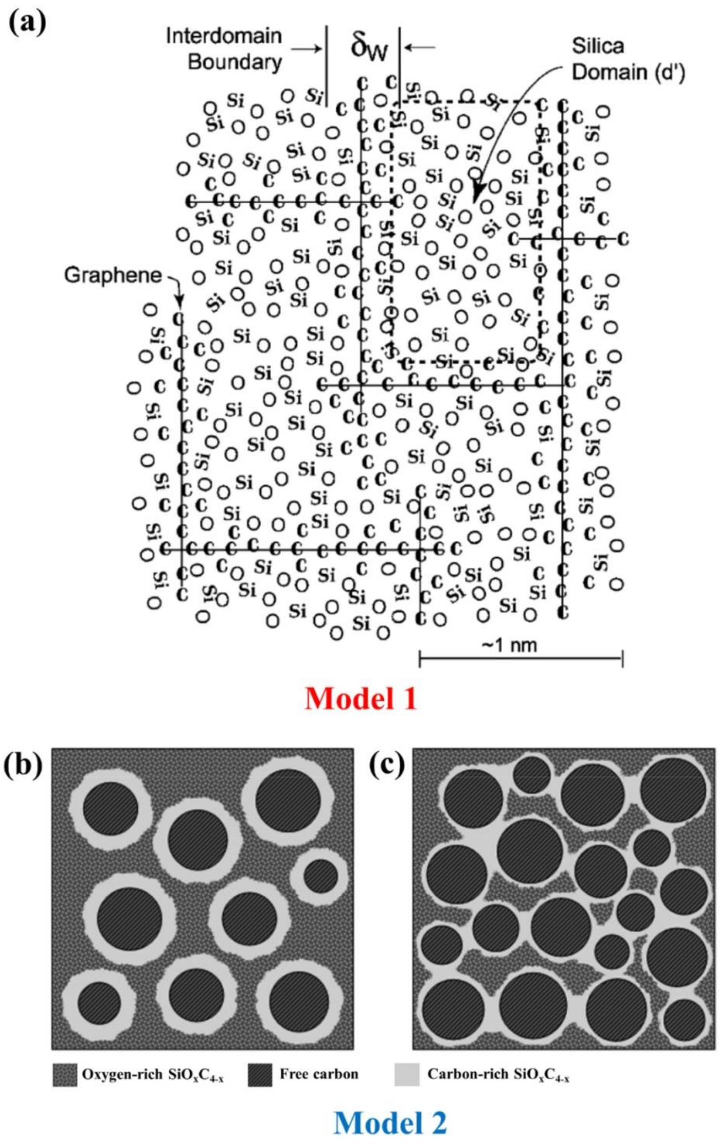

Figure 2.2. *Models of SiOC proposed by a) Saha and Raj*[33] *and b), c) Wigdeon et al.*[34]*. Image from ref.* [35]

2.2. Physicochemical properties of silicon oxycarbides

Although SiOCs include a large groups of materials, some of their properties are quite similar for all the materials. SiOCs exhibit high temperature stability up to 1000°C. Above that temperature there is a significant deterioration of the mechanical properties associated with the changes in SiO_3C, SiO_2C_2 and $SiOC_3$ tetraedara as well as with the crystallisation of the material. Thermal stability is directly related to free carbon content – a higher carbon content improves thermal properties. The thermal expansion coefficient is about 3 ppm K^{-1}, and it depends on the purity of the material. Metallic additives and conductive additives (such as graphite or carbon nanotubes) can increase the thermal expansion coefficient up to 6 ppm K^{-1}. Thermal conductivity is in the range of 0.5 to 2.7 W m^{-1} K^{-1}, depending on the porosity of the SiOCs and the separation between free carbon and ceramic phases.[36–38]

Other parameters, also related to the temperature, are creep and viscosity. SiOCs creep is very limited at temperatures up to 1300°C. The creep rate at high temperatures (above 1100°C) is time-dependent because then concurrent reactions occur, such as precipitation of β-SiC and β-cristobalite crystals. These crystalline forms decrease steady-state creep rates. In addition, the presence of carbides increases the hardness of the material. To obtain steady creep results, prolonged annealing is required. For example, at 1200°C it takes over 12 h to observe quasi-plateaus in Young's modulus and the ultimate creep rate is determined by the remaining glassy phase.[37,39] The activation energy for the creep is several hundred kJ/mol, depending on the material temperature and composition.[32]

The data obtained by interal friction experiments with SiOC glass suggest viscous elastic Maxwell model. This means that creep strains in SiOC are partially recoverable. Such behaviour is related to the presence of segregated free carbon, which deforms elastically.[32,39]

Electrical properties of SiOCs also depend on temperature. At low temperatures they behave like semiconductors, which is related to the electron tunnelling phenomenon, while at higher temperatures SiOCs exhibit high conductivity due to the presence of a carbon network. The term "low" and "high" temperature depends on the preceramic polymer, i.e. for poly(phenylmethylvinylhydrogensiloxane)-based SiOC, "low temperatures" are temperatures below 800°C.[40] Electrical conductivity of SiOCs is in the range of 10^{-13} to 1 S cm^{-1}, depending on the microstructure and the carbon content. Electrical conductivity may be improved by introducing additives, such as MoS_2 or Al_2O_3, or by applying higher temperature during the sintering of the preceramic polymer. This improvement can be explained by better phases separation, formation of a higher amount of free carbon, and creation of additional silicon compounds, like $MoSi_2$ or SiC, depending on the type of modification.[9,38]

2.3. Lithium storage in silicon oxycarbides

It is believed that lithium storage in SiOCs occurs *via* intercalation of lithium ions. The capacity values depend on SiOCs elemental composition and microstructure, and the highest capacity (~600 mAh g^{-1}) is achieved with a carbon-rich ceramic. The volume expansion upon lithiation is low (approx. 7%). However, the main drawback of SiOCs in terms of lithium storage is high irreversible capacity of the first cycle (40 − 50%)

SiOCs have an amorphous structure and therefore their storage mechanism is not fully understood. Over the past 30 years researchers have tried to find correlations between SiOCs elemental composition, microstructure and electric capacity values. The first studies were conducted by Dahn et al.[41–43] in the 1990s and they took into account only the elemental composition. Dahn et al. showed that the capacity increases with increasing the silicon content, but only up to 30 wt% of silicon. The oxygen content has negligible influence on the reversible capacity, but it causes high hysteresis and increases the irreversible capacity.

Later studies led to two main hypotheses of lithium storage in SiOC ceramics. The first one was created by Fukui et al.[44,45] and based on ^{29}Si MAS NMR and EELS studies before and after intercalation. According to their research, the free carbon phase, with properties similar to hard carbons, plays a major role in lithium storage capacity of SiOCs. The authors stated that during lithiation the majority of lithium ions are stored on the graphene edges and between the graphene layers of the free carbon phase. Graphene plains are responsible for high conductivity of the material, and create a flexible buffer for volume changes during the lithiation/delithiation process.[46] In this model, the role of silicon tetrahedra is to stabilize the highly disordered structure of the free carbon phase, and to increase the ionic character of the graphene layers. High irreversible capacity and hysteresis between the lithiation and delithiation curves was explained as a result of irreversible reactions of lithium ions with functional groups from the surface of graphene plains, and with SiOCs mixed bonds tetrahedra.[47]

The second hypothesis was created by Raj et al.[48,49] and based on experimental studies and big data analysis. They calculated that the capacity of the free carbon phase is about 5 000 mAh g^{-1}-atom, while for mixed bonds tetreadra it is in the range of 45 000 to 75 000 mAh g^{-1}-atom. Such a high capacity was rationalised by polarity of these tetrahedral units. High hysteresis, however, was explained by the diffusion limitation of lithium deinsertion from the material, and the creation of SEI.[50]

Further research on SiOC was conducted using both computational and experimental methods. Liu et al.[51] and Liao et al.[52] investigated the capacity of SiOC mixed bonds tetrahedra using ^{29}Si MAS NMR. They found that $\underline{Si}OC_3$ mixed bonds tetrahedra disappear after the first lithiation cycle and at the same time their forms of inactive SiC_4 and Li_2O. SiO_4 react irreversibly with lithium forming reversible Li_2SiO_3 and irreversible Li_4SiO_4. During the prolonged cycling, Li_2SiO_3 slowly transforms into Li_4SiO_4, which results in gradual capacity loss over time. The summary of the reversibility of the mixed bonds tetrahedra and lithium ions is collected in **Table 2.1**.

Table 2.1. *Reversibility of the reaction of various mixed bonds tetrahedral units of SiOCs with lithium ions*[51,52]

Form of SiOC	Reversibility
SiO_4	Partial – the creation of Li_2SiO_3 (reversible) and Li_4SiO_4 (irreversible)
SiO_3C	Full
SiO_2C_2	Full
$SiOC_3$	None – creation of SiC_4 and Li_2O
SiC_4	The lithiation does not occur

Kroll[53] showed, based on mathematical simulations, that during the reaction with SiOCs lithium ions preferably bond with oxygen. However, in the case of stochiometric SiOCs (i.e. without the free carbon phase) lithium ions insertion process is energetically unfavourable due to the high enthalpy of the process. The presence of free carbon and mixed bonds lowers enthalpy of this process, which facilitates the deinsertion of lithium. Structural imperfections create low-occupying energetic states which trap lithium ions and lead to irreversible capacity. According to Kroll[53], reversible lithium storage occurs mostly around the free carbon phase. Riedel et al.[54,55] determined the relationship between the free carbon and ceramic phases. They found the capacity rises with the increase of the ceramic phase up to 1300 mAh g^{-1}. This value, however, is never reached due to the low conductivity. Thus the free carbon phase is necessary to provide electrical conductivity and stability, especially when high charge/discharge current densities are applied.[54–56] To ensure effective lithium storage, SiOCs should have at least 20 wt% of free carbon. If the carbon content is lower, the minimum promotion energy required to transfer the electron from valence band to conduction band is very high due to the presence of strong Li-O bonds. Irreversible capacity depends primarily on the SiOC ceramic phase. Liao et al.[57] have recently presented a new insight into the energy storage. They showed that during the lithium insertion process small nanocracks appear in the structure of graphene, which leads to the creation of nanovoids (0.4-0.6 nm).

They are the major storage sites for lithium, while Li-silicates and Li_xO complexes are the main sources of irreversible capacity.

2.4. Factors influencing lithium storage in silicon oxycarbides

Lithium storage in SiOCs may be influenced by many factors, even if the same preceramic polymer is used. The most important are: pyrolysis conditions, incorporation of additives, and additional modifications such as etching.

The first factor influencing lithium storage in SiOCs are pyrolysis conditions of SiOCs precursor. During the synthesis of SiOCs, depending on the temperature, different structures may be formed from the same preceramic precursor. Raj et al.[49] and Fukui et al.[58] showed that samples pyrolysed at 700-800°C exhibit better electrochemical stability than those samples pyrolysed at higher temperatures. This is probably due to the presence of hydrogen residuals bonded with carbon, which increases their stability during the intercalation.[49] However, the ceramics obtained in these lower temperatures have high irreversible capacity, which is related to hybridisation transformation of graphite on the boundaries of graphene sheets from sp^2 to sp^3. Pradeep et al.[59] studied further the influence of hydrogen on electrochemical performance by pyrolysing a preceramic polymer in Ar/H_2 atmosphere. The authors found that pyrolysing in Ar/H_2 leads to lower free carbon content in the final SiOCs material and to the reduction of defects in the free carbon phase. The lower free carbon content was explained as a result of the additional CH_4 formation due to the reaction of excess carbon with hydrogen, while the less defected carbon phase resulted from the saturation of dangling carbon bonds. Ding et al.[60] conducted computer simulations of SiOCs obtained in atmosphere with and without the addition of hydrogen. According to their calculations, the presence of hydrogen promotes the formation of carbon-poor SiOC tetrahedral units and decreases the fraction of C-C bonds in favour of C-H bonds.

Depending on the pyrolysis temperature, different products may form. If the pyrolysis is conducted at low temperatures (1000-1200°C), SiOC mixed bonds are present. The structure is completely amorphous, and the free carbon content has negligible influence on the mixed bonds distribution. On the other hand, at higher temperatures (1200-1500°C) a phase separation within the ceramic phase occurs: mixed bonds tetrahedra transform into amorphous SiO_4 and SiC_4. Depending on the carbon content, the transformation may occur at lower or higher temperatures. Increasing the temperature also leads to ordering the free carbon structure which limits the space~~,~~ where lithium may be stored. SiC_4 content can be by pyrolysis in the atmosphere with water steam[61,62] According to Kaspar et al.[62], due to these transformations, increasing the pyrolysis temperature leads to a drop in reversible capacity and coulombic efficiency.

Another way of improving the electrochemical performance of SiOCs is by incorporating additives, which can be of two types: inorganic or carbonaceous. Inorganic additives include a large group of materials, such as silicon, tin, antimony, $MoSe_2$, or TiO_2. A common feature of these additives is good electrochemical properties such as high capacity of MoS_2, Si, Sb or Sn, or good stability of TiO_2. Kaspar et al.[63] and Liu et al.[64] tested SiOCs/nano-Si composites. In these composites, silicon provides high capacity, while SiOCs ensures good electrical contact and accommodates stresses created during the lithiation of silicon. In addition, introducing nano-silicon leads to electrical conductivity improvement (due to the formation of SiC) and shortens the diffusion path for lithium ions. Other authors [65–67] studied tin nanoparticles as additives in SiOCs. The idea behind combining SiOCs with nano-tin is the same as in the case of SiOCs/nano-Si nanocomposites. The main advantage of nano-tin over nano-silicon is its lower volume expansion (258% vs. 400%, respectively). Behera and Raj[68] produced a SiOC - TiO_2 composite with high electrical capacity and good stability. The authors attributed these properties to the creation of a new, hybrid SiOC - TiO_2 ceramic with a core-shell structure, and to its high specific surface area (SSA). Dey et al.[69] tested SiOCs in combination with $MoSe_2$ and polyvinylpyrrolidone. They attributed the high performance of SiOCs - $MoSe_2$ to the porous structure of the material, which facilitates lithium ion storage and protects electrode from volume expansion.

Another type of additives is carbonaceous additives, which may either directly extend the free carbon phase, or introduce a new carbonaceous phase with different properties. The first group of these additives includes mainly aromatic hydrocarbons. For example, Fukui et al.[70,71] mixed a preceramic blend with polystyrene and acenaphthylene. The major benefit of adding polystyrene was increasing microporosity, which results in coulombic efficiency improvement. However, as the authors mentioned, admixing of carbonaceous additives must be performed with caution as excess leads to their capacity decrease. Liu et al.[72] investigated further the influence of incorporating aromatic hydrocarbons. They found that an additional source of carbon improves the electrochemical performance of carbon-poor SiOCs, while in the case of a carbon-rich ceramic, the addition of carbonaceous additives causes deterioration of SiOCs electrochemical performance due to the changes in their structure.[72] The third group of carbonaceous additives includes various carbon forms, like graphene,[73,74] graphene aerogel,[75] CNTs,[76] and carbon nanofibers.[77] Utilisation of these materials is multipurpose and usually revolves around creating new lithium storage sites thus providing a continuous carbon network which ensures good electrical conductivity of the composite and also creates lithium diffusion pathways.[73,75] Moreover, depending on the additive, there may be additional benefits. David et al.[74] produced SiOC-graphene composite paper with good mechanical properties which could be used as a free standing electrode. Sang et al.[78] suggested that the combination of graphene nanosheets with SiOC may modify the chemical composition of SiOC mixed bonds tetrahedra. Sang et al.[73] additionally reported good tensile strength of graphene-covered SiOCs fibres.

The last method of modifying electrochemical properties of SiOCs is etching. The etching process can be conducted using acids, for example H_3BO_3,[79] HF,[80] or strong bases NaOH[81] or KOH[82]. The main idea behind etching is to remove a fragment of the SiOCs ceramic phase. This leads to an increase in the carbon content within the material, and formation of porous structure with a high specific surface area (SSA). In addition, in the elements originating from the etching agent, like boron or fluorine, may be doped in ceramic structure, which further improves electrochemical performance of the SiOCs material.[79,83]

2.5. Production of silicon oxycarbides

The methods of SiOCs production can be divided into two groups: *i)* historic, based on the introduction of carbon into the glass structure, and *ii)* new, involving production from preceramic precursors. The historic process was performed through impregnation of porous glass with organic compounds, followed by firing in a neutral or reducing atmosphere.[84] The modern process involves the pyrolysis of silicon organic compounds, whose general formula can be described as:

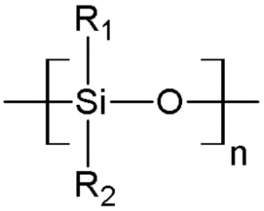

$$\left[-\overset{R_1}{\underset{R_2}{\mathrm{Si}}}-\mathrm{O}- \right]_n$$

10)

where R_1, R_2 are functional groups bonded to the silicon. These functional groups have a major impact on the physicochemical properties of the final SiOCs, such as chemical and thermal stability, wettability, rheological, optical and electrical properties.[28]

In the process of synthesis of SiOCs, three main stages can be distinguished: 1) synthesis of preceramic precursors, 2) crosslinking to obtain a 3D polymer, known as the green body, and 3) pyrolysis of the green body. Crosslinking is usually conducted using two main methods: curing or sol-gel method. The purpose of crosslinking is to increase the ceramic yield of preceramic polymer and to retain the shape of the material. The curing process involves crosslinking of linear polymers, while sol-gel the synthesis includes the synthesis of a 3D precursor from small-molecule monomers.

2.5.1. Curing

The curing process involves crosslinking of a precursor which may come in a few different forms: as a crosslinkable liquid, a meltable and curable solid, or an unmeltable and soluble solid. Curing is usually performed by: *i)* heating the preceramic precursor, *ii)* irradiating with electron beam, or *iii)* irradiating with UV light[28,35,85] Cross-links are created through different reactions depending on the functional groups present in the precursor: hydrosilylation (*via* Si-H and C=C groups), dehydrocoupling (*via* two Si-H groups or Si-H/N-H groups), oxidative curing (*via* Si-H and $Si-CH_3$), or polymerization (*via* vinyl and allyl groups).[35] The example of the hydrosilylation reaction is shown in **Figure 2.3**. This type of reaction requires a platinum catalyst, like chloroplatinic acid H_2PtCl_6 (Speier catalyst), Karstedt's catalyst (**Figure 2.4**), or a free radical initiator.[86] The process occurs at 100-120°C and leads to the formation of bonds that do not undergo thermal depolymerisation. The main advantages of hydrosilylation is the fast pace of the reaction, facile control of chemical properties and the crosslinking degree of the preceramic polymer, negligible mass loss, and minimal evolution of bubbles in the final product.[9,28]

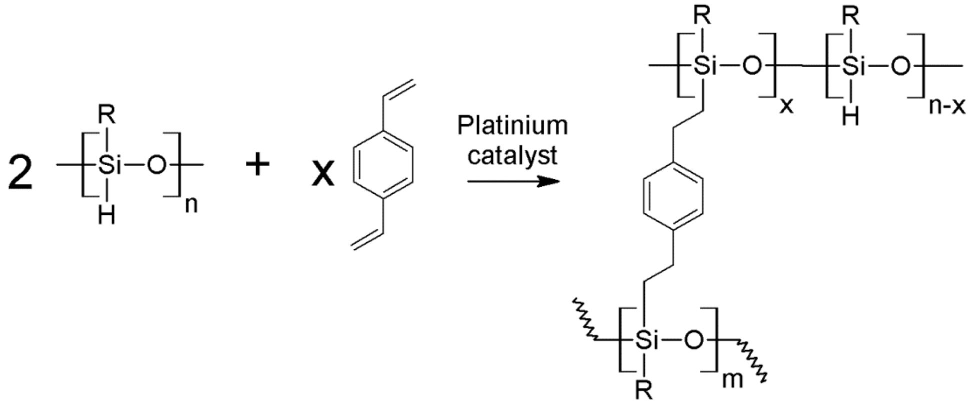

11)

Figure 2.3. *Crosslinking of a simple polysiloxane with p-divinylbenzene* via *hydrosilylation*

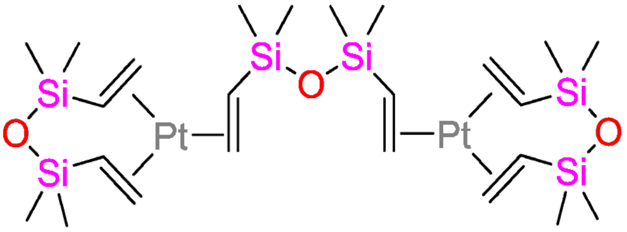

Figure 2.4. *Karstedt's catalyst*

The dehydrocoupling reaction is the second type of reaction that may occur in a preceramic precursor containing Si-H groups. Dehydrocoupling usually occurs in conjunction with hydrosilylation, but it begins at higher temperatures (~300°C). The main difference between dehydrocoupling and hydrosilylation is evolution of the by-product in ~~a~~ the form of hydrogen or water.[87] Dehydrocoupling is often catalysed by $Ru_3(CO)_{12}$. However, many catalysts based on a transition metal, such as Ru, Fe, Rh, Co, Os, can also be used.[9,88]

The simplest type of curing is oxidative curing, which can be performed *via* simple heating of a preceramic polymer to ~200°C, or by gamma-ray irradiation. This process does not require a catalyst. Oxidative curing leads to oxygen crosslinking according to the mechanism shown in **Figure 2.5**. The obtained SiOC ceramic contains SiOC mixed bonds, free carbon and a low content of SiC. The main problem with that method is that it yields a high oxygen content in the final material, which remarkably influences its tensile strength and high-temperature stability.[28,89,90]

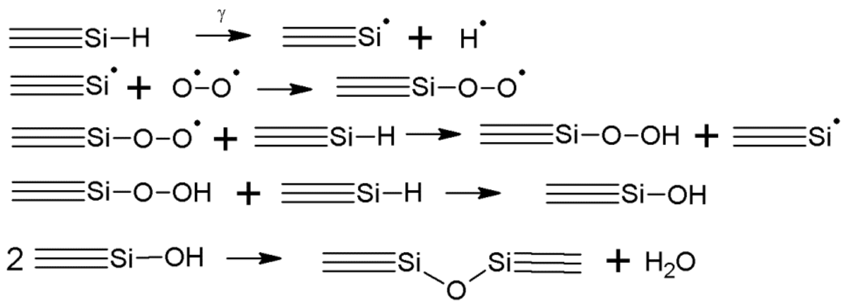

12)
13)
14)
15)
16)

Figure 2.5. *Gamma-ray assisted oxidative curing mechanism.*[90,91]

The last curing mechanism employs vinyl groups' polymerisation. This type of polymerisation involves polyaddition of vinyl groups or their crosslinking using a crosslinking agent, for example diacrylates. The main mechanism of the vinyl groups' polymerisation are radical reactions. In the case of UV curing of preceramic polymers containing vinyl functional groups, this is considered the main crosslinking mechanism. [35,92–94]

2.5.2. Sol-gel synthesis

Sol-gel synthesis is a very popular method of producing ceramic materials. The main advantage of the sol-gel process is its low cost, simplicity, and facile control of the end material properties. However, the method is very time-consuming, and there are sometimes problems with viscosity control during the reaction.[28,95,96] The sol-gel process involves 5 main stages: mixing, casting, gelation, aging, and drying.

The first step of the sol-gel synthesis is mixing, when a colloid suspension with particles of 1-1000 nm in size, known as sol, is created. The formation of precipitates is prevented by adding a dispersive agent - usually water is used with appropriate pH. At this stage, two reactions take place: hydrolysis and polycondensation.[96,97] During hydrolysis, the alkoxy groups are transformed into more reactive hydroxy groups. The reaction can be expressed as:

$$\equiv SiOR + H_2O \xrightarrow{hydrolysis} \equiv SiOH + ROH \qquad 17)$$

Where R represents alkoxy functional groups. Due to the insolubility of alkoxides (alkoxysilanes) in water a co-solvent, for example alcohol, has to be used. The amount of alcohol has to be limited due to the reverse reaction of esterification.[98,99] During the second reaction, polycondensation, di- and tri- oligosiloxanes are created and combine with each other to form colloids. This is related to the creation of Si-O-Si bonds which organize themselves into SiO_4 tetrahedra. The reaction can be described as follows:

$$\equiv Si - OH + \ RO - Si \xrightarrow{alcohol\ condensation} \equiv Si - O - Si \equiv \ + ROH \qquad 18)$$

$$\equiv Si - OH + \ HO - Si \xrightarrow{water\ condensation} \equiv Si - O - Si \equiv \ + H_2O \qquad 19)$$

There are several factors influencing the kinetics and pathway of the polycondensation reaction:

a) H_2O : Si ratio. The water content influences the condensation pathway. If the water content is stoichiometric or higher, water condensation is preferable, while when the water content is lower, alcohol condensation is more likely. The water content has no influence on the kinetics or the reaction progress.[98,99]

b) Presence of a catalyst. The sol-gel synthesis may be catalysed by an acidic (HF, HCl, HNO_3, CH_3COOH) or basic catalyst ($NH_{3(aq)}$, NaOH).[100] The general impact of a catalyst is shown in **Figure 2.6**.

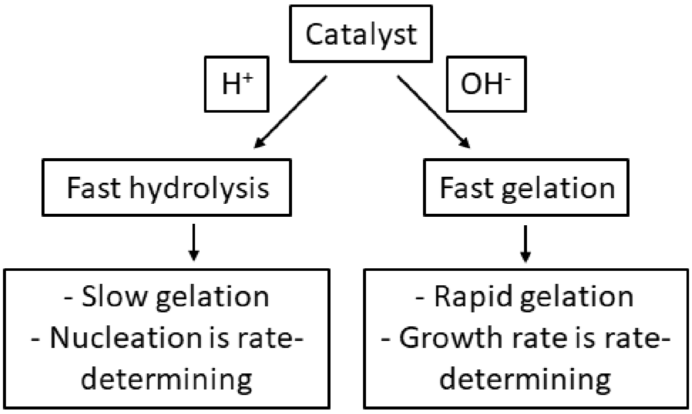

***Figure 2.6.** Influence of acidic and basic catalysts.*[99]

c) Influence of the solvent. The main task of a solvent is to prevent water-precursor phase separation at the initial stages of the reaction. However, due to esterification, a considerable amount of the solvent, which is a by-product of hydrolysis, would slow down the reaction progress. Thus in addition to a co-solvent, DDCA (*dry chemical control additives*), which remove excess solvent without damaging the structure of the material, are added. As DDCA agents, THF or formamide can be used.

In addition, the reaction process can also be affected by the solvent chemical properties. As studies demonstrate, polar aprotic solvents stabilize the intermediate products thus accelerating the reaction. On the other hand, polar protic solvents have negligible influence on the reaction kinetics.[98,99]

The second step in the sol-gel synthesis is casting. This stage is especially important during the production of materials with well-defined shapes. During casting, the sol is poured into the mould of the final product. The main parameter is adhesion forces between the mould and the sol, they should be low enough to enable demoulding.[96,97]

The third step in the sol-gel synthesis is gelation. During this process colloids merge to create an alcogel which is a tri-dimensional network the size of a vessel which contains the liquid particles (a solvent or reaction by-products) inside the pores.[98,100] From the chemical point of view, the gelation process is a continuation of polycondensation, initiated at the mixing stage. During gelation, the viscosity of the mixture rises and the material assumes the final form. The most important parameters of gelation are the point of gelation and the time of gelation. The point of gelation is the moment when all the colloids get connected to each other. The time of gelation is the time between the start of hydrolysis/condensation and the point of gelation. During this time it is still possible to incorporate additives or cast the mixture. Typical gelation times for $Si(OEt)_4$ are: 1000 h (no catalyst), 92 h (0,05 M HCl catalyst), and 107 h (NH_4OH catalyst).[101]

The next step in the sol-gel synthesis is aging. During this process stabilisation of the alcogel takes place. This is related to a further condensation reactions, which occur in the solid gel and vastly influences the structure as well as chemical and physical properties of the final material.[98] These reactions are conditioned by:

a) Changes of liquid phase inside the alcogel. After gelation the alcogel is saturated with the solvents and polycondensation by-products. After the release of the liquid phase unreacted colloids may precipitate and further react with the sol. Releasing the solvent leads to shrinkage of the material, which is defined as *syneresis*.

b) Dissolution and recrystallisation of colloids. Some colloids dissolve in solvents trapped in the material and re-precipitate. As a result, smaller particles and pores are removed, and a compact structure is created. This process does not lead to shrinkage of the material because the core of the gel remains intact. These processes are described in the literature as coarsening and ripening.[98,101]

The last step in the sol-gel process is drying, when water, solvents and by-products are removed from the pores and a dry gel structure, known as xerogel, forms. Drying is the most challenging process to carry out due to internal stresses occurring, which may cause cracks in the structure.

The liquid present in an alcogel can be of three types:

1) Liquid present in open pores. During the drying stage this liquid migrates towards the surface of the gel and is then removed. The gel shrinks and deforms but at the same time it becomes more durable due to further condensation reactions.

2) Liquid forming the thin film of the pores. This type of liquid is removed by evaporating from the material. At that stage, gel cannot shrink further, but the internal stresses rise due to the pressure differences between vapour contained in big and small pores, which causes many small internal cracks. These stresses may be reduced by using DCCA.

3) Liquid trapped inside the closed pores. This type of liquid cannot be removed. [97,100,101]

The end xerogel is characterised by low density as well as good mechanical and thermal properties.[28]

2.5.3. Pyrolysis

The main stage in creating SiOCs is polymer-to-ceramic conversion which occurs during the pyrolysis process. The process occurs at temperatures from 800 to 1400°C, and has to be conducted in vacuum or in inert gas (argon) depending on its structure and composition. Sometimes pyrolysis is performed in nitrogen or argon with a small addition of other gases, for example water steam, to modify the composition of the final ceramic.[35,61,62]

Pyrolysis of preceramic precursors is related to mass losses at various temperatures. The first mass loss takes place between 50 – 350°C and corresponds to the evaporation of water or other solvents which were used for the synthesis of the preceramic polymer. The mass loss at these stages reaches up to 5%. The second weight loss occurs around 550-800°C, and it relates to breaking the bonds between the –Si–O– chain and the functional groups. It is associated with the release of small molecules, such as CH_4, C_2H_4 or H_2, which relates to the mass loss of ~25% depending on the functional groups present in the preceramic polymer. At higher temperatures, usually ~800°C, the process of ceramization starts. During this process, reorganisation of Si-O and Si-C bonds takes place. Initially, low mass silanes are created, then there forms a dense network of Si-O, Si-C and C-C bonds, which corresponds to the final ceramic material. This process is not fully understood due to its complexity. At this stage, the mass loss is negligible. Heating to higher temperatures (1200°C and higher) leads to carbothermal reduction which creates high free carbon content, graphitisation of the carbon phase, and creation of crystalline SiC.[9,35,62,102]

Chapter 3. Graphite

3.1. Basic information

Graphite is one of the three allotropes of carbon that can be found in nature, besides diamond and amorphous carbon. The history of graphite reaches the XV-XVI century when a big deposit was found in the Borrowdale Parish in England.[103] The word “graphite” originates from the Greek word *graphein*, which means *to write* as graphite was initially used in pencils. During the centuries, the interest in graphite slowly increased, and it starts showing up in more and more applications.[103,104]

The graphite structure consists of carbon prismatic planes (graphene plains) connected to each other. A single prismatic plane is built of carbon atoms, bonded to their three closest neighbours via σ-bonds (the sp^2 hybridisation), while the remaining $2p_z$ orbitals participate in the creation of delocalised π-bond. The $2p_z$ orbitals overlap most effectively when they are parallel to each other, thus the most energetically beneficial state is when the plain is completely flat and that explains why plains of graphite are also flat.[105] The π-bonds are perpendicular to the plain, and they create connections between graphene sheets.[106] The in-plane bonds are short covalent bonds, with a length of 0.141 nm, while the interplanar connections are considered as the van der Waals forces with the length over twice as high (0.335 nm).[104] The plains are ended with two different edge shapes, i.e. zigzag and armchair (**Figure 3.1 a)**), which vastly influences the chemical properties of graphite.[107] The plains can be stacked in various fashions: AB, AA, ABC and turbostratic (**Figure 3.1 b)**). Due to various stacking fashions, two crystallographic structures emerge, namely hexagonal with AB or AA stacking, and rhombohedral with ABC stacking. Usually, the natural graphite is a mixture of the first three structures, but the most widespread is a structure with AB stacking, while around 10% of graphite exists in the rhombohedral structure with ABC stacking.[104] The existence of ABC stacking is present if graphite is under deformation.[108] On the other hand, the turbostratic structures occur when the plains are not explicitly bonded with each other. This state is experimentally achieved by annealing, heat treatment, neutron irradiation or ion insertion.[106]

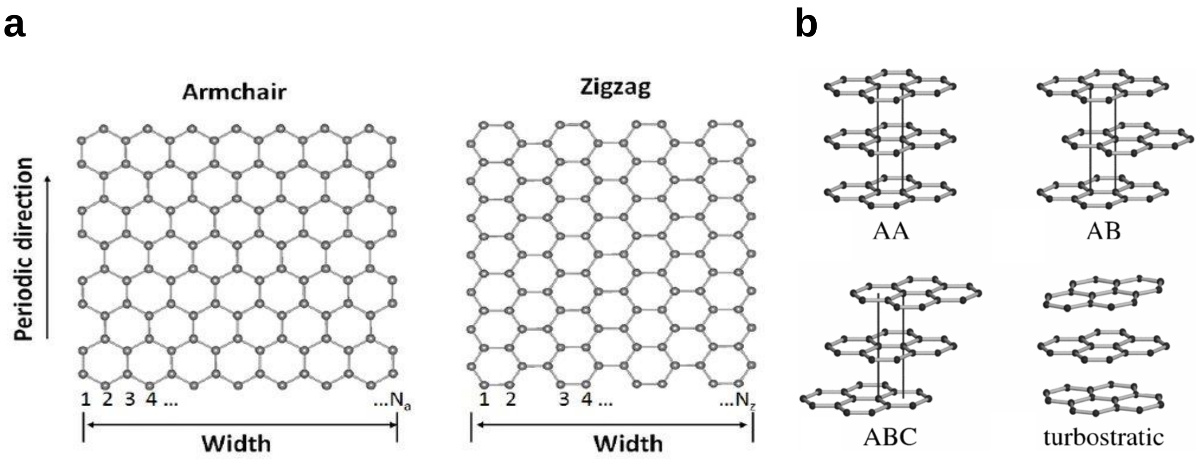

Figure 3.1. *a) Zig-zag and armchair plain ending, b) graphite stacking.*[109–111]

3.2. Physical properties of graphite

The unique layered structure vastly influences the properties of graphite. Due to differences between the bonding connections along and across the plains, graphite exhibits strong anisotropy in its properties. Therefore, graphite’s properties are often considered separately depending on the direction.

Concerning electrical resistivity, along the plains graphite is considered the conductor with resistivity similar to metals, while across the plains graphite exhibits an insulating behaviour. The in-plane conductivity is originating from the additional delocalized electrons, which do not participate in the creation of σ-bond and thus can move freely, [104,112] the other hand, across plains, such a mechanism does not exist. The electrical resistivity is enhanced by defects in the structure, which reduce the density and mobility of the carriers.[108] An increase in the temperature also causes the rise of the in-plane resistivity, but it gives a small conductivity increase across the plains.

Thermal properties are shaped in a similar pattern. Thermal conductivity along the plains of graphite can be over 5 times higher than the thermal conductivity of copper depending on the preparation, while thermal conductivity across the plains can be up to four orders of magnitude lower than along the plains. Such discrepancies arise from the movement of phonons, which is suppressed in the c-direction due to weak forces between basal planes.[113,114] The thermal conductivity is reduced by defects in the crystalline structure and scattering points of phonons. Moreover, it can also be limited by grain size.[104,113] The temperature increase in general causes a drop in thermal conductivity values, although increases it in the c-direction in temperatures above 1500°C.

Mechanical properties are also direction-dependent. Along the plains, graphite has high Young modulus and tensile strength, while the interactions between plains are feeble. When shearing forces are applied, the plains can slide against each other, which translates into a low coefficient of friction.[115]

Selected properties of graphite are collected in **Table 3.1**[104]

Table 3.1. *Selected properties of graphite*

Property	Across the plains	Along the plain
Electrical resistance	$3000 \cdot 10^{-6}$ Ωm	$2.5\text{-}5 \cdot 10^{-6}$ Ωm
Thermal conductivity at 25°C	2.2 W m^{-1} K^{-1}	~400 W m^{-1} K^{-1}
Young modulus	1060 GPa	36.5 GPa
Colour	Black/grey	
Boiling point	~4560 K	
Density	2.26 g cm^{-1} at 300 K	
Specific heat	8.033-8.635 J mol^{-1} K^{-1} at 25°C	

3.3. Battery-grade graphite

The term “battery-grade graphite” does not correspond to a specific form of graphite existing in nature, but rather to modifications and properties that are put onto the graphite to make it suitable for battery applications. The target goal for battery-grade graphite is the high electrochemical capacity (between 345 – 355 mAh g^{-1}),[116] high first cycle Coulombic efficiency (above 90%),[116] and good cycling stability of at least a few hundred cycles. Graphite for batteries is ultrapure graphite with spherical particles. Such graphite must be characterised with well-defined particle size, usually between 10 – 30 μm, with the biggest particle not exceeding 80 μm, and narrow size distribution.[117,118] Moreover, the battery-grade graphite should have a high degree of graphitisation (to ensure high capacity), high tap density (for high volumetric capacity), sufficient porosity (to provide electrolyte penetration), and a low specific surface area (increases life cycle). The typical requirements for battery-grade graphite are collected in **Table 3.2**.

Table 3.2. *Typical physical properties of ultrapure battery-grade graphite.*[119–122]

Requirement	Value/description
Particle size distribution	10 - 30 µm, mean around 20 µm
SSA	6 $m^2 g^{-1}$, ideally below 2 $m^2 g^{-1}$
Tap density	> 0.9 g cm^{-3}
pH	5.5 – 7
Moisture	0.1%
Ash content	Below 0.04%
Contaminants	Threshold values of 50 ppm and lower
Carbon content	>99.95%
Crystallisation level	Flake graphite used for the production of battery-grade graphite must have at least 94% of graphitic carbon

Battery-grade graphite is produced from a mixture of natural graphite and synthetic graphite. As for natural graphite, only flake and vein graphite can be used for battery-grade graphite production due to their sufficient crystallisation degree and purity Moreover, the choice is often further limited by the accessibility of graphite.[123] The ratio between natural/synthetic graphite is usually around 1:1.[116] The production of the battery-grade graphite consists of the following steps: grinding, spheroidisation, purification and coating.[124] During the graphite grinding process, the size of graphite lumps is reduced from >250 µm to around 10 µm. For the grinding process, multiple techniques can be used, such as jet milling, air milling, ball milling.[118] In the next step, purification is conducted to remove contamination. The impurities in graphite are usually in the form of ash occurring as silicate minerals.[125] This is a very expensive process as it leads to ~70% material loss.[126] The purification is performed in multiple ways, usually used subsequently. A short list of purification methods is collected in **Table 3.3**.

Table 3.3. *Selected methods for graphite purification.*[125]

Hydrometallurgical purification	a) flotation b) acid-base. In that process impurities initially react with NaOH at elevated temperatures creating insoluble hydroxides, followed by reaction with HCl, where impurities form soluble chlorides c) HF-based. HF reacts with impurities creating compounds soluble in water
Pyrometallurgy	a) chlorination – impurities react with chlorine gas to form low-temperature boiling compounds b) high-temperature methods – vaporising of the impurities at high temperatures (>2500°C)

Table 3.3. *Cont.*

Comminution	careful grinding of graphite to separate impurities stacked between layers followed by scrubbing and floating out the impurities
Froth flotation	flotation method which involves trapping graphite into air bubbles and removing it from a bath containing impurities
Air elutriation	using air with proper velocity to blow away graphite from heavier impurities
Gravity separation	utilizes differences in density between graphite and impurities, i.e. by employing Bartles-Mozley separator
Magnetic separation	using strong magnets (electromagnets) to remove magnetic impurities, such as iron compounds

In the next step, graphite is spheroidised by classifying fine particles, shaving off the edges and rounding the particles. The graphite particle is considered “spheroidised” if the ratio of the major axis to the minor axis equals “2” or lower.[117] The process of spheroidisation is performed by rubbing and solidifying graphite particles together using shearing forces or by plastically deforming the graphite particles.[127,128] Graphite spheroidisation can be performed using mechanofusion or the Nobilita process. In the case of mechanofusion, raw material is put into a rotating vessel with moving walls, where centrifugal forces are pushing graphite particles onto the walls of the vessel while rotating walls are shearing and form spherical particles. In the Nobilita process, the shearing and forming forces are created by the rotor, which is rotating in a perpendicular direction with regard to the vessel.[127]

During the last step, graphite spheres are coated with carbon coating. The role of carbon coating is to improve the first cycle efficiency of graphite. The conventional coating is conducted via pitch coating using pitches or resins. The process is performed by mechanochemical method or in a heating kneader. In the kneading process graphite particles are mixed and kneaded at elevated temperatures (150 – 180°C), and then backed in a nonoxidising atmosphere at 900 – 1500°C.[129,130] Besides, there are other methods of coating graphite, employing for example CVD processes, used by i.e. Imerys Graphite & Carbon Inc.[131]

3.4. Lithium storage in graphite

3.4.1. Intercalation of lithium

The main storage mechanism of graphite involves the intercalation of lithium ions into the structure. Intercalation is a process that occurs in compounds with anisotropic structures where interplanar forces are rather weak, i.e. in graphite or transition metal dichalcogenides.[132] During the intercalation process, small guest atoms are inserted and placed inside the free interlayer spaces of the host. In the literature, these empty interlayer spaces are usually called “galleries” and that term is used in the later sections of this work. The intercalation into graphite is possible thanks to the lowering of van der Waals forces between graphene layers. It is achieved through energy gain behind the addition or removal of an electron to the valence band due to the redox reaction between host and guest. With that regard, graphite is a unique material thanks to its amphoteric behaviour. The reversibility of the redox reaction of graphite is achieved thanks to the stability of graphitic planes combined with kinetic hindrances preventing from going straight to carbide form.[133]

One of the most important parameters describing the degree of intercalation is called the stage of intercalation. The stage of intercalation determines the number of graphene layers that separate the two closest guest interlayers, i.e. stage 1 means there is one layer of graphene that separates two closest guest interlayers, stage 2 means there are layers of graphene that separate two closest guest interlayers.[134] The intercalation stages vary depending on the intercalating cation. Graphite can successfully host lithium and potassium ions with stage “1”, i.e. every interlayer space is occupied by the guest atom. However, bigger cations, like sodium, can be located every 8th layer of graphene at most, therefore their intercalation stage is “8” or higher. Such discrepancies in intercalation degree are related to the required space for each ion. For lithium, the optimal space is around 3.489 Å, which is close to the interlayer space of graphite (3.35 Å), while for sodium at least 3.7 Å is required.[135,136] The intercalation stage directly influences the capacity of material: the theoretical capacity of Na^+ intercalated graphite is below 35 mAh g^{-1}, while Li^+ intercalated equals roughly 372 mAh g^{-1}.

Theoretical capacity obtained for a lithium-graphite compound can be calculated from the reaction:

$$Li^{+} + e^{-} + C_6 \leftrightarrow LiC_6 \qquad 20)$$

in which LiC_6 corresponds to stage I of graphite lithiation of the highest lithium content. In that process, one electron per six atoms of carbon is exchanged. In the molar ratios, it gives 96 500 C of charge, it is ~26 805 mAh, per 12 g x 6 = 72 g of carbon, which finally leads to 372 mAh g^{-1} of total theoretical capacity.

3.4.2. Staging mechanisms

Although the maximum lithiation stage of lithium-graphite compound equals “1”, the lithiation process occurs stepwise, through a few intermediate stages. This stepwise lithiation process was studied using multiple techniques, which resulted in two main models of staging. The first one was proposed by Rüdorff and Hofman in 1938. They based it on the XRD data of graphite treated with different oxidising and reducing agents.[137,138] In their work, they presented a simple staging mechanism where anions occupy every *n*-th interlayer space between graphite and the filling process occurs step by step, as shown in **Figure 3.2**. Rüdorff-Hofman model assumes a perfect scenario, where the structure is perfectly periodical and the interlayer space could be either fully occupied or empty. The model gave a basic overview of the lithiation process, but it faced some issues i.e. transition from stage III to II would require deintercalation of the entire gallery or migration of lithium ions through the graphene layers.[137,138]

The second model was proposed by Daumas and Herold[139] in 1969 to explain issues of Rüdorff’s and Hofman’s model. In that model, lithium ions are not filling galleries entirely but creating lithium-rich spots (islands) between graphene sheets. The size of the island is around 100 Å, while the distance is determined by the minimum of the binding energy curve.[140] Filling the gallery is done on principal extension of the size of each island and closing the gaps in the interlayer spaces.[141] The lithium movement within the interslabs occurs through an exchange mechanism. Li atom travels through the material by creating a local distortion of the space and by pushing Li atoms triangle (see **Figure 3.2 a)**). According to Kühne et al.[142], this diffusion through exchange mechanism with nearest Li atom can be understood as a Li-Li dimer motion. Moreover, at the end of the lithiation step lithium islands repels each other and create channels for lithium diffusion.[143] The other migration pathways are highly unlikely.[144] The layer-to-layer lithium movement is conducted through the rotation of domain walls and/or order-disorder transitions.[141]

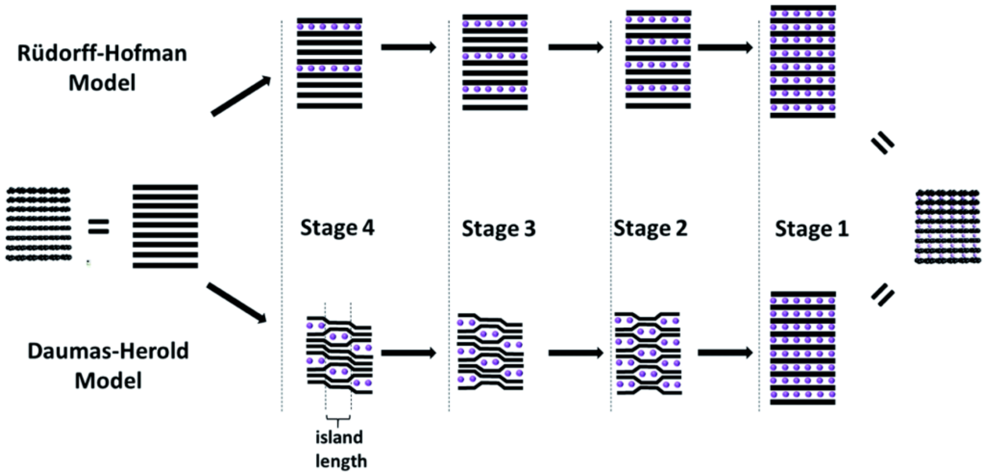

Figure 3.2. *Rüdorff and Hofman model (top) and Daumas and Herold model (bottom) of the staging mechanism of graphite. Image from ref.* [145]

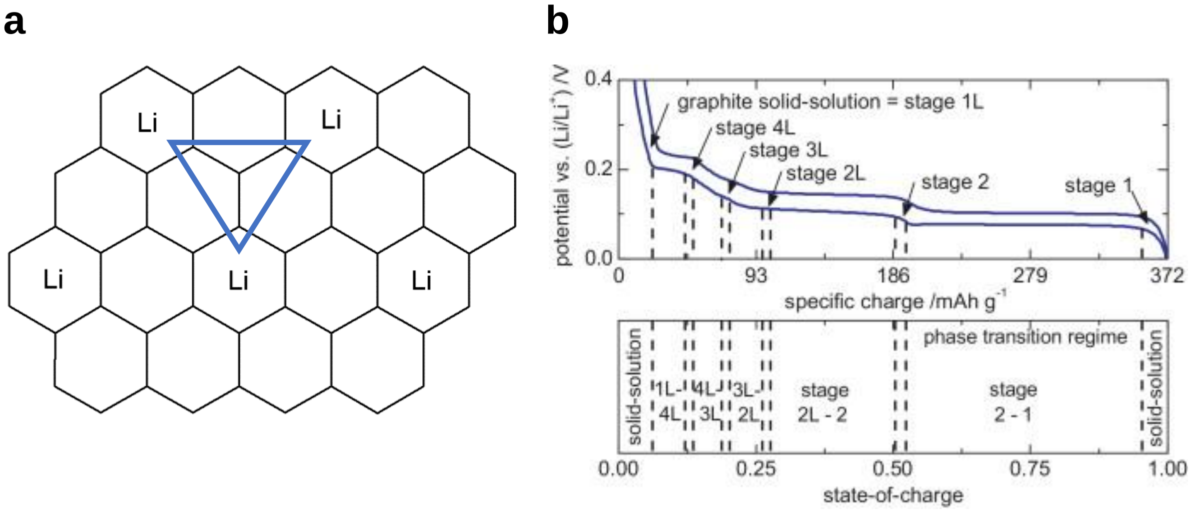

Figure 3.3. *a) Structure of LiC_6 with marked lithium triangle, b) Potential of each of the graphite – lithium phases. Image form ref.* [146]

3.4.3. Stage compounds of lithium-graphite

The intercalation of lithium into graphite occurs in a few distinct stages. There are multiple models of staging steps, however widely accepted is the one developed in the 80-90 s by Billaud et al.[147,148], Ozhuku et al.[149], and Woo et al.[150]. In this model, the delithiation route of graphite consists of the following stages: stage I, stage II, dilute stage II, stage III, stage IV, and dilute stage I. The potential-based existence of the following stages is presented in **Figure 3.3 b)**.

Stage I represents fully lithiated graphite with the formula of LiC_6, where lithium atoms are placed between every graphene sheet. This stage represents the highest possible lithium content within the graphite, with every equivalent adsorption site being occupied.[151] Misalignments of the graphene layers do not provide additional sites.[152] The crystallographic structure of stage I lithiated graphite is similar to pure graphitic structure (hexagonal with P63/mmc space group). The layer stacking along the c-axis is AαAα..., which means that both graphite and lithium atoms are exactly on top of each other in the periodic structure.[153] Interestingly, such a stacking pattern exists independently from the stacking of initial graphite, which is related to the reduction of lithiation energy barrier.[154]

Stage II corresponds to LiC_{12} compound. The stacking is similar to stage I (AαAAαA...); moreover, the space group is also hexagonal.

The next stage is called diluted stage II, sometimes considered stage III. Diluted stage II is a blue compound with the formula of "LiC_{18}".[147] There are still some confusements about that phase because it does not exist as a single phase and has a similar XRD pattern to stage II. However, the electrochemical data confirm the existence of diluted stage II in a form of the plateau as shown in **Figure 3.3 b)**. Diluted stage II is usually assigned to a new incomplete phase or a mixture of phases.[155] The layer stacking is described as AαABCβCABγBCA..., however more accurate should be AB/BA/AB with the lack of ordering within lithium interplane (placed as the "/" sign). Both these structures indicate the withdrawal of lithium ions from the ideal stacking structure of stage II, but keep every second layer filling pattern.[156]

Stage III is a black compound with a formula LiC_x, where x varies from 24 to 36.[155] For that stage, Billaud et al.[148] suggested the LiC_{30} formula, while Ozhuku et al. proposed a more accurate LiC_{27} formula.[157] The filling pattern is suggested to be mainly ABA/ACA .[148] It is often observed in the low-charged or strongly discharged anodes.[158]

The stage IV graphite interlayers are filled every fourth interslab.[159] The compound of stage IV graphite is described as LiC_{72}.[155] Further delithiation of stage IV graphite is not recommended, because it causes local dislocations in the structure (although without destroying hexagonal structure), which results in aging of the graphitic electrode.[155]

The last stage is called dilute stage I. This stage represents lithium ions randomly distributed between the graphene plains.

Among the listed stages, stage I is the best known. There are also consistent data for stage II, but the further stages are either proposed or the data concerning these stages are ambiguous. The biggest problem with analysing stages II and further is to obtain pure/semi pure stage Usually at that point there is a mixture of different stages with similar XRD patterns. Moreover, the structure of these stages may change depending on the preparation technique, which further complicates proper analysis.[148]

Each lithiation stage gives an impact on electric capacity and volume expansion. The values for each stage are given in **Table 3.4**. These values show that most of the lithium is intercalated in the last lithiation step (stages II → I), as well as the biggest volume change, occurs during this transformation (~6% more than during the previous step). This has both positive and negative impacts on the storage capability of graphite. On the one hand, graphite undergoes the highest volume change when most lithium is introduced, which may lower its stability. On the other hand, the last lithiation stage has the lowest potential (around 80 mV vs. Li/Li^+),[157] which translates into a wide potential window with any cathodic material.

Table 3.4. *Volume expansion and consecutive capacity required to fully delithiate (remove) the stage.*[147,160]

Lithiation stage	Volume expansion (with regard to pure graphite)	Consecutive capacity required to fully delithiate stage / mAh g^{-1}
I stage	+ 11.0%	~190
II stage	+ 4.8%	~250
diluted II stage	+ 3.6%	~300
III stage	+ 3.0%	~340
IV stage	+ 0.3 %	~372

3.5. Solid-electrolyte interphase (SEI) of graphite

Solid-electrolyte interphase (SEI) is an organic-inorganic layer, which is formed at the potentials above the formation of dilute stage I. Solid-electrolyte interphase is a thin layer that forms on an electrode as a result of the electrochemical reaction between electrode and electrolyte. SEI plays an important role in Li-ion batteries. On one hand, it protects the inner parts of the electrode from further degradation, and on the other, it allows lithium ions to pass through in both directions, which enables the battery to function properly. The protecting role is mainly fulfilled thanks to low electronic conductivity and the ability to remove the solvation shell for Li^+, which minimizes the conditions for the degradation of the electrode, known as lithium corrosion.[161–163]

The formation of SEI on graphite starts at around 1.4 V with the creation of lithium ions electrochemical double layer (EDL). The EDL is not SEI – it is fully reversible and can be removed by applying higher potential. In the next step, the electrolyte co-intercalates with lithium ions on the surface edges leading to partial exfoliation and breaking the graphitic C-C bonds. Then, complex compounds are formed due to the reaction between C-bonds with the electrolyte.[164] The reduction of solvent is a one or two-electron process, where electrons are transferred from graphite to the solvent molecules. The reactions end up with organic salts containing lithium, fluorine, and phosphorus, usually with the formation of small gas molecules. On the other hand, salt decomposes through the formation of radical anions, which further react with solvents to create inorganic precipitants.[165] The reaction pathways depend on the composition of the electrolyte. The SEI formation is more intense on the edges due to their reactivity than on the basal plains of graphite. Moreover, there are differences between zig-zag and armchair edges. Zig-zag edges are more reactive and lead to higher irreversible capacity.[166] The reactions usually proceed up to 0.04 V, where SEI is considered to be complete.[167]

From the structural point of view, SEI is a polycrystalline material of up to 100 nm thickness with compositions changing depending on the distance from the surface of graphite. The structure of SEI close to the surface of graphite is compact and it consists primarily of crystalline Li_2CO_3 A bit further from the surface, SEI contains inorganic compounds such as LiF, Li_2O, Li_2CO_3. SEI close to the electrolyte is looser and has a higher fraction of polyolephines, semicarbonates, smaller oligomers, and salts [$(CH_2OCO_2Li)_2$ and ROLi, where R is the organic group from solvent]. In addition, in that part of the SEI, there may be lithium ions trapped in the structure. [158,161,165,168] SEI composition varies depending on the reaction conditions. It was shown, that SEI formed on the basal plains contains more inorganic components, while formed on edges has more alkali carbonates and polymeric compounds. Due to these differences, SEI formed on basal plains is thinner and harder than that created on the edges.[169]

3.6. The failure mechanism of graphite

The failure of graphitic anodes is the most important reason for battery deterioration. Failure mechanism covers two main processes: *i)* SEI formation and reformation, *ii)* structural changes, *iii)* graphite disintegration.

SEI formation and reformation is the first cause of the failure and it is influencing electrode condition on different stages of battery life. In the case of unused (stored) Li-ion batteries, the main failure mechanism is lithium corrosion of graphite anode. Lithium corrosion involves a set of reactions between lithium, electrolyte, and graphite, which leads to active material loss and uncontrolled SEI growth.[163,170,171] This occurs mainly when SEI film is not formed properly. In the case of “working” electrodes, SEI cracking and rebuilding is the main failure factor. Cracking and rebuilding of SEI layer are related to volume expansion of graphite upon lithiation. Each expansion may lead to rupture of SEI film, which exposes graphite to direct contact with the electrolyte. This forces SEI rebuilding, which, like in the case above, consumes both graphite and electrolyte.[159] SEI cracking and rebuilding happens during the whole cycling process, but it is the most intense at around 65%-85% of the state of charge (SOC). It is related to stage transition stage I ↔ stage II, which occurs at that particular SOC.

That type of transition, as already has been mentioned, corresponds to the highest volume change and the highest lithium exchange. Thus, it is recommended to use batteries outside that SOC range, especially if the short use of the device is predicted.

Structural changes are the second degradation mechanism. They may be induced by multiple processes, such as lithium plating or electrolyte co-intercalation. Lithium plating is a process of the formation of metallic lithium on the surface of graphite. It occurs in many circumstances when lithium intercalation cannot keep up with lithium ions delivery, i.e. when the capacity of the anode is higher than the capacity of the cathode when the device works at low temperatures, but mostly when high current is applied.[172–174] Upon high current lithium, layers are initially formed between graphite and separator (electrolyte), and then they tend to massively intercalate. This causes wrinkling of the graphene layers, breaking of C-C bonds, and damaging the structure. These damages provide new migration paths for lithium, but they are also a source of irreversible reactions.[175] Solvent co-intercalation is another effect of the high current application. During charging, there is a possibility that a swarm of lithium ions may pull electrolyte with itself. Insertion of the electrolyte would normally require much greater interlayer space, so in the case of graphite, it leads to an extreme extension of interlayer spaces that cause graphite exfoliation.[176,177] Moreover, in the case of some electrolytes (like propylene carbonate), the reduction of electrolyte may occur leading to gas formation, which prevents proper SEI formation and makes the material more porous. [178] Therefore, for a long time, electrolytes like propylene carbonate or tetrahydrofuran are out of use in battery applications.

The last mechanism is graphite disintegration. This process occurs in contact with some electrolytes like propylene carbonate or tetrahydrofuran. During charging, there is a possibility of a reaction between graphite and electrolyte, which leads to gas formation. Bubbles of gas hinder the proper SEI formation, moreover, they make the material more porous, cause exfoliation, and, in the worst-case scenario, battery unsealing.[178]

3.7. Modifications of graphite

The electrochemical behaviour of graphite, i.e. the capacity, Coulumbic efficiency, cycling stability vary depending on the intrinsic properties of graphitic material. Thus, multiple modification methods have been developed to enhance the surface of graphite. One of the simplest and the most widespread methods to improve the electrochemical performance of graphite is mechanical grinding. The main purpose of mechanical grinding is to lower the particle size, which results in the shortening of Li^+ diffusion paths and leads to the extension of graphene plain's edges. Edge bonds are important because on the edges the lithiation chemistry is not limited by space and lithium can bind with graphite in higher quantities than in stage I (LiC_6), which eventually turns into a higher capacity of the final material. Moreover, the mechanical grinding leads to a higher fraction of the rhombohedral stacking of graphene plains, which were proven to have higher capacity and better resistance to exfoliation than ABAB or AAAA stacking. [179–181] Mechanical milling can be performed in two ways: dry milling and wet milling. Wet milling is considered superior because it preserves better crystallinity and prevents agglomeration. For wet milling, various media were suggested, but the best results were reported for ethanol.[180,182] Another way to improve the performance of graphitic electrodes is by magnetic alignment of graphitic particles. The magnetic alignment of the particles leads to a decrease in the tortuosity of diffusion paths, which finally results in better performance upon high current rates.[183] Another approach to improving graphite is by chemical surface modification. Surface modification can be performed by fluorination, oxidation, or coating. The idea behind the fluorination is to increase surface area and to make controlled defects in the basal plane structures, which improve electrolyte penetration, allow lithium transport through graphitic layers, and increase the content of edge bonds, leading to capacity increase.[184,185] A similar effect was achieved by nitrogen ion implementation.[186] The goal of oxidation is to remove structural imperfections from a graphitic structure such as sp^3 carbons or dangling carbon chains. These imperfection bond irreversibly lithium ions and are prone to create more complex SEI – the main source of irreversible capacity.[187–189] The last way of surface modification is coating. The coating materials are usually organic carbon precursors (i.e. tar pitch, phenolic resin, poly(vinyl chloride), polyethylene oxide). The main idea behind coating graphite particles with carbon is to cover the most vulnerable parts of graphite i.e. the edges on which decomposition of solvent occurs. By this approach, the decrease in irreversible capacity was reported.[190–193] Another way of surface modification is by functionalisation using diazonium chemistry.[194,195] Within this approach, strongly bonded functional groups are created, which make later a good base for stable SEI film. Besides coating graphite with organic compounds, there are also reports on the utilisation of inorganic compounds. For example, Kotegotta et al.[196] reported higher stability and capacity of zirconia-treated graphite. The improvement was attributed to the protecting role of zirconia film, preventing graphite from degradation. Other authors[197] were combining graphitic electrodes with tin. This approach not only leads to a vast increase in electrochemical capacity but also improved the electrode performance at low temperatures.

Chapter 4. Tin

4.1. Basic information

Tin is one of the first metals ever used by humans. It was used in conjunction with copper in a form of bronze starting from around 3500 B.C. Bronze was commonly used in all areas of human life from everyday objects to weapons and big containers. The utilisation of pure tin metal reaches the times of ancient Egypt of around 600 B.C.[198,199]

Tin is a relatively rare element. It makes up only roughly 0.001% of the earth's crust. The most important and industry-viable tin ore is cassiterite. Cassiterite contains ~78.6% of tin in the form of tin (IV) oxide. It is usually found next to sources of granite in hydrothermal veins and volcanic regions. The biggest cassiterite deposits are found in Malaysia, Bolivia, China, Indonesia, Peru and Brazil. Pure metallic tin is obtained from cassiterite during carbothermal reduction of tin oxide with coal.[198,200]

4.1.1. Allotropic forms of tin

Tin exists in four allotropic forms: grey tin (α-tin), white tin (β-tin), γ-tin and δ-tin. α-tin is a diamond-structured allotrope with a cubic lattice.[201–203] β-tin is a tetragonal allotrope, where Sn-Sn distances are higher than in α-tin. α-tin and β-tin are main tin forms due to their existence under ambient conditions. The reversible transition between $\alpha \leftrightarrow \beta$ tin occurs at 13.2°C. It is associated with high volume expansion (~27% increase during the transformation from $\beta \rightarrow \alpha$). Such a high volume expansion along with changes in properties often leads to damaging of items made of tin and thus is known as a "tin pest". To avoid β to α transition and *vice versa*, special alloys have been developed. The structure of β-tin is usually preserved by small addition (a couple of percent) of conductive metals, such as bismuth, antimony, lead, zinc, silver and indium, silver and copper.[204,205] On the other hand, the structure of α-tin can be kept by growing and pressing β-tin on materials with a structure similar to α-tin, i.e. on InSb, CdSb or Ge substrate.[206,207]

The properties between α-tin and β-tin are vastly different. β-tin is a soft, ductile, pliable metal with good electronic conductivity. β-tin is stable at room temperature and malleable above room temperatures. α-tin, on the other hand, is a very brittle material with a tendency to crumble into powder. From the electrical point of view, tin is a zero-gap semiconductor due to strong covalent bonds between tin atoms. The main physical properties of tin are collected in **Table 4.1.** [204,208]

***Table 4.1.** Selected physical properties of tin.* [204,208]

Property	α-tin	β-tin
Electrical resistivity	5×10^{-6} (at 0°C)	11.15×10^{-6} (at 25°C)
Colour	Grey	White
Density	5.765 g cm^{-1}	7.286 g cm^{-1}
Yield strength	2.55 N/mm^2, at 25°C	
Brinell hardness	4.12 (10 mm, 3000 N, 10s)	
Melting point	232°C	
Boiling point	2603°C	

The remaining two tin forms, γ-tin and δ-tin, are high-pressure tin forms. They exist in pressures above 9.7 and 10 GPa, respectively, at room temperature. δ-tin forms a body-centred cubic lattice, while γ-tin a tetragonal structure.[209,210] Due to lack of industrial application, there is limited knowledge about these forms of tin and some sources are neglecting the existence of such phases.

The stability of various tin phases changes in the case of tin nanoparticles. Hörmann et al.[210] reported that γ-tin is the most stable phase in the case of particles below 11 nm. Moreover, $\beta \rightarrow \alpha$ transition temperature is moved from 13.2°C to -20°C. Therefore, these structural features are important in the case of the chemistry of nanomaterials.

4.1.2. Chemical properties of tin

Tin is a chemically resistant metal, which hardly reacts with oxygen, brine and tap water. Tin also resists most of the multiple organic acids at room temperatures, which makes it an important component of food-containing cans. Tin has an amphoteric character, it reacts with HF even at low concentrations (as low as 0.05% at 0°C), and with concentrated strong acids, strong bases and acidic salts. When heated in air, it creates SnO_2, which can then form a stannic acid H_2SnO_4. Tin forms inorganic compounds with +2 and +4 oxidation states.

Organotin compounds are a broad group of tin compounds with the general formula of $R_xSn(L)_{(4-x)}$, where R is an organic group, and L is a ligand. Organotin compounds are classified based on the oxidation state, and compounds with up to 4 organic groups can be formed. Most of the organotin compounds are insoluble in water, but they are soluble in other organic solvents. Many organotin compounds are toxic for humans and animals.[202,208,211]

4.2. Lithium storage in tin

The lithium storage in the tin is based on the creation of alloys. The reaction can be described as follows:

$$xSn + yLI^{+} + Ye^{-} \leftrightarrow Sn_{x}Li_{y} \qquad 21)$$

The types of alloys of lithium-tin system existing in nature are presented in **Figure 4.1** [212]. $Li_{22}Sn_5$ is the highest lithium-containing alloy with the capacity of 994 mAh g^{-1} (2111 Ah L^{-1}). The lithiation pathway is as follows: [213–215]

$$\begin{aligned} Sn \overset{\pm Li}{\longleftrightarrow} Li_2\,Sn_5(0.72\,V) \overset{\pm Li}{\longleftrightarrow} LiSn\ (0.55\,V) \overset{\pm Li}{\longleftrightarrow} Li_7\,Sn_3(0.45\,V) \overset{\pm Li}{\longleftrightarrow} Li_5\,Sn_2 \\ \overset{\pm Li}{\longleftrightarrow} Li_{13}\,Sn_5\ (0.32\,V) \overset{\pm Li}{\longleftrightarrow} Li_7\,Sn_2\ (0.3\,V) \overset{\pm Li}{\longleftrightarrow} Li_{22}Sn_5\ (below\ 0.3\,V) \end{aligned} \qquad 22)$$

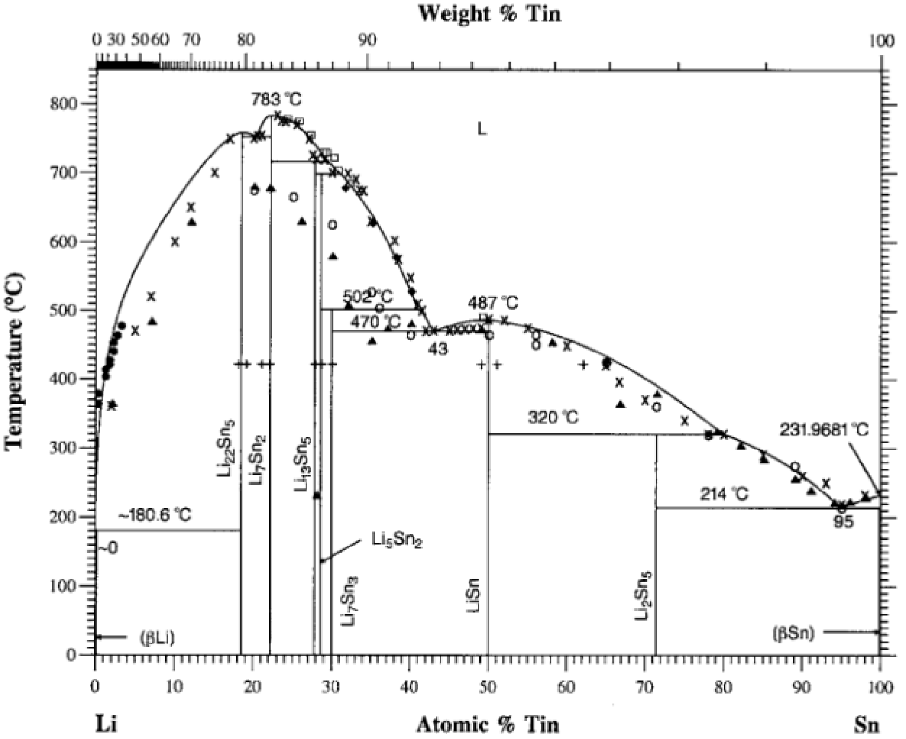

Figure 4.1. *Phase diagram of the lithium-tin system. Image from ref.* [212]

Table 4.2. *Volume expansion of lithium-tin alloys.*[216,217]

Phase	Volume expansion (w. regard to metallic tin)
Li_2Sn_5	+22%
LiSn	+52%
Li_7Sn_3	+126%
Li_5Sn_2	+138%
$Li_{13}Sn_5$	+142%
Li_7Sn_2	+197%
$Li_{22}Sn_5$	+258%

The Tin alloying pathway consists of several, similar to the lithiation of graphite. However, the potentials of creation Li-Sn alloys are higher than lithiation of graphite (0.7 – 0.3 V for tin, equilibrium potential of 0.51 V[218]) than for graphite (0.2 – 0.075 V). This results in a narrower voltage of the full cell, where tin as the anode is used, and therefore in lower energy of the battery. Nevertheless, tin lithiation potential is still lower than other anodic materials, i.e. LTO reacts with lithium ions at 1.5 V.[219]

The lithiation path presented in equation 22 corresponds to the high-temperature systems, above 400°C, when all phases can be formed. However, at room temperature some phases do not exist, such as Li_5Sn_2, thus the lithiation pathway may be different. [218,220] The electrochemical formation of different Li-Sn alloys under ambient conditions was broader investigated by Dahn et al.[216]. They found under normal conditions all the structures of Li_xSn, where $x<2.5$, exist in a bulk form. On the other hand, when $x \geq 2.5$, in particular in the case of $Li_{22}Sn_5$, long-range crystallographic ordering is not formed, but alloys exist rather as a mixture of structures. For instance, for $Li_{22}Sn_5$ they observed randomly placed tin tetrahedral units together with the typical BCC (body-centred cubic) structure of Li_2Sn_5.[220] This phenomenon of forming mixtures of alloys with short ordering is explained by low atom mobility upon room temperatures of these phases.[215]

4.3. The drawback of tin anodes

The main problem of tin anodes is a high volume expansion upon lithiation. The creation of high-lithium alloys leads to a volume increase of up to 260% (see **Table 4.2**). The cyclic volume changes of the tin anode (during lithiation and delithiation) lead to the effect known as pulverisation. Pulverisation causes contact loss between the active material and current collector, which leads to the loss of active material or, in the worst case, breaking of the electrical circuit. Moreover, it promotes aggregation of nanoparticles due to wielding effects, which extends the diffusion pathways for lithium, [221] and limits the ability for material to heal. [217] Pulverisation also has a negative impact on the SEI layer, which is described in more detail in subsection 4.4. These phenomena lead to a rapid deterioration of the electrode during cycling.

There are several ways to avoid the negative effects of pulverisation. The strategies involve the controlling of cell operation window, producing thin layers of anode material, and creating intermetallic compounds and particle size control.[221] The first approach is to limit the potential window. By limiting the potential window, only low-lithium alloys form, such as Li_2Sn_5 or LiSn, which exhibit a much smaller volume expansion than fully lithiated $Li_{22}Sn_5$ - (see **Table 4.2**). However, limiting the potential window vastly reduces the capacity of the electrode. Moreover, the low-lithium alloys exhibit higher volume expansion (+22% for Li_2Sn_5) than fully lithiated graphite (+11%), thus the problem with volume expansion is not solved completely.[221]

The second strategy is to produce a thin film of tin on the current collector. Producing a thin film enhances the bonding between the tin and the current collector, and reduces the volume expansion. Moreover, a thin layer of active material also shortens the average diffusion length of lithium ions. The drawback of this approach is a high mass ratio of current collector to active material, which increases the weight of the battery pack.[222]

Another approach to prevent pulverisation and to improve cycling performance is creating intermetallic compounds. This approach was studied by Kawakami and Asao ,[223] Fan et al.[224] and adopted by Sony company. The creation of intermetallic compounds changes the microstructure of the material from crystalline to amorphous. The amorphous structure can better withstand volume changes probably due to its powder nature. This translates into the better cycling performance of the amorphous electrodes compared to the crystalline ones.[224] One of the best-performing systems of intermetallic compounds was Si-Co alloy, however, the projects were withdrawn due to the high toxicity and price of cobalt.[225] Another approach to intermetallic compounds is the combination of tin with other alloying metals, such as antimony or silver. This idea is based on differences in kinetics and thermodynamics of lithiation processes of intermetallic phases Mixing tin with other alloying metals allows more controllable growth of nanocrystal domains and preservation of ductile structures of alloys during most of the lithiation process. [215,226]

Tin intermetallic compounds could be also used in a form of nanocomposites, where tin is an active material, while other metal serves as an inactive matrix. In such systems, the matrix buffers the expansion of the tin phase and prevents its agglomeration.[227] Moreover, the inactive metal also provides extra protection from the electrolyte.[225] Matrix metals used in that configurations were i.e. iron or copper.[228,229] The main disadvantage of this approach is the suppressing of the formation of high-tin alloys, which severely limits the capacity of the electrode.

The last, and most successful strategy to reduce the effect of pulverisation is particle size control. In this approach, tin is used in a form of nanoparticles, incorporated in a matrix. Carbon-based matrices are the most commonly reported due to their multiple advantages: good electrical conductivity, appropriate softness, activity towards lithium ions, and inactivity towards tin.[221,230,231] Using the matrix approach allows not only reduce the volume expansion of composite material but also reduces dead mass and volume of the composite material. Moreover, carbon properties may be tailored by surface modification. Many structures have been proposed, such as yolk-shell,[232] Sn-nanofibres,[233,234] Sn-graphene,[235] Sn-hollow carbon,[236] Sn-graphite,[237] Sn-activated carbon.[238] The general problem with that approach may be the high content of empty spaces, which translates into low volumetric capacity, and often multistage, complicated synthesis routes.[215,231]

4.4. Solid-electrolyte interphase on tin anodes

The SEI on tin electrodes forms in a few steps, similar to the SEI on graphite. SEI formation on tin starts at around 2.5 V vs Li/Li^+. At that potential, small crystallites of <50 nm in diameter creates, which form a compact layer of initial SEI layer 100 – 150 nm thick. This layer is very hard and it is composed mostly of inorganic compounds, like PF-containing species ($Sn\text{-}PF_3O$, $Sn\text{-}PF_5$) and Li_2O. PF-containing species are created as a result of the reaction of tin with lithium salts, while oxygen-based compounds are created through the reaction of lithium ions with oxygen originating from the thin SnO_2 layer and oxygen dissolved in the electrolyte. [239–242] Below 2 V the formation of the organic layer occurs. Initially, the organic reaction products are dissolved in the electrolyte, but as the potential goes down, they start to form a thin soft layer on top of the first layer.[239,240] This softer phase is composed of high-oxygen organic compounds with the formula of CH_2OCO_2Li, $R-CH_2OCO_2Li$, and $OPF_{3-y}(OR)_y$. Upon further lithiation, the composition of organic compounds changes and some carboxylate and alkyl carbonate salts transform producing Li_2CO_3.[240,243]

The SEI formation and degradation mechanism on tin anodes have a different origin from graphitic anodes. In contrast to graphitic anodes, tin anodes are densely packed, and thus co-insertion of electrolyte is negligible.[243] Moreover, SEI formed on the tin is more uniform as tin exhibits a relatively "homogeneous" structure compared to chemically different basal plains and graphene edges of graphite. Gas evolution on tin electrodes is insignificant compared to graphitic ones (only a slight amount of hydrogen can be created).[244] The main problem and challenge of the SEI layer on the tin electrode is the volume expansion of tin anodes, which causes cyclic SEI cracking. The SEI cracking occurs in a two-step process. Firstly, SEI is created on the expanded (lithiated) tin electrode, and then, during discharge, the electrode starts shrinking, which causes internal stresses inside the SEI. Since SEI cannot shrink along with the tin, it disconnects from the metal or cracks into small floes and exposes tin to further corrosion, which leads to SEI rebuilding and repetition of the process.[161]

Experimental part

Aim and scope of the work

The aim of this doctoral dissertation was to create composite material based on silicon oxycarbide, graphite and tin for the application as active anode material for lithium-ion batteries. Moreover, this work takes the attempt to explain the correlation between electrochemical performance and the composition of the obtained composite materials. The choice of these three components was dictated by the features of these materials, which can minimize the drawbacks of one another:

- graphite exhibits a very stable electrochemical response, but the capacity and rate capability is limited. The addition of tin and silicon oxycarbides may solve both of these drawbacks,

- tin can provide very high capacity, however, poor stability is a problem. The utilisation of active silicon-oxycarbide matrix together with reducing the size of tin to nanoparticles may stave off this problem,

- silicon oxycarbide is a high-capacity, high-performance material, but it exhibits high initial irreversible capacity and mediocre conductivity, depending on the composition. The first drawback could be solved by the addition of graphite, while the second by the addition of graphite and tin.

To achieve the goal, the following activities have been undertaken:

- sol-gel synthesis of preceramic polymers

- design and preparation of homogeneous mixtures (green bodies): (*i*) preceramic polymer + graphite, (*ii*) preceramic polymer + tin precursor, (*iii*) preceramic polymer + graphite + tin precursor

- optimisation of curing and pyrolysis conditions

- electrochemical testing of the obtained materials using various techniques (galvanostatic charge-discharge, cyclic voltammetry measurements, electrochemical impedance spectroscopy)

- physicochemical characterisation by elemental analysis, Raman spectroscopy, X-ray photoelectron spectroscopy, X-ray diffraction spectroscopy, ^{29}Si Solid State Nuclear Magnetic Resonance, Brunauer-Emmett-Teller surface area analysis, thermogravimetry, differential scanning calorimetry, Fourier-transform infrared spectroscopy, imaging techniques like scanning and transmission electron microscopy.

- correlation of the physicochemical and electrochemical properties with the composition and microstructure of the materials.

Materials

- Preceramic precursors:
  - Phenyltriethoxysilane (PhTES), >97%, Sigma Aldrich, Germany
  - Vinyltriethoxysilane (VTES), >98%, Sigma Aldrich, Germany
  - Octyltriethoxysilane (OTES), >97%, Sigma Aldrich, Germany
  - Polyramic® SPR-684, Starfire Systems, Inc., USA
  - Polymethylhydrosiloxane (PMHS, MW ≈ 1900), Sigma Aldrich, Switzerland

- Graphite:
  - Flake graphite, powder, synthetic, <20 microns, Sigma Aldrich, Germany

- Additional reagents for synthesis:
  - Ethanol (EtOH), absolute, 99.8%, reagent grade, POCH, Poland
  - Acetone, >99%, reagent grade, Sigma Aldrich, Switzerland
  - Isopropanol, absolute, regent grade, POCH, Poland
  - Chloric acid, 30%, reagent grade, Chempur, Poland
  - Line-EtOH, Linegal Chemicals, Poland
  - 1,4-Butanediol diacrylate (BDDA), technical grade, 90%, Sigma Aldrich, Switzerland
  - Photoinitiatior Genocure* LTM, Rahn AG
  - Tin octoate, 92.5-100.0%, Sigma-Aldrich, Switzerland
  - Karstedt's catalyst (platinum(0)-1,3-divinyl-1,1,3,3-tetramethyldisiloxane complex solution in xylene, Pt ≈2%), Sigma-Aldrich, Switzerland
  - p-Divinylbenzene (DVB), technical grade, 80%, Sigma Aldrich, Switzerland

- Materials for electrode fabrication:
  - Copper foil, 10 μm, Copper SE-Cu58 Schlenk Metallfolien GmbH & Co. KG, Germany
  - polyvinylidene fluoride (PVDF), Solef5130, Solvay, Germany

- N-methyl 2-pyrrolidone (NMP), BASF, Germany
- Carbon Black Super P®, Imerys Graphite & Carbon, Switzerland
- Carboxymethyl cellulose (CMC), SUNROSE MAC 500LC, Nippon Paper Group

- Materials for cell assembly:

  - MN GF-2, 45 µm, Macherey-Nagel GmbH & Co. KG, Germany
  - 1 M $LiPF_6$ in 1:1 v/v ethylene carbonate:dimethyl carbonate, Sigma-Aldrich, Germany,
  - Lithium foil, Sigma-Aldrich, Germany,

- Equipment:

  - Ultrasonic homogeniser UP200St, Hielscher Ultrasound Technology, Germany
  - Tubular furnace Protherm Furnace PTF 12/105/500, Protherm Furnace, Poland
  - Tubular furnace Type 16-610, Carbolite GmbH, Germany
  - Mixer Mill MM200, Retsch, Germany
  - Glass vacuum oven B-585, Büchi, Germany
  - Glove box, MBraun Glove Box Systems, Germany
  - UV curing chamber, 365 nm
  - Potentiostat-Galvanostat Biologic Potentiostat SP200, BioLogic Science Instruments, France,
  - Potentiostat-Galvanostat MPG-2, Bio-Logic SAS, France
  - Battery tester Atlas 0961, Atlas Solllich, Poland,
  - Carbon analyzer Leco C-200, Leco Corporation, USA
  - Nitrogen/oxygen analyzer Leco TC-436, Leco Corporation, USA
  - TGA analyzer SDT 2960 Simultaneous, TA Instruments, USA
  - TGA analyzer, Netzsch STA449 F3 Jupiter
  - Powder diffractometer Stoe STADI P equipped with a Mo Kα anode
  - X-ray diffractometer X'Pert Pro MPD, PANalytical, Netherlands
  - Raman spectrometer with 514 nm argon ion laser InVia, Renishaw, UK
  - XPS spectrometer VG Escalab 250Xi, Thermo-Fischer Scientific, USA
  - FTIR spectrometer Tensor 27 using Golden Gate ATR, Bruker, USA
  - TEM, FEI, G2 F20X-Twin 200 kV, FEG, USA

- NMR spectrometer Bruker Avance Ultrashield 500 MHz, Bruker, USA
- SEM, Phenom XL Scanning Electron Microscope, Thermo-Fischer Scientific, Poland

Chapter 5. Synthesis of the active materials

Synthesis of the active materials was performed using three different methods:

- sol-gel synthesis of the preceramic polymers followed by high-power ultrasounds-assisted homogenization and subsequent pyrolysis to obtain SiOCs/graphite composites,
- UV-assisted curing followed by pyrolysis to obtain SiOCs/tin nanoparticles composites based on commercially available preceramic polymer,
- hydrosilylation-based curing followed by pyrolysis to obtain SiOCs/graphite/tin nanoparticles composites based on commercially available preceramic polymer.

The schematic representation of methods and used materials are shown in **Figure 5.1**.

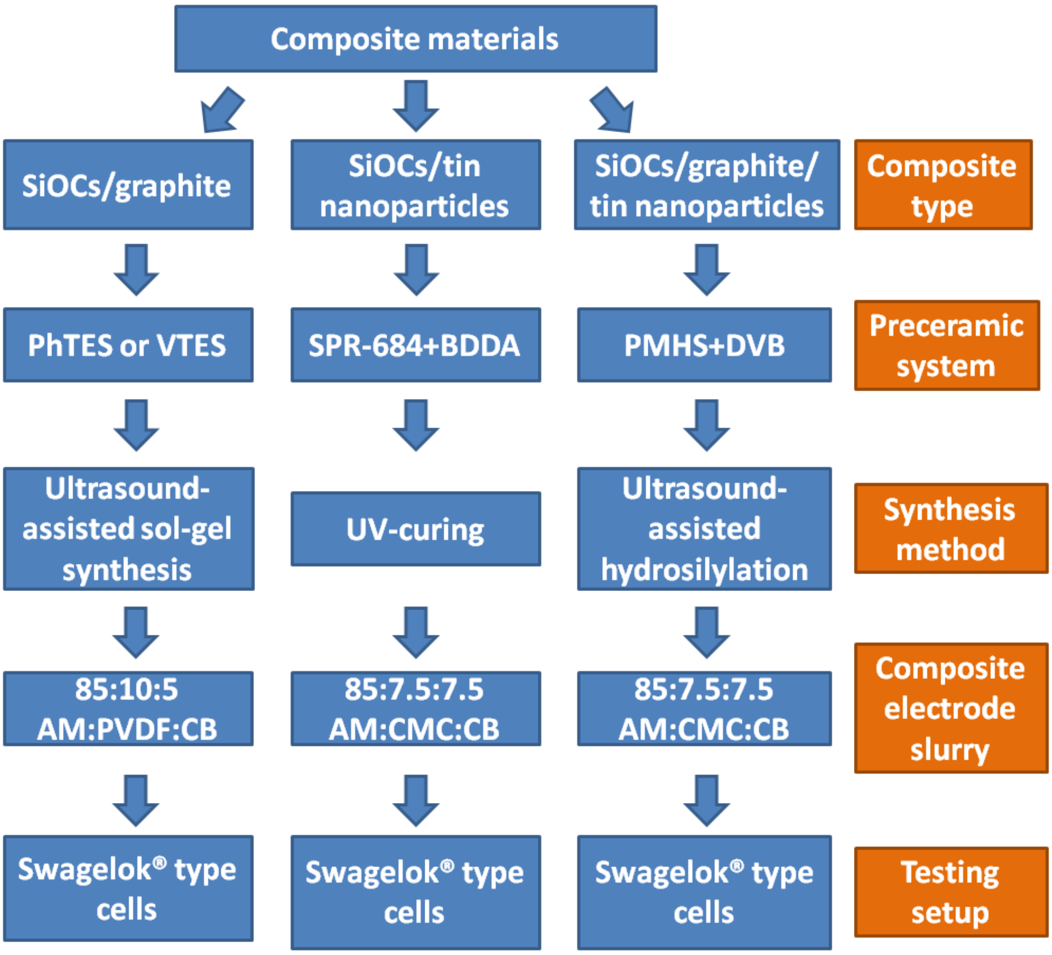

Figure 5.1. *Material preparation scheme. PhTES – phenyltriethoxysilane, VTES – vinyltriethoxysilane, SPR-684 – a polymer resin, BDDA - 1,4-butanediol diacrylate, PMHS – polymethylhydrosiloxane, DVB – divinylbenzene, AM – active material, PVDF - polyvinylidene fluoride, CB – carbon black, CMC - carboxymethyl cellulose*

5.1. Synthesis of SiOCs/graphite composites

The sol-gel method was used for the synthesis of SiOCs/graphite composites. Firstly, 2, 4, and 10 g of graphite were poured into a three-neck flask, then a 0.072 M of preceramic precursor, i.e. PhTES or VTES was added (chemical structures of PhTES and VTES are shown in **Figure 5.2**). Next, the preceramic precursor was mixed with ethanol (EtOH/Si = 2). Afterwards, HCl-acidified water (pH=4.2, H_2O/Si = 3) was added dropwise, and the mixture was boiled for 1.5 h. Then, obtained sols were cooled down and transported to propylene test tubes for gelation. The gelation process was performed using high-power ultrasounds to *i)* ensure the homogeneity of the mixture and *ii)* speed up the gelation and drying process. The ultrasonic treatment was stopped after obtaining solid gel in the case of VTES-based composites, or tar-like consistency for PhTES-based composites. As-obtained green bodies were dried in an oven for 5 days, at temperatures from 80 to 120°C. The green bodies were then ground in a mortar into powder, followed by pyrolysis at 1000°C for 1 h in an argon atmosphere. The flux rate of argon was ~40 cm^3 min^{-1}. The heating rate was set to 100°C h^{-1}. Materials were cooled down at natural speed (the furnace was switched off).

SiOCs/graphite composites are denoted as $SiOC_{precursor}$/Cxg, where “precursor” is assigned either as VTES or PhTES and the annotation Cxg corresponds to the grams of graphite used per 0.072 M of preceramic precursor, as mentioned in the procedure.

As-prepared ceramic composites were then milled in the ball mill for 60 min using two zirconia balls with 10 mm diameter to obtain a fine powder. The obtained powders were further used for characterization and preparation of the electrodes for electrochemical testing.

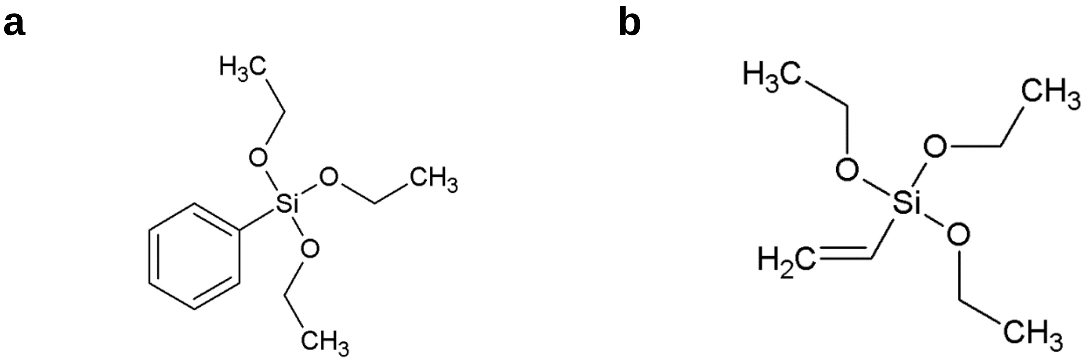

Figure 5.2. *Chemical structure of a) PhTES and b) VTES*

5.2. Synthesis of SiOCs/tin nanoparticles composites

For the synthesis of SiOCs/tin nanoparticles composites, a UV-assisted curing method was used. Firstly, 0.6 g of BDDA (**Figure 5.3**) was mixed with 3.4 g of SPR-684 (**Figure 5.4)**. Then, after a couple of minutes of mixing, 0.08 g photoinitiator and 2.67 g tin (II) ethylhexanoate were added to the preceramic mixture (2 and 40 wt% of the preceramic mixture, respectively). The substrates were mixed for 15 min at 400 rpm to obtain a homogeneous solution. Then, the mixture was cast on a Petri dish and crosslinked under a UV light (365 nm) for 30 minutes. Finally, the obtained green body was washed using ethanol and acetone and dried at 80°C for 2 days.

As-obtained green bodies were then ground in an agate mortar and pyrolysed in an argon atmosphere. The heating program was as follows: ramping to 250°C with the rate of 100°C h^{-1}, dwell at 250°C for 2 h, ramping to 1000°C with the rate of 150°C h^{-1}, dwell at 1000°C for 1 h, cooling to room temperature with the rate of 60°C h^{-1}. The reference SiOCs sample was prepared using the same method, but without the addition of tin octoate.

Samples synthesized by this method are denoted as $SiOC_{UV}$/Sn-40% for the composite sample and $SiOC_{UV}$ for the reference sample.

As-prepared ceramic composites were further milled in the agate mortar for 30 min. The obtained powders were used for the characterisation and preparation of electrodes for electrochemical testing.

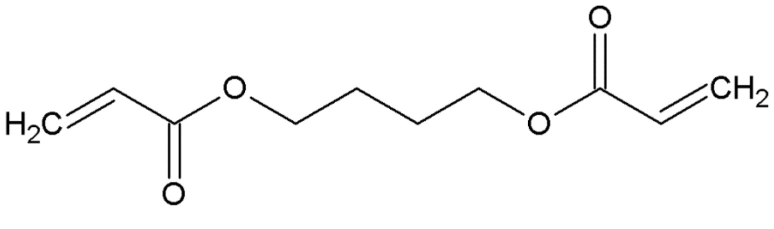

Figure 5.3. *Chemical structure of BDDA*

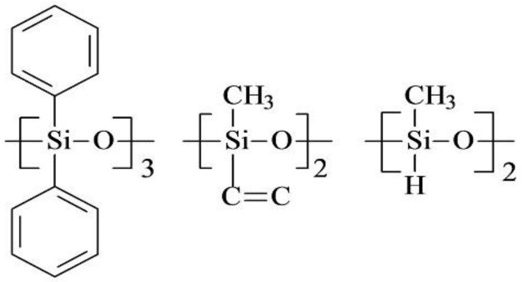

Figure 5.4. *Chemical structure of SPR-684*

5.3. Synthesis of SiOCs/graphite/tin nanoparticles composites

For the synthesis of the SiOCs/graphite/tin nanoparticles composites, curing *via* hydrosilylation reaction was used. In this system, the reference binary SiOCs/Sn material was synthesized with a modified procedure described by Dubey's et al.[66], while the ternary SiOCs/graphite/tin nanoparticles composites were obtained by replacing a part of the ceramic with graphite. The synthesis was conducted as follows: firstly, 5 µL of Karstedt's catalyst and 2 g of DVB were mixed together. Then, 2 g of PMHS, 2.5 g of acetone, and different contents of graphite and tin octoate were added to the mixture. After 5 minutes of mixing, the suspension was subjected to high-power ultrasounds for couple of minutes to obtain solid gel. As-obtained gels were dried for 48 h at 80°C, and then ground in an agate mortar. The gels were pyrolysed using the same program as in the case of SiOCs/tin nanoparticles composites.

The ternary composite samples are denoted using the following annotation: SiOC:C$_x$/Sn-y%, where the "x" value corresponds to the mass fraction of the preceramic polymer replaced by graphite, and "y" assigns to the weight percentage of the tin precursor with regard to the mass of the whole preceramic polymeric blend. The compositions of preceramic blends are given in **Table 5.1**.

Table 5.1. *The compositions of preceramic blends.*

Composite	Tin octoate	Matrix Graphite	 PMHS / DVB; 1 : 1 w/w
SiOC$_H$	-	-	5 g
SiOC$_H$/Sn-40%	3.33 g	-	5 g
SiOC$_H$:C$_{0.2}$/Sn-40%	3.33 g	1 g	4 g
SiOC$_H$:C$_{0.2}$/Sn-60%	7.5 g	1 g	4 g
SiOC$_H$:C$_{0.1}$/Sn-60%	7.5 g	0.5 g	4.5 g

As-prepared ceramic composites were then milled in an agate mortar for at least 30 min. The obtained powders were further used for characterization and preparation of electrodes for electrochemical testing.

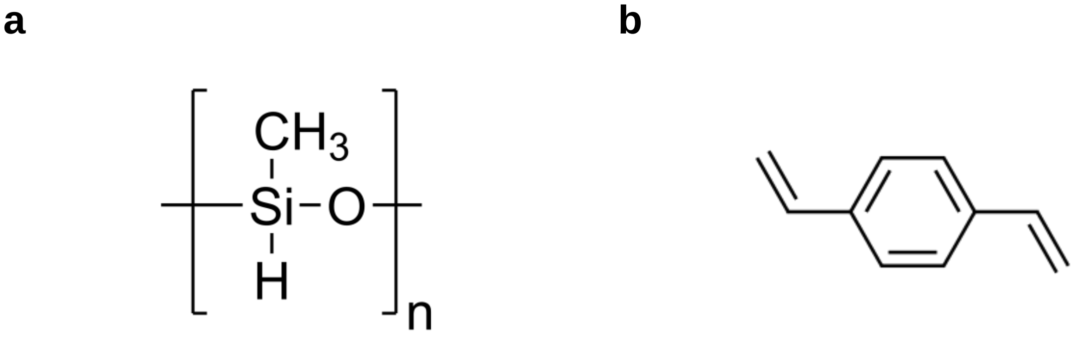

Figure 5.5. *Chemical structure of a) PMHS and b) p-DVB*

5.4. Pyrolysis conditions

During the pyrolysis process, the environment of the sample may contaminate the final product. The contaminations may originate from the atmosphere and crucible. To limit the contaminations, the argon atmosphere was used, as argon is inert towards the used substrates and does not build in the structure like other gases, i.e. nitrogen. For the same purpose, quartz tube and quartz crucibles were used due to chemical similarities of the final products (SiOCs-based composites).

As for the temperature, the maximum of 1000°C was chosen based on the performance of ceramics pyrolyzed at various temperatures. Kaspar et al.[62] showed that SiOC obtained at lower pyrolysis temperatures exhibit better electrochemical performance due to the lower content of inactive SiO_4 and SiC_4 units. In the case of composites with tin, the program was additionally modified, *i.e*. 1 h dwell time at 250°C was added and a cooling rate was slower. Such changes were conducted to allow a smooth transition from tin octoate to tin nanoparticles and to achieve good crystallinity and uniform distribution of tin nanoparticles.

5.5. Preparation of electrodes

Electrodes were prepared by coating copper foil with a thin layer of active material. The composition of the layer was different for materials with and without tin. For materials, without tin, the PVDF binder was used – the binder used in commercial battery systems [14]. The active material – binder – conductive agent ratio was 85:10:5, similar to the compositions reported previously.[56,245,246] For the composites with tin, the CMC binder was used, as it was [66,247] was 85:7.5:7.5.

The layer preparation procedure was as follows: firstly, the active material, the binder solution (10 wt% of PVDF in NMP or 7.5 wt% of CMC in water) and carbon black were poured into the ball mill vessel with zirconia covering. Then, the proper amount of NMP or water was added to adjust the obtain the slurry. Next, the mixture was homogenised in a mixer mill using the following programs:

a) for materials without tin: 10 minutes, 10 Hz followed by 10 minutes, 25 Hz, using 25 zirconia balls (5 mm diam.)

b) for materials with tin: 1 h 45 min, 15 Hz, 10 min, 25 Hz, using 25 zirconia balls (5 mm diam.)

Then, the active material slurries were uniformly distributed on copper foil (degreased with isopropanol) using the dr Blade technique. As-received layers were dried overnight at 80°C. Afterwards, layers were pouched into 10 mm or 6 mm electrodes. The obtained electrodes were finally dried overnight at 80°C in a vacuum oven and transferred to an inert-atmosphere glove box without contact with air. The thickness of the wet electrode was ~100 μm, after drying the thickness was not measured. The mass loading of the electrode layer was between 1 – 2 mg cm^{-2}.

5.6. Preparation of electrochemical cells

Electrochemical cells used for the most of experiments were 2-electrode Swagelok® type cells. The schematic view of the Swagelok® type cell is shown in **Figure 5.6 a)**. The Swagelok® cell is composed of Swagelok® company's tube fitting, which is considered very hermetic thanks to double sealing. In this system, steel bolts (steel 304) were used as current collectors. All of the parts of the Swagelok® cell were carefully cleaned using water and Line-EtOH in the ultrasonic cleaner. In addition, steel bolts were rubbed to remove lithium compounds and lithium residuals, which may potentially react with bolts. Swagelok® parts were dried in Büchi oven at 100°C before transferring to the glove box.

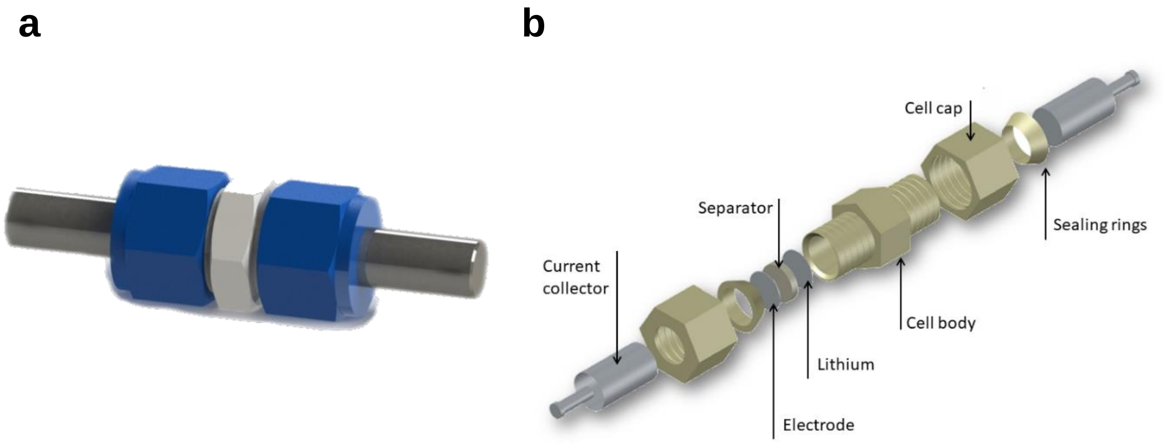

Figure 5.6. *Swagelok® cell a) main view, b) scheme of the electrochemical cell*

The Swagelok® electrochemical cells were assembled as shown in **Figure 5.6 b)**. The active material layer was placed on the first steel bolt (active material directed towards the separator), while on the second bolt lithium coin was put. Between them, a separator soaked with electrolyte (a few droplets) was applied. The size of the separator was greater than the size of the electrode (~13 mm) to prevent direct contact of the electrode with the counter/reference electrode. The whole setup was tightly compressed by hands and screwed together.

Chapter 6. Characterisation techniques

6.1. Elemental analysis

Elemental analysis was conducted to determine the chemical composition of the samples. The composites without tin were studied using two analysers: Carbon analyzer Leco C-200 for the carbon content estimation and nitrogen/oxygen analyzer Leco TC-436 for the oxygen content evaluation. The elemental analysis of materials with tin was performed by the company Mikroanalytisches Labor Pascher (Germany). The carbon, oxygen, and tin content were determined directly, while the amount of silicon was calculated as a padding up to 100%. The errors in carbon and oxygen content were determined based on the three independent results, while the errors in silicon content were calculated using the propagation of the uncertainty equation.

The empirical formula of SiOCs and free carbon content were calculated using the Soraru et al.[248] approach. First, the molar content of silicon, oxygen and carbon were calculated assuming there is 100 g of composite material. Then, the empirical formula was obtained by dividing the number of moles of oxygen/carbon by the number of moles of silicon. The free carbon content was calculated in the following way: first, the number of moles of each element was determined, then, the amount of silicon bonded to oxygen was calculated assuming 1 silicon atom can bind 2 atoms of oxygen. Next, the number of Si - C bonds were determined by subtracting the number of moles of carbon from the number of moles of remaining silicon, assuming silicon and carbon are bounded in a 1:1 ratio. The excess of carbon was considered as free carbon, and it was converted back to weight percentage by multiplying by 12 (molar mass of carbon).

6.2. X-ray diffraction

X-ray diffraction measurement was performed to qualitatively evaluate the presence of crystalline phases within the composite materials. The expected crystallographic forms were graphite (for SiOCs/graphite and SiOCs/graphite/tin nanoparticles composites), and various crystallographic structures of tin, i.e. α, β, γ, and SiO_2 forms (for SiOCs/tin nanoparticles and SiOCs/graphite/tin nanoparticles composites). The SiOCs obtained at 1000°C, are amorphous materials with only a broad halo at ~22°, typical for amorphous silica and SiOCs.[248–250]

6.3. Raman spectroscopy

Raman spectroscopy is a characterisation technique that is particularly sensitive to the microstructure of carbon. Thus, in this work, it was used to evaluate the changes in carbon forms present in the investigated materials. Raman spectroscopy was used to observe the relative changes between ordered and disordered carbon forms upon the addition of different amounts of graphite, tin precursor, and both of these materials together in the final ceramic materials. The main interest was put on D and G bands, which represent disordered and ordered forms of carbon, respectively. To get the most precise information, the broad D and G bands were deconvoluted into five peaks, namely D1, D2, D3, D4 and G, according to Sadezky et al.[251]. The description of each peak is given in **Table 6.1**.

Table 6.1. *First-order Raman shifts. Placement and description.*[35,251–253]

Peak	Raman shift	Description
D1	~1350 cm^{-1}	Vibration within A_{1g} symmetry, typical for disoredered carbons, graphene edges
D2	~1620 cm^{-1}	E_{2g} symmetry, defected graphitic lattice, Stone-Wales defects
D3	~1525 cm^{-1}	Amorphous carbon
D4	~1200 cm^{-1}	Vibration within A_{1g} symmetry, typical for disordered carbons, C sp^2 – sp^3 bonds or ionic impurities
G	~1580 cm^{-1}	E_{2g} symmetry, ideal graphitic lattice

Raman spectra were deconvoluted using OriginPro2016 software. All of the modes were fitted using Lorentzian peaks except for the D3 mode, in which the Gaussian curve was used. Before the analysis, the background was removed using custom settings. The peaks were analysed using the intensity (height of the peaks), according to the suggestion provided by Ferrari and Robertson[254] for amorphous carbons fitted with different fitting curves.

In this work, the size of the carbon clusters was not calculated, as it gave different results depending on the selected model.

6.4. Thermal gravimetric analysis

Thermal gravimetric analysis (TGA) was performed in argon atmosphere within the temperature range of 20 – 1000°C with the green body as the input material. The TGA analysis was performed to track the reactions which occur during the pyrolysis process. The two main processes which take place upon heating are polymer-to-ceramic conversion (SiOCs) and carbothermal reduction. The information obtained during TGA analysis are evaporation of unreacted substrates, thermal decomposition and release of volatile compounds, the final yield of the process. In the case of the $SiOC_{UV}$ and $SiOC_{UV}$/Sn-40% sample, the TGA analysis was coupled with DSC measurement, which helped to understand the processes which occur without the mass loss.

6.5. ^{29}Si Solid State Nuclear Magnetic Resonance

^{29}Si Solid State Nuclear Magnetic Resonance technique (^{29}Si NMR) is considered as the most reliable method to identify the mixed bonds tetrahedra: $\underline{Si}O_4$, $\underline{Si}O_3C$, $\underline{Si}O_2C_2$, $\underline{Si}OC_3$ and $\underline{Si}C_4$. The ^{29}Si NMR was conducted with the following parameters: single pulse sequence, ^{29}Si frequency: 139.11 MHz, π/8 pulse length: 2.5 ms, recycle delay: 100 s, 1 000 scans, external secondary reference: DSS. The samples were placed into 3.2 mm zirconia rotors and then spun at 8 kHz under airflow. The obtained spectra were analysed using OriginPro2016 software after background subtraction (straight line). ^{29}Si NMR was fitted using Voigt fitting curve, depending on the fitting quality. However, each family of composites obtained from a certain preceramic precursor, i.e. VTES, PhTES, PMHS or SPR-684 was fitted using only one of these three fitting patterns. The results were analysed based on literature reports.[34,56,245]

6.6. X-ray photoelectron spectroscopy

X-ray photoelectron spectroscopy (XPS) was conducted to confirm the results of Raman spectra analysis and ^{29}Si NMR. Although XPS is inferior to these two techniques in terms of characterisation of SiOCs-based material, mainly due to limitation to the surface area, it is also a way cheaper alternative to ^{29}Si NMR for investigating mixed bonds tetrahedra. The XPS measurement was conducted to identify the chemical bonds created by carbon and by silicon. Because the method is surface sensitive, the results were treated qualitatively.

6.7. Fourier-transformed infrared spectroscopy

Fourier-transformed infrared spectroscopy (FTIR) is a technique that reveals chemical bonds within the material. FTIR was used to investigate the changes in chemical bonds during the curing process.

6.8. Brunauer-Emmett-Teller (BET method)

The BET method was conducted to measure the specific surface area (SSA) of the composites with tin nanoparticles to investigate the porosity created during the carbothermal reduction process. The BET measurement was conducted at 77 K, based on the amount of adsorbed nitrogen.

6.9. Scanning electron microscopy

Scanning electron microscopy (SEM) imaging was conducted in two modes: secondary electrons (SE) and backscattering electrons (BSE). SEM imaging was performed on composite powders and electrode layers: both fresh and electrochemically cycled (post mortem). Depending on the type of material, different preparation method was used. Powders were directly glued to carbon tape and the excess was blown away using compressed air. Fresh electrodes were pouched directly from the dried coating layer. The post-mortem electrodes were prepared in the following way: first, Swagelok® cells were fully delithiated (charged to 3 V), then cells were transported to the glove box and disassembled. Cycled electrodes were carefully removed and rinsed a couple of times with DMC to remove electrolyte residuals. As-prepared electrodes were initially dried at RT in argon, further dried in an oven at 80°C in air, and then used for SEM imaging. The same preparation method was applied for preparing electrodes for post-mortem XRD analysis.

SE mode was used to investigate the morphology and topography of the samples. Representative samples were additionally studied using an energy-dispersive X-ray spectrometer, to create chemical maps and to check the elemental composition of certain species. Moreover, SE mode was used to investigate microdamage on the SEI layer after electrochemical cycling.

BSE mode was used primarily to study the distribution and size of tin nanoparticles. This was achievable due to the high elemental mass of the tin in contrast to other elements present in the material.

6.10. Transmission electron microscopy

Transmission electron microscopy (TEM) was conducted to get a deeper insight into the nanostructure of the obtained composite materials. The measurements were conducted on powder materials, prepared as follows: firstly, a few milligrams of composite material was dispersed in ethanol using ultrasounds, then a droplet of material was applied on a carbon-coated copper mesh with holes, and finally, ethanol was evaporated at room temperature. The TEM imaging was conducted using bright and dark field (TEM and STEM modes), employing HAADF and EDX detectors.

6.11. Galvanostatic charge-discharge

Galvanostatic charge-discharge (GCD) was used as a basic technique to study the applicability of the material for LIBs. The GDC was conducted in the two potential ranges: 5 mV-3 V and 5 mV – 1.5 V with constant voltage step. The first potential region was used to compare the materials with literature reports, which are most often measured in this way. The narrower potential range was used as a reference for commercial application, as this region is considered commercially useful. The applied current density was constant over time, it was the same for the charging and discharging process, and it was set as a multiplicity of the 1 C value. The 1 C value in this research is considered as the current required to fully lithiate 1 g of graphite with a maximum theoretical capacity in 1 h, i.e. for 1 g of graphite 1 C current is equal to 372 mA. Other designations of currents correspond to the multiplication of the 1 C value, i.e. C/2 assigns to half of the 1 C value, 186 mA g^{-1} (charging graphite with theoretical capacity value in 2 h), or 2 C corresponds to 744 mA g^{-1} (charging graphite with theoretical capacity value in 0.5 h). All of the current density values are calculated with regard to the mass of active material. The graphite reference was used in this research for three reasons: *i)* graphite is by far the most popular, commercially used anode material and therefore it is a good benchmark, *ii)* graphite is an integral part of the investigated composites, *iii)* there is no available equation nor theoretical capacity value for SiOCs due to amorphous structure.

The GDC results include three types of results: *i)* voltage profiles, which provide information about the potential of Faradaic reaction, hysteresis and coulombic efficiency, *ii)* cyclic stability measurements, which give information about stability upon prolonged charge-discharge cycles, and *iii)* rate capability measurements, which indicate the performance of the composites upon high charge-discharge currents.

All electrochemical measurements were conducted in half-cells with lithium as a counter/reference electrode.

6.12. Cyclic voltammetry measurements

Cyclic voltammetry measurements (CV) were conducted to get further insight into Faradaic reactions, which takes place in the composite materials. CV measurements were conducted similarly to GDC tests, in 5 mV – 3V and 5 mV – 1.5 V potential regions. The selected scan rate was 0.1 mV s^{-1} (unless stated otherwise). This scan rate gives a good peak separation along with a relatively short measurement time. The number of scans was 3 or 10, depending on the composite and the expected outcome. Measurements were conducted using half-cells. To avoid the influence of external electric fields, the electrochemical cells were placed in the Faraday cage.

6.13. Electrochemical impedance spectroscopy

Electrochemical impedance spectroscopy (EIS) was conducted to evaluate the changes in the internal resistances upon the addition of tin or graphite to the system. The EIS measurement was conducted in the potentiostatic mode with an amplitude of 5 mV within 100 kHz – 100 mHz frequency range (unless there were important features at lower frequencies) in a fully charged or fully discharged state of the electrodes. The measurements were conducted using half-cells. To avoid the influence of external electric fields, electrochemical cells were placed in the Faraday cage.

Chapter 7. SiOC/graphite composites

7.1. Deeper context

As it was discussed in the theoretical part, the electrochemical properties of SiOCs are still not fully understood. There are two main models of energy storage: the model, where the ceramic phase is the main storage site, and the model where the free carbon phase is the main storage site. The free carbon phase-based approach, although takes into consideration the importance of carbon content,[44–46] it misses the influence of the structure of the carbon and takes into the consideration only one SiOCs material. To best of my knowledge, there is only one work[72] which discusses effect of the carbon addition to carbon-poor and carbon-rich ceramic. However, the the work compares SiOCs with SiCNs, which are two different ceramic materials. This work provides deeper insight into the influence of carbon content and carbon structure on the electrochemical properties of composites based on carbon-poor and carbon-rich SiOCs ceramics.

Few words have to be added about graphite choice for this research. Graphite was selected as a carbon source for a couple of reasons. It is a cheap, abundant material, broadly investigated as anodic material for LIBs. It has low lithiation potential as well as high coulombic efficiency (after coating with carbon). The main problems of graphite are fast degradation related to SEI cracking, especially upon charging and discharging with high current. Blending graphite with SiOCs seems to be beneficial, as SiOCs may serve as a protective matrix which prevents from the deterioration of SEI.[255,256]

7.2. Results

The SiOCs/graphite composites were synthesized using the ultrasonic-assisted gelation method. The homogeneity was checked by SEM-EDX imaging of dried gel. As a test object, a flat particle of pre-pyrolysed SiOC$_{\mathrm{VTES}}$/C10g was used. The SEM image of that sample is shown in **Figure 7.1**. One can see the surface of the SiOC$_{\mathrm{VTES}}$/C10g sample consists of darker spots mixed with the lighter ones. The EDX measurement reveals darker spots contain mainly of carbon, while the remaining part consists also of silicon and oxygen. Thus, one can conclude, darker spots correspond to graphitic flakes, while the rest to the ceramic matrix. Graphitic flakes are ~20 μm in size, which corresponds well to the size of graphite used for the synthesis, and they are uniformly distributed within the matrix. Therefore it can be stated, that the synthesis route allows for the uniform distribution of graphite within the preceramic polymer.

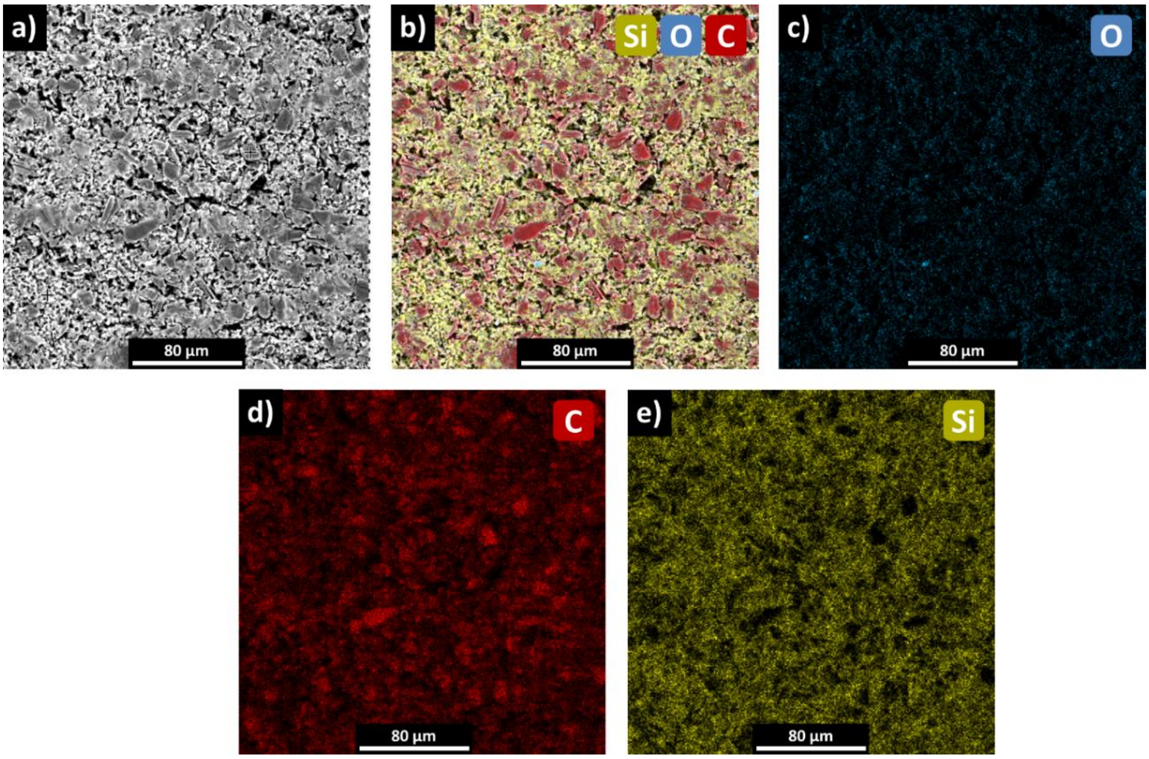

Figure 7.1. *a) SEM image of the surface of SiOC$_{VTES}$/C10g gel, b) EDX maps of the surface of SiOC$_{VTES}$/C10g gel.*[257]

The pyrolysis process of SiOCs/graphite composites was tracked by means of TGA. The thermographs of selected SiOCs/graphite composites are shown in **Figure 7.2**. The thermographs show a typical thermal conversion plot for materials synthetized via sol-gel synthesis. There are two main mass losses in each sample. The first one, between 50°C and ~400°C is related to the evaporation of solvents, unreacted residuals and by-products of polycondensation reaction (EtOH, H_2O, preceramic precursors). The second one, between 500-800°C corresponds to the redistribution reactions between Si-O, Si-C and Si-H bonds (release of H_2, CH_4 or C_2H_2).[102,258] The ceramic yields of reference SiOC$_{VTES}$ and SiOC$_{PhTES}$ are 88.7 and 60.9% respectively, which corresponds well to the literature reports.[56,259] Upon the addition of graphite to preceramic precursor, a gradual increase of the mass yield of the obtained materials is observed. The mass yields of SiOC$_{PhTES}$/C2g, SiOC$_{PhTES}$/C4g, and SiOC$_{PhTES}$/C10g are equal to 77.4, 79.5, and 83.7%, respectively, whilst for SiOC$_{VTES}$/C10g sample is around 93.4%. The higher mass yield of the composite materials is related to the lower content of the preceramic polymer in the green body. This indicates the content of graphite did not change during pyrolysis and the final mass yield is proportional to the amount of graphite in the polymer/graphite blend.

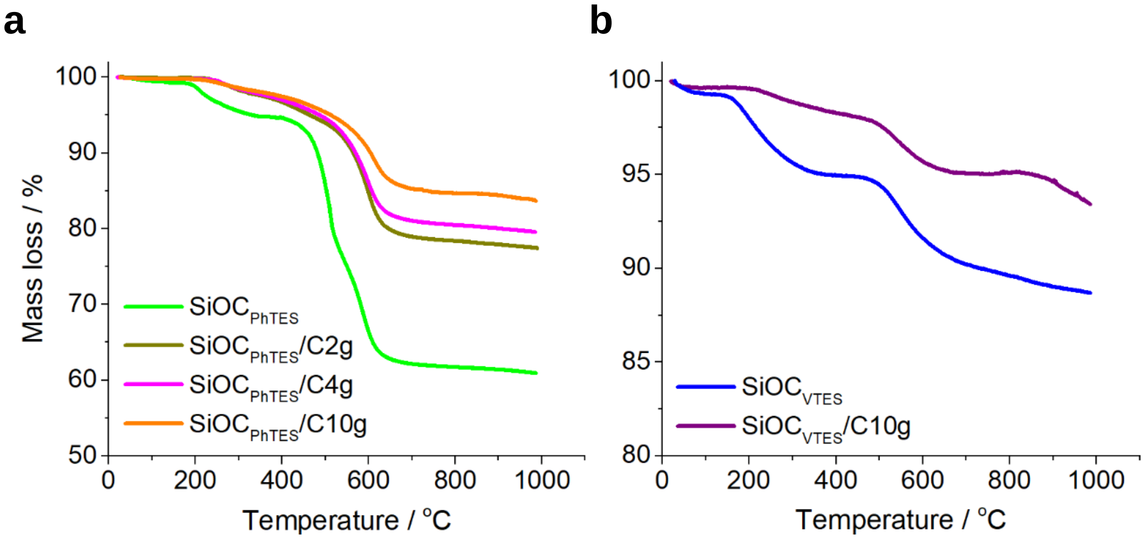

Figure 7.2. *Selected thermographs of selected a) SiOC$_{PhTES}$/graphite and b) SiOC$_{VTES}$/graphite composites.*[260]

After pyrolysis, the elemental analysis was conducted to investigate the changes mainly in carbon content in the final materials. The elemental compositions of both sets of composites are shown in **Table 7.1**. One can observe a significant increase of carbon content in the materials with the addition of graphite.

Table 7.1. *Elemental composition of SiOCs/graphite composites.*[257,260]

Material	C	O	Si	C$_{free}$	% share of C$_{free}$ in C	Empirical formula
	wt.%				%	
SiOC$_{VTES}$	27.1±0.1	32.2±1.5	40.7±1.5	21.8	80.4	$SiO_{1.39}C_{1.56}$
SiOC$_{VTES}$/C2g	44.4±0.8	26.0±0.4	29.6±0.9	41.5	93.5	$SiO_{1.54}C_{3.51}$
SiOC$_{VTES}$/C4g	54.7±0.3	21.6±0.3	23.7±0.4	52.6	96.1	$SiO_{1.59}C_{5.39}$
SiOC$_{VTES}$/C10g	74.0±0.2	13.1±0.5	12.9±0.5	73.4	99.2	$SiO_{1.78}C_{13.41}$
SiOC$_{PhTES}$	37.4±0.8	29.3±1.4	33.3±1.6	34.2	91.1	$SiO_{1.546}C_{2.632}$
SiOC$_{PhTES}$/C2g	51.3±1.1	22.9±1.3	25.8±1.7	48.7	95.0	$SiO_{1.537}C_{4.604}$
SiOC$_{PhTES}$/C4g	55.9±3.0	22.5±0.7	21.6±3.1	55.1	98.6	$SiO_{1.825}C_{6.055}$
SiOC$_{PhTES}$/C10g	68.7±1.4	16.6±0.5	14.7±1.5	68.5	99.7	$SiO_{1.968}C_{10.877}$

Further insights into carbon changes upon the addition of graphite are presented in **Figure 7.3 a)**. One can notice that the carbon curve creates a logarithmic pattern. These patterns suggest that the addition of graphite to the preceramic blends is an effective way to tailor the carbon content within the material, and, based on a rather simple relation, it is relatively easy to produce the material with a specific amount of carbon, independently from the starting precursors.

Such a pattern was further confirmed by a set of $SiOC_{OTES}$/graphite samples (**Figure 7.3 b)**). $SiOC_{OTES}$/graphite is the SiOCs/graphite composite material synthetised with the same method as $SiOC_{PhTES}$/graphite or $SiOC_{VTES}$/graphite, but octyltriethoxysilane was used as a preceramic precursor.

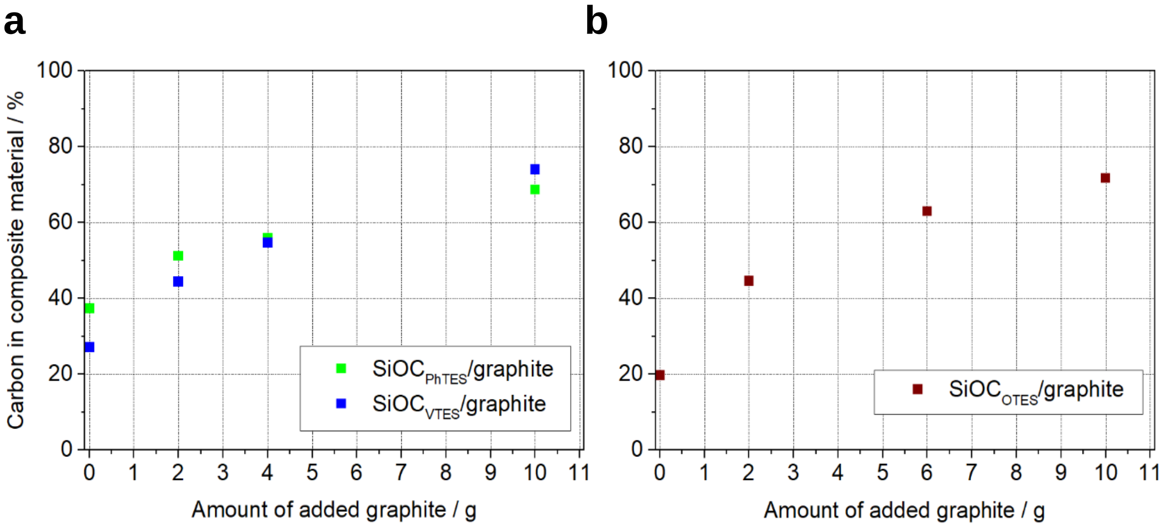

Figure 7.3. *The changes in carbon content with the function of added graphite, a) $SiOC_{VTES}$ and $SiOC_{PhTES}$, b) $SiOC_{OTES}$.*

Further studies on the composite materials were conducted using ^{29}Si NMR. The ^{29}Si NMR spectra for the reference pure ceramic $SiOC_{VTES}$ and $SiOC_{PhTES}$ and composite $SiOC_{VTES}$/C2g and $SiOC_{PhTES}$/C2g are shown in **Figure 7.4 a) and b)**. The samples show broad peaks at −109, −73 and −48 ppm, which corresponds to $\underline{Si}O_4$ and mixed bonds $\underline{Si}O_3C$, and $\underline{Si}O_2C_2$. The peaks of composite materials are slightly shifted towards higher values, and the spectra are noisier. The noise increases with the addition of graphite probably due to the lower Si content, and thus only the low-graphite samples are presented, as only from these samples the reliable data has been collected. The obtained spectra were deconvoluted as shown in **Figure 7.4 c) and d)**, and the results are presented in **Table 7.2**.

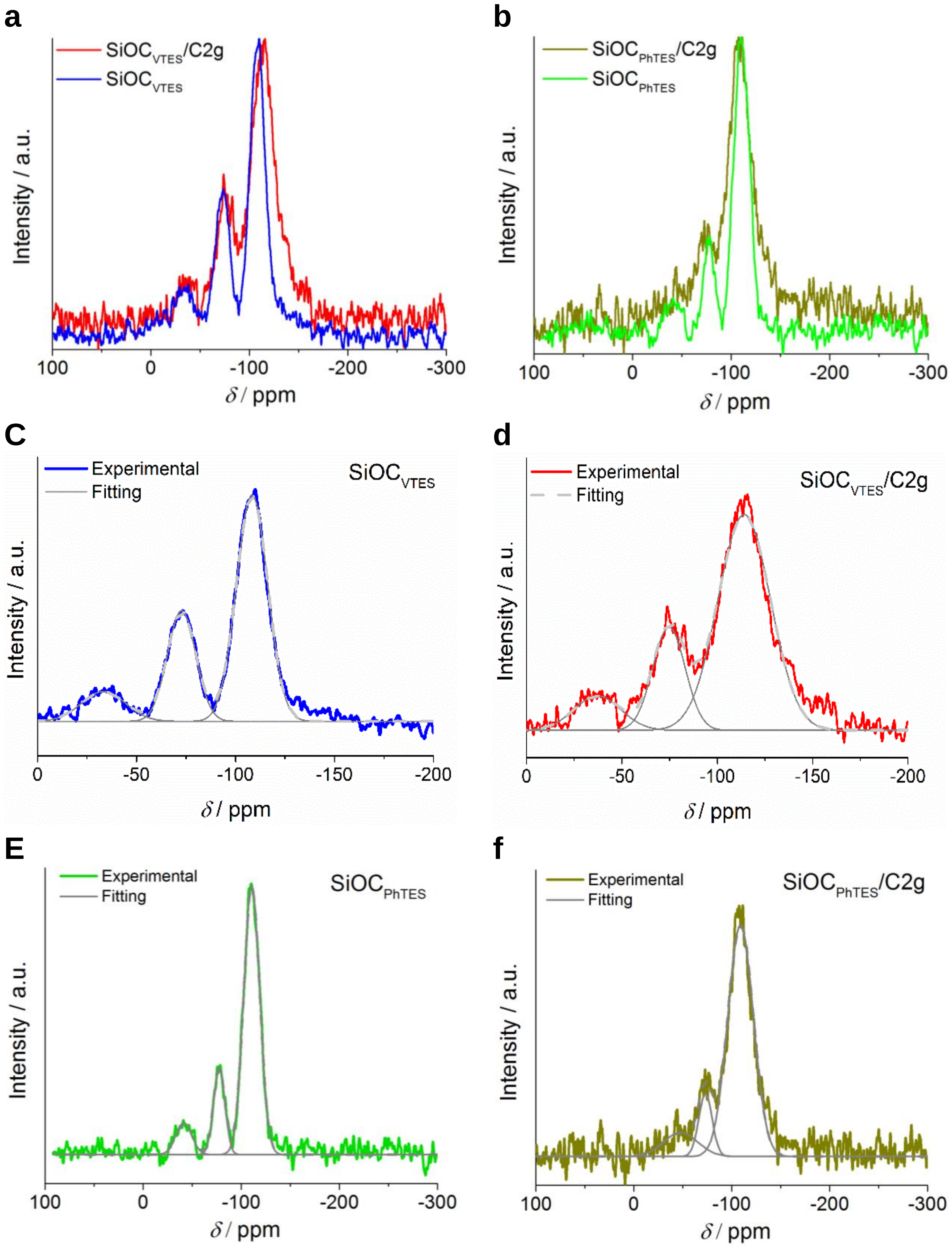

Figure 7.4. *^{29}Si NMR spectra of a) SiOC$_{VTES}$ and SiOC$_{VTES}$/C2g b) SiOC$_{PhTES}$ and SiOC$_{PhTES}$/C2g; deconvolution of c) SiOC$_{VTES}$, d) SiOC$_{VTES}$/C2g, e)SiOC$_{PhTES}$ and f) SiOC$_{PhTES}$/C2g.*[257,260]

As the deconvolution results show, the ceramic structure is dominated by the $\underline{\text{Si}}\text{O}_4$ and high-oxygen tetrahedral units, i.e. SiO_3C and SiO_2C_2. These results stay in agreement with the literature, which suggests $\underline{\text{Si}}\text{C}_4$ forms at higher temperatures.[62]

Table 7.2. *Results of ^{29}Si NMR spectra fitting.*[257,260]

Material	$\underline{\text{Si}}\text{O}_4$		$\underline{\text{Si}}\text{O}_3\text{C}$		$\underline{\text{Si}}\text{O}_2\text{C}_2$	
	δ / ppm	%	δ / ppm	%	δ / ppm	%
$\text{SiOC}_{\text{VTES}}$	-108.3	61.3	-72.7	27.2	-33.3	11.4
$\text{SiOC}_{\text{VTES}}$/C2g	-114.1	69.5	-74.6	23.1	-37.1	9.9
$\text{SiOC}_{\text{PhTES}}$	−104.6	76.0	−69.9	16.4	−22.1	0.6
					−38.2	7.1
$\text{SiOC}_{\text{PhTES}}$/C2g	−109.0	78.2	−73.0	11.0	−48.8	10.8

No significant differences between reference SiOC and composite SiOCs/graphite were observed. This indicates that no reactions between graphite and preceramic polymer take place during synthesis, homogenisation and pyrolysis. However, in the case of $\text{SiOC}_{\text{VTES}}$ samples, some discrepancies in the share of the mixed bonds tetrahedral units are observed for the samples obtained with and without the high-power ultrasounds assistance (**Figure 7.5**). Therefore, one can expect some impact of ultrasounds on the final structure of the ceramics. High power ultrasounds may cause additional reactions involving functional groups, faster mixing and more rapid temperature rising. This may lead to the creation of new bonds within the green body, and better solvent evaporation. These small changes in the dried gel translate into slightly different polymer-to-ceramic conversion paths of ultrasound-gelated sols.

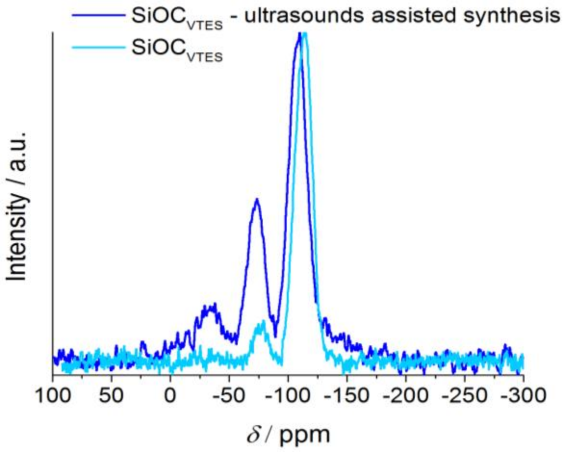

Figure 7.5. *Comparison between ^{29}Si NMR spectra of $\text{SiOC}_{\text{VTES}}$ produced with and without ultrasonic assistance*

Information about bonds present in the obtained SiOCs/graphite composites was provided by means of XPS. For the XPS measurement, reference $SiOC_{VTES}$ and $SiOC_{PhTES}$ and composite $SiOC_{VTES}$/C10g and $SiOC_{PhTES}$/C10g were selected (**Figures 7.6-9).** The Si2p spectra of $SiOC_{PhTES}$ and $SiOC_{PhTES}$/C10g (**Figure 7.6**) exhibit only one peak doublet at ~103.2–103.4 and 103.7–103.8 eV, which correspond to $\underline{Si}O_4$ tetrahedra. Similarly, $SiOC_{VTES}$/C10g reveals only $\underline{Si}O_4$ (**Figure 7.8 b)**). The reference $SiOC_{VTES}$ (**Figure 7.8 a)**) shows an additional doublet at 102 and 102.8 eV, which can be assigned to SiO_3C and SiO_2C_2 tetrahedra. The Si2p XPS results reveal only the most intense peak of $\underline{Si}O_4$. One has to keep in mind, XPS is a surface technique and therefore the results are slightly different from ^{29}Si NMR. However, the general trend of Si-bonds provided by both of these techniques is retained.

More information about composite materials was provided by C1s XPS spectra. The deconvolution of C1s spectra of studied materials (**Figure 7.7 and Figure 7.9**) reveals the following signals: 284.0-284.4 eV, assigned to C=C bonds, which represents ordered graphitic layers and/or C-Si bonds from mixed bonds tetrahedral units.[261–263] signals between 284.8-285.2 eV, originating from C-C bonds of disordered free carbon phase[264] and signals with higher energy, attributed to C-O and C=O.[265] The composite materials show the lower intensity of the signal coming from C-O and C=O bonds in comparison to the pure ceramics, which is a direct consequence of the introduction of graphite. $SiOC_{PhTES}$/C10g exhibits also a smaller share of the peak ~284.4 eV (C=C graphitic bonds or C-Si bonds of SiOC tetrahedra) in contrast to $SiOC_{PhTES}$. The low signal coming from C-Si bonds may be rationalised by the low SiOC tetrahedra content due to the high share of graphite (law of mixtures). On the other hand, a low signal coming from graphite may result from the coverage of graphite particles with the carbon-rich ceramic phase. However, XPS is a surface technique, where the signal is gathered from nanometer scale area, whereas the composite samples are uniform at the micrometer scale.

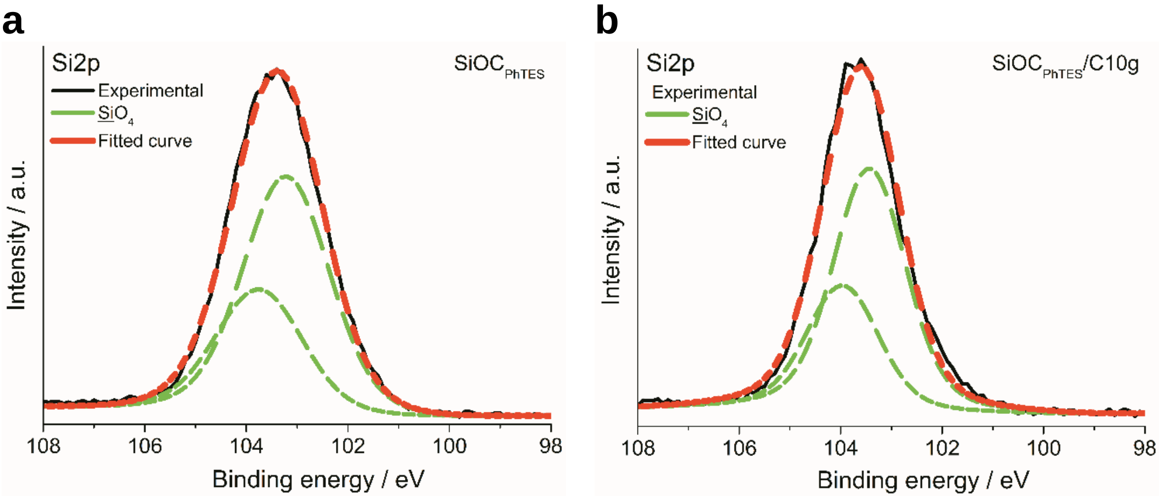

Figure 7.6. *XPS Si2p spectra of (a) SiOC$_{PhTES}$ and (b) SiOC$_{PhTES}$/C10g samples.*[260]

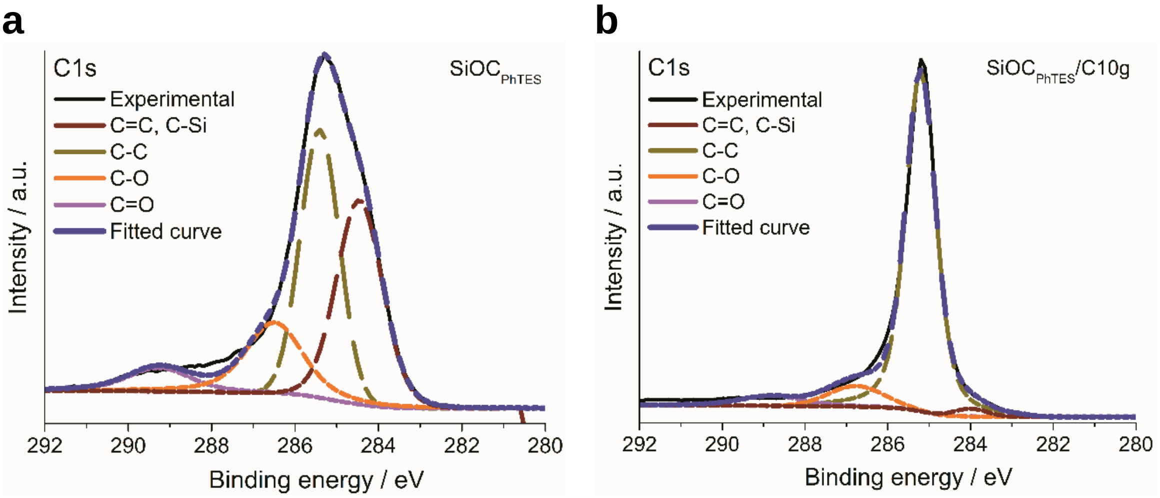

Figure 7.7. *XPS C1s spectra of (a) SiOC$_{PhTES}$ and (b) SiOC$_{PhTES}$/C10g samples.*[260]

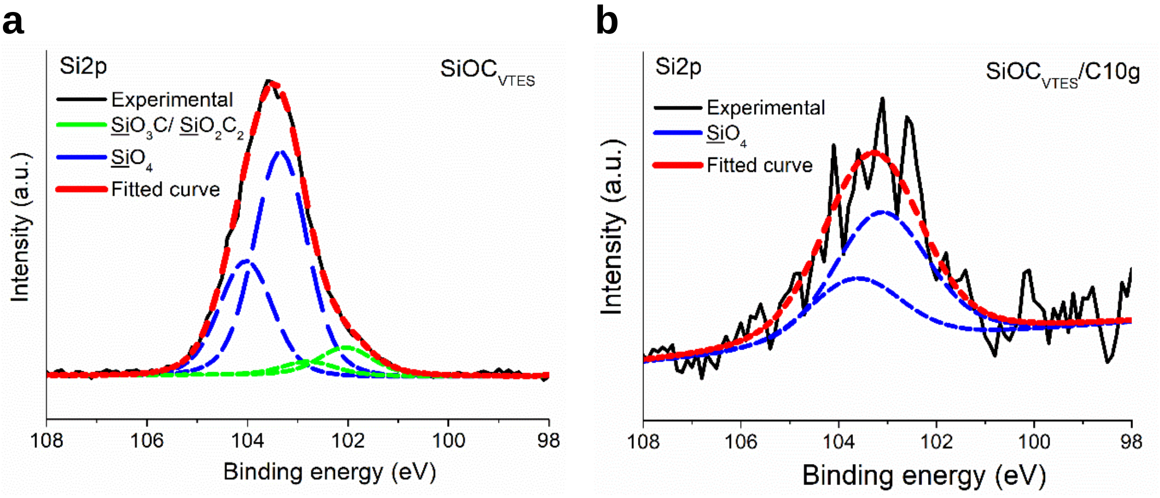

Figure 7.8. *XPS Si2p spectra of a) SiOC$_{VTES}$, b) SiOC$_{VTES}$/C10g samples.*[257]

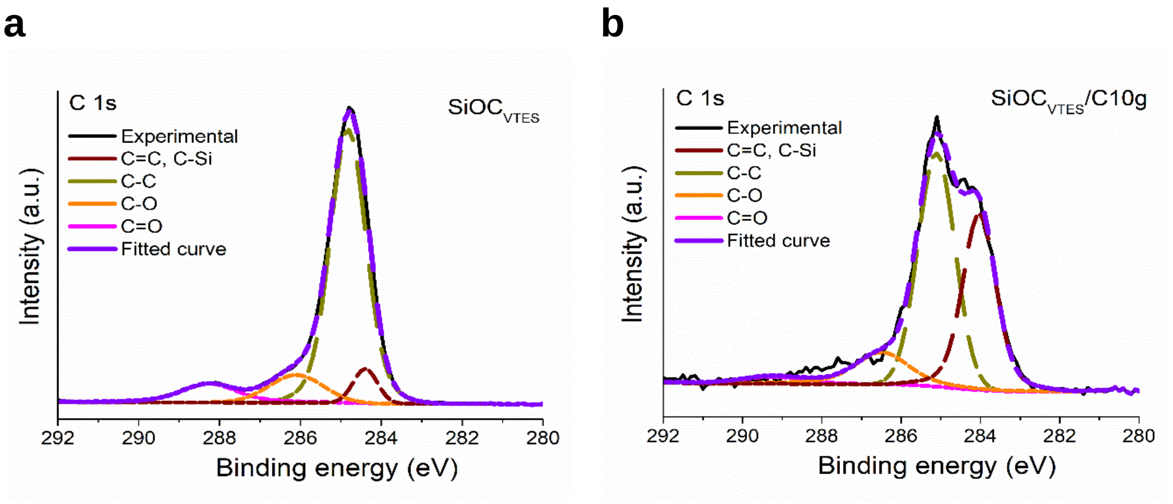

Figure 7.9. *XPS C1s spectra of a) SiOC$_{VTES}$, b) SiOC$_{VTES}$/C10g samples.*[257]

Detailed information about the microstructure of carbon present in SiOCs/graphite composite materials was provided by Raman spectroscopy. The Raman spectra along with the deconvoluted peaks are given in **Figure 7.10** and **Figure 7.11.** All spectra consist of two modes D and G, which were deconvoluted according to.[251] In both cases, there is a significant decrease of intensities ratios I_{D1}/I_G and I_{D2}/I_G with the increase of graphite content in the composites. The details are shown in **Tables 7.3-6**. The intensity ratios I_{D1}/I_G and I_{D2}/I_G dropped from 2.69 and 1.61 for SiOC$_{PhTES}$ to 1.24 and 0.76 for SiOC$_{PhTES}$/C10g respectively, while for SiOC$_{VTES}$ and SiOC$_{VTES}$/C10g samples I_{D1}/I_G decreased from 3.88 to 0.3 and I_{D2}/I_G 2.15 to 0.13. These results suggest that the addition of graphite to the material leads to the increase of the fraction of ordered carbons in the composite materials, and it is proportional to the amount of the added graphite. The comparison between changes of I_{D1}/I_G and I_{D2}/I_G between both series of composites indicates a much higher increase of the ordered carbon upon addition of graphite in the case of VTES-based composited in comparison to PhTES-based ones. This might be rationalised by the higher content of free carbon phase in the pure ceramic SiOC$_{PhTES}$ in contrast to SiOC$_{VTES}$ one.

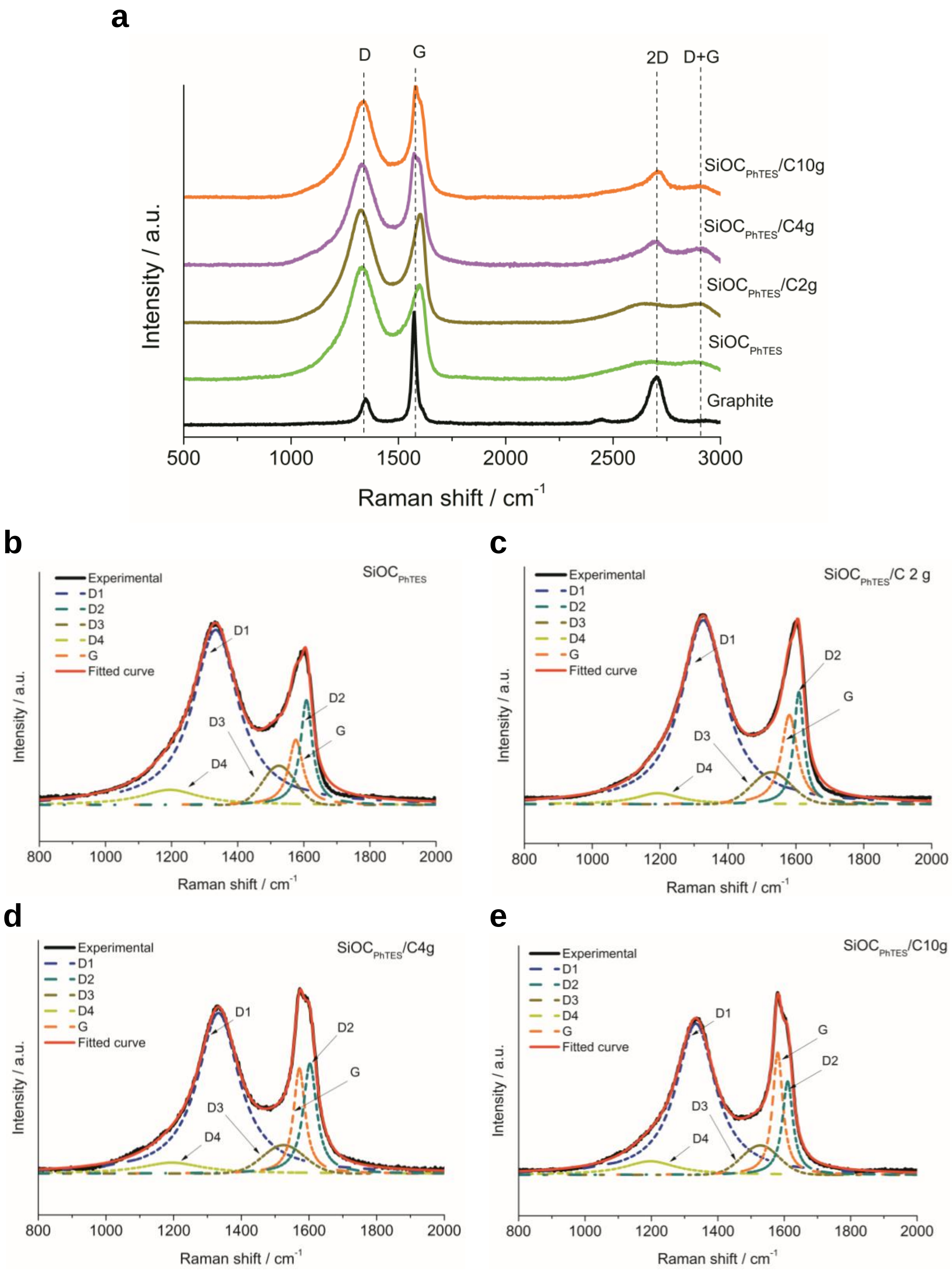

Figure 7.9. *a) Comparison of Raman spectra recorded for investigated samples. Fitting of the Raman spectra of: b)* SiOC_{PhTES}*, c)* SiOC_{PhTES}*/C2g, d)* SiOC_{PhTES}*/C4g and e)* SiOC_{PhTES}*/C10g sample.* [260]

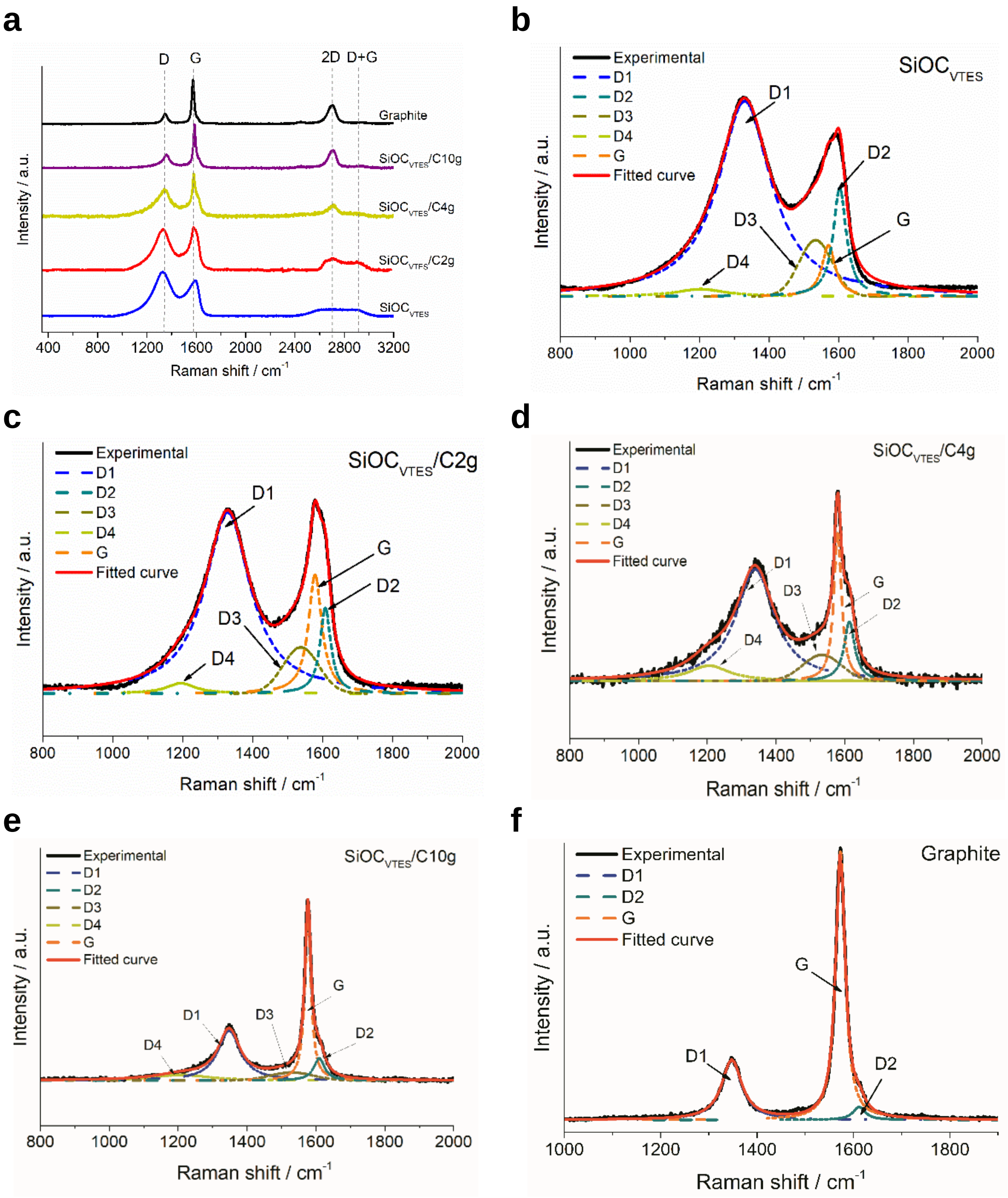

Figure 7.10. *Raman spectra of the a) SiOC$_{VTES}$, SiOC$_{VTES}$/graphite composites and pure graphite (spectra after background subtraction). Deconvoluted Raman spectra of b) SiOC$_{VTES}$, c) SiOC$_{VTES}$/C2g, d) SiOC$_{VTES}$/C4g, e) SiOC$_{VTES}$/C10g, f) graphite samples.* [257]

Table 7.3. *Peaks positions and area obtained from curve fitting of the Raman spectra of the* $SiOC_{PhTES}$ *and* $SiOC_{PhTES}$*/graphite and graphite samples.*[260]

Material	D4		D1		D3		G		D2	
	cm^{-1}	Area	cm^{-1}	Area	cm^{-1}	Area	cm^{-1}	Area	cm^{-1}	Area
Graphite	-	-	1347	15.7	-	-	1573	36.3	-	-
$SiOC_{PhTES}$	1194	7.07	1333	65.82	1525	7.61	1575	8.34	1608	11.17
$SiOC_{PhTES}$/C2g	1193	4.04	1327	66.23	1528	7.41	1580	12.39	1609	9.93
$SiOC_{PhTES}$/C4g	1195	5.72	1332	60.78	1525	7.62	1571	11.72	1603	14.16
$SiOC_{PhTES}$/C10g	1197	6.90	1333	60.78	1528	7.97	1580	13.65	1610	10.71

Table 7.4. *Full width values at half-maximum obtained from Raman spectra curve's fitting for graphite,* $SiOC_{PhTES}$ *and* $SiOC_{PhTES}$*/graphite samples.*[260]

Material	D4	D1	D3	G	D2
	FWHM	FWHM	FWHM	FWHM	FWHM
Graphite	-	47.4	-	24.2	-
$SiOC_{PhTES}$	213.73	164.19	114.24	52.61	43.63
$SiOC_{PhTES}$/C2g	159.73	155.38	135.00	56.85	35.85
$SiOC_{PhTES}$/C4g	219.73	149.48	143.96	41.50	48.20
$SiOC_{PhTES}$/C10g	188.33	142.96	131.37	37.54	38.59

Table 7.5. *Peaks positions and area obtained from curve fitting of the Raman spectra of the SiOC$_{VTES}$ and SiOC$_{VTES}$/graphite and graphite samples.*[257]

Material	D4		D1		D3		G		D2	
	cm^{-1}	Area	cm^{-1}	Area	cm^{-1}	Area	cm^{-1}	Area	cm^{-1}	Area
Graphite	-	-	1347	15.7	-	-	1573	36.3	-	-
SiOC$_{VTES}$	1203	10.05	1329	292.6	1534	35.00	1570	46.05	1603	45.30
SiOC$_{VTES}$/C2g	1195	8.08	1328	228.6	1537	30.12	1578	44.01	1607	25.39
SiOC$_{VTES}$/C4g	1205	17.16	1339	120.12	1534	18.53	1579	31.45	1613	17.68
SiOC$_{VTES}$/C10g	1210	9.24	1348	33.30	1530	6.28	1577	30.24	1610	7.15

Table 7.6. *Full width values at half-maximum obtained from Raman spectra curve's fitting for graphite, SiOC$_{VTES}$ and SiOC$_{VTES}$/graphite samples.*[257]

Material	D4	D1	D3	G	D2
	FWHM	FWHM	FWHM	FWHM	FWHM
Graphite	-	47.4	-	24.2	-
SiOC$_{VTES}$	141.8	187.0	118.5	46.6	33.3
SiOC$_{VTES}$/C2g	98.41	157.6	120.4	46.4	37.0
SiOC$_{VTES}$/C4g	144.3	135.6	131.9	26.9	37.8
SiOC$_{VTES}$/C10g	196.3	78.3	148.8	21.2	38.1

Information about crystalline phases present in both series of composites was provided by XRD measurement. The XRD spectra of both materials are presented in **Figure 7.11**. The pure ceramic materials $\mathrm{SiOC_{PhTES}}$ and $\mathrm{SiOC_{VTES}}$ exhibit only a broad halo, centred at around 10° (21.8° for Cu Kα), typical for amorphous SiOCs. In contrast, composite materials reveal a number of peaks at 26.2, 42.2, 44.5 and 77.4°, respectively. These peaks can be ascribed to [002], [100], [101] and [110] Bragg reflexes of typical hexagonal graphite structure.[266,267] For both composite series, the peaks are more intense for materials with higher graphite content. The XRD measurements confirm the observation from Raman spectroscopy and further proves the presence of graphite in the composite materials.

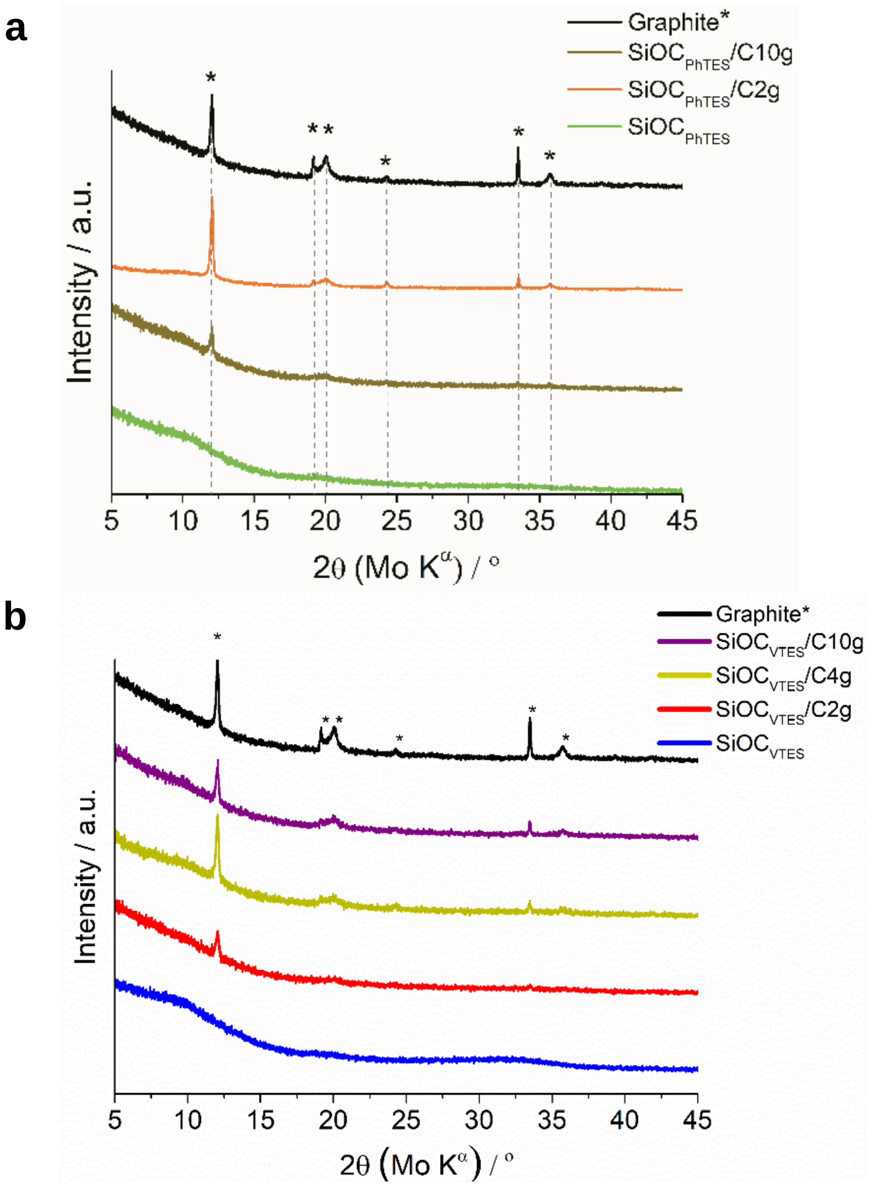

Figure 7.11. *Diffractograms of a) $\mathrm{SiOC_{PhTES}}$/graphite and b) $\mathrm{SiOC_{VTES}}$/graphite composites.*[257,260]

The arrangement of ceramic and graphite phases within the composite materials was tracked using the TEM imaging technique. The pure ceramic materials (**Figure 7.12 a)** and **Figure 7.13 b)**) show only a featureless amorphous structure of SiOCs.[268,269] In contrast, all composite materials reveal also the ordered carbon phase. Based on the previously described characterisation techniques, one may assume that phase corresponds to flakes of graphite. To get more precise information, EDX spectra from both regions have been taken, as presented in **Figure 7.14.** and **Figure 7.15.** These spectra confirm amorphous phase is composed of silicon, oxygen and carbon, which corresponds to SiOCs, while the ordered part consists exclusively of carbon.

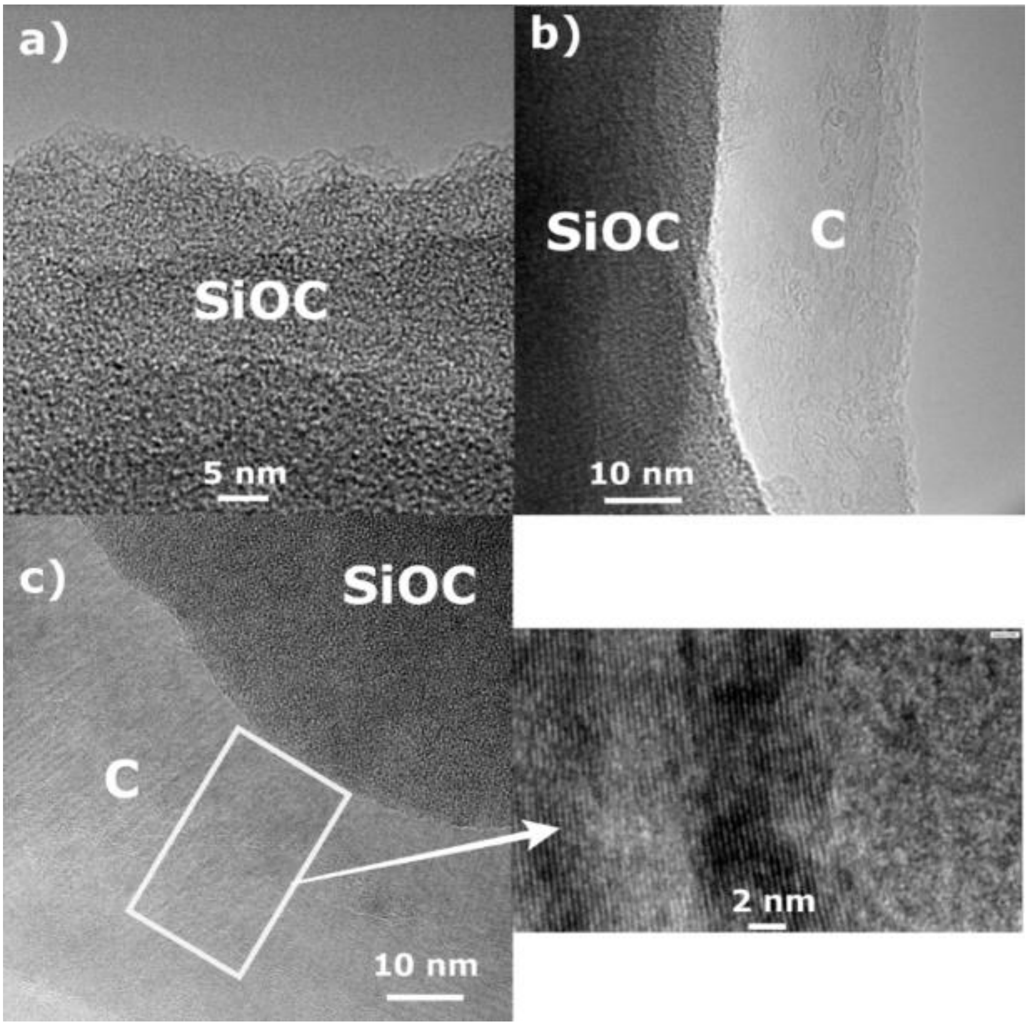

Figure 7.12. *TEM images of a) SiOC$_{VTES}$, b) SiOC$_{VTES}$/C2g, c) SiOC$_{VTES}$/C10g.* [257]

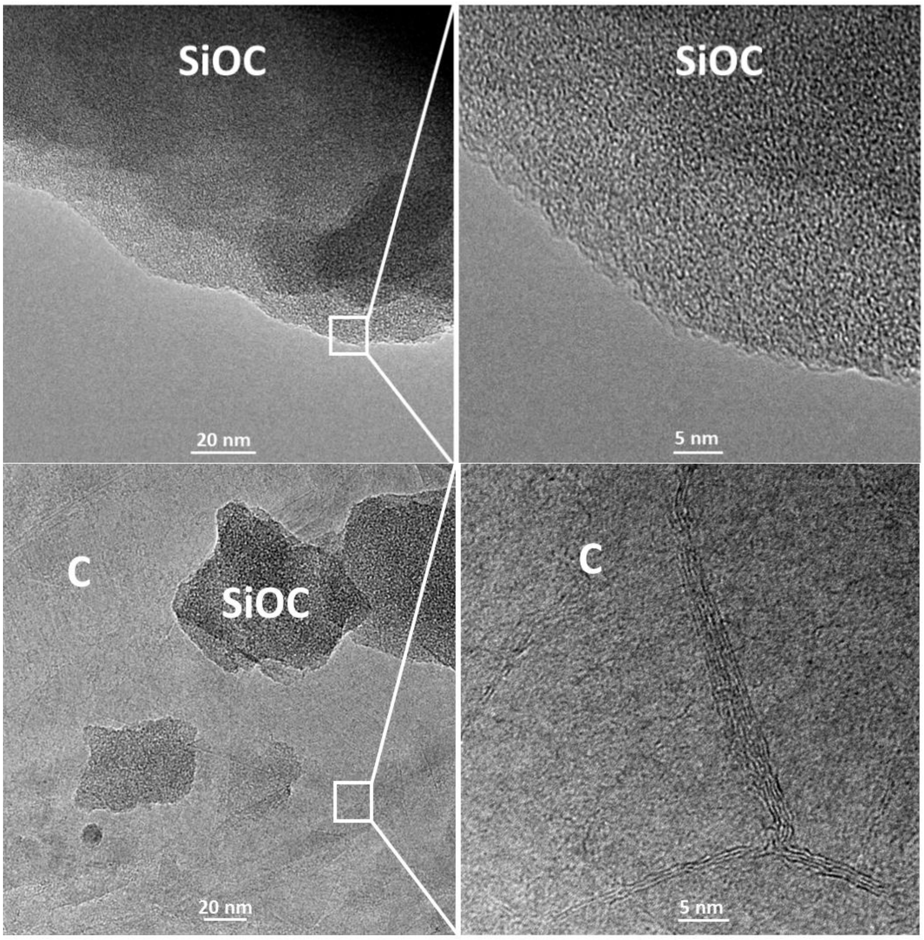

Figure 7.13. *TEM images of SiOC$_{PhTES}$ (top) and SiOC$_{PhTES}$/C10g (bottom).*[260]

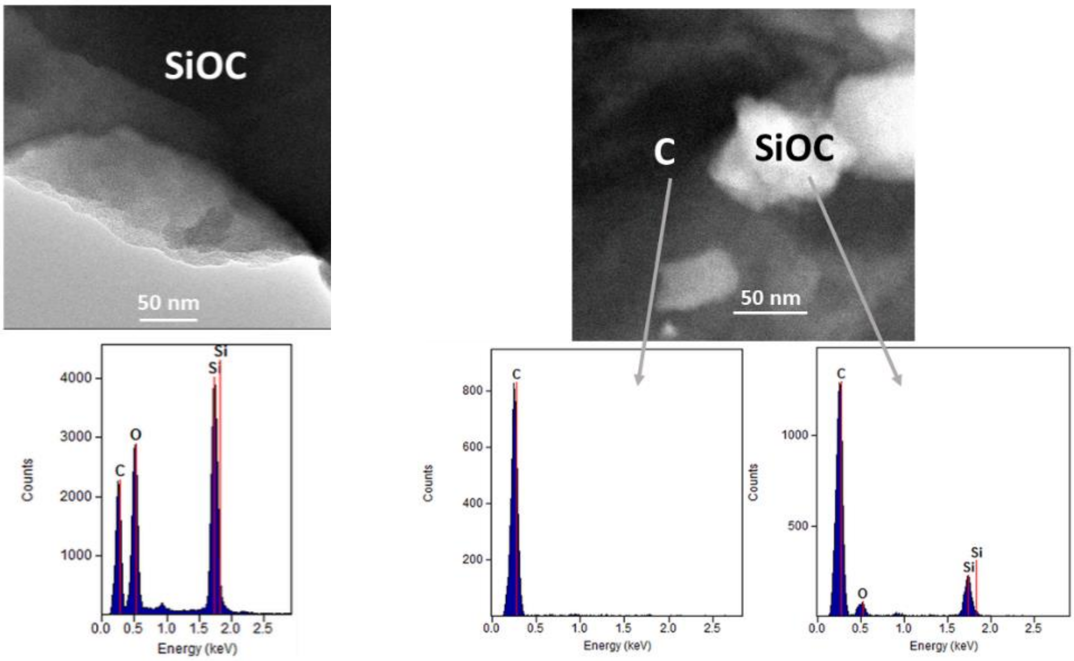

Figure 7.14. *TEM-EDX spectra of SiOC$_{PhTES}$ and SiOC$_{PhTES}$/C10g.* [260]

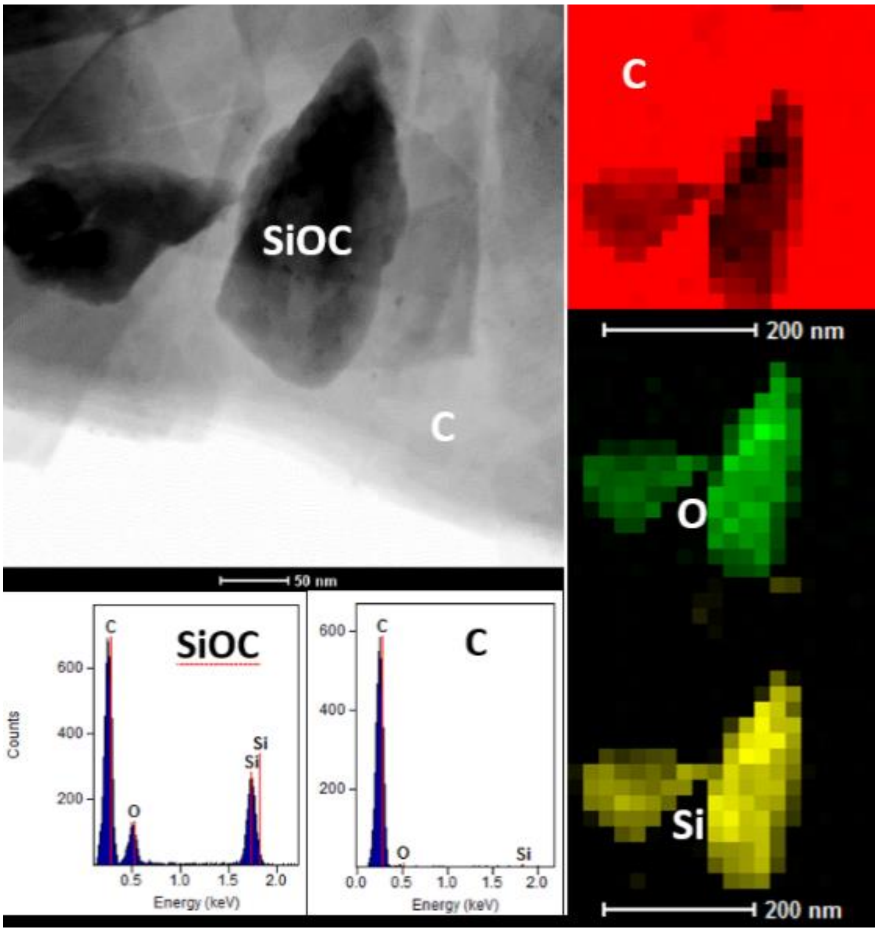

Figure 7.15. *TEM-EDX spectra of SiOC$_{VTES}$/C2g.*[257]

Electrochemical activities of the components of SiOCs/graphite composites were investigated using cyclic voltammetry. **Figure 7.16** shows the CV curves of both series of composites and, for comparison, the pure components – SiOC and graphite. The SiOC$_{PhTES}$/graphite composites exhibit two broad peaks on the cathodic site: the first at around 0.7 V (market as *I*), which corresponds to the creation of SEI layer, typical for SiOC materials.[82,270] and the second, broad peak between 0.3-0 V (*II*) which is assigned to lithium intercalation into the ceramics.[245,270,271] The peak *II* gradually decreases with increasing graphite content and becomes more graphite alike, which might be explained by the increased share of graphite intercalation processes. A similar pattern has been observed for SiOC$_{VTES}$/graphite. However, here the peak *I* is much smaller, which may indicate the SEI layer forms on the ceramic phase of SiOC$_{VTES}$ to a lesser extent in comparison to SiOC$_{PhTES}$ composites. Such results correspond well with the XPS results, which show a higher signal coming from graphitic carbon for SiOC$_{VTES}$/graphite sample in contrast to SiOC$_{PhTES}$/graphite.

On the anodic site, there are also two distinguishable peaks: the first one, between 0-0.25 V (III) corresponds to graphite delithiation, and the second one, above 0.25 V (IV), very broad, which originates to delithiation from the ceramic phase. Both III and IV peaks correspond well to the ceramic:graphite ratio within the composites, with III peak being more pronounced for graphite-rich composites and IV peak being more intense for graphite-poor materials.

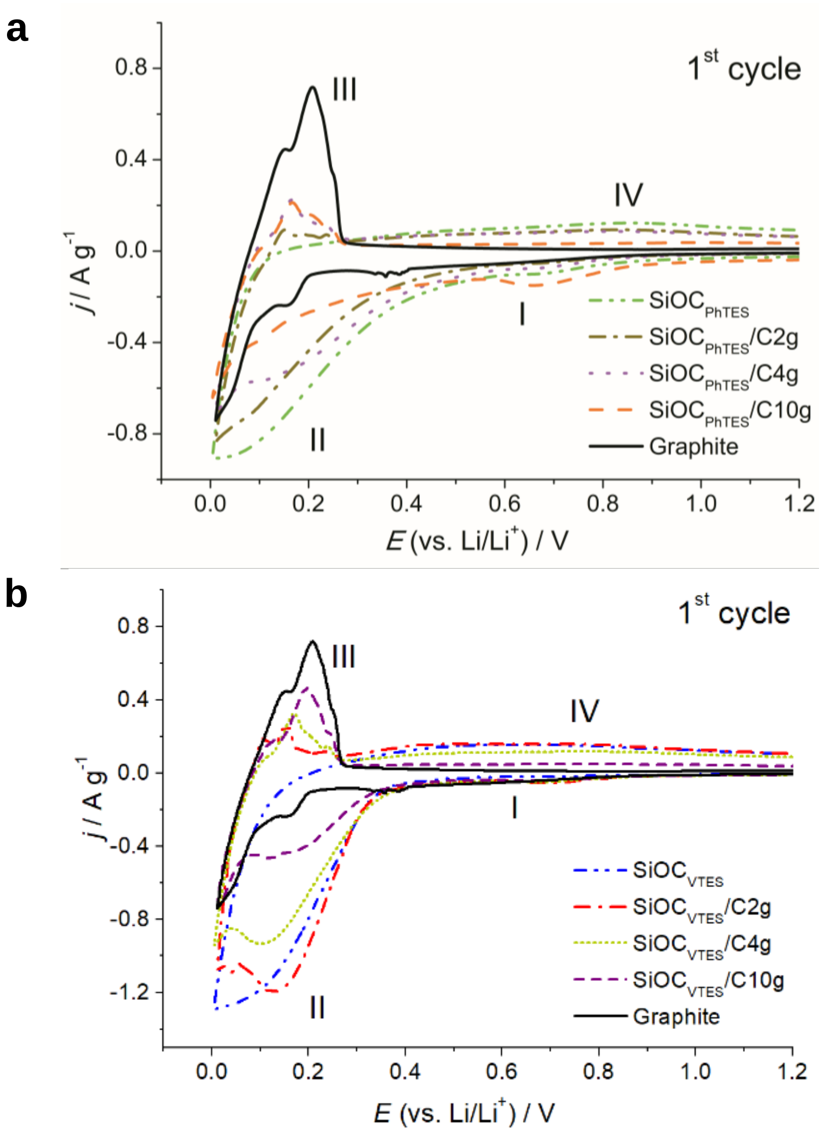

Figure 7.16. *Cyclic voltammetry curves of a) SiOC$_{PhTES}$/graphite, b) SiOC$_{VTES}$/graphite composites.*[257,260]

Figure 7.17 shows voltage profiles of the first and the second cycles of SiOC$_{PhTES}$/graphite and SiOC$_{VTES}$/graphite composites series, collected at 186 mAh g^{-1} current rate. The voltage profiles correspond well to the cyclic voltammetry curves. The lithiation curves of all materials exhibit a fast potential drop followed by a smooth curve starting below 1 V. The majority of the capacity value is recovered below 0.5 V, which indicates the lithiation process occurs mainly at the low potentials. The delithiation curves start with quasi-plateau at 0.11-0.15 V, followed by a smooth, ceramic-like increase. The quasi-plateau coincides well with the curve for graphite. Its length depends on the graphite content within the material and it is longer for graphite-rich composites. The average delithiation potentials of SiOCs/graphite electrodes are noticeably lower than for pure SiOC (see **Table 7.7**). Therefore, the composites with graphite may provide the higher voltage of the full cell, which is beneficial in terms of the overall energy of the device. The materials show significant hysteresis, similar to SiOCs materials.

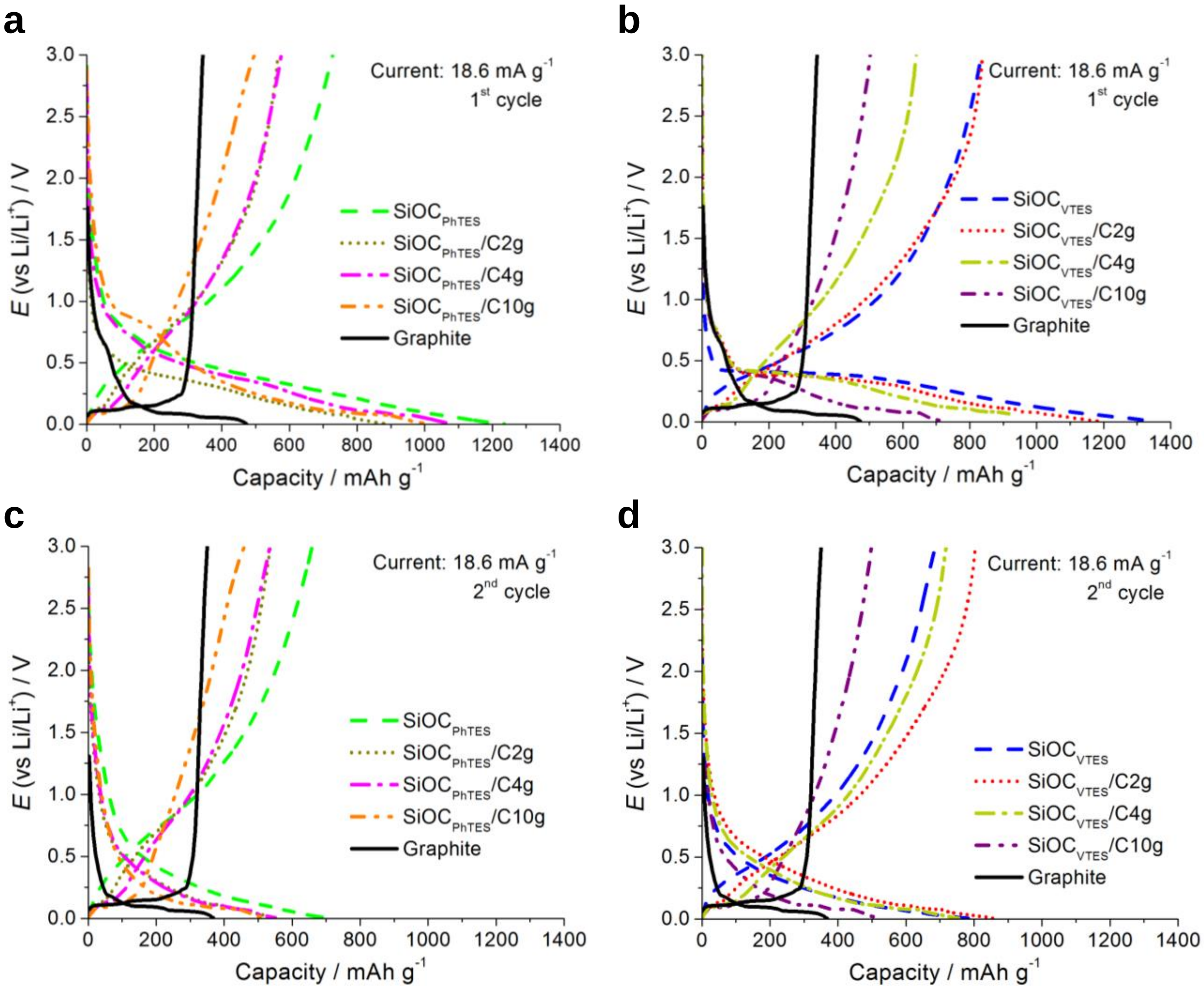

Figure 7.17. *Galvanostatic charge-discharge curves: a) the first, c) the second cycle of SiOC$_{\mathrm{PhTES}}$/graphite composites; b) the first d) the second cycle of SiOC$_{\mathrm{VTES}}$/graphite composites.*

The first cycle Coulombic efficiencies of SiOC$_{\mathrm{VTES}}$ and SiOC$_{\mathrm{PhTES}}$ electrodes are equal to approx. 55%, which is typical value for SiOC ceramics.[56,245] On the other hand, the FCE of graphite is about 70%, which is lower than the FCE reported by electrode materials suppliers[272,273] and stated in literature[274,275] This is mainly because composites were prepared from a flake graphite instead of high-performance battery-grade graphite. One of the features observed for the graphite used, is a small hump at 0.5 V in the lithiation curve (**Figure 7.17**), which is typical for graphite with a high quantity of zig-zag plain edges.[166] The FCE of $SiOC_{PhTES}$/graphite is around 55-60%, which is a similar value to the FCE of pure $SiOC_{PhTES}$. In contrast, the FCE of $SiOC_{VTES}$/graphite is around 70%, which is similar to the FCE of graphite used in this study. These discrepancies correspond well to the CV and XPS results, which suggest in the case of $SiOC_{PhTES}$ ceramic that graphite particles are more uniformly covered with carbon-rich ceramic than carbon-poor one.

Table 7.7. *Average values of reversible C_{rev} and irreversible C_{irrev} capacity of the first cycle at 186 mA g^{-1} current density, Coulombic efficiencies of the first cycle (η) and the capacity retention after prolonged cycling. The values based on data presented in Figures 7.17 and 7.19.*[257,260]

Material	**1st cycle C_{rev} / mAh g^{-1}**	**1st cycle C_{irrev} / mAh g^{-1}**	**54th cycle C_{rev} / mAh g^{-1}**	**1st cycle C_{rev} recovered below 1.5 V / %**	**η / %**	**η' / %**
Graphite	342	470	360	93	72	105
$SiOC_{VTES}$	835	1358	365	76	61	43
$SiOC_{VTES}$/C2g	838	1189	627	78	70	74
$SiOC_{VTES}$/C4g	687	985	543	77	69	79
$SiOC_{VTES}$/C10g	502	721	441	79	69	87
$SiOC_{PhTES}$	727	1235	530	70	58	72
$SiOC_{PhTES}$/C2g	566	886	497	78	63	87
$SiOC_{PhTES}$/C4g	575	1077	482	78	53	83
$SiOC_{PhTES}$/C10g	496	1005	406	68	49	81

The first charge/discharge curves at various current rates were measured for $SiOC_{VTES}$/C2g and $SiOC_{PhTES}$/C2g samples. The results are shown in **Figure 7.18**. The Coulombic efficiencies of both materials do not change significantly for currents in the range of C/20 to C/2. However, there is a high Coulombic efficiency drop of ~10% in both cases when the current was increased to 1 C rate.

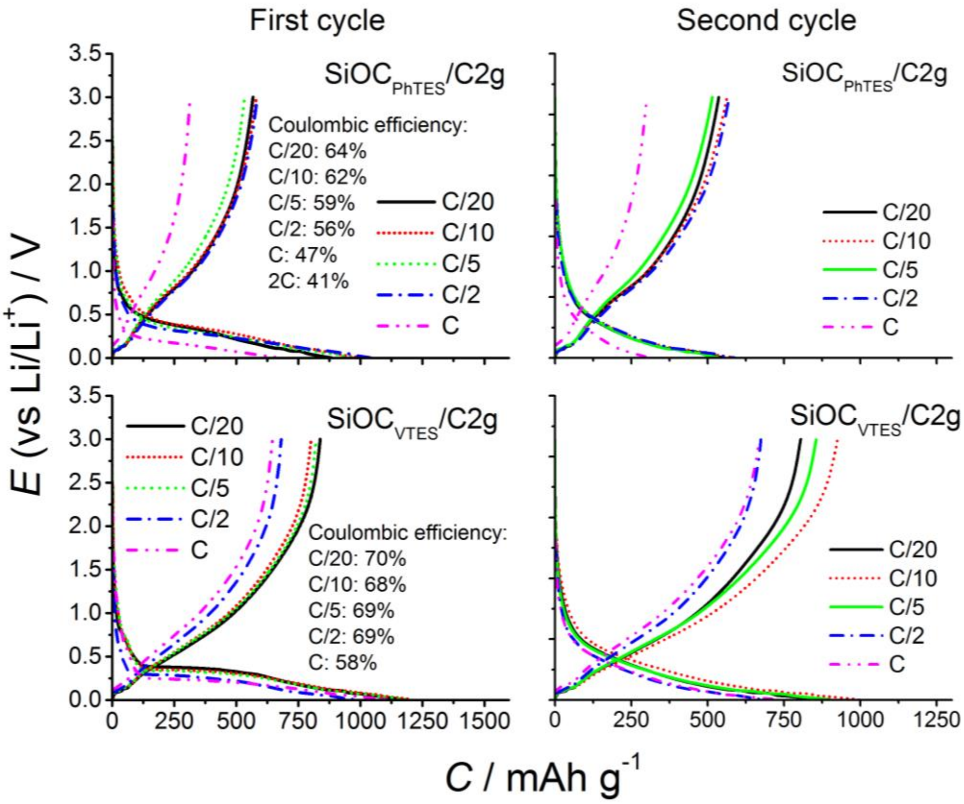

***Figure 7.18.** The first and the second cycle lithiation/delithiation curvesfor SiOC$_{PhTES}$/C2g and SiOC$_{VTES}$/C2g obtained at various current rates*

To further investigate the electrochemical properties of the composites, galvanostatic charge-discharge tests were conducted. **Figure 7.19** shows the results of the GCD for both series of materials, using the following program: C/20x2, C/2x50 and C/20x2. The first two cycles were conducted to form stable SEI. The capacities of pure SiOC$_{PhTES}$, SiOC$_{VTES}$ and graphite are equal to approx. 430, 220 and 290 mAh g^{-1}, respectively. All materials exhibit high stability, with the capacity retention over 50 cycles above 90% of the initial reversible capacity. The capacity values of SiOC$_{PhTES}$/graphite composites are between the capacity of pure SiOC$_{PhTES}$ and graphite. The highest capacity of ~378 mAh g^{-1} was recorded for SiOC$_{PhTES}$/C2g sample, which is around 70 mAh g^{-1} lower than for pure SiOC$_{PhTES}$. In contrast, the capacity values of the SiOC$_{VTES}$/graphite composites are significantly higher than the capacity obtained for the pure components. The highest capacity was registered for SiOC$_{VTES}$/C2g, and it was almost triple the capacity of pure ceramic SiOC$_{VTES}$ (613 mAh g^{-1} vs 220 mAh g^{-1} for SiOC$_{VTES}$) and double the capacity of graphite.

To give a deeper insight, the arithmetic capacity values were calculated. The comparison between average and calculated capacities is given in **Table 7.8**, along with the calculated percentage content of graphite. One can see, the capacity values obtained during the experimental test for $\text{SiOC}_{\text{PhTES}}$/graphite composites are similar to those obtained by a simple calculation using rule of mixture. These results suggest that during prolonged cycling, both components of the $\text{SiOC}_{\text{PhTES}}$/graphite composites contribute independently from each other. On the other hand, the calculated arithmetic capacities calculated for $\text{SiOC}_{\text{VTES}}$/graphite composites show big discrepancies from the experimental results. This indicates the synergistic effect between $\text{SiOC}_{\text{VTES}}$ and graphite.

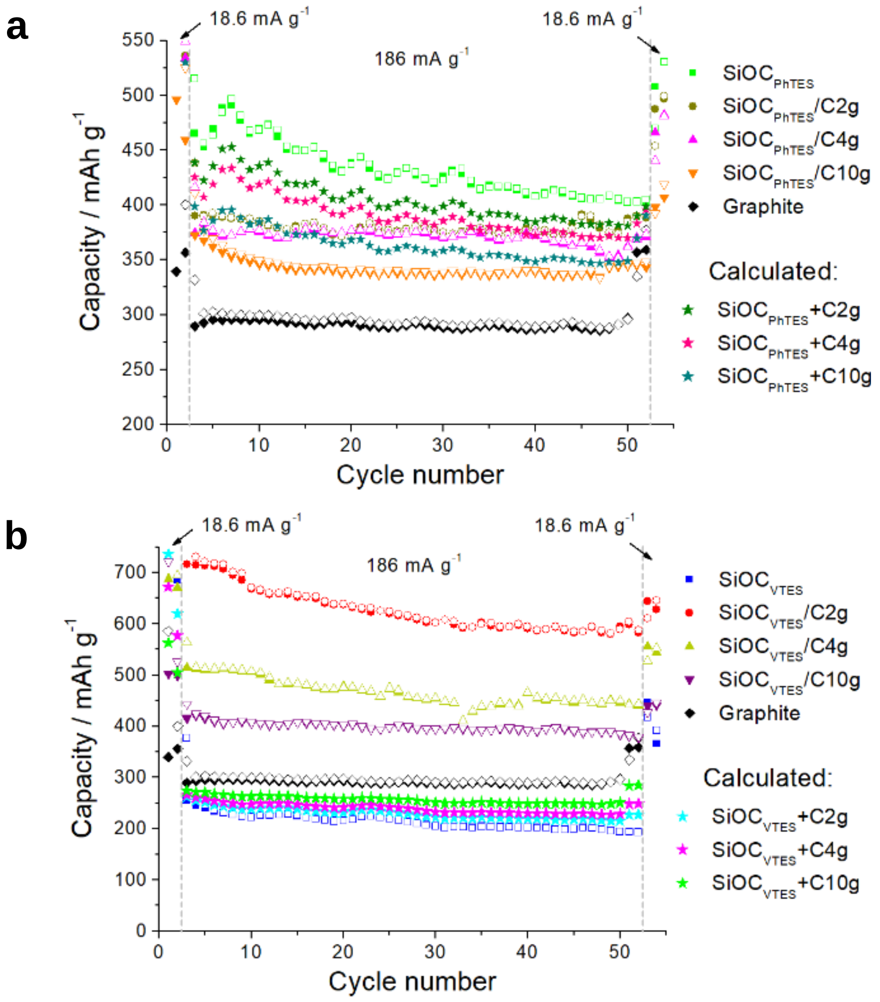

Figure 7.19. *Average (experiment) and calculated* capacity values as a function of cycle number for a) PhTES-based and b) VTES-based composites. *calculated arithmetically taking into account the ratio of the components (SiOC and graphite) in the composites (depicted as stars).*[257]

The electrochemical stability is different for both series of the composites. VTES-based composites exhibits lower stability over cycling (70-80% of the initial capacity is preserved after 50 cycles). On the other hand, the stabilities of composites based on carbon-rich precursorare much higher (80-90%), which may result from better stability of carbon-rich SiOCs in comparison to carbon-poor one.

Table 7.8. *Experimental and calculated capacity values for SiOCs/graphite composites and calculated weight percentage of graphite within the composites*[257]

Material	$SiOC_{PhTES}$/ C2g	$SiOC_{PhTES}$/ C4g	$SiOC_{PhTES}$/ C10g	$SiOC_{VTES}$/ C2g	$SiOC_{VTES}$/ C4g	$SiOC_{VTES}$/ C10g
Experiment	378 mAh g^{-1}	375 mAh g^{-1}	337 mAh g^{-1}	613 mAh g^{-1}	460 mAh g^{-1}	400 mAh g^{-1}
Calculated	395 mAh g^{-1}	381 mAh g^{-1}	356 mAh g^{-1}	230 mAh g^{-1}	240 mAh g^{-1}	256 mAh g^{-1}
wt% of graphite	22	30	50	20	33	55

The $SiOC_{VTES}$/graphite composites were further tested using the following program: C/2x100, 2Cx50, 5Cx100 and C/2x20. The prolonged cycling, also at high-current densities, was conducted to assess the stability of the materials and their rasistance to high currents. **Figure 7.20** shows the prolonged cycling performance of $SiOC_{VTES}$/graphite composites. Similarly as in the case of the short cycling stability study, the highest capacity of ~630 mAh g^{-1} was obtained for $SiOC_{VTES}$/C2g sample. In the case of all of these composites, there is a noticeable capacity drop over dozens of cycles, followed by capacity plateau. For the least stable composites, $SiOC_{VTES}$/C2g, the full stabilisation is achieved after around 75 cycles, where the capacity reaches ~520 mAh g^{-1}. That capacity is preserved after 270 cycles, despite cycling with high C-rates for 100 cycles. The charging with high current densities reveals a high capacity drop in the case of all of the samples. The most affected composites are those with low graphite content. The results suggest $SiOC_{VTES}$/graphite composites exhibit vastly improved capacity and good stability after the stabilisation period. The high currents do not destroy the structure of the materials, but the electrochemical performance at high current rates is low.

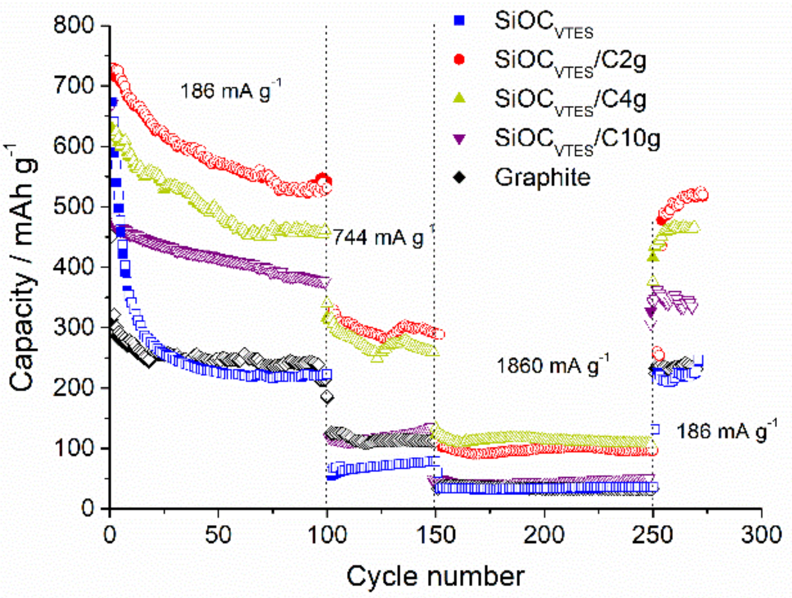

Figure 7.20. *Prolonged cyclic performance of SiOC$_{VTES}$/graphite composites.*[257]

To get some insight into the electric properties of of SiOC$_{VTES}$/graphite composites, electrochemical impedance spectroscopy measurements during the first intercalation step were conducted. The EIS measurements were performed for the selected samples: SiOC$_{VTES}$/C2g (due to the highest capacitance among the SiOC/graphite composites) and the reference SiOC$_{VTES}$ and graphite. The Nyquist plots for these materials are presented in **Figure 7.21**. At 2 V all of the materials reveal one semicircle and a straight vertical line. The size of the semicircle is the biggest for the SiOC$_{VTES}$ electrode and the smallest for graphite one. Lowering the potential to 1-0.75 V leads to the emergence of a second semicircle in the mid-frequency region, which corresponds to the adsorption of electrolyte species to the surface of the electrode. At low potentials below 0.35 V, the SiOC$_{VTES}$ exhibit only a typical Warburg straight line, while both graphite and SiOC$_{VTES}$/C2g reveal flat semicircle followed by the Warburg straight line.

High-frequency semicircle corresponds to surface processes i.e. lithium ions migration through the surface, formation of SEI and the resistance of electric contacts (binder, conductive additive, current collectors).[276–280] The mid-frequency semicircle originates from the charge transfer resistance of reaction at electrode/electrolyte interphase. The Warburg response relates to solid-state lithium ions diffusion into the particle of the active material. If the line becomes steep, then it can also correspond to lithium accumulation in the bulk.[277,280]

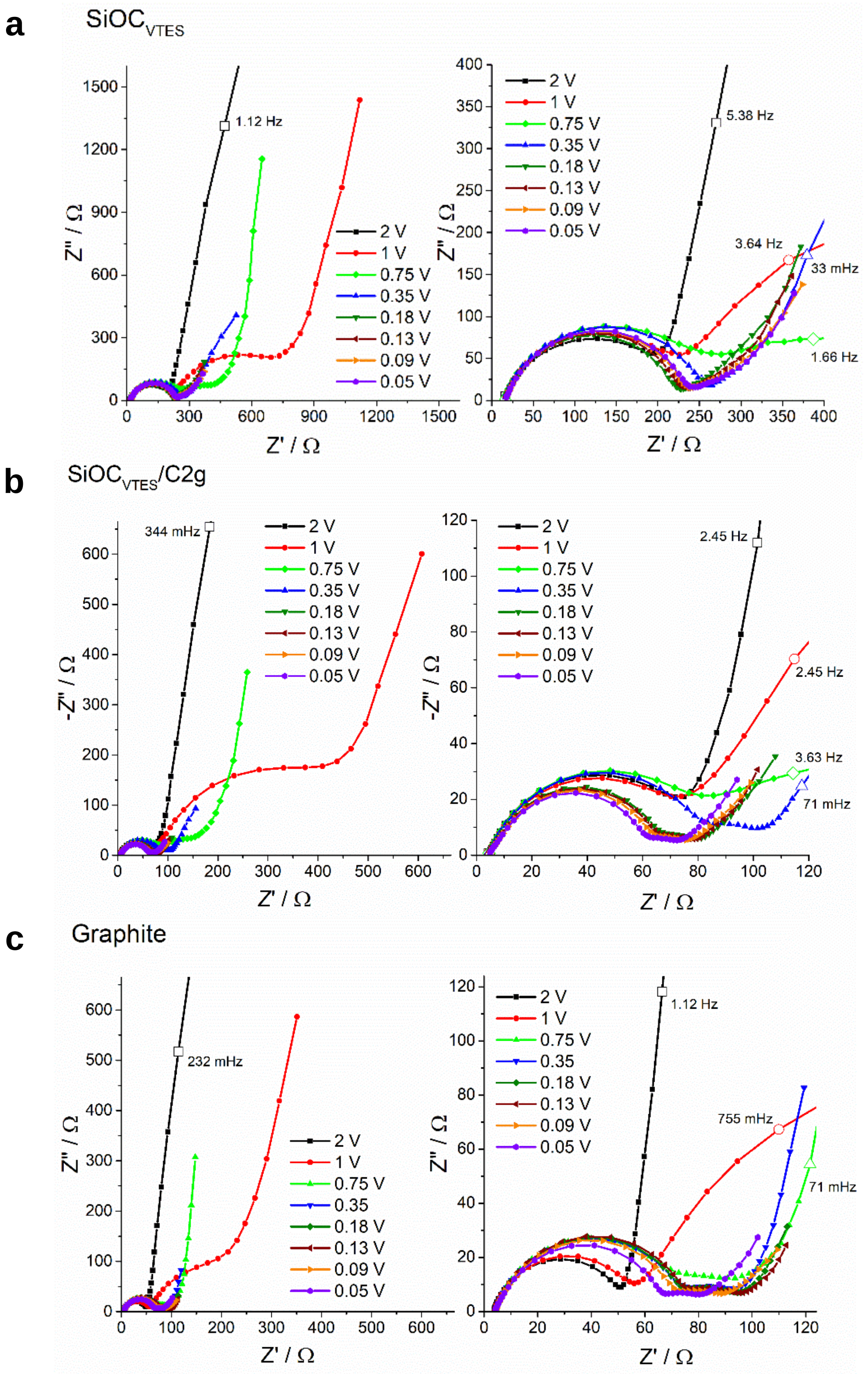

Figure 7.21. Nyquist plot electrochemical impedance spectroscopy measurements for a) SiOC$_{VTES}$, b) SiOC$_{VTES}$/C2g and c) graphite. [257]

The sizes of the high-frequency semicircles in the case of pure SiOC$_{VTES}$ indicate that the material exhibits similar resistance and impedance level during the entire lithiation process. In contrast, in the case of $SiOC_{VTES}$/C2g and graphite both high- and mid-frequency semicircles become smaller, which suggest decreasing of the resistance and impedance during the lithiation stage. These results are in contrast to some literature reports for pure graphite electrodes.[277,278] Changes of impedance during lithiation process of graphite at low potentials is a complicated phenomenon, due to opposite effects:

- formation of a conductive film (decreases the resistance),[278]
- reversible changes in SEI structure upon lithiation (decreases the resistance),[281]
- expansion of graphite (increases the resistance).[278]

Taking into consideration these processes, one can assume the addition of graphite to $SiOC_{VTES}$ leads to the creation of low-resistive SEI, improves the electric conductivity and creates lithium diffusion paths, similarly to other carbon additives.[76,78]

As it was shown in **Figure 7.18**, $SiOC_{PhTES}$/graphite composites showed better high rate capability performance than $SiOC_{VTES}$/graphite composites. For this reason, $SiOC_{PhTES}$/graphite composites were further cycled at high currents. The following program was applied: C/2x20, 5Cx20 and finally C/2x20. The purpose of the initial 20 cycles was to get a stable electrochemical response before testing the material with high currents. The return step was conducted to assess the condition of the electrode after cycling with a 5C rate. The results are presented in **Figure 7.22 a)**. All the investigated materials exhibit good electrochemical stability during the entire cycling test. Moreover, the capacity before and after the 5 C step was on the same level, which suggests electrodes were not damaged during cycling with high-current. The capacity at C/2 rate of the $SiOC_{PhTES}$/graphite composites varies between ~450 – 350 mAh g^{-1}. When the current rate was increased to 5C, the capacity values for all the materials decreased. The highest drop was registered for the pure ceramic and the samples with low-graphite content. The highest capacity was registered for the $SiOC_{PhTES}$/C10g sample of 293 mAh g^{-1}. This capacity vastly exceeds the values received for pure components. These results suggest combining graphite with $SiOC_{PhTES}$ leads to the rate capability improvement.

To get a deeper insight into the electrochemical behaviour of $SiOC_{PhTES}$/graphite, the voltage profiles at 5C rate are shown in **Figure 7.22 b)**. The shape of the voltage profiles indicates a big part of the lithium has been stored at low potentials, i.e. below 0.5 V, especially in the case of the SiOC$_{PhTES}$/C10g sample. In this potential region, it is known that energy storage occurs primarily in the graphitic phase (see CV curves, **Figure 7.16**). Thus, one may expect upon high current rates graphite is a major storage site, while the SiOCs plays a protective role. Such observations have been already made for SiCN/graphite composites.[255,256]

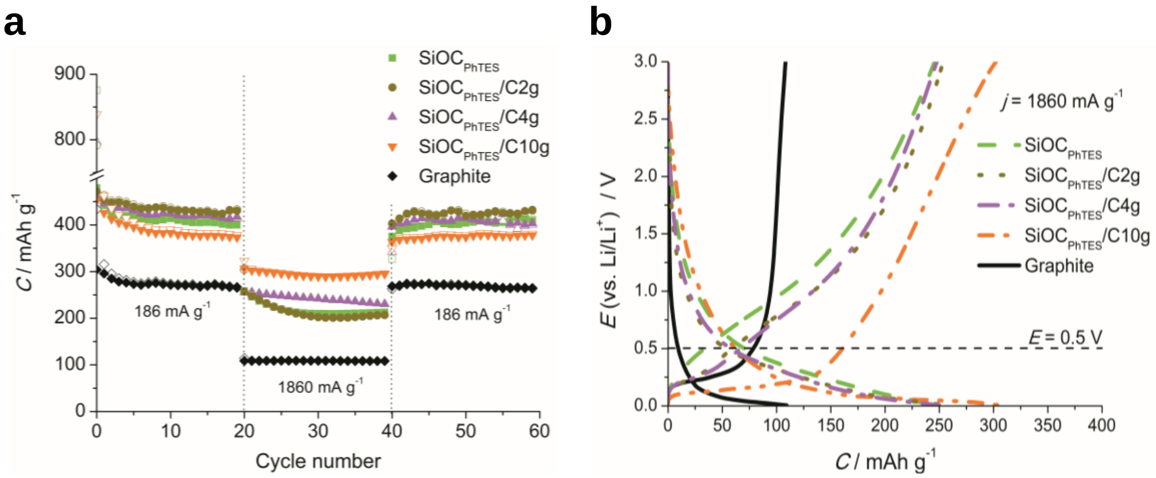

Figure 7.22. *a) results of electrochemical cycling of the SiOC$_{PhTES}$/graphite composites with C/2x20 → 5Cx20 →C/2x20 program, b) voltage profile of SiOC/graphite composites registered during cycling with 5C current rates.*[260]

The electrochemical performance of the presented SiOC$_{VTES}$/graphite and SiOC$_{PhTES}$/graphite composites was vastly different. This might be related to many various parameters that the samples differ from each other, such as composition or microstructure. To limit the number of variables, SiOC$_{PhTES}$/graphite composite was synthesised with a tailored amount of graphite to get the same carbon content as in SiOC$_{VTES}$/C2g sample. The newly synthesised PhTES-based composite is denoted as SiOC$_{PhTES}$/C$_{Tailored}$. The comparison between elemental analyses of both of these samples is given in **Table 7.9**.

Table 7.9. *Elemental composition of SiOC$_{PhTES}$/C$_{Tailored}$ and SiOC$_{VTES}$/C2g.*[257]

Material	C	O	Si	C$_{free}$	Empirical formula
	wt.%				
SiOC$_{VTES}$/C2g	44.4±0.8	26.0±0.4	29.6±1.2	41.5	$SiO_{1.54}C_{3.51}$
SiOC$_{PTES}$/C$_{Tailored}$	45.1±1.5	26.9±0.7	28.0±2.2	43.3	$SiO_{1.68}C_{3.77}$

The elemental analysis shows almost identical carbon content of ~45% in both samples and similar amounts of oxygen and silicon. The difference in composition between the samples is less than 2%. Thus, one can assume, SiOC$_{\text{VTES}}$/C2g and SiOC$_{\text{PhTES}}$/C$_{\text{Tailored}}$ are chemically almost the same.

In the next step, materials were compared based on their microstructure. The percentage fraction of SiOC tetrahedra share and the Raman spectroscopy results are shown in **Table 7.10.**, **Figure 7.23**, and **Table 7.11**.

Table 7.10. *Data obtained from the fitting of Raman spectra recorded for SiOC$_{\text{PhTES}}$/C$_{\text{Tailored}}$ and SiOC$_{\text{VTES}}$/C2g samples.*[257]

Material		**D4**	**D1**	**D3**	**G**	**D2**	**I_{D1}/I_G**	**I_{D2}/I_G**
SiOC$_{\text{VTES}}$/C2g	cm^{-1}	1195	1328	1537	1578	1607	**1.53**	**0.73**
	Intensity	0.052	0.92	0.23	0.60	0.44		
SiOC$_{\text{PhTES}}$/C$_{\text{Tailored}}$	cm^{-1}	1195	1328	1530	1582	1610	**2.08**	**1.35**
	Intensity	0.059	1.00	0.21	0.48	0.65		

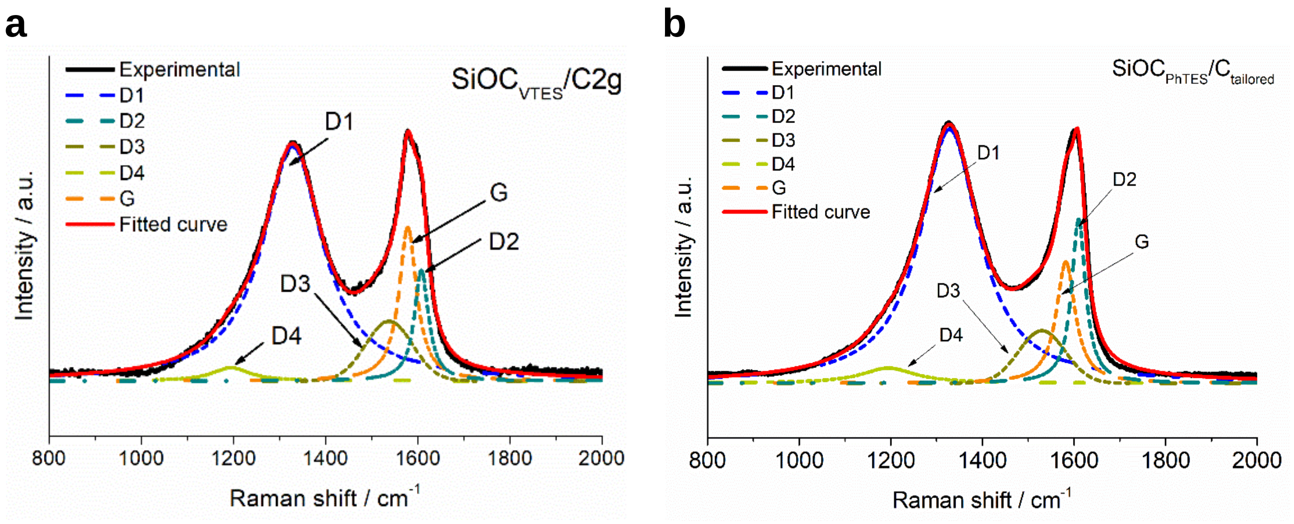

Figure 7.23. *Raman spectra of a) SiOC$_{\text{VTES}}$/C2g, b) SiOC$_{\text{PhTES}}$/C$_{\text{tailored}}$.*[257]

The results of ^{29}Si NMR reveals the SiOC tetrahedral units share for both composites. The discrepancies between both of these samples are around 2-3%, which can be considered as the uncertainty of the measurement. Thereofore, one can assume that the ceramic microstructure is very similar. The Raman spectroscopy, on the other hand, reveals differences between SiOC$_{\text{VTES}}$/C2g and SiOC$_{\text{PhTES}}$/C$_{\text{tailored}}$ samples. Based on the deconvolution of Raman spectra, it is revealed that the SiOC$_{\text{VTES}}$/C2g composite has a higher share of the G-band, while SiOC$_{\text{PhTES}}$/C$_{\text{tailored}}$ has a higher share of D2 peak. These differences suggest the structure of carbon within SiOC$_{\text{VTES}}$/C2g is more ordered than within SiOC$_{\text{PhTES}}$/C$_{\text{tailored}}$. This is rationalized by the higher graphite content in the preceramic blend of VTES-based material, which was necessary to equalize the carbon content between these two materials.

Table 7.11. *Comparison between SiOC tetrahedral units share of* $SiOC_{PhTES}/C_{Tailored}$ *and* $SiOC_{VTES}/C2g$ *based on the deconvoluton of* ^{29}Si *solid state NMR spectra.*[257]

Material	$\underline{SiO_4}$		$\underline{SiO_3C}$		$\underline{SiO_2C_2}$	
	δ / ppm	%	δ / ppm	%	δ / ppm	%
$SiOC_{VTES}/C2g$	-114.1	69.5	-74.6	20.6	-37.1	9.9
$SiOC_{PhTES}/C_{Tailored}$	-105.3	67.3	-72.1	23.1	-38.0	9.6

The electrochemical performance of both $SiOC_{VTES}/C2g$ and $SiOC_{PhTES}/C_{tailored}$ samples is presented in **Figure 7.24**. The cycling stability measurements unveil much higher capacity values for $SiOC_{VTES}/C2g$ in comparison to $SiOC_{PhTES}/C_{tailored}$ (difference of approx. 150 mAh g^{-1}), and much better first cycle Coulombic efficiency (~70% vs. ~50%, for $SiOC_{VTES}/C2g$ and $SiOC_{PhTES}/C_{tailored}$, respectively). On the other hand, $SiOC_{PhTES}/C_{tailored}$ exhibits slightly better stability (82% vs. 75% after 100 cycles for $SiOC_{VTES}/C2g$ and $SiOC_{PhTES}/C_{tailored}$, respectively) and improved rate capability performance. If we take into the consideration that the main difference between $SiOC_{VTES}/C2g$ and $SiOC_{PhTES}/C_{tailored}$ is the share of ordered and disordered carbon forms, we can state: *i)* carbon plays an important role in the shaping electrochemical properties, *ii)* the proportion between ordered and disordered carbon form has crucial impact on the electrochemical performance of the final composite material, *iii)* the properties of the composites are significantly affected by their microstructure.

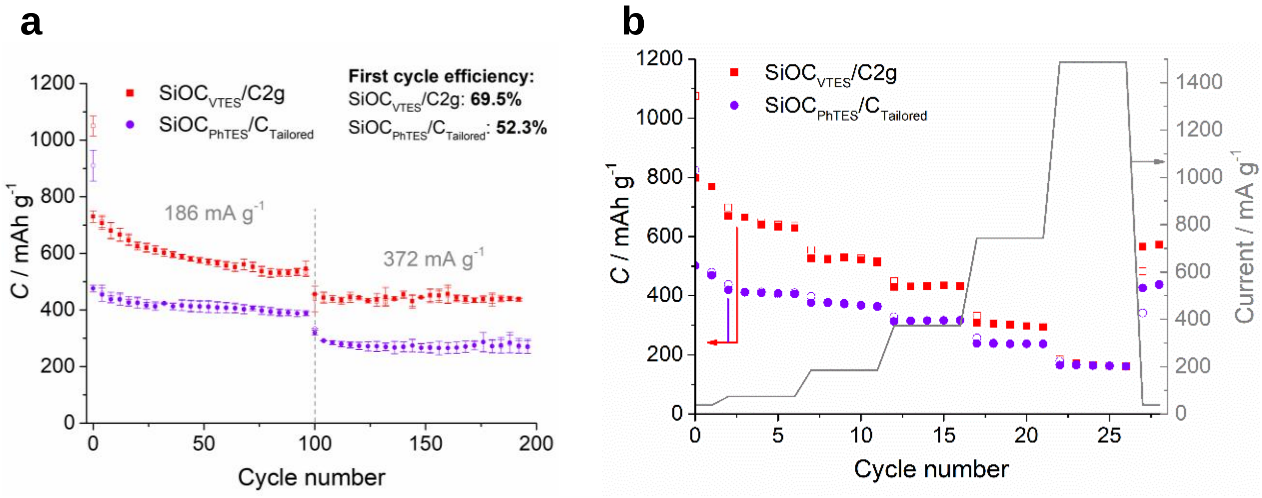

Figure 7.24. *Electrochemical performance of* $SiOC_{VTES}/C2g$ *and* $SiOC_{PhTES}/C_{tailored}$ *samples, a) cycling stability and b) rate capability.*[257]

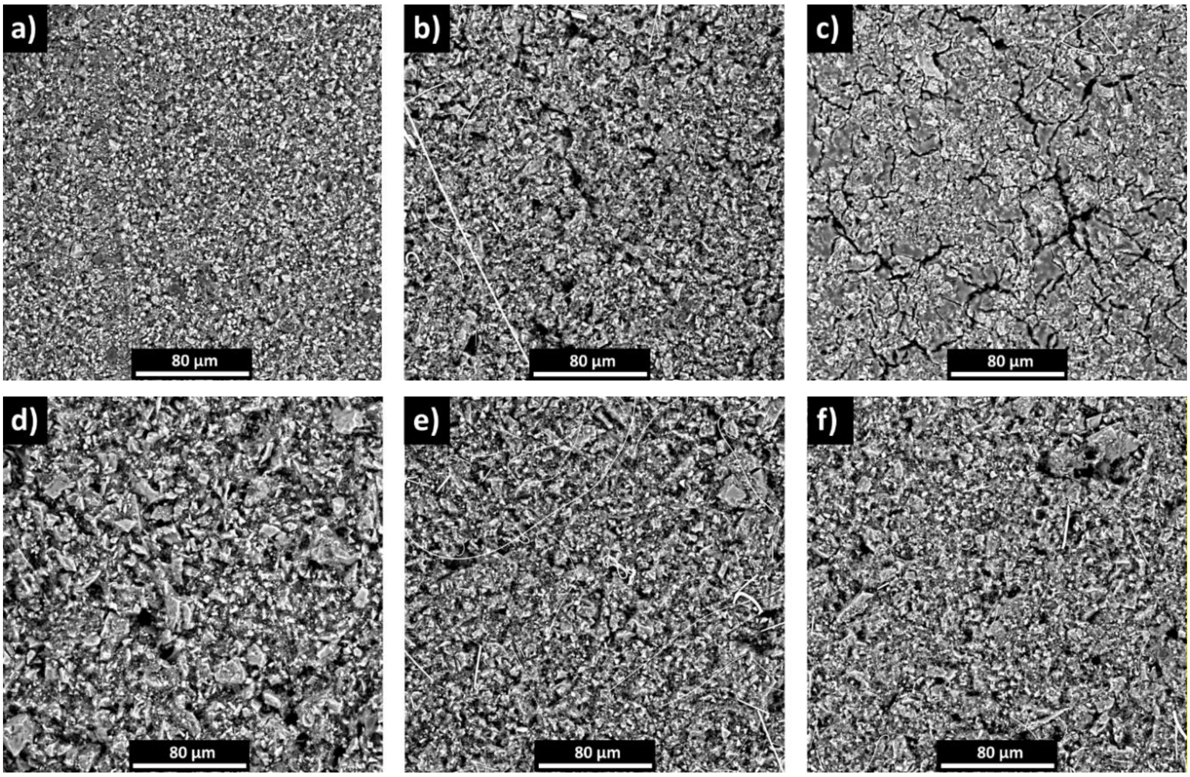

***Figure 7.25**. SEM images of composite electrodes before electrochemical measurements, after the rate capability (C/10x2 → C/5x5 → C/2x5 → Cx5 → 2Cx5 → 5Cx5 → C/10x5) and the prolonged cycling (C/2x100 → Cx100), a) $SiOC_{VTES}/C2g$ fresh electrode, b) $SiOC_{VTES}/C2g$ after the rate capability, c) $SiOC_{VTES}/C2g$ after the prolonged cycling, d) $SiOC_{PhTES}/C_{Tailored}$ fresh electrode, e) $SiOC_{PhTES}/C_{Tailored}$ after the rate capability, f) $SiOC_{PhTES}/C_{Tailored}$ after the prolonged cycling.*[257]

To get some insight into this phenomenon, the SEM images of $SiOC_{VTES}/C2g$ were taken after three different stages: freshly prepared electrodes, after the rate capability measurements using the program described in **Figure 7.24 b)** (C/10x2 → C/5x5 → C/2x5 → Cx5 → 2Cx5 → 5Cx5 → C/10x5), and after the prolonged cycling measurements, according to the program from **Figure 7.24 a)** (C/2x100 → Cx100). The obtained SEM images are presented in **Figure 7.25**. The electrodes before cycling reveal in both cases a compact structure with uniform particles distribution. After the rate capability measurements, small microcracks are observed, which indicate the damages in the SEI layer. After prolonged cycling, the number of cracks on both samples increased. The $SiOC_{VTES}/C2g$ electrode layer is more damaged than $SiOC_{PhTES}/C_{tailored}$, which explains the better stability of the $SiOC_{PhTES}/C_{tailored}$ sample. Such discrepancies may originate from the hardness of the sample. Carbon-poor ceramics tend to be harder and more rigid, and thus they are more susceptible to cracking. Moreover, as it was mentioned before, the SEI layer of $SiOC_{VTES}$/C2g forms on the graphite which tend to be more fragile to high C-rates, as described in the chapter 3 of this work.

7.3. Conclusion

In this work, a series of SiOCs/graphite composites have been synthesized based on carbon-poor ($SiOC_{VTES}$) and carbon-rich ceramic ($SiOC_{PhTES}$). The materials were homogeneous, which has been proven by SEM and TEM images, in addition, they exhibit repeatable electrochemical results. The characterisation results revealed materials consists of mixed bonds tetreaedra and carbon in two different forms: ordered, graphitic carbon, and disordered free carbon phase coming from organic functional groups of the preceramic polymer. The ^{29}Si NMR spectra reveal that in both cases, the dominant tetrahedral form is $\underline{Si}O_4$, above 60% for $SiOC_{VTES}$/graphite composites and almost 80% for $SiOC_{PhTES}$/graphite, while the remaining part consists of oxygen-rich tetrahedra. The carbon content in SiOCs/graphite depends on the graphite fraction in the preceramic blend and it changes proportionally. Similarly, the share of ordered carbon increases proportionally depending on the graphite content, as shown by the Raman spectra and the diffractograms.

The main concern of this work were the electrochemical properties of the obtained composite materials. Cyclic voltammetry measurements prove that both components in all the composites are electrochemically active and they have their share in electrochemical capacity. However, the electrochemical response of both series of the composite is vastly different. The $SiOC_{VTES}$/graphite series exhibit high capacity which exceed the capacity of the components ($SiOC_{VTES}$ and graphite) used separately. The first cycle efficiencies of these composites are similar to FCE of graphite. However, it requres precycling to obtain the stable values of capacity. In the case of $SiOC_{VTES}$/graphite, the best performing material was that with the lowest graphite content, i.e. $SiOC_{VTES}$/C2g. On the other hand, $SiOC_{PhTES}$/graphite composites provide capacity values between the values achieved for the pure components. The first Coulombic efficiency of the PhTES-based composites is similar to the Coulombic efficiency of the pure ceramic ($SiOC_{PhTES}$), but the rate capability performance was much better than for the pure $SiOC_{PhTES}$ or graphite.

The deeper explanation of these differences require more sophisticated characterization methods, like i.e. operando ^{6}Li NMR or SECM, which were not available at the time of this research. Thus, here I present only a hypothetical explanation based on the results that have been obtained, which may not be entirely correct, but gives a good starting point for further research.

First of all, let's establish the lithium storage spaces present in the material. For the SiOCs there are SiOC tetrahedral units,[48,49] free carbon phase[44,45] and nanocracks in the graphitic structure,[57] while for graphite interlayer spaces. Based on the above research and literature reports, I assume the following properties of the storage sites:

- SiOC tetrahedra. These storage sites may provide mostly the irreversible capacity due to low conductivity,[48,49]
- free carbon phase. This storage site provides a small capacity, but it has good electrical conductivity, both electronic and ionic,
- nanocracks and spaces between tetrahedral units and free carbon phase (called later *voids* for simplicity) - main storage site of ceramic. Provides high capacity thanks to the adjacency of SiOC tetrahedra, and reversibility due to the free carbon phase,[53,57] Provides high capacity at low and high current rates.
- graphite. Provides mediocre capacity values, but good stability and reversibility. Moreover, it has good electrical conductivity.

With such an assumption of storage sites, we can explain the following electrochemical behaviour.

Pure $SiOC_{VTES}$ ceramic consists mainly of SiOC tetrahedra with a small addition of free carbon phase and therefore small amount of *voids*. Therefore, we observe very high initial capacity (SiOC tetrahedra) which quickly drops. SiOC tetrahedra binds lithium irreversibly, which translates into low Coulombic efficiency. The capacity stabilises on a certain value, which is a capacity of *voids*. Notice, that the capacity obtained during these studies is higher than reported in the literature[245] tested in a similar setup. These differences arise from higher carbon content which translates into more *voids*.

The addition of graphite gives a rise to not only the graphitic carbon content in the material but also new boundaries between SiOC tetrahedra and carbon, thus new *voids* are created.

These changes give an enormous increase of the capacity values. Moreover, the FCE increases, which may be explained by the creation of SEI mainly on the surface of graphite, which is in agreement with the EIS and CV measurements. The long stabilisation period of $SiOC_{VTES}$/C2g may be explained by high non-boundary SiOC tetrahedra, which binds irreversibly part of the lithium. Such an assumption not only explains the results obtained in the presented work but also the high capacity provided by other $SiOC_{VTES}$/carbon systems. [282–284]

The further addition of graphite to ceramic ($SiOC_{VTES}$/C4g and $SiOC_{VTES}$/C10g) leads to the increase of graphite, and the reduction of the amount of SiOC and *voids*. This in turn leads to lowering the capacity values, but also the improvement of stability. The FCE remains the same as graphite.

Pure $SiOC_{PhTES}$ ceramic contains a high share of *voids* as well as SiOC tetrahedra. The high fraction of free carbon phase leads to high capacity and good stability of that material, while the presence of non-boundary SiOC tetrahedra leads to a small capacity drop. The SEI layer is formed on SiOC tetrahedra/free carbon phase, which translates into low FCE.

The addition of graphite does not create the higher amount of *voids*, therefore no improvements of calacity value is noticed for these composites. The FCE is also not improved, because the graphite is thoroughly covered with the SiOCs ceramic phase. Therefore, in the case of $SiOC_{PhTES}$/graphite composites, the SEI layer was created mainly on the ceramic surface, which is in agrrement with cyclic voltammetry (characteristic cathodic peak at 0.7 V, absent in the case of $SiOC_{VTES}$/graphite composites). However, that structure also has its advantages. The ceramic phase protects the internal graphite from deterioration when the high current rates are applied. That phenomenon was explained by Chen et al. [285] for graphitic and disordered (hard carbon) anodes. They show disordered carbons leads to the better dissipation of current, whichprevents local overcharging. That phenomenon explains the high capacity at 5C current rate achieved for $SiOC_{PhTES}$/C10g.

The most interesting differences are provided by the results obtained for $SiOC_{VTES}$/C2g and $SiOC_{PhTES}/C_{Tailored}$ samples. These materials have similar composition and structure, except for the differences in the carbon forms. $SiOC_{VTES}$/C2g sample has more graphitic carbon, which provides a higher capacity than disordered one. On the other hand, the carbon-rich ceramics covering graphite particles in the case of $SiOC_{PhTES}/C_{Tailored}$ allows to obtain better rate capability performance and overall less damaged composite layer.

The results of mixing SiOCs with graphite show the importance of carbon content within the material, and the importance of the carbon structure. The changes in electrochemical performance were revealed for both carbon-poor and carbon-rich ceramic. These results put a new light on understanding the electrochemical mechanism of lithium storage in SiOCs and SiOC/carbon composites and is a good new starting point for further research.

Chapter 8. SiOCs/Tin Nanoparticles Composite

8.1. Deeper context

Very recently Dubey et al.[66] published a paper, where they described a new SiOCs/tin nanoparticles composite which exhibits high capacity of ~600 mAh g^{-1} and outstanding electrochemical stability. The composite was produced from polymethylhydrosiloxane mixed with divinylbenzene and tin octoate. That combination of substrates allows to obtain a homogeneous preceramic blend, which was a key factor to produce SiOCs/tin nanoparticles composite with uniformly distributed tin nanoparticles. The authors pointed out, the best-performing composite was obtained when the ratio between preceramic blend and tin octoate was 3:2 (40 wt% of tin octoate with regard to the mass of the mixture).

The work of Dubey et al.[66] was focused on material synthesis using laboratory reagents for the preceramic polymer synthesis, i.e. polymethylhydrosiloxane and divinylbenzene, and was employing simple catalyst-based curing method. To further develop the SiOCs/tin nanoparticles composites, in this work the new synthesis method was developed based on UV photocuring. The UV photocuring opens the possibility for additive manufacturing of the anode material, which in the future can allow to print self-standing anodes. In this work, SPR-684 resin and 1,4-butanediol diacrylate were used for the green body synthesis, while tin octoate served as tin source. The 1,4-butanediol diacrylate was added to: *i)* increase the crosslinking degree,[93] *ii)* lower the viscosity of the synthesis mixture, and *iii)* provide an extra source of carbon. The preceramic precursor - tin octoate ratio, used in the synthesis, was the same as in the work of Dubey et al. [66]. In this part, the composite material sample are denoted $SiOC_{UV}/Sn$. For comparative purposes, pure ceramic obtained from the SPR-684 (the $SiOC_{UV}$ sample) was also produced.

8.2. Results

The study on $SiOC_{UV}/Sn$ composite obtained via photocuring started with the analysis of the photocrosslinking process by means of FT-IR. **Figure 8.1 a)** presents the FT-IR spectra of pure SPR-684, crosslinked green body of the pure SiOC (the $SiOC_{UV}$-Pre sample) and green body of the composite ($SiOC_{UV}/Sn$-Pre). The FT-IR spectrum of the SPR-684 resin reveals number of bands, which may be described as follows: 2950 cm^{-1} (C-H), ~2150 cm^{-1} (Si-H),

~1730 cm^{-1} (C=O), ~1592 cm^{-1} (C=C), ~1024 cm^{-1} (Si-OR), and ~892 cm^{-1} (Si-C and/or Si-H).[286,287] Photocrosslinked $SiOC_{UV}$-Pre sample exhibits higher absorption at ~1730 cm^{-1}, which is directly related to the introduction of BDDA to the sample. In addition, the $SiOC_{UV}$-Pre sample shows a lower signal coming from -C=C- and Si-H bonds. These changes are related to the curing process. Based on literature reports, the curing reactions present in that type of synthesis are dehydrocoupling and/or hydrosilylation.[35,87] The $SiOC_{UV}$/Sn-Pre sample reveals new bands at 2800 - 2995 cm^{-1} and 1750-1100 cm^{-1}, which are directly related to the introduction of tin octoate. The signal from -C=C- and Si-H bands is lower than in the case of SPR-684 and $SiOC_{UV}$-Pre samples, which suggest that the presence of tin octoate may catalyse the crosslinking process and lead to the higher crosslinking degree. [288–290]

The next synthesis step, pyrolysis, was tracked using TGA-DSC (**Figure 8.1 b)**). At low temperatures (below 140°C) a small weight loss in both $SiOC_{UV}$ and $SiOC_{UV}$/Sn samples is observed, which is related to the evaporation of unreacted substrates (BDDA, tin octoate, etc.) and residuals of water/acetone/ethanol from the washing procedure.[258] The mass loss is slightly higher in the case of the $SiOC_{UV}$/Sn sample, which is related to the presence of unbonded tin octoate, which may evaporate to some extent. For $SiOC_{UV}$/Sn on the DSC plot, a peak at ~290°C appears, combined with a substantial mass loss, which is associated with the thermal decomposition of tin octoate and release of volatile by-products. Mass changes at higher temperatures correspond to the decomposition and removal of organic functional groups, Si-bonds rearranging,[258,291] and the carbothermal reduction of tin octoate in the $SiOC_{UV}$/Sn sample. At 394°C a DSC peak appears for the $SiOC_{UV}$ sample. This peak was identified as thermal decomposition of acrylates and/or thermal decomposition of poorly crosslinked polysiloxanes.[292] Interestingly, this peak is absent in the case of $SiOC_{UV}$/Sn sample. This can be rationalized by a higher crossliniking degree of $SiOC_{UV}$/Sn, as it was revealed by FT-IR measurement. The thermal reactions are finished at 500°C for $SiOC_{UV}$/Sn sample, and 600°C for $SiOC_{UV}$. The consecutive mass loss is lower for $SiOC_{UV}$/Sn sample in comparison to $SiOC_{UV}$, which may be related to the higher crosslinking degree and the presence of metallic tin.

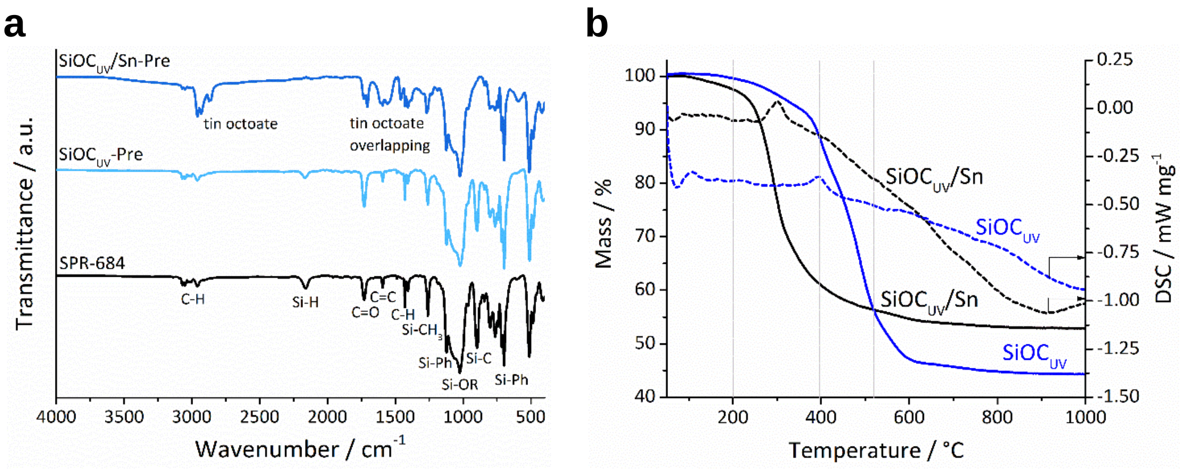

Figure 8.1. *a) FT-IR spectra of SPR-684, pre-pyrolysed SiOC$_{UV}$ (SiOC$_{UV}$-Pre) and SiOC$_{UV}$/Sn (SiOC$_{UV}$/Sn-Pre), b) TGA-DSC curves for both samples.*[293]

The results of elemental analysis of the investigated samples are presented in **Table 8.1**. The pure SiOC$_{UV}$ material contains 48.34 wt% of carbon, which classifies this material as a high-carbon ceramic. The free carbon phase-to-ceramic ratio is 56:44 which, according to the literature,[55,246,294] is considered to be optimal to achieve good electrochemical performance. The carbon content in SiOC$_{UV}$/Sn sample is significantly lower. This may be explained as the effect of carbothermal reduction, which transforms tin oxide (coming from tin octoate) into metallic tin. The tin content in SiOC$_{UV}$/Sn sample equals to approx. 20 wt%, which is a bit lower value than obtained by Dubey et al.[66].

Table 8.1. *Elemental analysis results of SiOC$_{UV}$ and SiOC$_{UV}$/Sn samples.*[293]

Sample	Elemental content (wt%)				$SiC_xO_{2(1-x)}$	C_{free}	Wt% C_{Free}	Wt% SiOC	Wt% Sn
	Si	C	O	Sn					
SiOC$_{UV}$/Sn	31.39	22.61	25.30	20.70	$SiC_{0.29}O_{1.41}$	1.39	18.64	60.66	20.70
SiOC$_{UV}$	29.56	48.34	22.10	0	$SiC_{0.34}O_{1.31}$	3.47	43.96	56.04	0.00

The formation of β-tin particles was investigated using the XRD (**Figure 8.2**). Reference SiOC$_{UV}$ sample exhibits the diffractogram for typical SiOCs materials: broad halo at 23° characteristic for amorphous silica and amorphous SiOCs,[250] and broad peak at 43° related to graphene sheets creating amorphous structure.[248,249] In contrast, SiOC$_{UV}$/Sn sample reveals a number of sharp, well-defined peaks, associated with the β-tin crystallographic structure. The absence of peaks corresponding to SnO_2 suggests that the carbothermal reduction was complete.

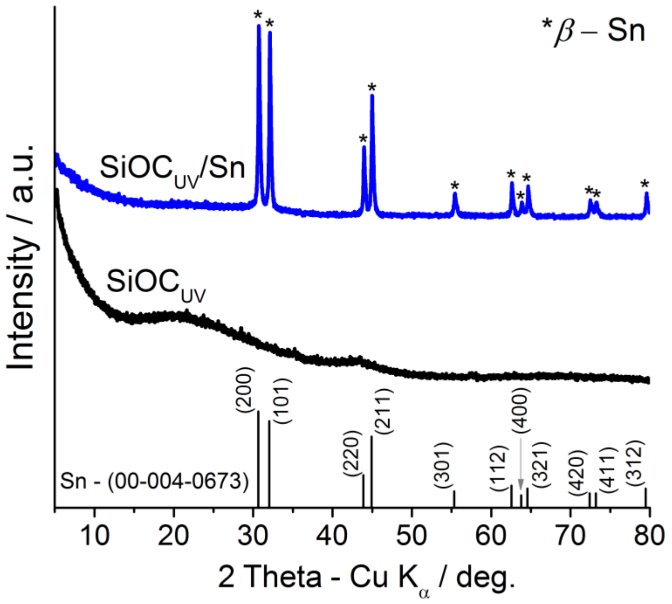

Figure 8.2. *X-ray diffractograms of SiOC and SiOC/Sn samples. On the bottom: the reference crystallographic data for β-Sn (00-004-0673).*[293]

Table 8.2*. Data obtained from the Raman spectra deconvolution: peak positions, intensity and integrated area of the deconvoluted peaks, intensity ratio between D1 and G peaks (I_{D1}, I_G – max height of deconvoluted D1, G peaks, respectively).*[293]

Material	D4				D1				D3				G				D2				I_{D1}/I_G	I_{D2}/I_G
	cm^{-1}	I_{D4}	Area intg. %	FWHM	cm^{-1}	I_{D1}	Area intg. %	FWHM	cm^{-1}	I_{D3}	Area intg. %	FWHM	cm^{-1}	I_G	Area intg. %	FWHM	cm^{-1}	I_{D2}	Area intg. %	FWHM		
SiOC$_{UV}$	1170	0.08	5.7	192	1335	0.96	66.3	173	1520	0.18	6.6	122	1581	0.56	16.0	66.9	1605	0.31	5.5	41.5	1.70	0.55
SiOC$_{UV}$/Sn	1170	0.09	6.1	166	1334	0.93	66.2	177	1521	0.16	5.7	118	1590	0.58	17.9	72.3	1612	0.28	4.2	34.1	1.60	0.48

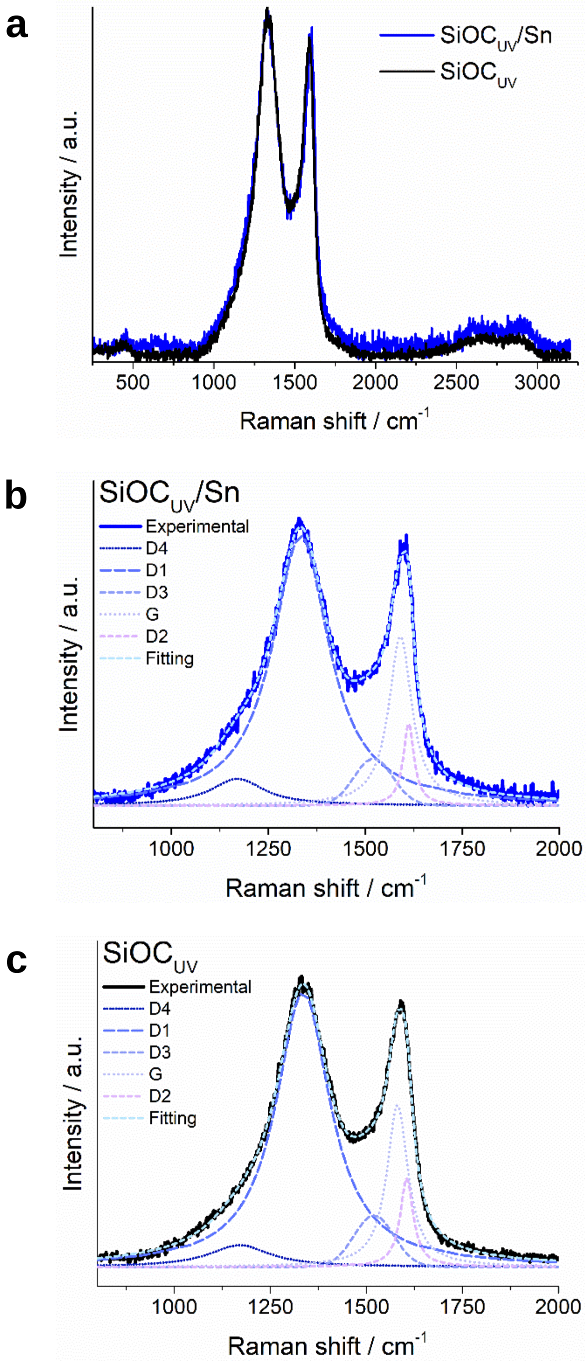

Figure 8.3. *a) Raman spectra of SiOC$_{UV}$ and SiOC$_{UV}$/Sn samples. Deconvolution results of b) SiOC$_{UV}$ and c) SiOC$_{UV}$/Sn samples.*[293]

The changes in carbon structure upon the addition of tin source were examined using Raman spectroscopy. The Raman spectra after background subtraction along with deconvolution results are presented in **Figure 8.3** and in **Table 8.2**. Both spectra of SiOC$_{UV}$ and SiOC$_{UV}$/Sn overlap almost ideally, and their deconvolution results reveal only minor changes. These results indicate that the introduction of tin octoate does not influence the carbon structure of SiOCs.

The influence of tin octoate addition on SiOC tetrahedra was checked using ^{29}Si MAS NMR. The results are given in **Table 8.3**. and **Figure 8.4**. Pure $SiOC_{UV}$ reveals a wide spectrum of various SiOC tetrahedra, with $\underline{Si}O_3C$ and $\underline{Si}O_2C_2$ being most intense (around 30% for each form), and $\underline{Si}O_3C$ being least represented (around 5%). The introduction of tin octoate to the preceramic mixture leads to a reduction of the share of the mixed bonds tetrahedra. These results suggest the carbothermal reduction of SnO_x may lead to the oxidation of carbon and, to some extent, the SiOC tetrahedra.[67]

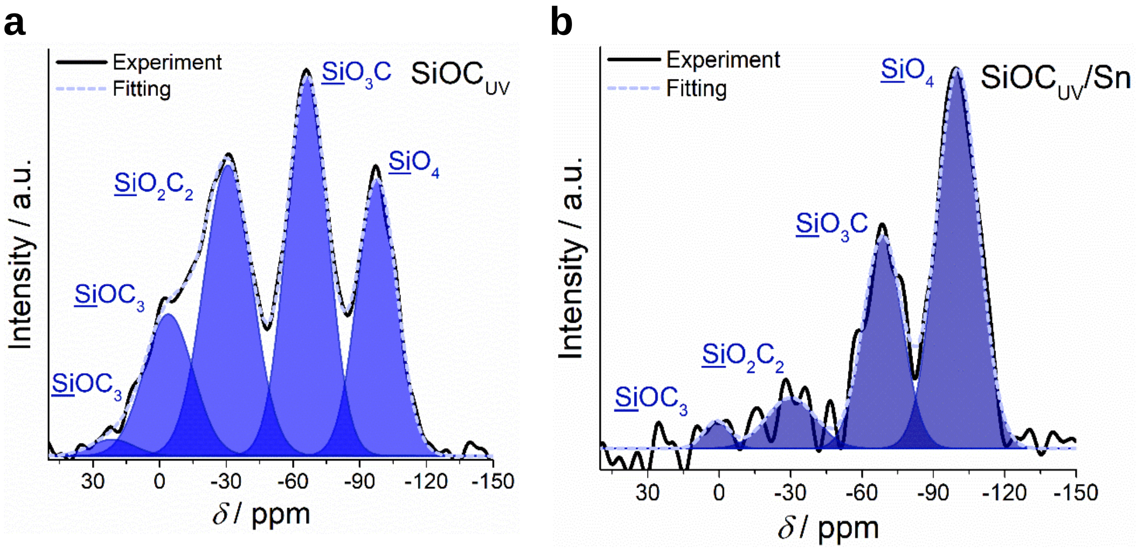

Figure 8.4. *^{29}Si MAS NMR spectra of a) $SiOC_{UV}$ and b) $SiOC_{UV}/Sn$ samples.*

Table 8.3. *Data from the deconvolution of ^{29}Si MAS NMR spectra of $SiOC_{UV}/Sn$ and $SiOC_{UV}$ samples.*

Material	$\underline{Si}O_4$		$\underline{Si}O_3C$		$\underline{Si}O_2C_2$		$\underline{Si}OC_3$	
	δ / ppm	%	δ / ppm	%	δ / ppm	%	δ / ppm	%
$SiOC_{UV}$	-97.8	22.7	-66.4	32.4	-30.7	29.0	-3.9 21.3	14.4 1.5
$SiOC_{UV}/Sn$	-100.1	60.0	-68.7	30.3	-30.1	9.1	1.1	0.6

The TEM imaging of $SiOC_{UV}$ (**Figure 8.6. a-c)**) reveals only an amorphous structure, probably originating from SiOCs. The amorphousness was confirmed by the diffraction pattern (**Figure 8.6. d)**). In contrast, the $SiOC_{UV}/Sn$ sample (**Figure 8.5-6.**) reveals a number of well-separated black spots with a diameter of 15 nm. The diffraction pattern of black spots reveals a number of reflexes, which corresponds to interplanar distances of 0.2764 and 0.2000 nm, which may originate from β-tin.[210,294,295] The elemental composition of both areas was obtained via TEM-EDX maps (**Figure 8.5**) to confirm these assumptions. Indeed, the elemental maps show that the amorphous structure consists of silicon, oxygen and carbon, while black spots reveal the presence of tin. These results ultimately confirm the $SiOC_{UV}/Sn$ composites consists of tin nanoparticles immersed in the amorphous SiOC structure.

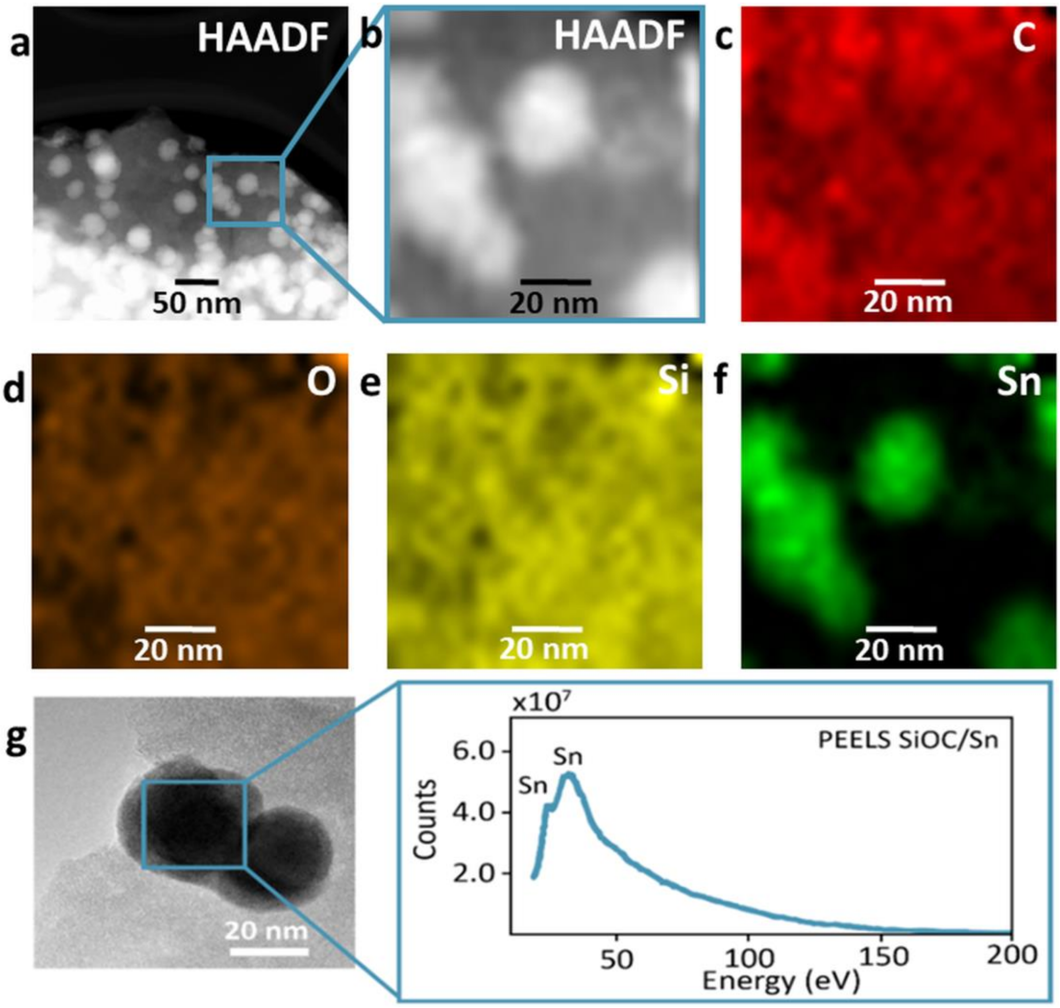

***Figure 8.5**. a,b) HAADF-STEM image and c-f) STEM-EDX mapping of $SiOC_{UV}/Sn$ samples, g) STEM-PEELS of $SiOC_{UV}/Sn$ nanocomposite.*[293]

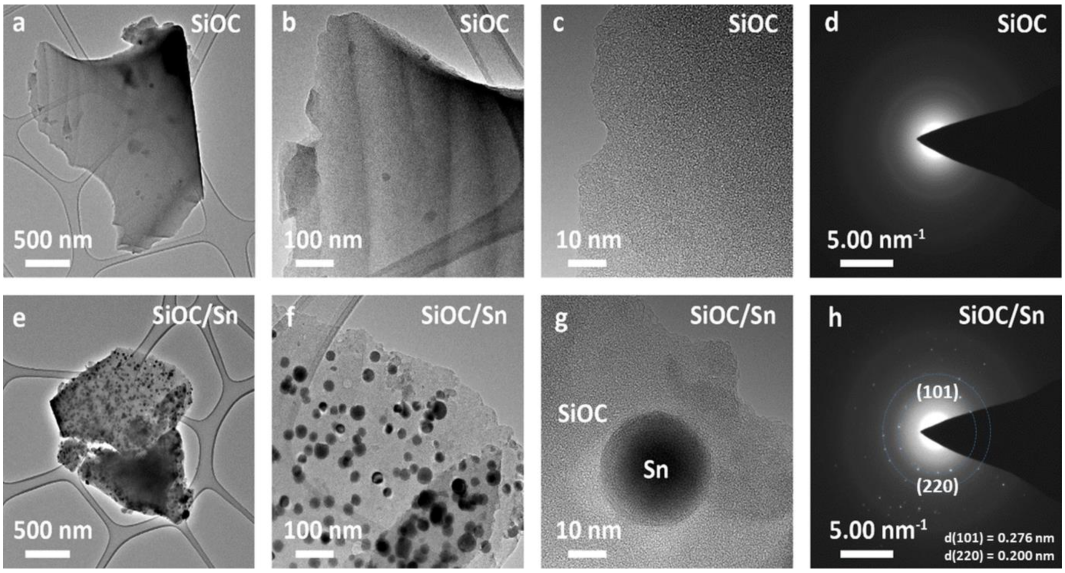

Figure 8.6. *TEM images of a-c) SiOC$_{UV}$ and e-g)SiOC$_{UV}$/Sn and the corresponding diffraction patterns for g) SiOC$_{UV}$ and h) SiOC$_{UV}$/Sn.*[293]

Electrochemical properties of SiOC$_{UV}$ and SiOC$_{UV}$/Sn composites were investigated by means of cyclic voltammetry (**Figure 8.7. a, b**). On the cathodic site, the reference SiOC$_{UV}$ sample exhibits a gradual current increase starting at ~0.9 V, which corresponds to gradual lithium insertion into the ceramic, while on the anodic site, a broad peak is observed, which is typical for SiOCs materials.[271] Both peaks, the cathodic and anodic, increse in the subsequent cycles, which is probably related to the creation of Li^{+} diffusion pathways. The SiOC$_{UV}$/Sn samples reveal two distinctive peaks on the cathodic site, at 0.56 and 0.25 V, which appear during second and subsequent cycles, and two peaks at 0.68 and 0.86 V on the anodic site. These peaks correspond to the formation of lithium alloy.[65,227] The lack of cathodic peaks during the first cycle suggest that the tin nanoparticles have to be activated beforehand.

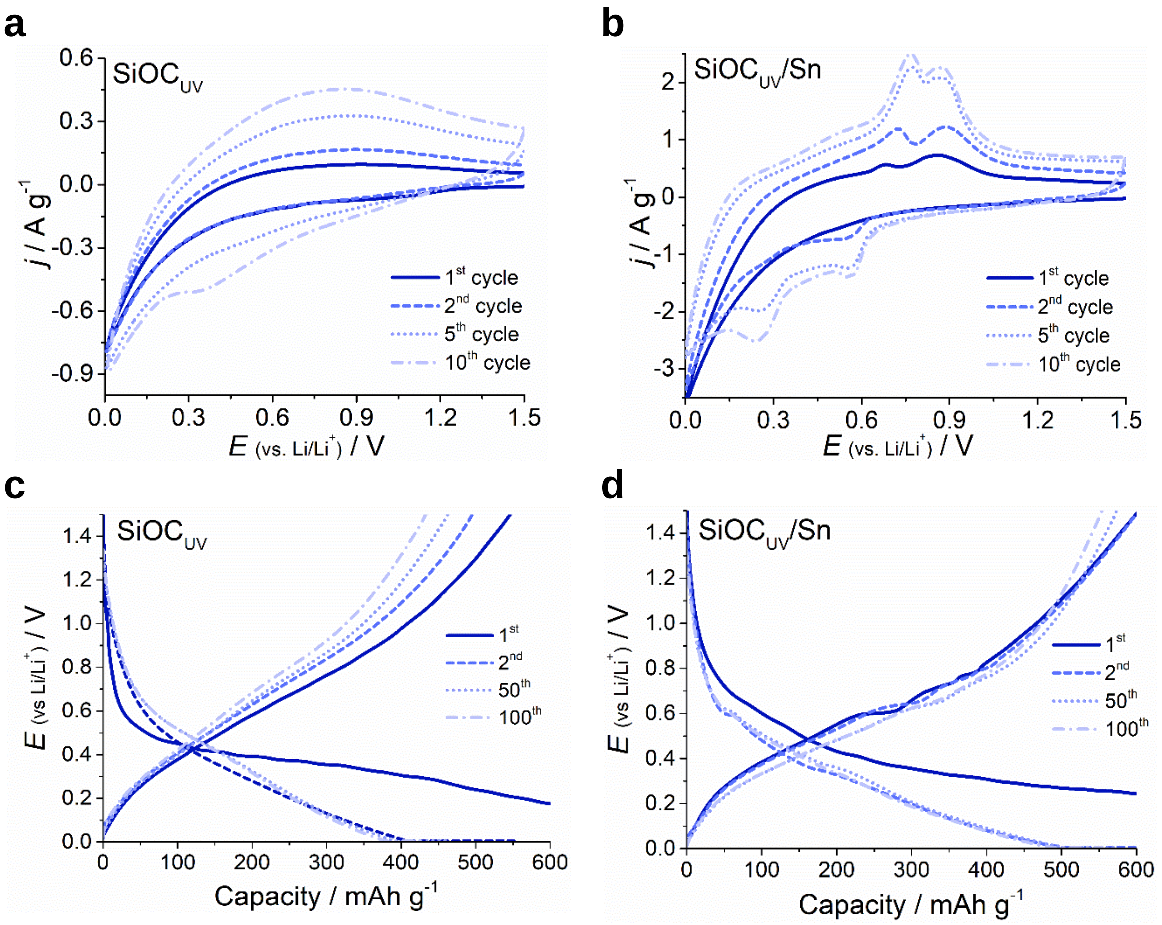

Figure 8.7. *Cyclic voltammetry curves of a) $SiOC_{UV}$ and b) $SiOC_{UV}$/Sn nanocomposite; scan rate 1 mV s^{-1}, electrolyte 1 M $LiPF_6$ (EC:DMC 1:1 v/v), half-cell configuration, Li-counter/reference electrode. Charge-discharge profiles for selected cycles of c) $SiOC_{UV}$ and d) $SiOC_{UV}$/Sn samples, at 372 mA g^{-1}.*[293]

The voltage profiles of $SiOC_{UV}$ and $SiOC_{UV}$/Sn samples are presented in **Figure 8.7. c, d**. The voltage profiles correspond well to the CV curves. During the first lithiation step, the $SiOC_{UV}$ sample exhibits a potential decrease to ~0.5 V followed by a smooth, plateau-like curve, which becomes downward in the next cycles. That change is related to the irreversibility of some reactions between lithium and SiOCs, like the creation of the SEI layer and the bonding of lithium ions with oxygen-rich tetraedra.[296] The voltage profile of $SiOC_{UV}$/Sn composite reveals small, blurred plateaus during both lithiation and delithiation cycles between 0.9-0.4 V, which corresponds to alloying/dealloying steps of tin nanoparticles. The initial capacities of $SiOC_{UV}$ and $SiOC_{UV}$/Sn are 546 and 603 mAh g^{-1}, and they are slightly fading in the subsequent cycles.

The electrochemical stability of $SiOC_{UV}$ and $SiOC_{UV}$/Sn samples was evaluated by prolonged GDC cycles (**Figure 8.8 a)** and **Table 8.4**). The prolonged GDC was conducted in the following way: first, two cycles were performed using C/20 rate to create a stable SEI layer, and then 250 cycles at 1C rate were performed using CCCV protocol, with data collected in 5 mV - 1.5 V potential range. The SiOC$_{UV}$/Sn sample exhibits good stability (82% after 250 cycles) and high capacity (almost 500 mAh g^{-1} after 250 cycles), which are superior results in comparison to pure SiOC$_{UV}$ (capacity of 400 mAh g^{-1} and stability of 73% after 250 cycles).

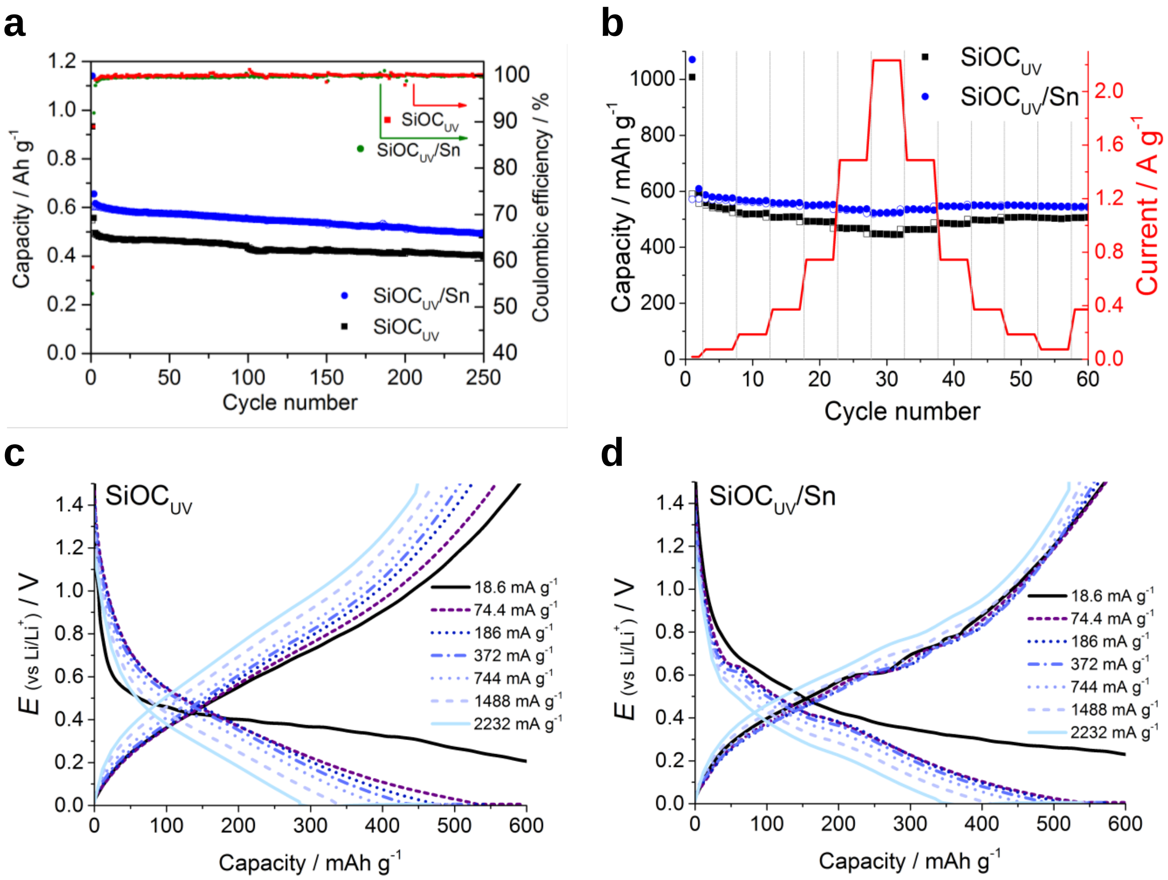

Figure 8.8. *a) Cycling performance of SiOC$_{UV}$ and SiOC$_{UV}$/Sn samples at 1C rate and the corresponding Coulombic efficiency of each cycle, b) rate capability of SiOC$_{UV}$ and SiOC$_{UV}$/Sn samples, current density rates in the range from C/20 to 6C and the respective charge-discharge profiles of c) SiOC$_{UV}$ and d) SiOC$_{UV}$/Sn.*[293]

Table 8.4. *Irreversible capacity (C$_{irrev}$) of the 1st cycle (calculated by subtracting first lithiation capacity from first delithiation capacity), reversible delithiation capacity (C$_{rev}$) of the 1st and 250th cycle, Coulombic efficiency of the 1st cycle (η) and capacity retention of SiOC and SiOC/Sn samples. The capacity retention was calculated by dividing the 250th cycle C$_{rev}$ to the 1st cycle C$_{rev}$ (%).*[293]

Material	1st cycle C$_{irrev}$/mAh g^{-1}	1st cycle C$_{rev}$/mAh g^{-1}	250th cycle C$_{rev}$/mAh g^{-1}	η / %	Capacity retention / %
SiOC$_{UV}$	386	546	397	59	73
SiOC$_{UV}$/Sn	537	603	494	53	82

To assess the high current stability of SiOC$_{UV}$/Sn composites, rate capability measurements were performed (CCCV, 5 mV-1.5 V).The current density was increased every five cycles starting from C/20 and ending on 6 C. **Figure 8.8 b-d)** present the results of the rate capability measurements. The SiOC$_{UV}$/Sn composite exhibits better rate capability performance than pure SiOC ceramic. The capacity regained at 6 C current rate was 524 and 450 mAh g^{-1} for SiOC$_{UV}$/Sn and SiOC$_{UV}$, respectively. This implies that the SiOC$_{UV}$/Sn composite preserved 92% of the capacity achieved at C/5, in contrast to 83% for reference SiOC$_{UV}$.

The electrochemical properties of the SiOC$_{UV}$/Sn sample were also measured at a 5 mV - 3 V potential range (**Figure 8.9**), which is a typical potential range for literature reports. The cycling performance measurements indicate a stable capacity values of over 800 mAh g^{-1}, while the rate capability tests show the capacity values over 1050 and 800 mAh g^{-1}, obtained at C/5 and 6 C current densities, respectively. In comparison to literature reports on various tin-based anodes,[297] these results put SiOC$_{UV}$/Sn composite among one of the best-performing materials.

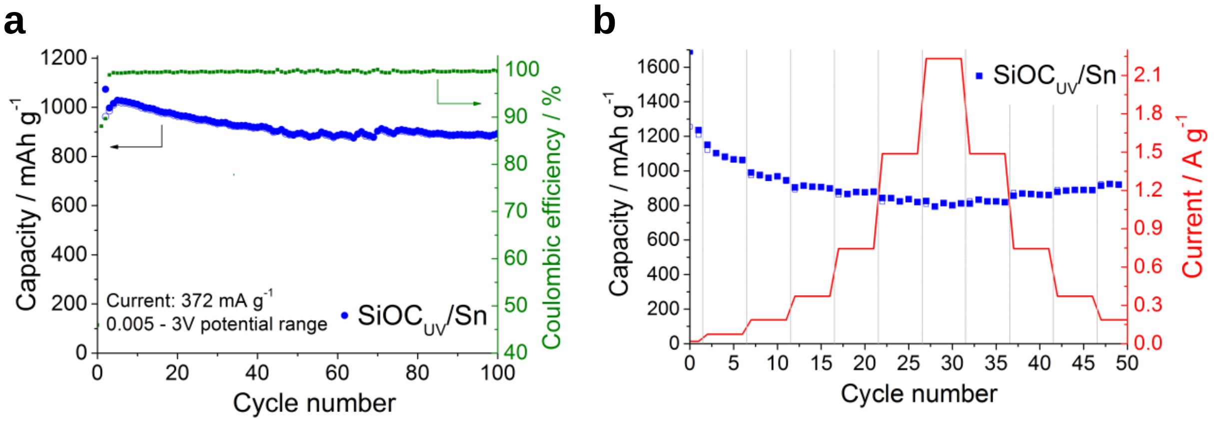

Figure 8.9. *a) Cycling stability and b) rate capability performance of SiOC/Sn sample in 5 mV- 3 V potential range.*[293]

The SiOC$_{UV}$/Sn composites over SiOC$_{UV}$ ceramic were additionally studied through EIS. **Figure 8.10. a)** and **b)** show EIS curves obtained at various lithiation cycles for SiOC$_{UV}$/Sn and SiOC$_{UV}$, respectively. The SiOC$_{UV}$/Sn sample reveals decreasing impedance between the first and 50th cycles, which relates to the creation of diffusion paths between these cycles. After the 50th cycle selected EIS spectra overlap quite well, which indicates good stability of the material. In contrast, the pure SiOC$_{UV}$ sample after initial resistance drop (curves 1st – 50th) shows a slight resistance increase with the subsequent cycles. These results suggest that the $SiOC_{UV}/Sn$ material exhibits better stability than the $SiOC_{UV}$ sample. The comparison of spectra recorded after the 1st and the 250th lithiation, reveals the lower charge transfer resistance for $SiOC_{UV}/Sn$ sample, which further confirms good stability of the composite material and indicates that the addition of tin nanoparticles increase conductivity of the material.

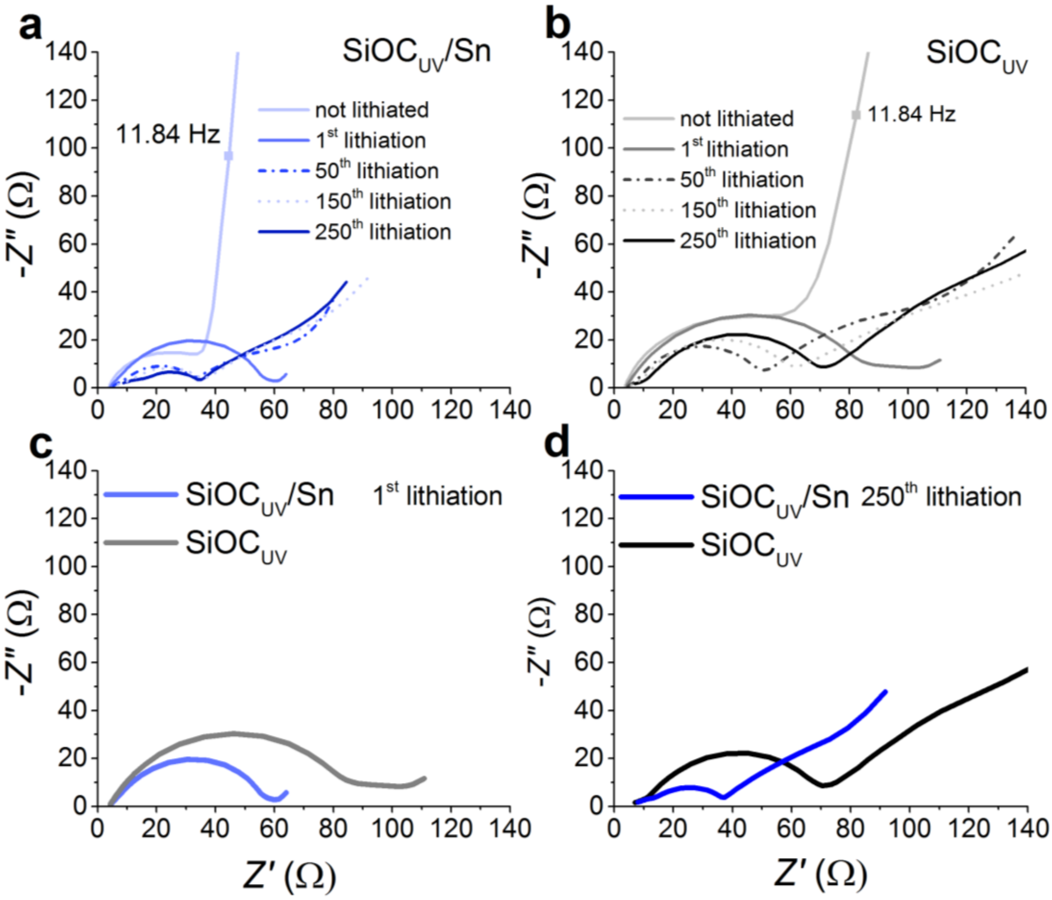

Figure 8.10. *a) Electrochemical impedance spectroscopy results recorded after various lithiation cycles for a) $SiOC_{UV}/Sn$ and b) $SiOC_{UV}$. Comparison between electrochemical impedance spectra of $SiOC_{UV}/Sn$ and $SiOC_{UV}$ sample, c) first, d) 250th lithiation cycle.*[293]

8.3. Conclusions

Silicon oxycarbide – tin nanoparticles composite has been synthesised using the photocuring method. The utilisation of tin octoate not only introduces tin into the SiOCs matrix but also leads to a higher crosslinking degree due to catalysing dehydrocoupling/hydrosilylation reactions. This turns in a higher material yield after pyrolysis. The capacity values and the electrochemical stability of obtained $SiOC_{UV}/Sn$ composite indicates good electrochemical properties of the obtained composite in comparison to other tin-based materials. The good electrochemical properties are attributed to the uniform distribution of β-tin nanoparticles, as was shown in the TEM images.

Chapter 9. SiOCs:graphite/tin nanoparticles composites

9.1. Deeper context

As it was mentioned in the previous chapter, Dubey et al.[66] recently published a paper, where they described a carbon-rich SiOCs/tin nanoparticles composite with high capacity and good stability. However, according to their research, the tin content was limited to 30 wt% (40 wt% of the preceramic precursor with regard to green body composition). Using the higher content of tin precursor led to fast capacity fading and therefore limited stability. These treats are attributed to carbon consumption from the free carbon phase during carbothermal reduction, which is essential to maintain proper material softness and electrical conductivity.[9,38,65]

Having this in mind, in this part of the research, to mitigate the effect of carbon consumption, part of the ceramic was replaced with graphite. Graphite was introduced using high-power ultrasounds, similarly to the procedure described in SiOCs/graphite chapter during the sol-gel synthesis. Three compositions were tested, namely $SiOC_H$:$C_{0.2}$/Sn-40%, and $SiOC_H$:$C_{0.1}$/Sn-60% and $SiOC_H$:$C_{0.2}$/Sn-60% (description provided in subsection 5.3). The $SiOC_H$:$C_{0.2}$/Sn-40% was tested to evaluate if graphite replacement improves the properties of the basic composite. The remaining compositions were studied to check wheather the replacement of SiOCs by graphite allows to increase the tin content within the material without losing electrochemical stability.

Other SiOCs-graphite-tin composition were also tried. However, mixtures with tin precursor content higher than 60% exhibit very low material yield (around 25%), thus mixtures containing 60 wt% of the tin precursor was set as the maximum amount. On the other hand, systems with higher graphite content were also synthesized, but in such composites the bigger tin particles were formed (diameter above 100 nm), and therefore the samples were not tested electrochemically.

9.2. Results and discussion

The ternary SiOCs:graphite/tin nanoparticles composites were extensively examined for microstructure. The information about carbon structure was provided by Raman spectroscopy. The results are presented in **Figure 9.1** and in **Table 9.1-2**. All the materials reveal typical D and G modes at ~1340 cm^{-1} and ~1580 cm^{-1}, and the overtone at 2720 cm^{-1}, described as 2D mode. To get more precise information about carbon structure, first-order spectra were deconvoluted according to Sadezky et al.[251] The pure ceramic exhibits dominating peak (normalized intensity I_{D1} = 0.950), which is typical for SiOCs materials. The addition of tin precursor at the gelation stage leads to minor changes in the carbon structure of the final composite, i.e. the normalized intensities of disordered D1 and D2 bands slightly decreased (I_{D1} = 0.881 and I_{D2} = 0.347, in comparison to I_{D1} = 0.950 and I_{D2} = 0.379 for pure $SiOC_H$). The ternary SiOCs:graphite/tin nanoparticles composites reveal on the other hand significantly higher G band intensity in comparison to $SiOC_H$ and $SiOC_H$/Sn-40%, which is typical behaviour of samples with introduced graphite (see chapter 7). The carbon structure differs depending on the composition. For example, the comparison between $SiOC_H:C_{0.2}$/Sn-60% and $SiOC_H:C_{0.2}$/Sn-40% shows the sample with higher tin content exhibits a lower I_{D1}/I_G ratio (0.481 vs. 0.551, respectively), which indicates higher carbon ordering of the $SiOC_H:C_{0.2}$/Sn-60% sample. This implies tin oxide consumes preferably disordered carbon from the free carbon phase during the carbothermal reduction process.

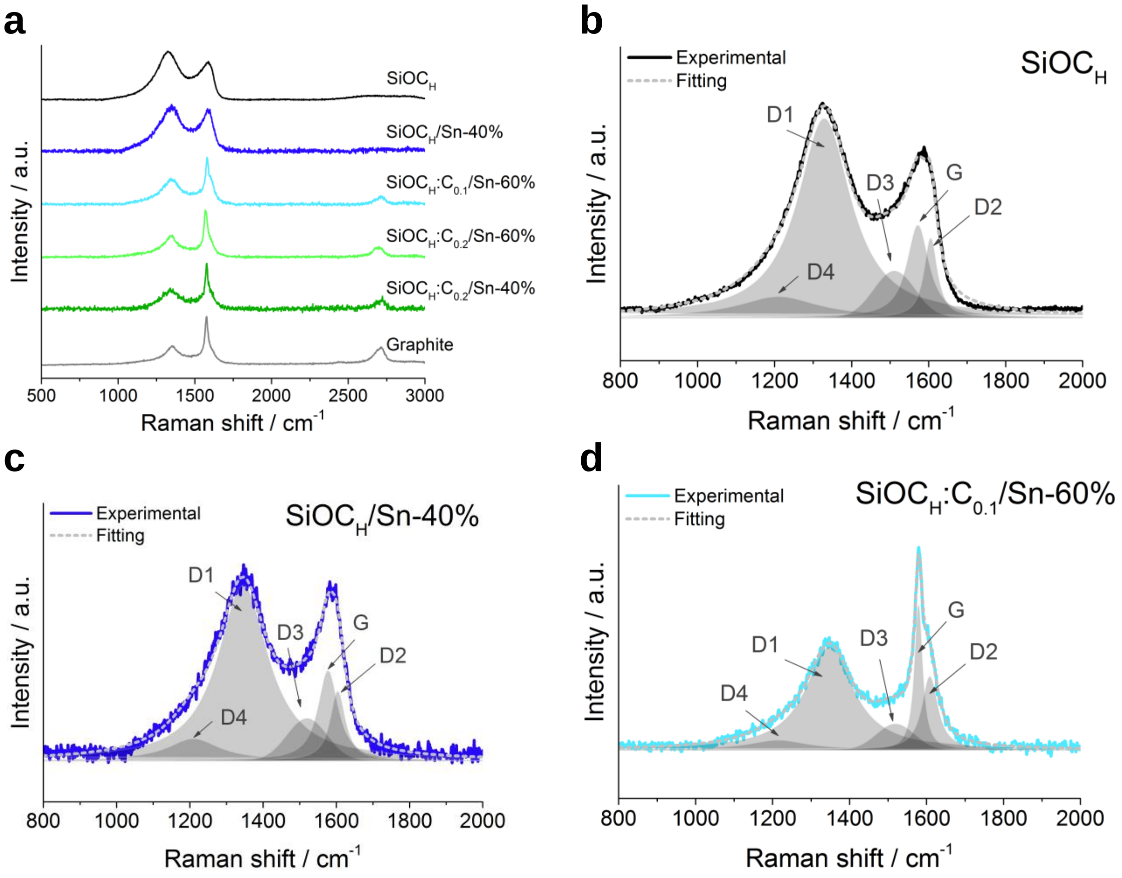

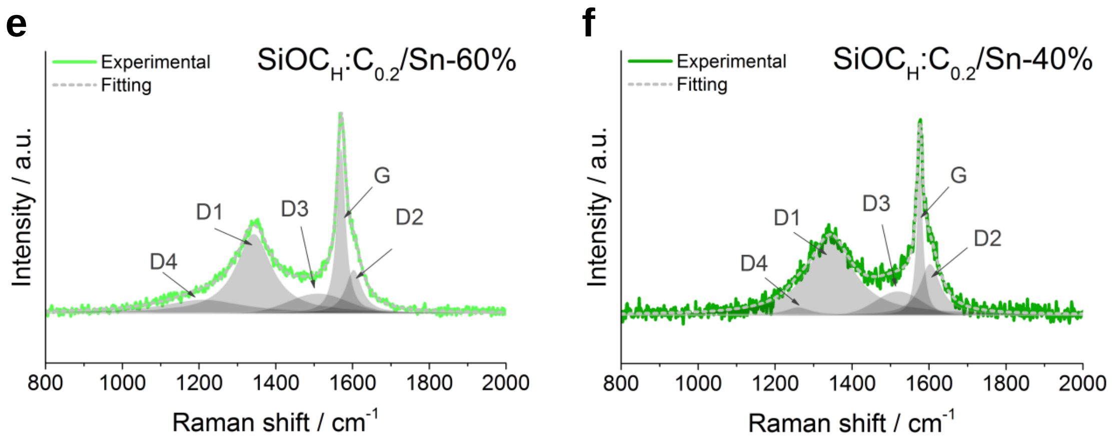

Figure 9.1. *a) Results of Raman spectroscopy for reference $SiOC_H$, graphite and composite materials after background subtraction using custom settings, fitting results for b) reference $SiOC_H$, c) $SiOC_H/Sn-40\%$, d) $SiOC_H:C_{0.1}/Sn-60\%$, e) $SiOC_H:C_{0.2}/Sn-60\%$ and f) $SiOC_H:C_{0.2}/Sn-40\%$.*[298]

Table 9.1. *The results of deconvolution of Raman spectra for ternary composite materials.*[298]

Material	D4		D1		D3		G		D2		I_{D1}/I_G	I_{D2}/I_G
	cm^{-1}	Int.	cm^{-1}	Int.	cm^{-1}	Int.	cm^{-1}	Int.	cm^{-1}	Int.		
Graphite	1209	0.054	1352	0.325	1515	0.103	1575	0.754	1603	0.193	0.431	0.256
SiOC	1210	0.100	1329	0.950	1510	0.223	1572	0.441	1605	0.379	2.154	0.859
SiOC/Sn-40%	1210	0.102	1345	0.881	1520	0.212	1577	0.451	1604	0.347	1.953	0.769
SiOC:$C_{0.2}$/Sn-40%	1260	0.036	1344	0.375	1520	0.112	1576	0.681	1603	0.244	0.551	0.323
SiOC:$C_{0.2}$/Sn-60%	1210	0.064	1342	0.380	1510	0.094	1570	0.790	1603	0.208	0.481	0.263
SiOC:$C_{0.1}$/Sn-60%	1214	0.045	1347	0.493	1519	0.124	1579	0.692	1608	0.351	0.712	0.507

Table 9.2. *The results of deconvolution of Raman spectra for studied materials – continuation.*[298]

Material	D4		D1		D3		G		D2	
	cm^{-1}	Area. %	cm^{-1}	Area. %	cm^{-1}	Area. %	cm^{-1}	Area. %	cm^{-1}	Area. %
Graphite	1209	12.6	1352	38.5	1515	13.8	1575	19.6	1603	15.4
SiOC	1210	9.3	1329	63.2	1510	8.3	1572	12.5	1605	6.6
SiOC/Sn-40%	1210	7.8	1345	62.5	1520	8.7	1577	13.2	1604	7.8
SiOC:$C_{0.2}$/Sn-60%	1210	14.4	1342	41.7	1510	18.9	1570	21.4	1603	10.6
SiOC:$C_{0.2}$/Sn-40%	1260	3.0	1343	54.1	1520	11.8	1576	14.1	1603	16.9
SiOC:$C_{0.1}$/Sn -60%	1214	6.1	1347	57.3	1519	8.2	1579	14.1	1608	14.2

The changes of SiOC tetrahedra upon the addition of the tin precursor during the synthesis step was tracked by means of ^{29}Si NMR (**Figure 9.2**). The pure $SiOC_H$ contains SiO_4 units and a number of SiOC mixed bonds tetrahedra.[299] The $SiOC_H$:graphite/tin nanoparticles composites on the other hand show only a peak at -114 ppm, which corresponds to SiO_4 units.[34,300] These results indicate, the carbon from SiOC tetrahedral units is also consumed during carbothermal reduction, which is explained as oxidation of Si and C during the reduction of SnO_2 to metallic Sn.[67]

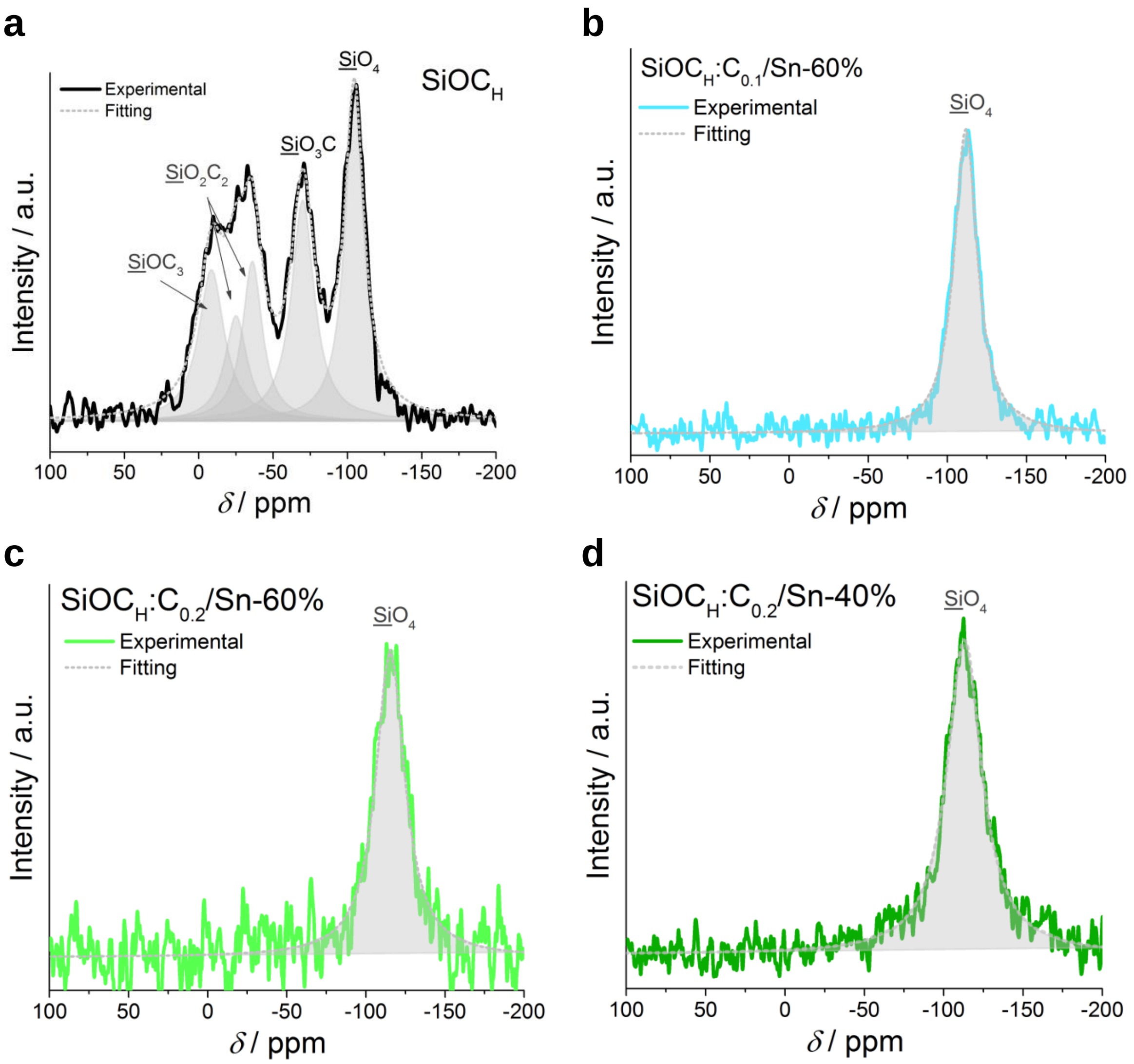

Figure 9.2. *^{29}Si NMR results for a) SiOC$_H$ b) SiOC$_H$:C$_{0.1}$/Sn-60%, c) SiOC$_H$:C$_{0.2}$/Sn-60% and d) SiOC$_H$:C$_{0.2}$/Sn-40%.*[298]

The presence of crystalline structures within the material was further studied using XRD analysis (**Figure 9.3.**). The pure SiOC$_H$ material exhibits only a broad halo at ~22°, which is typical for SiOCs materials.[248] In contrast, ternary SiOC$_H$:graphite/tin nanoparticles composite displays a series of sharp peaks. The peaks at 26.2° and 55° are attributed to the hexagonal structure of graphite, while the rest is assigned to *β*-tin. The remaining graphitic peaks are probably hindered due to the high background signal from ceramic. These results confirm the presence of ordered graphitic carbons within the material. Moreover due to the lack of signal coming from SnO_2, one can assume the carbothermal reduction of tin oxides was complete in the case of all the ternary composites. The normalized intensities of graphitic and β-tin peaks correspond well to the amount of graphite/tin precursor used for the material synthesis.

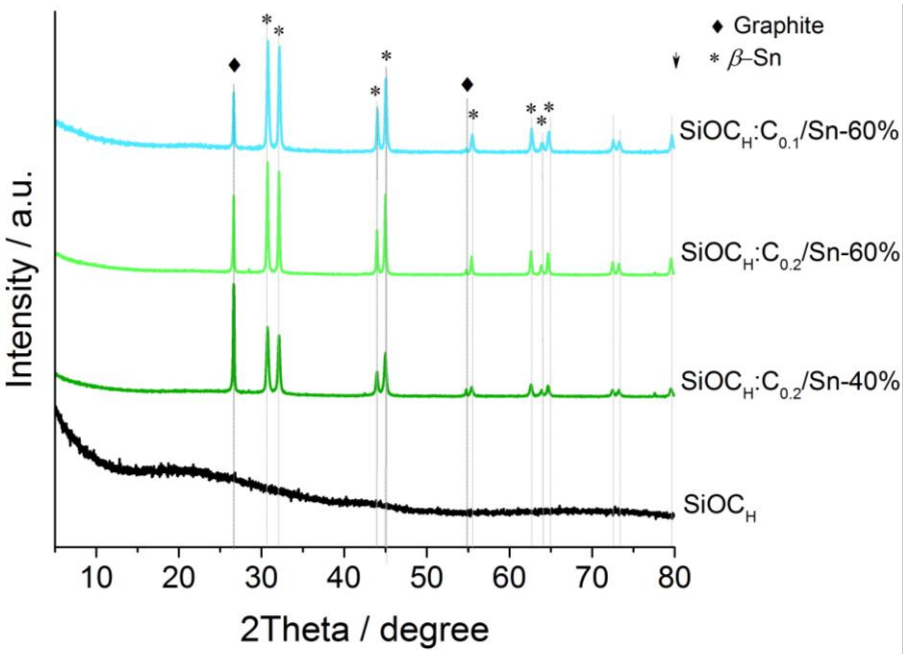

Figure 9.3. *XRD spectra of SiOC$_H$ and ternary composite materials.*[298]

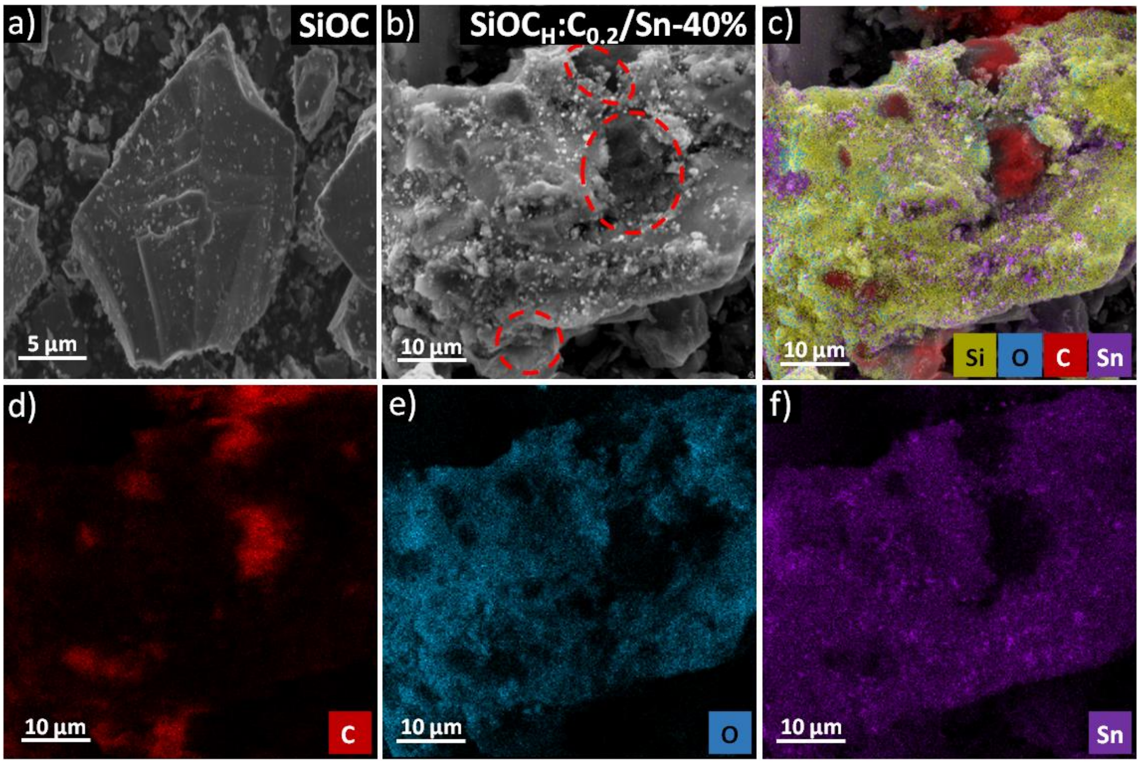

Figure 9.4. *SEM image of a) SiOC$_H$, b) SiOC$_H$:C$_{0.2}$/Sn-40% sample. c-f) EDX elemental maps of silicon, oxygen, carbon and tin.*[298]

The formation of tin nanoparticles and ceramic/graphite/tin nanoparticles distribution was tracked using SEM imaging (**Figure 9.4 a) and b**)). Reference $SiOC_H$ sample powder consists exclusively of various size slate-rock like particles. The ternary $SiOC_H$:graphite/tin nanoparticles samples reveal in contrast a number of particles with crumble-like facture. The texture consists of dark regions (marked by red circles), grey regions and white precipitants. The elemental composition of these phases was studied by EDX. The EDX maps show dark zones are composed mainly of carbon, while the grey part consists of silicon, oxygen, tin and, carbon. The white precipitants on the other hand seem to be areas with a high concentration of tin. Therefore one may assign a black part to graphite, grey to SiOCs ceramic, and white precipitants to bigger or surface tin particles. Interestingly, the tin map coincides with the map of SiOCs, while there is a low tin signal coming from graphitic regions. These results further confirm the carbon from the free carbon phase is preferably consumed during carbothermal reduction over carbon from graphite. Such a phenomenon may be explained by better mixing of tin octoate with PMHS-DVB than with graphite (liquid-liquid vs. liquid-solid mixing) and to the relatively high activation energy for the carbothermal reduction of tin oxide with graphite.[301,302] These observations are further supported by the unique morphology of $SiOC_H$:graphite/tin nanoparticles composites which have a lot of pores related to CO_2 release during carbothermal reduction. To give a better insight into that process, BET measurement has been conducted. The nitrogen adsorption curves are given in **Figure 9.5**, while the calculated SSA is provided in **Table 9.3**. The pure $SiOC_H$ is a dense material with a low SSA of 3.18 $m^2\ g^{-1}$, while the binary $SiOC_H$/Sn-40% composite has a SSA of 118.1 $m^2\ g^{-1}$. Such a great SSA increase suggest that a lot of small pores must have been created after carbothermal reduction, which led to local carbon removal. The ternary $SiOC_H$:graphite/tin nanoparticles composites exhibit various SSA, depending on the composition. The SSA of $SiOC_H$:$C_{0.2}$/Sn-40% is slightly lower than $SiOC_H$/Sn-40% sample, which relates to the introduction of graphitic particles, which have high density and does not undergo carbothermal reduction. Interestingly, the SSA of samples with 60% of precursor in the preceramic mixture is even lower. That phenomenon may be explained by the process of collapsing the walls of the pores. Due to high tin precursor content, the carbothermal reduction is more intense, which leads to the creation of a large number of pores, while the lower ceramic content weakens the strength of the walls. This causes collapsing of small pores and creating bigger ones, which ultimately translates into lower SSA.

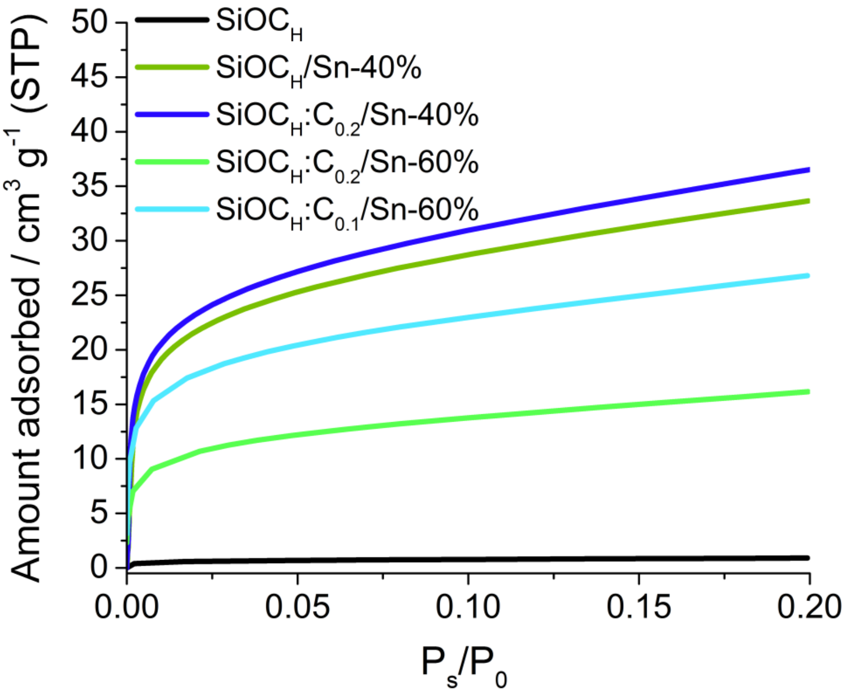

Figure 9.5. *The adsorption curves of nitrogen at 77 K for obtained ternary $SiOC_H$:graphite/tin nanoparticles composites.*[298]

Table 9.3. *BET specific surface area for ternary SiOCs:graphite/tin nanoparticles composites.*[298]

Sample composition	BET surface area [m^2 g^{-1}]
$SiOC_H$	3.18
$SiOC_H$/Sn-40%	118.2
$SiOC_H$:$C_{0.2}$/Sn-40%	106.9
$SiOC_H$:$C_{0.2}$/Sn-60%	55.1
$SiOC_H$:$C_{0.1}$/Sn-60%	94.7

The microstructure of $SiOC_H$:graphite/tin nanoparticles composites were further studied by the TEM imaging technique. The comparison between the TEM images of reference and $SiOC_H$:$C_{0.2}$/Sn-60%, which is representative for all the ternary composites samples, are given in **Figure 9.6**. Pure $SiOC_H$/Sn-40% sample consists of black spots immersed in an amorphous structure. The TEM image of $SiOC_H$/Sn-40% is similar to the structure of $SiOC_{UV}$/Sn (see chapter 8), which suggest black dots corresponds to tin nanoparticles material while amorphous part to the ceramic. The $SiOC_H$:$C_{0.2}$/Sn-60% sample reveals a similar structure to $SiOC_H$/Sn-40%, however, there are in addition parallel smudges observed i.e. in the bottom right corner of the image (**Figure 9.6 b)**), which interpenetrate the ceramic part. These smudges correspond to stacked layers of graphite. In both cases, tin spots are well separated and uniformly distributed.

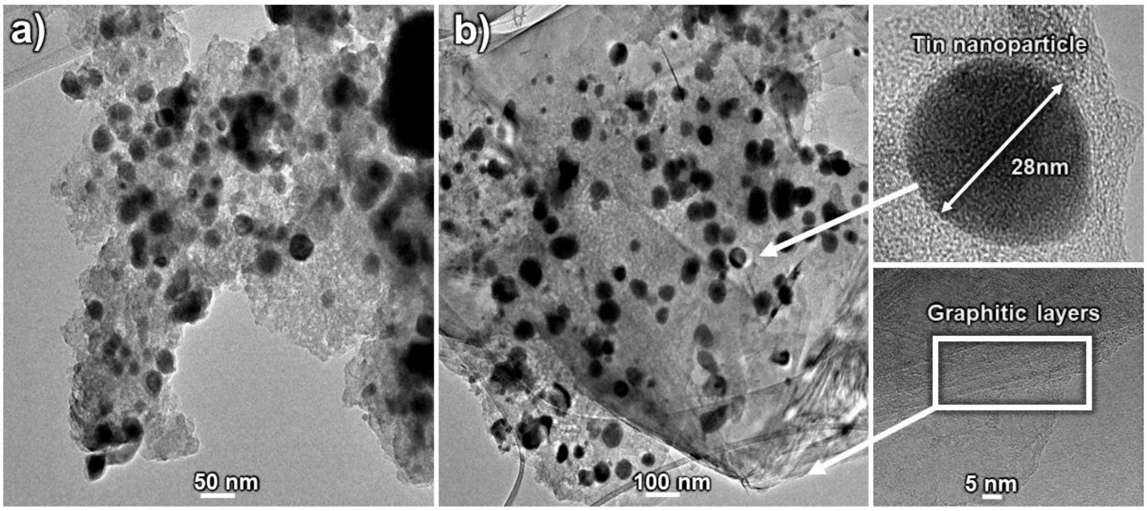

Figure 9.6. *TEM images of a) $SiOC_H$/Sn-40% and b) $SiOC_H:C_{0.2}$/Sn-60% composites.*[298]

Figure 9.7 presents the view on $SiOC_H:C_{0.2}$/Sn-60% particle with separated graphitic and ceramic phases. The EDX local analysis (**Figure 9.7**) confirms the elemental composition of each phase. This image confirms tin nanoparticles are mainly present in the ceramic part, while in the graphitic phase, only traces of tin nanoparticles has been found.

The comparison between tin accumulation in $SiOC_H$:graphite/tin nanoparticles composites with various tin content are given in **Figure 9.8**. One can see that the tin accumulation in the tin precursor-rich sample in the ceramic phase is densely distributed, while in the tin precursor-poor sample there is some greater space between tin nanoparticles. These differences are very pronounced even though the $SiOC_H:C_{0.2}$/Sn-40% sample contains more graphite than $SiOC_H:C_{0.1}$/Sn-60%.

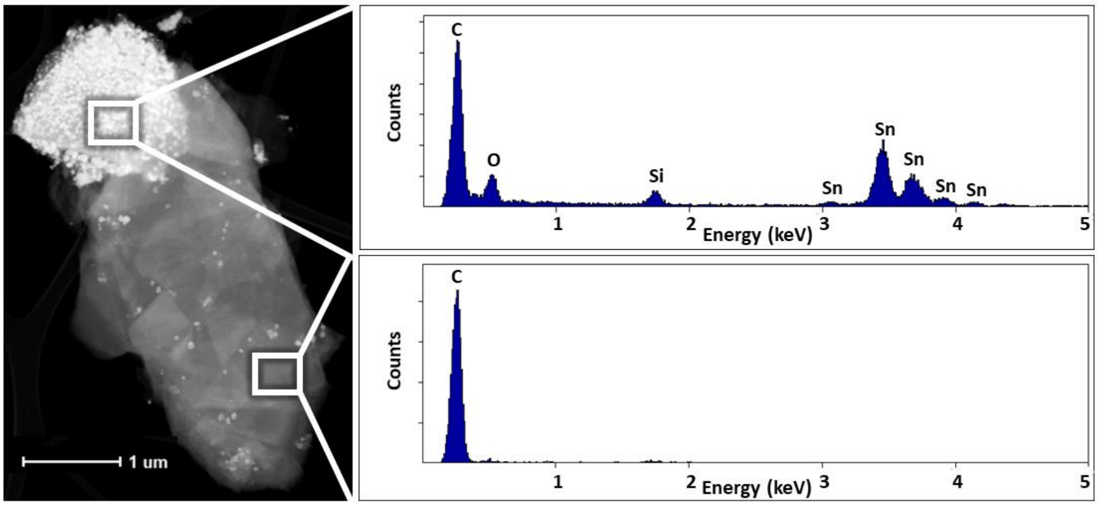

Figure 9.7*. EDX elemental composition of tin-rich (SiOC) and tin-poor (graphite) regions of the $SiOC_H:C_{0.2}$/Sn-60% sample.*[298]

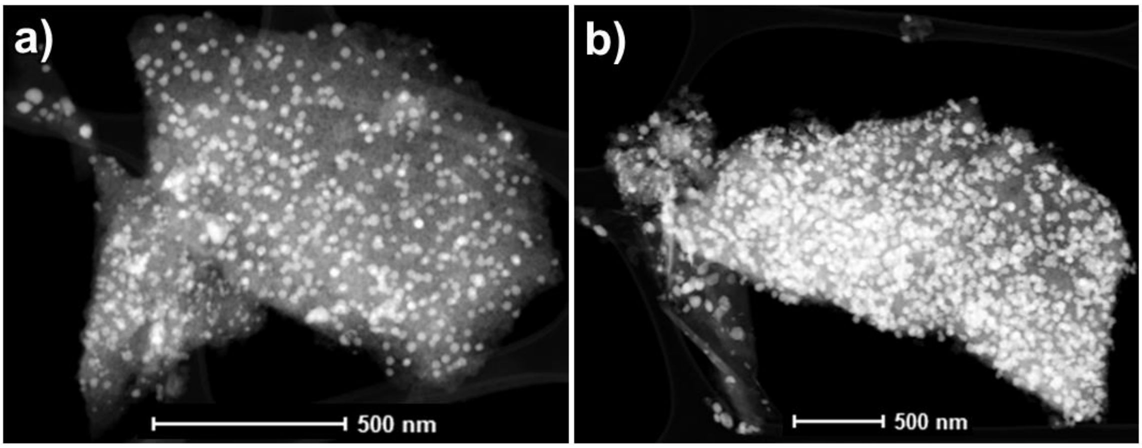

Figure 9.8. *TEM images of a) $SiOC_H$:$C_{0.2}$/Sn-40% and b) $SiOC_H$:$C_{0.1}$/Sn-60% composites showing accumulation of tin nanoparticles in the ceramic phase.*[298]

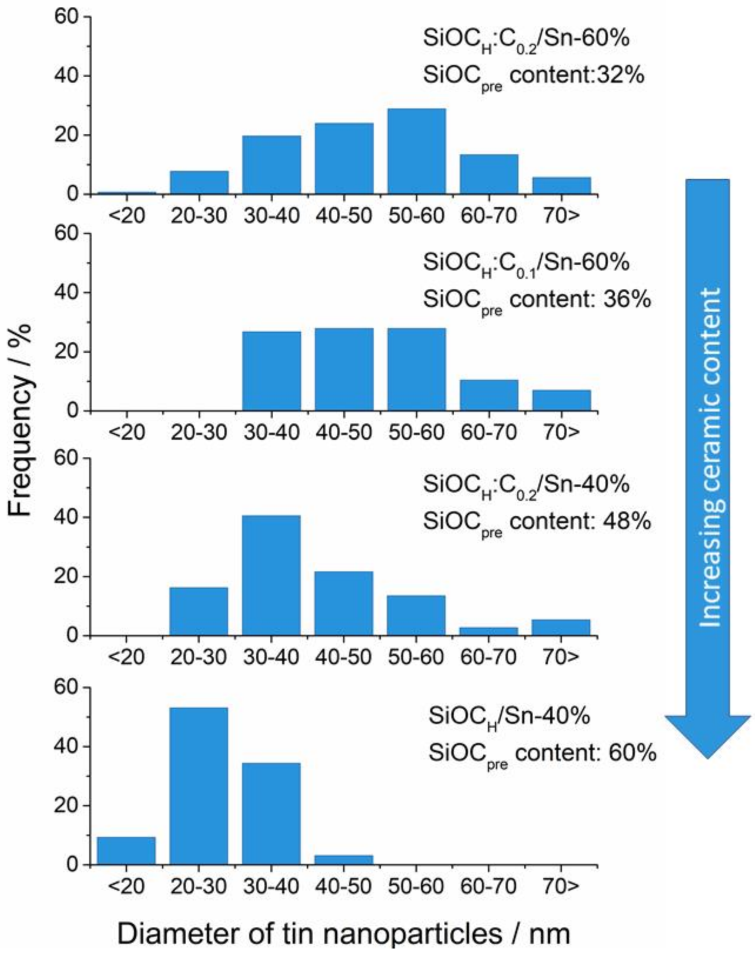

Figure 9.9. *The size distribution of the Sn nanoparticles in the $SiOC_H$:C/Sn and $SiOC_H$/Sn nanocomposites. $SiOC_{Pre}$ content assigns to the amount of preceramic polymer (in wt%) in the preceramic blend.*[298]

Figure 9.9 presents the tin particles size distribution calculated based on size measurement conducted by TIA software on TEM images. The figure also presents the tin precursor content (in wt%) within the preceramic blend. The lowest average size of nanoparticles was registered for reference $SiOC_H$/Sn-40% sample (around 20-30 nm), while the biggest for $SiOC_H:C_{0.2}$/Sn-60% composite (around 50-60 nm). One can observe, the tin nanoparticles size decreases with increasing tin precursor content. Such behaviour may be explained by more densely tin nanoparticles distribution of tin in high-tin – low ceramic compositions, as shown in **Figure 9.8.** Higher tin accumulation may promote the process of connecting of neighbouring tin nanoparticles and forming bigger ones which leads in a shift of the average particle size into the higher values.

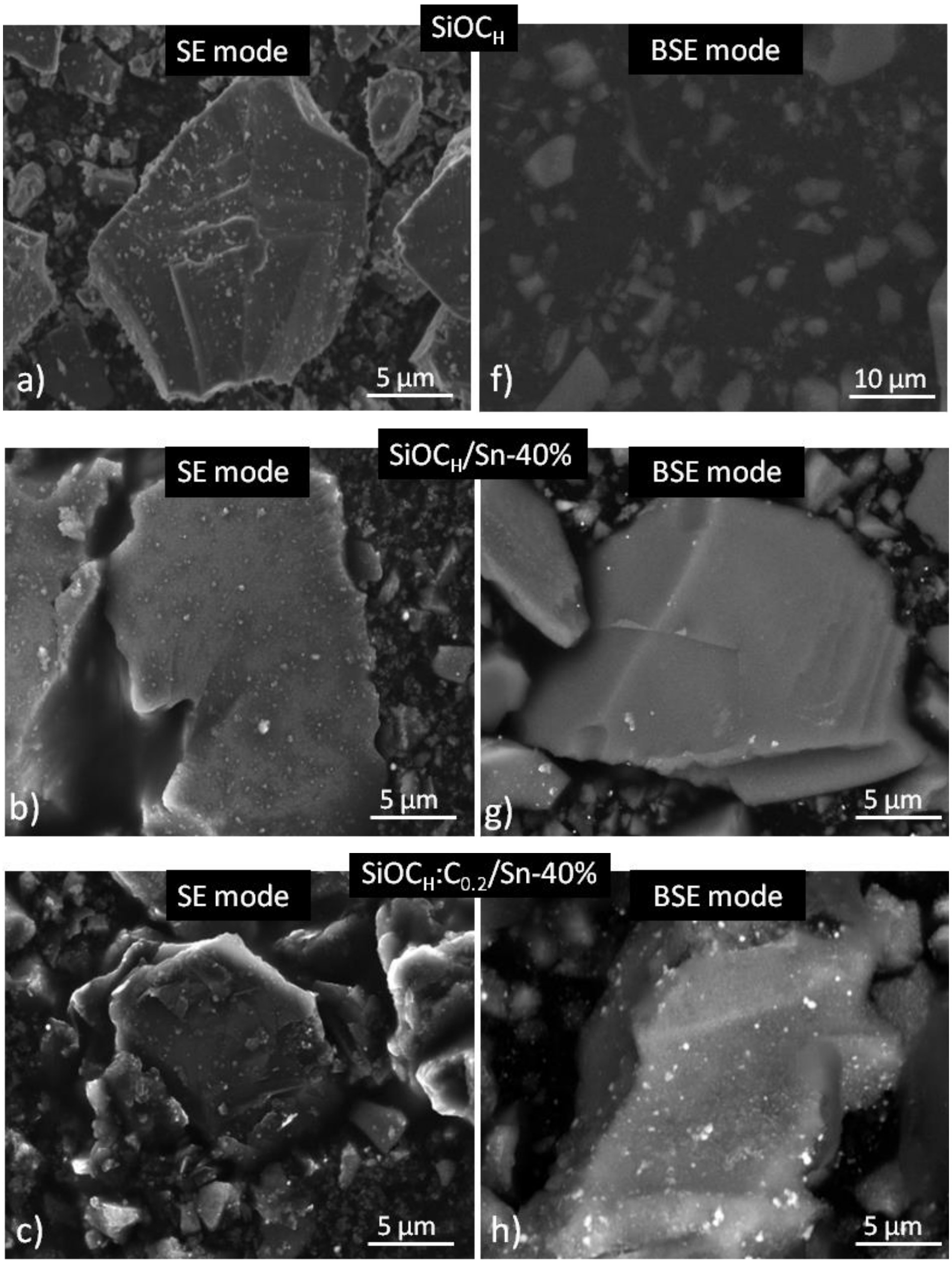

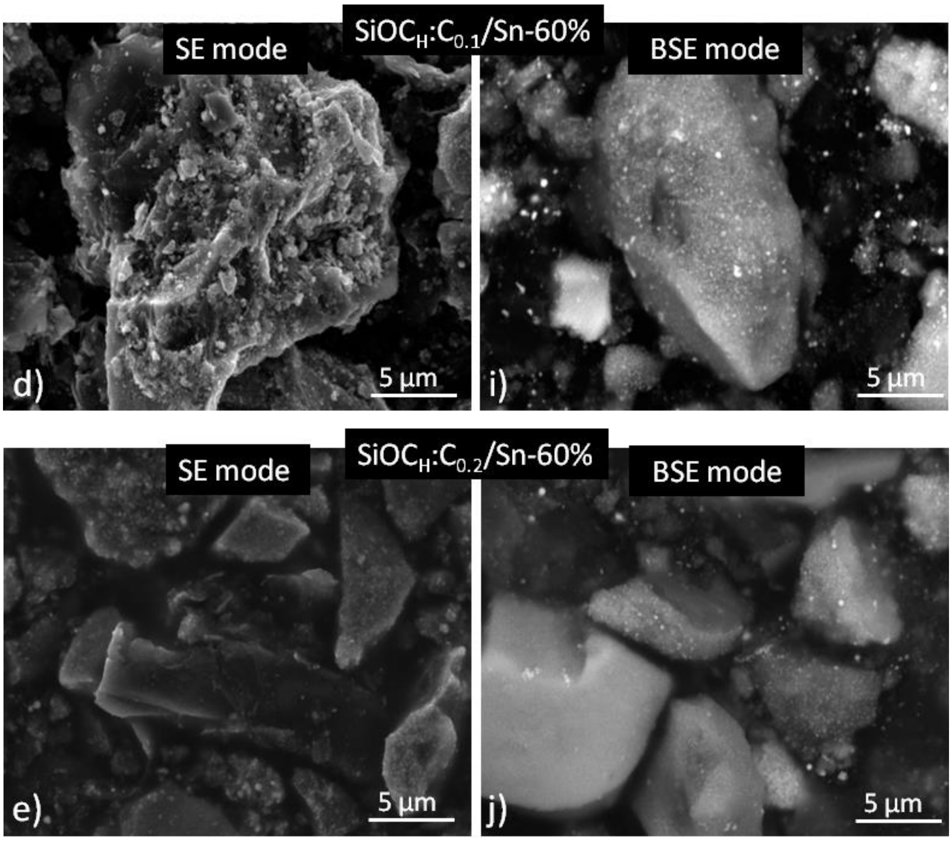

Figure 9.10. *SEM images of $SiOC_H$, $SiOC_H$/Sn and ternary $SiOC_H$:graphite/nano-tin composites, a-e) secondary electrons mode, f-j) backscattering mode.*[298]

Figure 9.10 presents the SEM images of selected $SiOC_H$:graphite/tin nanoparticles composites in both secondary electrons (SE) and backscattering mode (BSE). The SE mode confirms the presence of crumble-like particles of ternary composites and the slate rock-like structure of pure $SiOC_H$. The BSE mode shows the tin nanoparticles distribution within the material. Tin nanoparticles are represented as the white spots as tin is the only heavy element in that system. The BSE images confirm the average size of tin nanoparticles increase with the lowering of the tin precursor content in the preceramic blend. **Figure 9.11** presents the SEM images of $SiOC_H:C_{0.5}$/Sn-40% sample. One can see the $SiOC_H:C_{0.5}$/Sn-40% reveals plenty of tin particles with the size of a few hundred nanometers. Thus, for that reason, that sample was not further tested and for that research, the highest amount of preceramic precursor mixture replaced by graphite was 20 wt%.

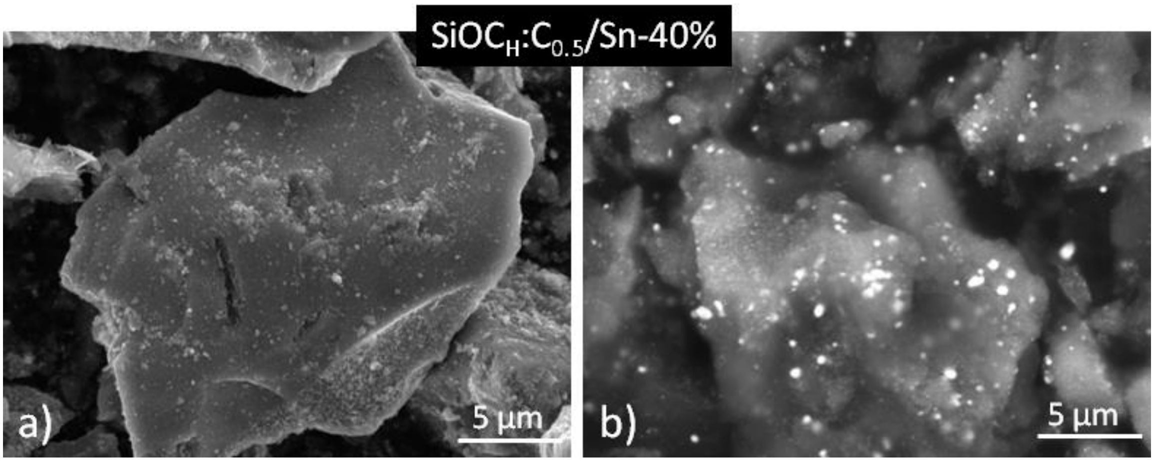

Figure 9.11. *SEM images of SiOC$_H$:C$_{0.5}$/Sn-40% sample, a) SE and b) BSE mode.*[298]

The electrochemical activity of SiOC$_H$:graphite/tin nanoparticles composites was tested through cyclic voltammetry measurements. The CV curves of SiOC$_H$:C$_{0.1}$/Sn-60%, SiOC$_H$:C$_{0.2}$/Sn-60%, SiOC$_H$:C$_{0.2}$/Sn-40% and the comparison of the 10th cycle of each of the materials are given in **Figure 9.12**. **Figure 9.12 a)** presents the CV curve with peaks designation. During the first cathodic peak, a long shoulder between 1.4 and 0.66 V appears, which corresponds to the creation of SEI on all components of the composites.[82,164,167,303] At a lower potential of ~0.46 V, a broad feature emerges, which corresponds to the creation of various Li_xSn_y alloys, in particular LiSn. In the following cycles that feature splits into two peaks with maxima at 0.32 V (Li_7Sn_2) and 0.61 (Li_2Sn_5).[213,227,303] At even lower potentials between 0.36 V and 0.005 V many processes occurs, which may be assigned to intercalation of lithium ions into the ceramic / graphite phases, further transformations of SEI layer and formation of high-lithium alloys.[164,271,304,305] During the reverse sweep, the three peaks at the 0.1, 0.17 and 0.24 V emerge, which correspond to the gradual deinsertion of lithium from graphite.[164,304] The following peaks placed between 0.3 and 0.9 V come from the gradual dealloying of lithium-tin alloys.[213] Finally, during the anodic sweep, a small broad peak at ~1.1 V appears, which could relate to the partial oxidation of small (~1 nm size) tin nanoparticles.[306,307] The electrochemical pattern remains the same for all the ternary composites, the only differences are in the peaks' height. The activity of graphite is the lowest for SiOC$_H$:C$_{0.1}$/Sn-60% sample, which is related to the lowest graphite content in the sample. On the other hand, the tin alloying peaks are the smallest for SiOC$_H$:C$_{0.2}$/Sn-40%. On the other hand, the tin alloying peaks are the smallest for SiOC$_H$:C$_{0.2}$/Sn-40%. These results suggest the current value corresponding to a certain electrochemical process is proportional to the fraction of corresponding component related to that process.

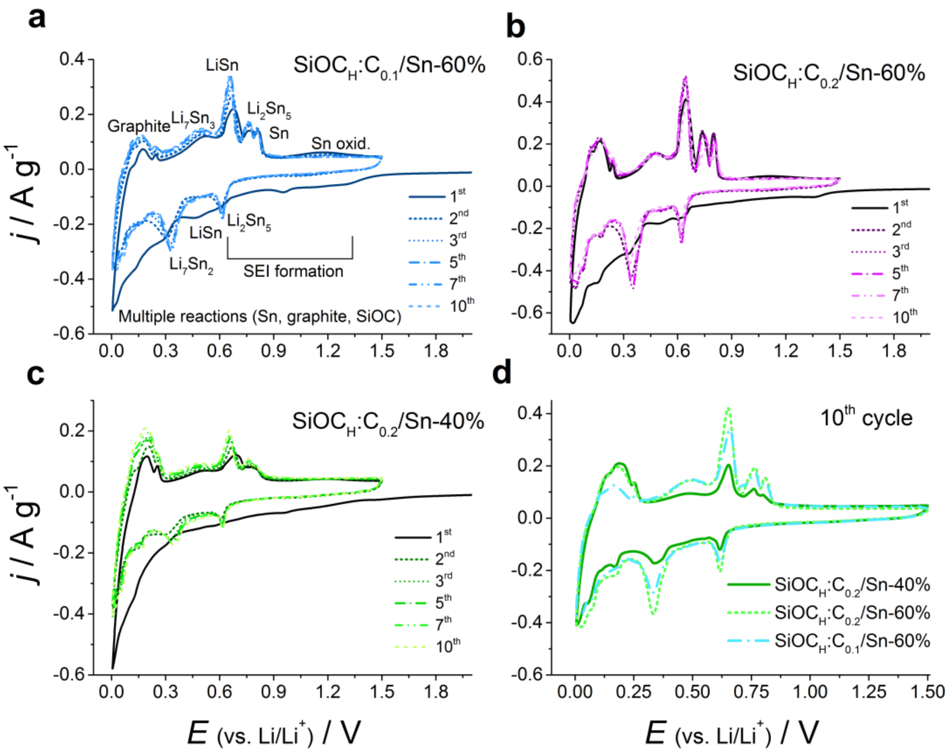

Figure 9.12. *Cyclic voltammetry curves for a) SiOC$_H$:C$_{0.1}$/Sn-60% (along with peaks assignment), b) SiOC$_H$:C$_{0.2}$/Sn-60%, c) SiOC$_H$:C$_{0.2}$/Sn-40% and d) the comparison of 10th cycle of ternary composites.*[298]

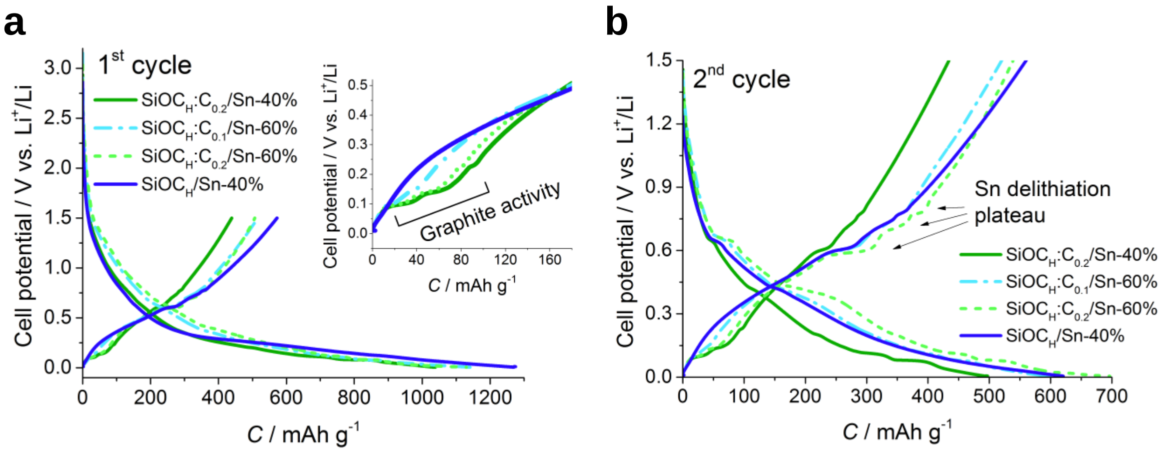

Figure 9.13. *Voltage profiles for the SiOC$_H$:graphite/tin nanoparticles composites: a) 1st cycle, b) 2nd cycle.*[298]

Figure 9.13 presents the first and second cycles of the voltage profiles for $SiOC_H$:graphite/nano-tin composites. The first lithiation curves of all studied materials exhibit a downward curve followed by quasi-plateau. No distinctive peaks are observed, which corresponds well to the CV curves. In the next cycles, multiple plateaux appear, which corresponds to the formation of tin alloys and intercalation of lithium ions into the graphite. The delithiation curves show the redox activities of graphite (**Figure 9.13 a) inset**) and tin (**Figure 9.13 b)**). The delithiation curves exhibit a sloping shape, which is typical for SiOCs. The voltage profiles correspond well to CV curves and confirm the electrochemical activity of all components. The first lithiation capacity depends on the material, and it is between 1000 – 1300 mAh g^{-1}, and drops by ~half of the value over the first few cycles. The first delithiation capacity was recorded as 439, 507 and 515 mAh g^{-1} for $SiOC_H:C_{0.2}$/Sn-40%, $SiOC_H:C_{0.2}$/Sn-60% and $SiOC_H:C_{0.1}$/Sn-60% composites, respectively, which translates into the FCE in the 0.005 V – 1.5 V potential range of ~45% (57-63% in the 0.005 V – 3 V potential range). Low FCE may be explained by the creation of complex SEI on the surface of tin, ceramic and graphite, and by irreversible reactions involving lithium ions.[55,296] The complex SEI formation is additionally enhanced by high SSA, which increases the length of the material/electrolyte contact area and therefore encourages higher Li^+ consumption.[308] The exact data for the first charging-discharging cycles are collected in **Table 9.4**.

Table 9.4. *Selected electrochemical results for SiOCs:graphite/tin nanoparticles composites. FCE η within 0.005 V-1.5 V and 0.005 V-3 V potential regions were calculated as a quotient of first lithiation capacity and first delithiation capacity obtained in certain potential region.*[298]

Material	1st cycle C_{irrev}/mAh g^{-1}	1st cycle C_{rev}/mAh g^{-1}	η (0.005 V-1.5 V) / %	η (0.005 V -3 V) / %
$SiOC_H:C_{0.2}$/Sn-40%	600	439	42	56,5
$SiOC_H:C_{0.2}$/Sn-60%	623	507	45	62
$SiOC_H:C_{0.1}$/Sn-60%	625	515	45	63
$SiOC_H$/Sn-40%	699	572	45	65

Figure 9.14 a) presents the cycling stability results of the ternary $SiOC_H$:graphite/tin nanoparticles composites obtained in 0.005 V – 3 V potential range. After initial few stabilisation cycles, the capacity of $SiOC_H:C_{0.2}$/Sn-60% and $SiOC_H:C_{0.1}$/Sn-60% reaches around 610 mAh g^{-1}, while the capacity of $SiOC_H:C_{0.2}$/Sn-40% stays around 480 mAh g^{-1}. These results suggest tin nanoparticles are the most efficient lithium storage site in the material, and increasing the tin content within the materials leads to capacity increase. During

the next lithiation-delithiation cycles, the capacity of $SiOC_H:C_{0.1}/Sn$-60% fades, while the cycle performance of $SiOC_H:C_{0.2}/Sn$-40% and $SiOC_H:C_{0.2}/Sn$-60% remains rather stable. Rapid capacity decrease of SiOCs/tin nanoparticles composites was reported as a result of rigid SiOCs matrix, which is a result of insufficient carbon content.[65] This was observed as an issue of samples where more than 40 wt% of the tin precursor was used with regard to the preceramic mixture.[294] Higher tin precursor content translates into lower SiOCs amount, which is a source of carbon and increases the intensity of carbothermal reduction. In the case of ternary $SiOC_H$:graphite/tin nanoparticles composites, rapid capacity fading was observed for $SiOC_H:C_{0.1}/Sn$-60%, but not for $SiOC_H:C_{0.2}/Sn$-60% (capacity retention of 52.7 vs. 86.5% over 100 cycles), which suggests graphite although does not protect the carbon from SiOCs phase from carbothermal reduction, it can provide softness and electrical conductivity, which may lead into an extension of electrochemical stability.

To give deeper insight on electrochemical properties of $SiOC_H$:graphite/tin nanoparticles composites, the materials were compared to $SiOC_H/Sn$-40%, which was claimed to be the best-performing SiOCs/tin nanoparticles sample according to Dubey et al.[66] The capacity recorded for $SiOC_H/Sn$-40% sample was ~520 mAh g^{-1} with stability above 90% over 100 cycles. The capacity of reference $SiOC_H/Sn$-40% is higher than $SiOC_H:C_{0.2}/Sn$-40%, but lower in contrast to $SiOC_H:C_{0.2}/Sn$-60%, while the capacity stability was similar. These results suggest the capacity of ternary composite material decreases with increasing graphite content but rises with a higher amount of tin. Nevertheless, as the study show, a certain amount of graphite is necessary to maintain good material stability.

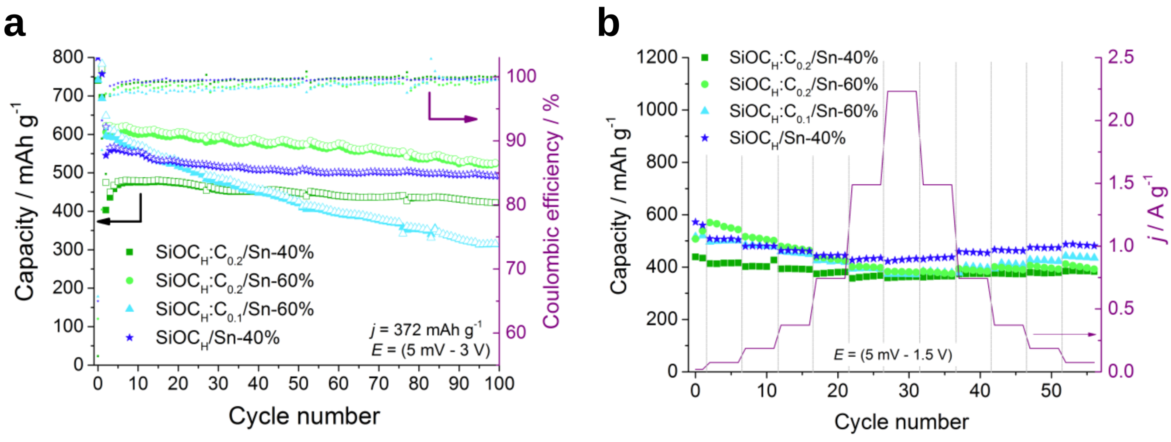

Figure 9.14. *a) Cycling stability measured at 1 C current rate and the corresponding Coulombic efficiencies, b) rate capability of the composite materials.*[298]

Figure 9.14 b) presents the rate capability results measured within 0.005V – 1.5 V potential range at current densities varying from C/2 to 6 C. At low current rates, the highest capacity was recorded for $SiOC_H$:$C_{0.2}$/Sn-60%. However, when the current rates were increased to higher values, the capacity values for ternary composites dropped more rapidly in comparison to binary $SiOC_H$/Sn-40%. After returning to low current rates the capacity was not regained. These results indicate samples containing graphite are more susceptible to high current rates. These results are consistent with the high-current response of each of the materials, i.e. graphite exhibits poor performance due to SEI formation and deformation, lithium plating, [175,309] while SiOC is stable at high current rates.[245,310,311] Interestingly, the high current behaviour was reminding the high current behaviour of $SiOC_{VTES}$/graphite composites rather than $SiOC_{PhTES}$/graphite. This is rationalized, as the ceramic is depleted from disordered carbon, which was consumed during carbothermal reduction.

The electrochemical behaviour of $SiOC_H$:graphite/tin nanoparticles composites was studied by SEM imaging and XRD of post-mortem samples and XRD. **Figure 9.15** presents the SEM images of $SiOC_H$/Sn-40%, $SiOC_H$:$C_{0.2}$/Sn-40% and $SiOC_H$:$C_{0.2}$/Sn-60% samples. The samples with 40% of tin precursor reveal a compact layer, while $SiOC_H$:$C_{0.2}$/Sn-60% exhibits some cracks. These results suggest higher tin content may lead to higher internal stresses during lithiation, which turns into some structural damage. The XRD diffractograms of investigated samples are shown in **Figure 9.16**. The diffractograms reveal the presence of multiple crystalline species like graphite, β-tin (from the composite materials), Li_2CO_3 and tin oxides (originating from SEI layer – see chapter 4) Li_2Sn_5 (one of the lowest lithiation states of Li-Sn alloys – see chapter 4) and Cu from current collector. The XRD patterns are quite complex but similar for all of the studied materials. Although some peaks may be assigned to a few species, one can see the peaks at ~43° and 50° are higher in the case of ternary composite in contrast to reference $SiOC_H$/Sn-40%. These results indicate that the SEI layer created on $SiOC_H$:graphite/tin nanoparticles composite is more complex in contrast to $SiOC_H$/tin nanoparticles material.

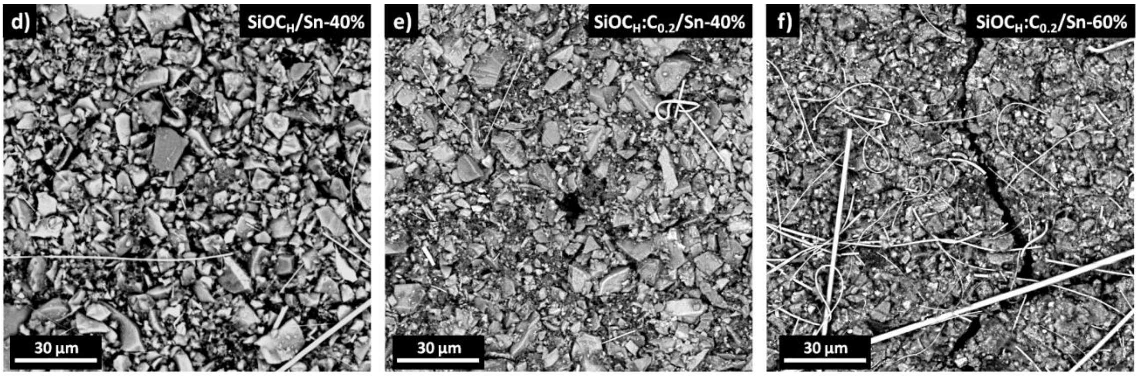

Figure 9.15. *SEM images of electrode layers after extended cycling tests (2 cycles at C/20 followed by 100 cycles at 1C) recorded for a) $SiOC_H$/Sn-40%, b) $SiOC_H:C_{0.2}$/Sn-40% and c) $SiOC_H:C_{0.2}$/Sn-60%.*[298]

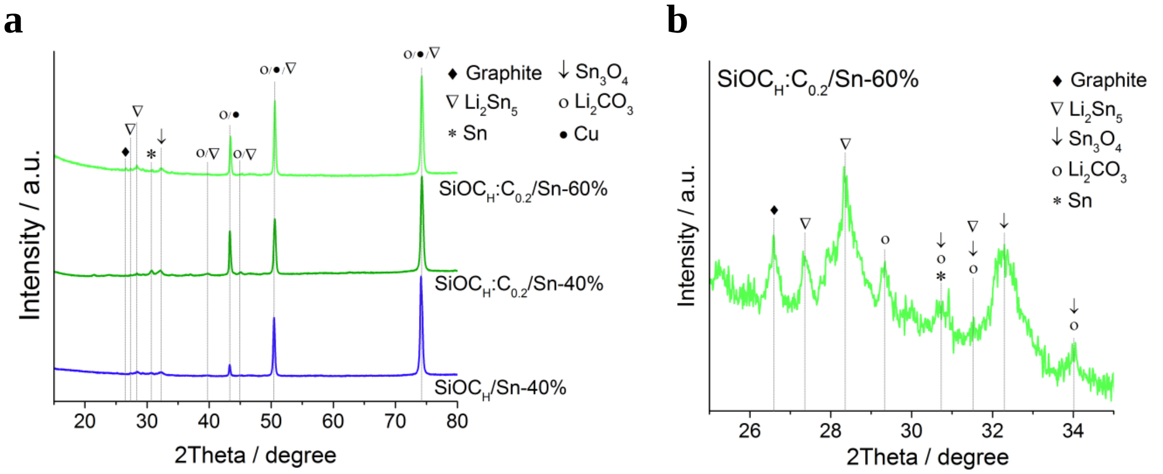

Figure 9.16. *a) XRD diffractograms of the cycled electrodes, b) the selected 2theta range of the XRD diffractogram of $SiOC_H:C_{0.2}$/Sn-60% composite.*[298]

9.3. Conclusions

In the last part of the work, ternary SiOCs:graphite/tin nanoparticles composites were investigated. The main idea was to assess the possibility of replacing part of the ceramic with graphite and simultaneously increase the tin content within the material. The results show that indeed the replacement of part of the ceramic by graphite allows for an increase of tin content. Unreacted SnO_x particles were not observed, and no bigger agglomerates were present. However, multiple techniques show that tin nanoparticles are formed mainly in the ceramic phase. These results indicate that carbon from the free carbon phase and SiOC tetrahedra are preferably consumed during carbothermal reduction over carbon coming from graphite. The most reasonable explanation is that tin octoate mixes well with the tin precursor, while it is not soaked into the graphite. Therefore, during the carbothermal reduction of SnO_2, tin nanoparticles are formed by oxidation of the “closest” carbon, i.e. carbon from SiOCs. However, there are traces of tin present on graphite particles and therefore graphite may be also consumed, although to a lesser degree.

The electrochemical results clearly show that the capacity values of the ternary (SiOC/graphite/Sn) and binary (SiOC/Sn) composites depend on the content of each component. Increasing the number of tin nanoparticles is profitable due to high theoretical capacity of lithium-tin alloy formation. On the other hand, graphite due to its softness, low volume expansion upon lithiation and good electrical conductivity, allows to accommodate stresses created upon tin lithiation and maintains electrical contact, which translates into good stability of the composite materials.

Final conclusions of the thesis

In this work, various SiOCs - based composites were synthesized and studied as potential anode materials for lithium-ion batteries. The main goal and motivation were to get a better understanding of the lithium storage mechanism, which may improve designing of high performance composites. The aim was also to correlate the chemical composition (elemental composition and ratio between the components) and microstructure of the materials with their electrochemical performance. The SiOCs-based composites were synthesized using various synthesis techniques: sol-gel, photocuring, and curing *via* hydrosilylation reaction. The composites with graphite were produced with the support of high-power ultrasounds. The addition of the sonication step allowed the uniform graphite distribution within the green body matrix and speed up the gelation and drying processes. As prepared green bodies were then pyrolysed to receive the final composite materials, and characterised using multiple techniques, like elemental analysis, Raman spectroscopy, XPS, XRD, solid state ^{29}Si MAS NMR, BET surface area analysis, TGA-DSC, FT-IR, imaging techniques like SEM, TEM, and electrochemical methods: galvanostatic charge-discharge, CV, and EIS.

The study on the binary SiOCs/graphite composites revealed that the graphite addition has a different effect depending on the free carbon content of the pure ceramic material. The $SiOC_{PhTES}$/graphite composites revealed the capacity, registered upon polarisation at low currents, is an arithmetic sum of the graphite and $SiOC_{PhTES}$, but the capacity values recorded at high C-rates are vastly improved. The best-performing $SiOC_{PhTES}$/graphite sample was the material with high graphite content, which is probably related to the good protection role of SiOCs ceramic. In contrast, $SiOC_{VTES}$/graphite composites showed the synergistic effect between SiOCs and graphite, which was manifested as very high capacity upon polarisation low with currents and high first cycle Coulombic efficiency. The high-C rate performance was also improved in comparison to pure $SiOC_{VTES}$ and graphite, but the improvement was smaller than in the case of $SiOC_{PhTES}$ composites.

The research on the binary $SiOC_{UV}$/tin nanocomposites, produced *via* the photocuring method revealed the benefits of creating such composites, compared to the photocuring of pure $SiOC_{UV}$. The obtained material not only was characterised by higher capacity at low and high C-rates, good stability, but also the post-pyrolysis material yield was higher than for pure

$SiOC_{UV}$ ceramic. This feature is explained as the catalysing role of tin octoate, which was used as a tin source. Tin octoate promotes the creation of links between preceramic polymer chains, leading to a higher crosslinking degree, which finally translated into higher mass yield. Good electrochemical properties are attributed to homogeneous tin nanoparticles distribution.

The investigation of ternary SiOCs:graphite/tin nanoparticles composites presented interesting chemical and electrochemical interactions between these three components. Characterisation study on tin nanoparticle formation *via* carbothermal reduction revealed the preferable source of carbon used in this reaction is originating from SiOCs, both free carbon phase and SiOC tetrahedral units. These results are related to the better mixing of tin source (tin octoate) with the preceramic mixture compared to the mixing with graphite, and with a higher activation energy of carbothermal reduction of SnO_x with graphite. This, in turn, leads to the accumulation of the tin nanoparticles mainly in the ceramic phase. The electrochemical properties of SiOCs:graphite/tin nanoparticles revealed, that it is possible to produce electrochemically stable nanocomposite based on SiOCs, graphite and tin nanoparticles, where tin precursor was used in greater amount than 40 wt% (based on the mass of composite green body). The improved stability is related to the presence of graphite which provides electric conductivity, and, due to softness and low expansion upon lithiation, helps to accommodate stresses created during tin alloying with lithium. The graphite content has to be limited, as it leads to the formation of bigger particles, which worsens the properties of the material upon cycling with high C-rates.

As a final remark, combining SiOCs with graphite and/or tin leads to very interesting outcomes in terms of structural and electrochemical properties. The good material characteristic makes them promising for future battery application. To maximize the electrochemical performance, careful selection of SiOCs precursors, tin sources, graphite and ratios between these components, as well as a proper choice of synthesis route has to be conducted.

Future perspective

The present work reports the electrochemical performance and structural characteristics of composite materials based on SiOCs, graphite and tin nanoparticles. This thesis attempts to explain the interactions between these components in the preparation stage and in the final composite material.

One may understand, research conducted and information obtained during this work was time and resource-limited, and therefore some conclusions may be overstated. Thus it is highly recommended to continue the work on these materials to get a better picture of the properties and to draw general conclusions. For the SiOCs/graphite composites, it will be very profitable to conduct more sophisticated measurements, like the scanning electrochemical microscopy (SECM) and operando ^{6}Li NMR spectroscopy to discover the electrochemical activities of each of the components, which could help to understand better the electrochemical propertie and lithium staorage mechanism. Moreover, characterisation test conducted on ceramic material synthesized using the same method, but with tetraethylhydrosiloxane as a preceramic precursor could reveal more information about the interactions between graphite and ceramic phase, as the ceramic obtained from tetraethylhydrosiloxane does not contain free carbon nor SiOC tetrahedra. In addition, tests missing in this work like hardness and electrical conductivity may also be very helpful to understand the properties.

The above suggestion could be applied to SiOCs/tin nanoparticles and SiOCs:graphite/tin nanoparticles composites as well, but here few words could be added. The main focus of SiOCs/tin nanoparticles composite in that work was put on the utilisation of commercially available resin, and simple, one-step synthesis method. Further work concerning SiOCs/tin nanoparticles might be focused on lowering the price by searching for cheaper preceramic polymers and tin salts, as well as the additive manufacturing of the anode using i.e. 3D printer. As for SiOCs:graphite/tin nanoparticles, the author’s interest focuses on the utilisation of other types of carbon additives like polystyrene or acenaphthylene. In addition, employing carbon black might also be profitable, as it has one of the lowest activation energy towards carbothermal reduction of tin oxide among various carbon forms.

References

1. *Handbook on Battery Energy Storage System*. (Asian Development Bank, 2018).
2. Grand View Research. Battery Market Size, Share & Trends Analysis Report By Product (Lead Acid, Li-ion, Nickle Metal Hydride, Ni-cd), By Application (Automotive, Industrial, Portable), By Region, And Segment Forecasts, 2020 - 2027. 1–4 (2019).
3. Lithium-Ion Battery Market with COVID-19 Impact Analysis, by Type (Li-NMC, LFP, LCO, LTO, LMO, NCA), Capacity, Voltage, Industry (Consumer Electronics, Automotive, Power, Industrial), & Region (North America, Europe, APAC & RoW) - Global Forecast to 2030,. https://www.marketsandmarkets.com/Market-Reports/lithium-ion-battery-market-49714593.html?gclid=Cj0KCQjwwr32BRD4ARIsAAJNf_1Mvxs-VJ5PC6-_sdGZirF6GU-A9cG47g9qHggY83bZyPO-t70L2scaAnGXEALw_wcB. [Accessed 28 May 2020].
4. Scott, A. In the battery materials world, the anode’s time has come, https://cen.acs.org/materials/energy-storage/battery-materials-world-anodes-time/97/i14; [accessed September 2021].
5. The Faraday Institution report. High-Energy Battery Technologies. 1–20 (2020).
6. Choi, J. W. & Aurbach, D. Promise and reality of post-lithium-ion batteries with high energy densities. *Nat. Rev. Mater.* **1**, 1 (2016).
7. Liu, Z. *et al.* Silicon oxides: A promising family of anode materials for lithium-ion batteries. *Chem. Soc. Rev.* **48**, 285–309 (2019).
8. Jiao, M. *et al.* High-capacity SiOx ($0 \leq x \leq 2$) as promising anode materials for next-generation lithium-ion batteries. *J. Alloys Compd.* **842**, 155774 (2020).
9. Ralf Riedel, I.-W. C. *Ceramics Science and Technology, Volume 3: Synthesis and Processing*. (Wiley Online Library, 2011).
10. Definition of lithium-ion battery, https://www.merriam-webster.com/dictionary/lithium-ion%20battery; [accesse December 2021].
11. Wu, F., Maier, J. & Yu, Y. Guidelines and trends for next-generation rechargeable lithium and lithium-ion batteries. *Chem. Soc. Rev.* **49**, 1569–1614 (2020).
12. Goonan, T. G. Lithium use in batteries: U.S. Geological Survey Circular 1371. 8 (2012).
13. Wong, K. W. & Chow, W. K. Principle for the Working of the Lithium-Ion Battery. *J. Mod. Phys.* **11**, 1743–1750 (2020).
14. Linden, D., Reddy, T. B., Beard, K. W., Croce, F. & Salomon, M. *Linden’s Handbook of Batteries. Fifth edition*. (McGraw-Hill Education, 2019).
15. Battery Univeristy. Select between maximum runtime, long service life, small size and low cost, https://batteryuniversity.com/article/bu-107-comparison-table-of-secondary-batteries; [accessed November 2021]
16. Deng, D. Li-ion batteries: Basics, progress, and challenges. *Energy Sci. Eng.* **3**, 385–418 (2015).
17. Chen, Y. *et al.* A review of lithium-ion battery safety concerns: The issues, strategies, and testing standards. *J. Energy Chem.* **59**, 83–99 (2021).
18. Lee, A. 4.5µA Li-Ion Battery Protection Circuit, https://www.analog.com/en/technical-

articles/battery-protection-circuit.html [accessed November 2021].

19. Yazami, R. & Maher, K. Thermodynamics of Lithium-Ion Batteries. in *Lithium-Ion Batteries: Advances and Applications* (ed. Pistoia, G.) 567–569 (Elsevier, 2014). doi:10.1016/B978-0-444-59513-3.00025-X.
20. Massé, R. C., Liu, C., Li, Y., Mai, L. & Cao, G. Energy storage through intercalation reactions: Electrodes for rechargeable batteries. *Natl. Sci. Rev.* **4**, 26–53 (2017).
21. Bruce, P. G. Energy storage beyond the horizon: Rechargeable lithium batteries. *Solid State Ionics* **179**, 752–760 (2008).
22. Niedzicki, L. *et al.* Modern generation of polymer electrolytes based on lithium conductive imidazole salts. *J. Power Sources* **192**, 612–617 (2009).
23. Niedzicki, L. *et al.* New type of imidazole based salts designed specifically for lithium ion batteries. *Electrochim. Acta* **55**, 1450–1454 (2010).
24. Pandur, Z., Šušnjar, M. & Bačić, M. Battery technology – use in forestry. *Croat. J. For. Eng.* **42**, 135–148 (2021).
25. Rubino, R. S., Gan, H. & Takeuchi, E. S. A Study of Capacity Fade in Cylindrical and Prismatic Lithium-Ion Batteries. *J. Electrochem. Soc.* **148**, A1029 (2001).
26. Cylindrical vs prismatic batteries comparison, https://www.lithiumion-batteries.com/cylindrical-vs-prismatic-cells.php [accessed November 2021]
27. Compare the pros and cons of the cylindrical cell, button cell, prismatic cell and pouch, https://batteryuniversity.com/article/bu-301a-types-of-battery-cells [accessed November 2021]
28. Colombo, P., Mera, G., Riedel, R. & Sorarù, G. D. Polymer-derived ceramics: 40 Years of research and innovation in advanced ceramics. *J. Am. Ceram. Soc.* **93**, 1805–1837 (2010).
29. Zz, P. Common examples of preceramic polymer families, https://commons.wikimedia.org/w/index.php?curid=105099549; [accessed: February 2022].
30. Jones, R. G., Ando, W. & J, C. *Silicon containing Polymers: The science and Technology of their synthesis.* (Springer Science & Business Media, 2000).
31. Soraru, G. D., Babonneau, F. & Mackenzie, J. D. Structural evolutions from polycarbosilane to SiC ceramic. *J. Mater. Sci.* **25**, 3886–3893 (1990).
32. Stabler, C., Ionescu, E., Graczyk-Zajac, M., Gonzalo-Juan, I. & Riedel, R. Silicon oxycarbide glasses and glass-ceramics: “All-Rounder” materials for advanced structural and functional applications. *J. Am. Ceram. Soc.* **101**, 4817–4856 (2018).
33. Saha, A., Raj, R. & Williamson, D. L. A model for the nanodomains in polymer-derived SiCO. *J. Am. Ceram. Soc.* **89**, 2188–2195 (2006).
34. Widgeon, S. J. *et al.* 29Si and 13C Solid-state NMR spectroscopic study of nanometer-scale structure and mass fractal characteristics of amorphous polymer derived silicon oxycarbide ceramics. *Chem. Mater.* **22**, 6221–6228 (2010).
35. Wen, Q., Yu, Z. & Riedel, R. The fate and role of in situ formed carbon in polymer-derived ceramics. *Prog. Mater. Sci.* **109**, 100623 (2020).
36. Stabler, C. *et al.* Thermal properties of SiOC glasses and glass ceramics at elevated temperatures. *Materials* **11**, 1–18 (2018).
37. Rouxel, T., Massouras, G. & Sorarù, G. D. High temperature behavior of a gel-derived SiOC glass: Elasticity and viscosity. *J. Sol-Gel Sci. Technol.* **14**, 87–94 (1999).

38. Mazo, M. A., Tamayo, A., Caballero, A. C. & Rubio, J. Electrical and thermal response of silicon oxycarbide materials obtained by spark plasma sintering. *J. Eur. Ceram. Soc.* **37**, 2011–2020 (2017).
39. Colombo, P. *Polymer Derived Ceramics: From Nano-structure to Applications*. (DEStech Publication, 2010).
40. Cordelair, J. & Greil, P. Electrical conductivity measurements as a microprobe for structure transitions in polysiloxane derived Si-O-C ceramics. *J. Eur. Ceram. Soc.* **20**, 1947–1957 (2000).
41. Wilson, A. M., Reimers, J. N., Fuller, E. W. & Dahn, J. R. Lithium insertion in pyrolyzed siloxane polymers. *Solid State Ionics* **74**, 249–254 (1994).
42. Xing, W., Wilsonb, A. M., Zank, G. & Dahn, J. R. Pyrolyzed pitch-polysilane blends for use as anode materials in lithium ion batteries. *Solid State Ionics* **93**, 239–244 (1997).
43. Wilson, A. M., Xing, W., Zank, G., Yates, B. & Dahn, J. R. Pyrolysed pitch-polysilane blends for use as anode materials in lithium ion batteries II: The effect of oxygen. *Solid State Ionics* **100**, 259–266 (1997).
44. Fukui, H., Ohsuka, H., Hino, T. & Kanamura, K. A Si-O-C composite anode: High capability and proposed mechanism of lithium storage associated with microstructural characteristics. *ACS Appl. Mater. Interfaces* **2**, 999–1008 (2010).
45. Fukui, H., Harimoto, Y., Akasaka, M. & Eguchi, K. Lithium Species in Electrochemically Lithiated and Delithiated Silicon Oxycarbides. *Appl. Mater. Interfaces* **6**, 12827–12836 (2014).
46. Liu, X., Xie, K., Zheng, C., Wang, J. & Jing, Z. Si-O-C materials prepared with a sol e gel method for negative electrode of lithium battery. *J. Power Sources* **214**, 119–123 (2012).
47. Fukui, H. *et al.* Lithiation and delithiation of silicon oxycarbide single particles with a unique microstructure. *ACS Appl. Mater. Interfaces* **3**, 2318–2322 (2011).
48. Sanchez-Jimenez, P. E. & Raj, R. Lithium Insertion in Polymer-Derived Silicon Oxycarbide Ceramics. *J. Am. Ceram. Soc.* **93**, 1127–1135 (2010).
49. Ahn, D. & Raj, R. Cyclic stability and C-rate performance of amorphous silicon and carbon based anodes for electrochemical storage of lithium. *J. Power Sources* **196**, 2179–2186 (2011).
50. Ahn, D. & Raj, R. Thermodynamic measurements pertaining to the hysteretic intercalation of lithium in polymer-derived silicon oxycarbide. *J. Power Sources* **195**, 3900–3906 (2010).
51. Liu, X., Zheng, M. C. & Xie, K. Mechanism of lithium storage in Si-O-C composite anodes. *J. Power Sources* **196**, 10667–10672 (2011).
52. Liao, N., Zheng, B., Zhang, M. & Xue, W. Atomic investigation on reversible lithium storage in amorphous silicon oxycarbide as a high power anode material. *J. Mater. Chem. A* **4**, 12328–12333 (2016).
53. Kroll, P. Tracing Reversible and Irreversible Li Insertion in SiCO Ceramics with Modeling and Ab-Initio Simulations. *MRS Proc.* **1313**, mrsf10–1313-kk11–07 (2011).
54. Pradeep, V. S., Graczyk-Zajac, M., Riedel, R. & Soraru, G. D. New insights in to the lithium storage mechanism in polymer derived SiOC anode materials. *Electrochim. Acta* **119**, 78–85 (2014).
55. Graczyk-Zajac, M. *et al.* New insights into understanding irreversible and reversible

lithium storage within SIOC and SICN ceramics. *Nanomaterials* **5**, 233–245 (2015).

56. Wilamowska, M., Pradeep, V. S., Graczyk-Zajac, M., Riedel, R. & Soraruù, G. D. Tailoring of SiOC composition as a way to better performing anodes for Li-ion batteries. *Solid State Ionics* **260**, 94–100 (2014).
57. Liao, N., Zhang, M., Zheng, B. & Xue, W. Understanding the high rate lithium storage capabilities of SiCO-derived porous carbon. *Appl. Mater. Today* 1–7 (2019) doi:10.1016/j.apmt.2019.07.010.
58. Fukui, H., Eguchi, K., Ohsuka, H., Hino, T. & Kanamura, K. Structures and lithium storage performance of Si-O-C composite materials depending on pyrolysis temperatures. *J. Power Sources* **243**, 152–158 (2013).
59. Pradeep, V. S., Graczyk-Zajac, M., Wilamowska, M., Riedel, R. & Soraru, G. D. Influence of pyrolysis atmosphere on the lithium storage properties of carbon-rich polymer derived SiOC ceramic anodes. *Solid State Ionics* **262**, 22–24 (2014).
60. Ding, H. & Demkowicz, M. J. Hydrogen reverses the clustering tendency of carbon in amorphous silicon oxycarbide. *Sci. Rep.* **5**, 1–8 (2015).
61. Bawane, K., Erb, D. & Lu, K. Carbon content and pyrolysis atmosphere effects on phase development in SiOC systems. *J. Eur. Ceram. Soc.* **39**, 2846–2854 (2019).
62. Kaspar, J., Graczyk-Zajac, M. & Riedel, R. Lithium insertion into carbon-rich SiOC ceramics: Influence of pyrolysis temperature on electrochemical properties. *J. Power Sources* **244**, 450–455 (2013).
63. Kaspar, J., Graczyk-Zajac, M., Lauterbach, S., Kleebe, H. J. & Riedel, R. Silicon oxycarbide/nano-silicon composite anodes for Li-ion batteries: Considerable influence of nano-crystalline vs. nano-amorphous silicon embedment on the electrochemical properties. *J. Power Sources* **269**, 164–172 (2014).
64. Liu, X., Xie, K., Wang, J., Zheng, C. & Pan, Y. Si/Si-O-C composite anode materials exhibiting good C rate performances prepared by a sol-gel method. *J. Mater. Chem.* **22**, 19621–19624 (2012).
65. Kaspar, J. *et al.* Stable SiOC/Sn nanocomposite anodes for lithium-ion batteries with outstanding cycling stability. *Adv. Funct. Mater.* **24**, 4097–4104 (2014).
66. Dubey, R. J. C. *et al.* Silicon Oxycarbide—Tin Nanocomposite as a High-Power-Density Anode for Li-Ion Batteries. *Adv. Sci.* **6**, (2019).
67. Tolosa, A., Widmaier, M., Krüner, B., Griffin, J. M. & Presser, V. Continuous silicon oxycarbide fiber mats with tin nanoparticles as a high capacity anode for lithium-ion batteries. *Sustain. Energy Fuels* **2**, 215–228 (2018).
68. Behera, S. K. & Raj, R. Extreme-rate capable and highly stable SiCO-TiO2 hybrids for Li ion battery anodes. *Chem. Commun.* **49**, 9657–9659 (2013).
69. Dey, S., Mujib, S. Bin & Singh, G. Enhanced Li-Ion Rate Capability and Stable Efficiency Enabled by MoSe 2 Nanosheets in Polymer-Derived Silicon Oxycarbide Fiber Electrodes. *Nanomaterials* **12**, 553 (2022).
70. Fukui, H., Ohsuka, H., Hino, T. & Kanamura, K. Influence of polystyrene/phenyl substituents in precursors on microstructures of Si-O-C composite anodes for lithium-ion batteries. *J. Power Sources* **196**, 371–378 (2011).
71. Fukui, H., Ohsuka, H., Hino, T. & Kanamura, K. Polysilane/acenaphthylene blends toward Si-O-C composite anodes for rechargeable lithium-ion batteries. *J. Electrochem. Soc.* **158**, 550–555 (2011).
72. Liu, G., Kaspar, J., Reinold, L. M., Graczyk-Zajac, M. & Riedel, R. Electrochemical

performance of DVB-modified SiOC and SiCN polymer-derived negative electrodes for lithium-ion batteries. *Electrochim. Acta* **106**, 101–108 (2013).

73. Sang, Z. *et al.* A graphene-modified flexible SiOC ceramic cloth for high-performance lithium storage. *Energy Storage Mater.* **25**, 876–884 (2020).
74. David, L., Bhandavat, R., Barrera, U. & Singh, G. Silicon oxycarbide glass-graphene composite paper electrode for long-cycle lithium-ion batteries. *Nat. Commun.* **7**, 10998 (2016).
75. Shao, G. *et al.* Polymer derived SiOC integrated with graphene aerogel as highly stable Li-ion battery anodes. *ACS Appl. Mater. Interfaces* **12**, 46045–46056 (2020).
76. Bhandavat, R. & Singh, G. Stable and efficient li-ion battery anodes prepared from polymer-derived silicon oxycarbide-carbon nanotube shell/core composites. *J. Phys. Chem. C* **117**, 11899–11905 (2013).
77. Li, Y. *et al.* One-dimensional SiOC/C composite nanofibers as binder-free anodes for lithium-ion batteries. *J. Power Sources* **254**, 33–38 (2014).
78. Sang, Z. *et al.* SiOC nanolayer wrapped 3D interconnected graphene sponge as a high-performance anode for lithium ion batteries. *J. Mater. Chem. A* **6**, 9064–9073 (2018).
79. Zhu, G. *et al.* Boron doping-induced interconnected assembly approach for mesoporous silicon oxycarbide architecture. *Natl. Sci. Rev.* **8**, nwaa152 (2021).
80. Dibandjo, P., Graczyk-Zajac, M., Riedel, R., Pradeep, V. S. & Soraru, G. D. Lithium insertion into dense and porous carbon-rich polymer-derived SiOC ceramics. *J. Eur. Ceram. Soc.* **32**, 2495–2503 (2012).
81. Xia, K. *et al.* Carbon-enriched SiOC ceramics with hierarchical porous structure as anodes for lithium storage. *Electrochim. Acta* **372**, 137899 (2021).
82. Xia, K. *et al.* Effect of KOH etching on the structure and electrochemical performance of SiOC anodes for lithium-ion batteries. *Electrochim. Acta* **245**, 287–295 (2017).
83. Ma, M. *et al.* High rate capabilities of HF-etched SiOC anode materials derived from polymer for lithium-ion batteries. *RSC Adv.* **6**, 43316–43321 (2016).
84. Bansal, N. P. *Handbook of Ceramic Composites*. (Springer Science & Business Media, 2005).
85. Jousseaume, V. *et al.* Comparison Between E-beam and Ultraviolet Curing to Perform Porous a-SiOC:H. *J. Electrochem. Soc.* **154**, G103 (2007).
86. Hofmann, R. J., Vlatkovic, M. & Wiesbrock, F. Fifty years of hydrosilylation in polymer science: A review of current trends of low-cost transition-metal and metal-free catalysts, non-thermally triggered hydrosilylation reactions, and industrial applications. *Polymers (Basel).* **9**, (2017).
87. Wang, L., Lu, K. & Ma, R. Effects of different polymer precursors on the characteristics of SiOC bulk ceramics. *Appl. Phys. A Mater. Sci. Process.* **125**, 1–13 (2019).
88. Blum, Y. D. & McDermott, G. A. DEHYDROCOUPLING TREATMENT AND HYDROSLYLATION OF SILICON CONTAINING POLYMERS, AND COMPOUNDS AND ARTICLES PRODUCED THEREBY. (1999).
89. Kakimoto, K. I., Wakai, F., Bill, J. & Aldinger, F. Synthesis of Si-C-O bulk ceramics with various chemical compositions from polycarbosilane. *J. Am. Ceram. Soc.* **82**, 2337–2341 (1999).
90. Okamura, K. & Seguchi, T. Application of radiation curing in the preparation of polycarbosilane-derived SiC fibers. *J. Inorg. Organomet. Polym.* **2**, 171–179 (1992).

91. Cubbon, R. C. P. *Polymeric Precursors for Ceramic Materials*. (Rapra technology LTD., 1994).
92. Yive, S. C. K., Corriu, R. J. P., Leclercq, D., Mutin, P. H. & Vioux, A. Silicon Carbonitride from Polymeric Precursors: Thermal Cross-Linking and Pyrolysis of Oligosilazane Model Compounds. *Chem. Mater.* **4**, 141–146 (1992).
93. de Hazan, Y. & Penner, D. SiC and SiOC ceramic articles produced by stereolithography of acrylate modified polycarbosilane systems. *J. Eur. Ceram. Soc.* **37**, 5205–5212 (2017).
94. Martínez-Crespiera, S., Ionescu, E., Kleebe, H. J. & Riedel, R. Pressureless synthesis of fully dense and crack-free SiOC bulk ceramics via photo-crosslinking and pyrolysis of a polysiloxane. *J. Eur. Ceram. Soc.* **31**, 913–919 (2011).
95. Gian, P., Sorarù, D., Gian, P. & Sorarù, D. Synthesis and Characterization of Multifunctional Polymer- Derived SiOCN Synthesis and Characterization of Multifunctional Polymer- Derived SiOCN Van Lam Nguyen Approved by : Ph . D . Commission : (2015).
96. Kumar, A. *et al.* Sol-Gel Derived Nanomaterials and It ' s Applications : A Review. *Res. J. Chem. Sci.* **5**, 98–105 (2015).
97. Hench, L. L. & West, J. K. The Sol-Gel Process. *Chem. Rev.* **90**, 33–72 (1990).
98. Brinker, C. J. & Scherer, G. W. *Sol-Gel Science*. (Academic Press, inc., 1990). doi:10.1186/1471-2105-8-444.
99. Young, S. K. Overview of Sol-Gel Science and Technology. *Army Res. Lab.* 1–17 (2002).
100. M. Makarska-Białokoz; A. Lipke; M. Majdan. Zastosowanie metody zol-żel do immobilizacji związków porfirynowych w matrycach krzemionkowych . Cz . II . Przykłady wykorzystania. *Przem. Chem.* **91**, 511–516 (2012).
101. Levy, D. & Zayat, M. *The Sol-Gel Handbook: Synthesis, Characterization, and Applications*. (Wiley-VCH, 2015).
102. Liu, C. *et al.* High temperature structure evolution of macroporous SiOC ceramics prepared by a sol-gel method. *Ceram. Int.* **41**, 11091–11096 (2015).
103. The history of graphite - Empowering pumps and equipment, https://empoweringpumps.com/egc-flexible-graphite-sealing/; [accessed October 2021].
104. Pierson, H. O. *Handbook of Carbon, Graphite, Diamonds and Fullerenes: Properties, Processing and Applications*. 43–63 (Noyes Publication, 1993).
105. Sengupta, R., Bhattacharya, M., Bandyopadhyay, S. & Bhowmick, A. K. A review on the mechanical and electrical properties of graphite and modified graphite reinforced polymer composites. *Prog. Polym. Sci.* **36**, 638–670 (2011).
106. Delhaes, P. *Graphite and Precursors*. (Overseas Publishers Associacion N.V., 2001).
107. Kobayashi, Y., Fukui, K. I., Enoki, T., Kusakabe, K. & Kaburagi, Y. Observation of zigzag and armchair edges of graphite using scanning tunneling microscopy and spectroscopy. *Phys. Rev. B - Condens. Matter Mater. Phys.* **71**, 2–5 (2005).
108. Dresselhaus, M. S. & Kalish, R. Carbon Materials: Graphite, Diamond and Others. in *Ion Implantation in Diamond, Graphite and Related Material* 3–25 (Springer-Verlag, 1992).
109. Kan, E., Li, Z. & Yang, J. Graphene Nanoribbons: Geometric, Electronic, and Magnetic Properties. in *Physics and Applications of Graphene - Theory* 332 (2011).

doi:10.5772/14112.

110. Liu, R., Chi, Y., Fang, L., Tang, Z. & Yi, X. Synthesis of carbon nanowall by plasma-enhanced chemical vapor deposition method. *J. Nanosci. Nanotechnol.* **14**, 1647–1657 (2014).
111. Kolmogorov, A. N. & Crespi, V. H. Registry-dependent interlayer potential for graphitic systems. *Phys. Rev. B - Condens. Matter Mater. Phys.* **71**, 235415 (2005).
112. Structures and properties, https://www.bbc.co.uk/bitesize/guides/zjfkw6f/revision/3; [accessed October 2021]
113. Klemens, P. G. & Pedraza, D. F. Thermal conductivity of graphite in the basal plane. *Carbon N. Y.* **32**, 735–741 (1994).
114. Sun, K., Stroscio, M. A. & Dutta, M. Graphite C-axis thermal conductivity. *Superlattices Microstruct.* **45**, 60–64 (2009).
115. Gupta, B. K., Janting, J. & Sørensen, G. Friction and wear characteristics of ion-beam modified graphite coatings. *Tribol. Int.* **27**, 139–143 (1994).
116. Focusgraphite. BATTERY-READY NATURAL GRAPHITE. (2015).
117. 本川健一, 河井隆伸, 片岡恭子 & 脇阪敬. Method for producing negative electrode material for high performance lithium ion secondary battery using natural graphite. (2002).
118. Zaghib, K. *et al.* Surface preparation of natural graphite and the effect of impurities on grinding and the particle distribution. (2007).
119. Syrah Resources Ltd. Battery anode succesfully produced from coated balama spherical graphite. (2015).
120. Hayes, T. Graphite for batteries. *Edison Report on Metals and Mining* 1–15 (2016).
121. Northern Graphite Corporation. Annual Information Form for the Year Ended December 31, 2013. 38 (2018).
122. ECO graph. Kibaran starts feasibility study on production of lithium-ion battery grade graphite, https://www.dgap.de/dgap/News/corporate/kibaran-starts-feasibility-study-production-lithiumion-battery-grade-graphite/?companyID=383553&newsID=963527; [accessed October 2021]
123. Moradi, B. & Botte, G. G. Recycling of graphite anodes for the next generation of lithium ion batteries. *J. Appl. Electrochem.* **46**, 123–148 (2016).
124. Peil, R. Battery Grade Graphite: It’s Not All About Carbon. (2020).
125. Jara, A. D., Betemariam, A., Woldetinsae, G. & Kim, J. Y. Purification, application and current market trend of natural graphite: A review. *Int. J. Min. Sci. Technol.* **29**, 671–689 (2019).
126. Banek, N. A., Abele, D. T., McKenzie Jr, K. & Wagner, M. J. Sustainable, Inexpensive Synthesis of High Purity Graphite from Biomass with Excellent Performance in Li-Ion Battery Anodes. *{ECS} Meet. Abstr.* **MA2017-02**, 2282 (2017).
127. Hosokawa Micron Corp. LIB Anode, Graphite, https://www.hosokawamicron.co.jp/en/product/industries/detail/253.html; [accessed October 2021]
128. 高博, 姜银珠, 王伟, 赵夫涛 & 李俊峰. Graphite spheroidization method and production system thereby. (2012).
129. Keller Lufttechnik Benelux. A popular choice: EIRICH systems for the preparation of compounds for graphite electrodes; https://www.keller.be/en/news/a-popular-choice-

eirich-systems-for-the-preparation-of-compounds-for-graphite-electrodes [accessed February 2022]

130. Takanobu, K., Ken-ichi, H., Hayato, M. & Kazuaki, Y. Negative electrode active material for lithium ion rechargeable battery and negative electrode using the same. (2007).

131. Slavnich, D. Imerys Graphite & Carbon acquires CVD coating technology, https://www.enginetechnologyinternational.com/news/metallurgy/imerys-graphite-carbon-acquires-cvd-coating-technology.html; [accessed February 2022]

132. Dresselhaus, M. S. & Dresselhaus, G. Advances in Physics Intercalation compounds of graphite. *Adv. Phys.* **51**, 1–186 (1981).

133. Schlögl, R. Graphite — A Unique Host Lattice. in *Progress in Intercalation Research* 83–90 (Springer, 1994). doi:10.1007/978-94-011-0890-4_2.

134. Moriwake, H., Kuwabara, A., Fisher, C. A. J. & Ikuhara, Y. Why is sodium-intercalated graphite unstable? *RSC Adv.* **7**, 36550–36554 (2017).

135. Lin, S.-Y. *et al.* Essential Properties of Li/Li+ Graphite-Intercalation Compounds. in *Green Energy Materials Handbook* 37–63 (CRC Press LLC, 2019). doi:10.1201/9780429466281-3.

136. Wen, Y. *et al.* Expanded graphite as superior anode for sodium-ion batteries. *Nat. Commun.* **5**, 4033 (2014).

137. Rüdorff, W. & Hofmann, U. Über Graphitsalze. *Zeitschrift für Anorg. und Allg. Chemie* **238**, 1–50 (1938).

138. Ulrich, H. & Walter, R. THE FORMATION OF SALTS FROM GRAPHITE BY STRONG ACIDS. *Trans. Faraday Soc.* **34**, 1017–1021 (1938).

139. Daumas, N. & Herold, A. Relations between phase concept and reaction mechanics in graphite insertion compounds. *C. R. Acad. Sci. Ser C* **268**, 373 (1969).

140. Kirczenow, G. Interference phenomena in the theory of Daumas-Hérold domain walls. *Phys. Rev. Lett.* **49**, 1853–1856 (1982).

141. Krishnan, S. *et al.* Revisiting the domain model for lithium intercalated graphite. *Appl. Phys. Lett.* **103**, 251904 (2013).

142. Kühne, M. *et al.* Reversible superdense ordering of lithium between two graphene sheets. *Nature* **564**, 234–239 (2018).

143. Levi, M. D., Levi, E. A. & Aurbach, D. The mechanism of lithium intercalation in graphite film electrodes in aprotic media. Part 2. Potentiostatic intermittent titration and in situ XRD studies of the solid-state ionic diffusion. *J. Electroanal. Chem.* **421**, 89–97 (1997).

144. Kühne, M. *et al.* Ultrafast lithium diffusion in bilayer graphene. *Nat. Nanotechnol.* **12**, 895–900 (2017).

145. Sole, C., Drewett, N. E. & Hardwick, L. J. Insitu Raman study of lithium-ion intercalation into microcrystalline graphite. *Faraday Discuss.* **172**, 223–237 (2014).

146. Heß, M. & Novák, P. Shrinking annuli mechanism and stage-dependent rate capability of thin-layer graphite electrodes for lithium-ion batteries. *Electrochim. Acta* **106**, 149–158 (2013).

147. Billaud, D., Henry, F. X., Lelaurain, M. & Willmann, P. Revisited structures of dense and dilute stage II lithium-graphite intercalation compounds. *J. Phys. Chem. Solids* **57**, 775–781 (1996).

148. Billaud, D. & Henry, F. X. Structural studies of the stage III lithium-graphite

intercalation compound. *Solid State Commun.* **124**, 299–304 (2002).

149. OHZUKU, T., IWAKOSHI, Y. & SAWAI, K. Formation of Lithium-Graphite Intercalation Compounds in Nonaqueous Electrolytes and Their Application as a Negative Electrode for a Lithium Ion (Shuttlecock) Cell. *J. Electrochem. Soc.* **140**, 2490–2498 (1993).
150. Woo, K. C. *et al.* Effect of in-plane density on the structural and elastic properties of graphite intercalation compounds. *Phys. Rev. Lett.* **50**, 182–185 (1983).
151. Basu, S. *et al.* Synthesis and properties of lithium-graphite intercalation compounds. *Mater. Sci. Eng.* **38**, 275–283 (1979).
152. Dahn, J. R., Zheng, T., Liu, Y. & Xue, J. S. Mechanisms for lithium insertion in carbonaceous materials. *Science (80-.).* **270**, 590–593 (1995).
153. Kambe, N. *et al.* Intercalate ordering in first stage graphite-lithium. *Mater. Sci. Eng.* **40**, 1–4 (1979).
154. Xu, B., Wu, M. S., Liu, G. & Ouyang, C. Y. Understanding the effect of the layer-to-layer distance on Li-intercalated graphite. *J. Appl. Phys.* **111**, 124325 (2012).
155. Allart, D., Montaru, M. & Gualous, H. Model of Lithium Intercalation into Graphite by Potentiometric Analysis with Equilibrium and Entropy Change Curves of Graphite Electrode. *J. Electrochem. Soc.* **165**, A380–A387 (2018).
156. Holzwarth, N. A. W., Louie, S. G. & Rabii, S. Lithium-intercalated graphite. Self-consistent electronic structure for stages one, two and three. *Phys. Rev. B* **28**, 1013–1025 (1983).
157. OHZUKU, T., IWAKOSHI, Y. & SAWAI, K. Formation of Lithium-Graphite Intercalation Compounds in Nonaqueous Electrolytes and Their Application as a Negative Electrode for a Lithium Ion (Shuttlecock) Cell. *ChemInform* **24**, no-no (2010).
158. Missyul, A., Bolshakov, I. & Shpanchenko, R. XRD study of phase transformations in lithiated graphite anodes by Rietveld method. *Powder Diffr.* **32**, S56–S62 (2017).
159. Gantenbein, S., Schönleber, M., Weiss, M. & Ivers-Tiffée, E. Capacity fade in lithium-ion batteries and cyclic aging over various state-of-charge ranges. *Sustainability* **11**, 1–15 (2019).
160. Gavilán-Arriazu, E. M. *et al.* Fractional and integer stages of lithium ion-graphite systems: The role of electrostatic and elastic contributions. *Phys. Chem. Chem. Phys.* **22**, 16174–16183 (2020).
161. Balbuen, P. B. & Xuan Wang, Y. *Lithium-ion Batteries: Solid-electrolyte Interphase*. (Imperial College Press, 2004).
162. Li, D. *et al.* Modeling the SEI-Formation on Graphite Electrodes in LiFePO 4 Batteries. *J. Electrochem. Soc.* **162**, A858 (2015).
163. Broussely, M. *et al.* Aging mechanism in Li ion cells and calendar life predictions. *J. Power Sources* **97–98**, 13–21 (2001).
164. Seidl, L., Martens, S., Ma, J., Stimming, U. & Schneider, O. In situ scanning tunneling microscopy studies of the SEI formation on graphite electrodes for Li+-ion batteries. *Nanoscale* **8**, 14004–14014 (2016).
165. Agubra, V. A. & Fergus, J. W. The formation and stability of the solid electrolyte interface on the graphite anode. *J. Power Sources* **268**, 153–162 (2014).
166. Bernardo, P. *et al.* Influence of graphite edge crystallographic orientation on the first lithium intercalation in Li-ion battery. *Carbon* **91**, 458–467 (2015).

167. Zhang, S., Ding, M. S., Xu, K., Allen, J. & Jow, T. R. Understanding solid electrolyte interface film formation on graphite electrodes. *Electrochem. Solid-State Lett.* **4**, 206–208 (2001).

168. Shi, S. *et al.* Direct calculation of Li-ion transport in the solid electrolyte interphase. *J. Am. Chem. Soc.* **134**, 15476–15487 (2012).

169. Zhang, Z. *et al.* Operando Electrochemical Atomic Force Microscopy of Solid-Electrolyte Interphase Formation on Graphite Anodes: The Evolution of SEI Morphology and Mechanical Properties. *ACS Appl. Mater. Interfaces* **12**, 35132–35141 (2020).

170. Yazami, R. & Reynier, Y. F. Mechanism of self-discharge in graphite-lithium anode. *Electrochim. Acta* **47**, 1217–1223 (2002).

171. Aurbach, D., Levi, M. D., Levi, E. & Schechter, A. Failure and stabilization mechanisms of graphite electrodes. *J. Phys. Chem. B* **101**, 2195–2206 (1997).

172. Zhang, S. S., Xu, K. & Jow, T. R. Study of the charging process of a LiCoO2-based Li-ion battery. *J. Power Sources* **160**, 1349–1354 (2006).

173. Finegan, D. P. *et al.* Spatial dynamics of lithiation and lithium plating during high-rate operation of graphite electrodes. *Energy Environ. Sci.* **13**, 2570–2584 (2020).

174. Takahashi, K. & Srinivasan, V. Examination of Graphite Particle Cracking as a Failure Mode in Lithium-Ion Batteries: A Model-Experimental Study. *J. Electrochem. Soc.* **162**, A635–A645 (2015).

175. Li, N. *et al.* Non-equilibrium insertion of lithium ions into graphite. *J. Mater. Chem. A* **9**, 12080–12086 (2021).

176. Aurbach, D., Zinigrad, E., Cohen, Y. & Teller, H. A short review of failure mechanisms of lithium metal and lithiated graphite anodes in liquid electrolyte solutions. *Solid State Ionics* **14**, 405–416 (2002).

177. Sivakkumar, S. R., Nerkar, J. Y. & Pandolfo, A. G. Rate capability of graphite materials as negative electrodes in lithium-ion capacitors. *Electrochim. Acta* **55**, 3330–3335 (2010).

178. Aurbach, D., Markovsky, B., Weissman, I., Levi, E. & Ein-Eli, Y. On the correlation between surface chemistry and performance of graphite negative electrodes for Li ion batteries. *Electrochim. Acta* **45**, 67–86 (1999).

179. Simon, B. *et al.* On the choice of graphite for lithium ion batteries. *J. Power Sources* **81–82**, 312–316 (1999).

180. Janot, R. & Guérard, D. Ball-milling: The behavior of graphite as a function of the dispersal media. *Carbon N. Y.* **40**, 2887–2896 (2002).

181. Zhou, W. L., Ikuhara, Y., Zhao, W. & Tang, J. A transmission electron microscopy study of amorphization of graphite by mechanical milling. *Carbon N. Y.* **33**, 1177–1180 (1995).

182. Ratynski, M. *et al.* Impact of natural and synthetic graphite milling energy on lithium-ion electrode capacity and cycle life. *Carbon* **145**, 82–89 (2019).

183. Billaud, J., Bouville, F., Magrini, T., Villevieille, C. & Studart, A. R. Magnetically aligned graphite electrodes for high-rate performance Li-ion batteries. *Nat. Energy* **1**, 16097 (2016).

184. Nakajima, T. *et al.* Electrochemical behavior of plasma-fluorinated graphite for lithium ion batteries. *J. Power Sources* **104**, 108–114 (2002).

185. Nakajima, T., Koh, M., Singh, R. N. & Shimada, M. Electrochemical behavior of

surface-fluorinated graphite. *Electrochim. Acta* **44**, 2879–2888 (1999).

186. Hai, Y. *et al.* Surface modification of graphite by ion implantation for promoting the electrochemical property in Li-ion batteries. *Appl. Surf. Sci.* **484**, 726–731 (2019).
187. Amaraweera, T. H. N. G. *et al.* Surface modification of natural vein graphite for the anode application in Li-ion rechargeable batteries. *Ionics (Kiel).* **24**, 3423–3429 (2018).
188. Wu, Y. P., Jiang, C., Wan, C. & Holze, R. Anode materials for lithium ion batteries by oxidative treatment of common natural graphite. *Solid State Ionics* **156**, 283–290 (2003).
189. Wu, Y., Jiang, C., Wan, C. & Tsuchida, E. Effects of catalytic oxidation on the electrochemical performance of common natural graphite as an anode material for lithium ion batteries. *Electrochem. commun.* **2**, 272–275 (2000).
190. Li, B., Li, K., Lu, Y., Lu, C. & Ling, L. Surface modification of natural graphite by phenolic resin carbon coating for improvement of cyclic performances in lithium ion batteries. *Energy Sources* **25**, 827–836 (2003).
191. Lee, H. Y. *et al.* Characteristics of carbon-coated graphite prepared from mixture of graphite and polyvinylchloride as anode materials for lithium ion batteries. *J. Power Sources* **101**, 206–212 (2001).
192. Tsumura, T. *et al.* Surface modification of natural graphite particles for lithium ion batteries. *Solid State Ionics* **135**, 209–212 (2000).
193. Yoon, S., Kim, H. & Oh, S. M. Surface modification of graphite by coke coating for reduction of initial irreversible capacity in lithium secondary batteries. *J. Power Sources* **94**, 68–73 (2001).
194. Pan, Q., Wang, H. & Jiang, Y. Natural graphite modified with nitrophenyl multilayers as anode materials for lithium ion batteries. *J. Mater. Chem.* **17**, 329–334 (2007).
195. Pan, Q., Wang, H. & Jiang, Y. Covalent modification of natural graphite with lithium benzoate multilayers via diazonium chemistry and their application in lithium ion batteries. *Electrochem. commun.* **9**, 754–760 (2007).
196. Kottegoda, I. R. M., Kadoma, Y., Ikuta, H., Uchimoto, Y. & Wakihara, M. Enhancement of rate capability in graphite anode by surface modification with zirconia. *Electrochem. Solid-State Lett.* **5**, 0–4 (2002).
197. Nobili, F., Mancini, M., Dsoke, S., Tossici, R. & Marassi, R. Low-temperature behavior of graphite-tin composite anodes for Li-ion batteries. *J. Power Sources* **195**, 7090–7097 (2010).
198. Commodities and Export Projection Divisions Economic and Projections Department. *Tin Handbook*. (Commodities and Export Projection Divisions Economic and Projections Department, 1981).
199. Basic information about tin element, https://education.jlab.org/itselemental/ele050.html; [accessed November 2021]
200. Bowles, J. F. W. Oxides. in *Encyclopedia of Geology (Second Edition).* (eds. Alderton, D. & Elias, S. A. B. T.-E. of G. (Second E.) 428–441 (Academic Press, 2021). doi:https://doi.org/10.1016/B978-0-08-102908-4.00185-5.
201. Pöttgen, R. Stannides and intermetallic tin compounds - Fundamentals and applications. *Zeitschrift fur Naturforsch. - Sect. B J. Chem. Sci.* **61**, 677–698 (2006).
202. Ostrakhovitch, E. A. Tin. in *Handbook on the Toxicology of Metals (Fourth Edition)* (eds. Nordberg, G. F., Fowler, B. A. & Nordberg, M.) 1241–1285 (Academic Press, inc., 2015). doi:10.1016/B978-0-444-59453-2.00056-1.

203. Nogita, K. *et al.* XRD study of the kinetics of β ↔ transformations in tin. *Philos. Mag.* **93**, 3627–3647 (2013).
204. Cornelius, B., Treivish, S., Rosenthal, Y. & Pecht, M. The phenomenon of tin pest: A review. *Microelectron. Reliab.* **79**, 175–192 (2017).
205. Lide, D. L. *CRC Handbook of Chemistry and Physics, 85th Edition, Tom 85*. (CRC Press LLC, 2004).
206. Song, H. *et al.* Thermal Stability Enhancement in Epitaxial Alpha Tin Films by Strain Engineering. *Adv. Eng. Mater.* **21**, 1–7 (2019).
207. Farrow, R. F. C. *et al.* The growth of metastable, heteroepitaxial films of α-Sn by metal beam epitaxy. *J. Cryst. Growth* **54**, 507–518 (1981).
208. Habashi, F. *Encyclopedia of Metalloproteins*. *Encyclopedia of Metalloproteins* (Springer, 2013). doi:10.1007/978-1-4614-1533-6.
209. Molodets, A. M. & Nabatov, S. S. Thermodynamic potentials, diagram of state, and phase transitions of tin on shock compression. *High Temp.* **38**, 715–721 (2000).
210. Hörmann, N. G., Gross, A., Rohrer, J. & Kaghazchi, P. Stabilization of the γ -Sn phase in tin nanoparticles and nanowires. *Appl. Phys. Lett.* **107**, 1–4 (2015).
211. Lide, D. L. *CRC Handbook of Chemistry and Physics*. (CRC Press LLC, 2005).
212. Sangster, J. & Bale, C. W. The Li-Sn (Lithium-Tin) System. *J. Phase Equilibria Diffus.* **19**, 70–75 (1998).
213. Lorie Lopez, J. L., Grandinetti, P. J. & Co, A. C. Phase transformations and capacity fade mechanism in LixSn nanoparticle electrodes revealed by operando 7Li NMR. *J. Mater. Chem. A* **7**, 10781–10794 (2019).
214. Goward, G. R., Taylor, N. J., Souza, D. C. S. & Nazar, L. F. The true crystal structure of Li17M4 (M=Ge, Sn, Pb)-revised from Li22M5. *J. Alloys Compd.* **329**, 82–91 (2001).
215. Obrovac, M. N. & Chevrier, V. L. Alloy Negative Electrodes for Li-Ion Batteries. *Chem. Rev.* **114**, 11444−11502 (2014).
216. Courtney, I. & Tse, J. Ab initio calculation of the lithium-tin voltage profile. *Phys. Rev. B - Condens. Matter Mater. Phys.* **58**, 15583–15588 (1998).
217. Wang, J. *et al.* Structural Evolution and Pulverization of Tin Nanoparticles during Lithiation-Delithiation Cycling. *J. Electrochem. Soc.* **161**, F3019–F3024 (2014).
218. Wang, J., Raistrick, I. D. & Huggins, R. A. Behavior of Some Binary Lithium Alloys As Negative Electrodes in Organic Solvent Based Electrolytes. *J. Electrochem. Soc.* **133**, 457–460 (1984).
219. Ferg, E., Gummow, R. J., de Kock, A. & Thackeray, M. M. Spinel Anodes for Lithium-Ion Batteries. *J. Electrochem. Soc.* **141**, L147–L150 (1994).
220. Dahn, J. R., Courtney, I. A. & Mao, O. Short-range Sn ordering and crystal structure of Li4.4Sn prepared by ambient temperature electrochemical methods. *Solid State Ionics* **111**, 289–294 (1998).
221. Zhang, W. J. A review of the electrochemical performance of alloy anodes for lithium-ion batteries. *J. Power Sources* **196**, 13–24 (2011).
222. Du, Z., Zhang, S., Jiang, T. & Bai, Z. Preparation and characterization of three-dimensional tin thin-film anode with good cycle performance. *Electrochim. Acta* **55**, 3537–3541 (2010).
223. Kawakami, S. & Asao, M. Electrode material for anode of rechargeable lithium

battery, electrode structural body using said electrode material, rechargeable lithium battery using said electrode structural body, process for producing said electrode structural body, and process for. vol. 1 1–86 (2014).

224. Fan, Q., Chupas, P. J. & Whittingham, M. S. Characterization of amorphous and crystalline tin-cobalt anodes. *Electrochem. Solid-State Lett.* **10**, 274–278 (2007).
225. Xin, F. & Whittingham, M. S. Challenges and Development of Tin-Based Anode with High Volumetric Capacity for Li-Ion Batteries. *Electrochem. Energy Rev.* **3**, 643–655 (2020).
226. Yang, J., Winter, M. & Besenhard, J. O. Small particle size multiphase Li-alloy anodes for lithium-ion-batteries. *Solid State Ionics* **90**, 281–287 (1996).
227. Winter, M. & Besenhard, J. O. Electrochemical lithiation of tin and tin-based intermetallics and composites. *Electrochim. Acta* **45**, 31–50 (1999).
228. Kepler, K. D., Vaughey, J. T. & Thackeray, M. M. Copper-tin anodes for rechargeable lithium batteries: An example of the matrix effect in an intermetallic system. *J. Power Sources* **81**–**82**, 383–387 (1999).
229. Mao, O. & Dahn, J. R. Mechanically Alloyed Sn-Fe(-C) Powders as Anode Materials for Li-Ion Batteries: II. The Sn-Fe System. *J. Electrochem. Soc.* **146**, 405–413 (1999).
230. Xu, Y. *et al.* Uniform nano-Sn/C composite anodes for lithium ion batteries. *Nano Lett.* **13**, 470–474 (2013).
231. Kamali, A. R. & Fray, D. J. Tin-based materials as advanced anode materials for lithium ion batteries: A review. *Rev. Adv. Mater. Sci.* **27**, 14–24 (2011).
232. Li, S. *et al.* Yolk-Shell Sn@C Eggette-like Nanostructure: Application in Lithium-Ion and Sodium-Ion Batteries. *ACS Appl. Mater. Interfaces* **8**, 19438–19445 (2016).
233. Li, S. *et al.* Comparison of Si/C, Ge/C and Sn/C composite nanofiber anodes used in advanced lithium-ion batteries. *Solid State Ionics* **254**, 17–26 (2014).
234. Shafiei, M. & Alpas, A. T. Electrochemical performance of a tin-coated carbon fibre electrode for rechargeable lithium-ion batteries. *J. Power Sources* **196**, 7771–7778 (2011).
235. Wang, C. *et al.* Three-dimensional Sn-graphene anode for high-performance lithium-ion batteries. *Nanoscale* **5**, 10599–10604 (2013).
236. Lee, K. T., Jung, Y. S. & Oh, S. M. Synthesis of tin-encapsulated spherical hollow carbon for anode material in lithium secondary batteries. *J. Am. Chem. Soc.* **125**, 5652–5653 (2003).
237. Veeraraghavan, B., Durairajan, A., Haran, B., Popov, B. & Guidotti, R. Study of Sn-Coated Graphite as Anode Material for Secondary Lithium-Ion Batteries. *J. Electrochem. Soc.* **149**, A675 (2002).
238. Egashira, M., Takatsuji, H., Okada, S. & Yamaki, J. I. Properties of containing Sn nanoparticles activated carbon fiber for a negative electrode in lithium batteries. *J. Power Sources* **107**, 56–60 (2002).
239. Lucas, I. T., Pollak, E. & Kostecki, R. In situ AFM studies of SEI formation at a Sn electrode. *Electrochem. commun.* **11**, 2157–2160 (2009).
240. Eom, K. S. *et al.* Improved stability of nano-Sn electrode with high-quality nano-SEI formation for lithium ion battery. *Nano Energy* **12**, 314–321 (2015).
241. Ayache, M., Syzdek, J., Lucas, I., Norberg, N. & Kostecki, R. Interfacial Studies of the SEI Layer on a Tin Electrode. *Meet. Abstr.* **MA2014-02**, 222 (2014).
242. Baek, S. W., Hong, S. J., Kim, D. W. & Song, S. W. Studies of interfacial reactions on

thin film electrodes of Sn during initial cycling using infrared spectroscopy. *J. Power Sources* **189**, 660–664 (2009).

243. Besenhard, J. O., Yang, J. & Winter, M. Will advanced lithium-alloy anodes have a chance in lithium-ion batteries? *J. Power Sources* **68**, 87–90 (1997).
244. Wagner, M. R. *et al.* Electrolyte decomposition reactions on tin- And graphite-based anodes are different. *Electrochem. Solid-State Lett.* **7**, 2–7 (2004).
245. Wilamowska-Zawlocka, M. *et al.* Silicon oxycarbide ceramics as anodes for lithium ion batteries: influence of carbon content on lithium storage capacity. *RSC Adv.* **6**, 104597–104607 (2016).
246. Pradeep, V. S., Graczyk-Zajac, M., Riedel, R. & Soraru, G. D. New insights in to the lithium storage mechanism in polymer derived SiOC anode materials. *Electrochim. Acta* **119**, 78–85 (2014).
247. Li, J., Lewis, R. B. & Dahn, J. R. Sodium Carboxymethyl Cellulose: A Potential Binder for Si Negative Electrodes for Li-Ion Batteries. *Electrochem. Solid-State Lett.* **10**, A17 (2007).
248. Sorarù, G. D. *et al.* Chemical Durability of Silicon Oxycarbide Glasses. *J. Am. Ceram. Soc.* **85**, 1529–1536 (2002).
249. Bréquel, H. *et al.* Systematic structural characterization of the high-temperature behavior of nearly stoichiometric silicon oxycarbide glasses. *Chem. Mater.* **16**, 2585–2598 (2004).
250. Graetsch, H., Mosset, A. & Gies, H. XRD and 29Si MAS-NMR study on some non-crystalline silica minerals. *J. Non. Cryst. Solids* **119**, 173–180 (1990).
251. Sadezky, A., Muckenhuber, H., Grothe, H., Niessner, R. & Pöschl, U. Raman microspectroscopy of soot and related carbonaceous materials: Spectral analysis and structural information. *Carbon* **43**, 1731–1742 (2005).
252. Mera, G., Navrotsky, A., Sen, S., Kleebe, H. J. & Riedel, R. Polymer-derived SiCN and SiOC ceramics-structure and energetics at the nanoscale. *J. Mater. Chem. A* **1**, 3826–3836 (2013).
253. Eckmann, A. *et al.* Probing the nature of defects in graphene by Raman spectroscopy. *Nano Lett.* **12**, 3925–3930 (2012).
254. Ferrari, A. C. Raman spectroscopy of graphene and graphite: Disorder, electron-phonon coupling, doping and nonadiabatic effects. *Solid State Commun.* **143**, 47–57 (2007).
255. Kolb, R., Fasel, C., Liebau-Kunzmann, V. & Riedel, R. SiCN/C-ceramic composite as anode material for lithium ion batteries. *J. Eur. Ceram. Soc.* **26**, 3903–3908 (2006).
256. Graczyk-Zajac, M., Fasel, C. & Riedel, R. Polymer-derived-SiCN ceramic/graphite composite as anode material with enhanced rate capability for lithium ion batteries. *J. Power Sources* **196**, 6412–6418 (2011).
257. Knozowski, D. *et al.* New insights on lithium storage in silicon oxycarbide/carbon composites: impact of microstructure on electrochemical properties. *Compos. Part B Eng.* **225**, 109302 (2021).
258. Bahloul-Hourlier, D., Latournerie, J. & Dempsey, P. Reaction pathways during the thermal conversion of polysiloxane precursors into oxycarbide ceramics. *J. Eur. Ceram. Soc.* **25**, 979–985 (2005).
259. Latournerie, J., Dempsey, P., Hourlier-Bahloul, D. & Bonnet, J. P. Silicon oxycarbide glasses: Part 1-thermochemical stability. *J. Am. Ceram. Soc.* **89**, 1485–1491 (2006).

260. Knozowski, D., Graczyk-Zajac, M., Trykowski, G. & Wilamowska-Zawłocka, M. Silicon oxycarbide-graphite electrodes for high-power energy storage devices. *Materials* **13**, 4302 (2020).
261. Bashouti, M. Y., Paska, Y., Puniredd, R. & Stelzner, T. Silicon nanowires terminated with methyl functionalities exhibit stronger Si – C bonds than equivalent 2D surfaces. *Phys. Chem. Chem. Phys.* **11**, 3845–3848 (2009).
262. Blyth, R. I. R., Buqa, H., Netzer, F. P., Ramsey, M. G. & Besenhard, J. O. XPS studies of graphite electrode materials for lithium ion batteries. *Appl. Surf. Sci.* **167**, 99–106 (2000).
263. Anderson, R. T. *et al.* Direct Conversion of Hydride- to Siloxane-Terminated Silicon Quantum Dots. *J. Phys. Chem. C* **120**, 25822–25831 (2016).
264. Abass, M. A., Syed, A. A., Gervais, C. & Singh, G. Synthesis and electrochemical performance of a polymer-derived silicon oxycarbide/boron nitride nanotube composite. *RSC Adv.* **7**, 21576–21584 (2017).
265. Renlund, G. M., Prochazka, S. & Doremus, R. H. Silicon oxycarbide glasses: Part II. Structure and properties. *J. Mater. Res.* **6**, 2723–2734 (1991).
266. Wu, N. L. & Phillips, J. XRD evidence of preferental orientation of platinium crystallites on graphite. *Surf. Sci.* **184**, 463–482 (1987).
267. Liou, Y. J. & Huang, W. J. High Temperature Phase Transitions of Graphene Oxide Paper from Graphite Oxide Solution. *J. Mater. Sci. Technol.* **30**, 1088–1091 (2014).
268. Kleebe, H. J. & Blum, Y. D. SiOC ceramic with high excess free carbon. *J. Eur. Ceram. Soc.* **28**, 1037–1042 (2008).
269. Swain, I. P., Sadual, N. & Behera, S. K. Porosity and nanostructure of silicon oxycarbide derived carbon. *Open Ceram.* **6**, 100116 (2021).
270. Lv, P. *et al.* SiOx-C dual-phase glass for lithium ion battery anode with high capacity and stable cycling performance. *J. Power Sources* **274**, 542–550 (2015).
271. Graczyk-Zajac, M., Toma, L., Fasel, C. & Riedel, R. Carbon-rich SiOC anodes for lithium-ion batteries : Part I . Influence of material UV-pre-treatment on high power properties. *Solid State Ionics* **225**, 522–526 (2012).
272. MSE Supplies product information. https://www.msesupplies.com/products/natural-graphite-powder-lithium-ion-battery-anode-a?variant=7138017860; [accessed January 2021] (2021).
273. Pyrotek Inc. product information. https://www.pyrotek.com/primary-solutions/battery-materials; [accessed January 2021] (2021).
274. Mao, C. *et al.* Selecting the Best Graphite for Long-Life, High-Energy Li-Ion Batteries. *J. Electrochem. Soc.* **165**, A1837–A1845 (2018).
275. Bai, L. Z. *et al.* A comparative study of electrochemical performance of graphene sheets, expanded graphite and natural graphite as anode materials for lithium-ion batteries. *Electrochim. Acta* **107**, 555–561 (2013).
276. Putra, R. N. *et al.* High-rate sodium insertion/extraction into silicon oxycarbide-reduced graphene oxide. *New J. Chem.* **44**, 14035–14040 (2020).
277. Markovsky, B., Levi, M. D. & Aurbach, D. The basic electroanalytical behavior of practical graphite-lithium intercalation electrodes. *Electrochim. Acta* **43**, 2287–2304 (1998).
278. Zhang, S. S., Xu, K. & Jow, T. R. EIS study on the formation of solid electrolyte interface in Li-ion battery. *Electrochim. Acta* **51**, 1636–1640 (2006).

279. Kaspar, J., Graczyk-Zajac, M. & Riedel, R. Determination of the chemical diffusion coefficient of Li-ions in carbon-rich silicon oxycarbide anodes by electro-analytical methods. *Electrochim. Acta* **115**, 665–670 (2014).

280. Funabiki, A. *et al.* Impedance Study on the Electrochemical Lithium Intercalation into Natural Graphite Powder. *J. Electrochem. Soc.* **145**, 172–178 (1998).

281. Gnanaraj, J. S. *et al.* Comparison Between the Electrochemical Behavior of Disordered Carbons and Graphite Electrodes in Connection with Their Structure. *J. Electrochem. Soc.* **148**, A525 (2001).

282. Liu, Z. *et al.* Monodisperse and homogeneous SiOx/C microspheres: A promising high-capacity and durable anode material for lithium-ion batteries. *Energy Storage Mater.* **13**, 112–118 (2018).

283. Xiao, W. *et al.* Preparation of core-shell structural single ionic conductor SiO 2@Li+ and its application in PVDF-HFP-based composite polymer electrolyte. *Electrochim. Acta* **85**, 612–621 (2012).

284. Zheng, Y. *et al.* Rational design of the pea-pod structure of SiO: x/C nanofibers as a high-performance anode for lithium ion batteries. *Inorg. Chem. Front.* **7**, 1762–1769 (2020).

285. Chen, K. H. *et al.* Enabling 6C Fast Charging of Li-Ion Batteries with Graphite/Hard Carbon Hybrid Anodes. *Adv. Energy Mater.* **11**, 1–12 (2021).

286. Erb, D. & Lu, K. Additive and pyrolysis atmosphere effects on polysiloxane-derived porous SiOC ceramics. *J. Eur. Ceram. Soc.* **37**, 4547–4557 (2017).

287. Erb, D. & Lu, K. Effect of additive structure and size on SiO2 formation in polymer-derived SiOC ceramics. *J. Am. Ceram. Soc.* **101**, 5378–5388 (2018).

288. Zhang, R., Zhang, Z., Amine, K. & West, R. Modification of polymethylhydrosiloxane by dehydrocoupling reactions catalyzed by transition metal complexes: Evidence for the preservation of linear siloxane structures. *Silicon Chem.* **2**, 271–277 (2005).

289. Wang, J. *et al.* Metal-containing ceramic nanocomposites synthesized from metal acetates and polysilazane. *Open Ceram.* **1**, 100001 (2020).

290. Malinowski, J., Zych, D., Jacewicz, D., Gawdzik, B. & Drzeżdżon, J. Application of coordination compounds with transition metal ions in the chemical industry—a review. *Int. J. Mol. Sci.* **21**, 1–26 (2020).

291. Hourlier, D., Venkatachalam, S., Ammar, M. R. & Blum, Y. Pyrolytic conversion of organopolysiloxanes. *J. Anal. Appl. Pyrolysis* **123**, 296–306 (2017).

292. Caminoa, G., Lomakin, S. M. & Lazzari, M. Polydimethylsiloxane thermal degradation. Part 1. Kinetic aspects. *Polymer (Guildf).* **42**, 2395–2402 (2001).

293. Knozowski, D. *et al.* Silicon oxycarbide-tin nanocomposite derived from a UV crosslinked single source preceramic precursor as high-performance anode materials for Li-ion batteries. *Appl. Mater. Today* **27**, 101424 (2022).

294. Dubey, R. J. -C. *et al.* Silicon Oxycarbide—Tin Nanocomposite as a High-Power-Density Anode for Li-Ion Batteries. *Adv. Sci.* 1901220 (2019) doi:10.1002/advs.201901220.

295. Wang, G. *et al.* Sn/graphene nanocomposite with 3D architecture for enhanced reversible lithium storage in lithium ion batteries. *J. Mater. Chem.* **19**, 8378–8384 (2009).

296. Kroll, P. Tracing Reversible and Irreversible Li Insertion in SiCO Ceramics with Modeling and Ab-Initio Simulations. *MRS Proc.* **1313**, (2011).

297. Liang, S., Cheng, Y. J., Zhu, J., Xia, Y. & Müller-Buschbaum, P. A Chronicle Review of Nonsilicon (Sn, Sb, Ge)-Based Lithium/Sodium-Ion Battery Alloying Anodes. *Small Methods* **4**, (2020).
298. Knozowski, D. *et al.* Material Design and Optimisation of Electrochemical Li-Ion Storage Properties of Ternary Silicon Oxycarbide / Graphite / Tin Nanocomposites. (2022).
299. Dubey, R. J. C. *et al.* Silicon oxycarbide-antimony nanocomposites for high-performance Li-ion battery anodes. *Nanoscale* **12**, 13540–13547 (2020).
300. Zhang, H. & Patano, C. G. Synthesis and Characterization of Silicon Oxycarbide Glasses. *J. Am. Ceram. Soc.* **73**, 958–963 (1990).
301. Leveîque, G. & Abanades, S. Thermodynamic and kinetic study of the carbothermal reduction of SnO 2 for solar thermochemical fuel generation. *Energy and Fuels* **28**, 1396–1405 (2014).
302. Padilla, R. & Sohn, H. Y. The reduction of stannic oxide with carbon. *Metall. Trans. B* **10**, 109–115 (1979).
303. Yan, Y., Ben, L., Zhan, Y. & Huang, X. Nano-Sn embedded in expanded graphite as anode for lithium ion batteries with improved low temperature electrochemical performance. *Electrochim. Acta* **187**, 186–192 (2016).
304. Levi, M. D. & Aurbach, D. Simultaneous measurements and modeling of the electrochemical impedance and the cyclic voltammetric characteristics of graphite electrodes doped with lithium. *J. Phys. Chem. B* **101**, 4630–4640 (1997).
305. Smrekar, S. *et al.* A Mapping of the Physical and Electrochemical Properties of Composite Lithium-Ion Batteries Anodes Made from Graphite, Sn, and Si. *Batter. Supercaps* **3**, 1248–1256 (2020).
306. Böhme, S., Edström, K. & Nyholm, L. On the electrochemistry of tin oxide coated tin electrodes in lithium-ion batteries. *Electrochim. Acta* **179**, 482–494 (2015).
307. Dufficy, M. K., Huang, S. Y., Khan, S. A. & Fedkiw, P. S. Effects of composition and structure on the performance of tin/graphene-containing carbon nanofibers for Li-ion anodes. *RSC Adv.* **7**, 15428–15438 (2017).
308. Ruggeri, I., Martin, J., Wohlfahrt-Mehrens, M. & Mancini, M. Interfacial kinetics and low-temperature behavior of spheroidized natural graphite particles as anode for Li-ion batteries. *J. Solid State Electrochem.* (2021) doi:10.1007/s10008-021-04974-2.
309. Zhang, P. *et al.* Influence of Current Density on Graphite Anode Failure in Lithium-Ion Batteries. *J. Electrochem. Soc.* **166**, A5489–A5495 (2019).
310. Vallachira Warriam Sasikumar, P. *et al.* Structural Design of Polymer-Derived SiOC Ceramic Aerogels for High-Rate Li Ion Storage Applications. *J. Am. Ceram. Soc.* **99**, 2977–2983 (2016).
311. Pradeep, V. S., Ayana, D. G., Graczyk-Zajac, M., Soraru, G. D. & Riedel, R. High Rate Capability of SiOC Ceramic Aerogels with Tailored Porosity as Anode Materials for Li-ion Batteries. *Electrochim. Acta* **157**, 41–45 (2015).

List of figures

List of tables

Publications

1. **Knozowski D.**, Warriam. P.V.S., Dubey R., Aebli M., Kravchyk K.V., Trykowski G., Kovalenko M.V., Graule T., Wilamowska-Zawłocka M., Blugan G., (2022). *Silicon oxycarbide-tin nanocomposite derived from a UV crosslinked single source preceramic precursor as high-performance anode materials for Li-ion batteries*, Appl. Mater, Today, 27, 101424, https://doi.org/10.1016/j.apmt.2022.101424
2. **Knozowski, D.**; Vallachira Warriam Sasikumar, P.; Madajski, P.; Blugan, G.; Gazda, M.; Kovalska, N.; Wilamowska-Zawłocka, M. (2022). *Material Design and Optimisation of Electrochemical Li-Ion Storage Properties of Ternary Silicon Oxycarbide/Graphite/Tin Nanocomposites*, Nanomaterials, 12 (3), 410, https://doi.org/10.3390/nano12030410
3. **Knozowski, D.**; Graczyk-Zajac, M.; Vrankovic, D.; Trykowski, G.; Sawczak, M.; De Carolis, D.M.; Wilamowska-Zawłocka, M., (2021). *New insights on lithium storage in silicon oxycarbide/carbon composites: Impact of microstructure on electrochemical properties*, Compos. B. Eng, 225, 109302, https://doi.org/10.1016/j.compositesb.2021.109302
4. **Knozowski D.**, Graczyk-Zajac M., Trykowski G., Wilamowska-Zawłocka M., (2020). *Silicon Oxycarbide-Graphite Electrodes for High-Power Energy Storage Devices*, Materials, 13(19), 4302, https://doi.org/10.3390/ma13194302
5. **Knozowski, D.**, Wilamowska-Zawłocka, M., & Klugmann-Radziemska, E. (2019). *Elektrolity stosowane w kondensatorach elektrochemicznych.* Przemysł Chemiczny, 98(3), 429-433. https://doi.org/10.15199/62.2019.3.14

Conferences

1. Oral presentation „Overview of electrode materials for supercapacitor applications" during III Interdyscyplinarna Akademicka Konferencja Ochrony Środowiska in Gdańsk, 13-15.04.2018. Authors: **Dominik Knozowski**, Monika Wilamowska-Zawłocka, Ewa Klugmann-Radziemska
2. Poster presentation „Influence of electrolyte type on electrochemical performance of supercapacitors" during III Interdyscyplinarna Akademicka Konferencja Ochrony Środowiska in Gdańsk, 13-15.04.2018. Authors: **Dominik Knozowski**, Monika Wilamowska-Zawłocka, Ewa Klugmann-Radziemska
3. Poster presentation „Badania impedancyjne kompozytowych materiałów elektrodowych w różnych elektrolitach wodnych" during XV Symposium "Fast Ionic Conductors" in Gdańsk, 26-29.09.2018. Authors: **Dominik Knozowski**, Mateusz Leśniewski, Monika Wilamowska-Zawłocka
4. Poster presentation „Silicon Oxycarbide-Graphite Composite For High Power Batteries and Hybrid Devices" during 6th International Symposium on Enhanced Electrochemical Capacitors in Nantes, 5-10.05.2019. Authors: **Dominik Knozowski**, Monika Wilamowska-Zawłocka, Ewa Klugmann-Radziemska
5. Poster presentation „Silicon Oxycarbide-Graphite Composites as Negative Electrodes for Lithium-Ion Capacitors" during 62. Zjazd Naukowego Polskiego Towarzystwa Chemicznego in Warsaw, 2-6.09.2019. Authors: **Dominik Knozowski**, Magdalena Graczyk-Zajac, Ralf Riedel, Ewa Klugmann-Radziemska, Monika Wilamowska-Zawłocka